ADVANCED COMPUTATIONAL TECHNIQUES FOR UNSTEADY AERODYNAMIC-DYNAMIC INTERACTIONS OF BLUFF BODIES

A Thesis
Presented to
The Academic Faculty

by

Daniel T. Prosser

In Partial Fulfillment
of the Requirements for the Degree
Doctor of Philosophy in the
School of Aerospace Engineering

Georgia Institute of Technology
August 2015

ADVANCED COMPUTATIONAL TECHNIQUES FOR UNSTEADY AERODYNAMIC-DYNAMIC INTERACTIONS OF BLUFF BODIES

Approved by:

Professor Marilyn Smith,
Committee Chair
School of Aerospace Engineering
Georgia Institute of Technology

Professor Ari Glezer
School of Mechanical Engineering
Georgia Institute of Technology

Professor Mark Costello
School of Aerospace Engineering
Georgia Institute of Technology

Dr. Marvin Moulton
Aviation and Missile Research,
Development, and Engineering Center
U.S. Army

Professor Daniel Schrage
School of Aerospace Engineering
Georgia Institute of Technology

Dr. Thomas Thompson
Aviation and Missile Research,
Development, and Engineering Center
U.S. Army

Date Approved: May 21, 2015

Dedicated to my wife,

Irma Prosser.

ACKNOWLEDGEMENTS

I would first like to thank my advisor, Prof. Marilyn Smith, for supporting me as a graduate student. Not only has she provided the financial means for me to do my research, but she has also been instrumental in pushing me to always aim high with my work. I am extremely grateful that she took time every week to sit down with me to discuss my research and provide guidance. She has also made it a point to thoroughly read through and edit all my papers, including this thesis, and they always were improved because of that.

The U.S. Army/Navy/NASA Vertical Lift Rotorcraft Center of Excellence has provided the funding for my research under Task 10, "Dynamic-Aerodynamic Interactions of Bluff Bodies: Computational Investigations." Without that assistance, I never would have been able to finish my degree. A number of people connected with this project have been mentors to me, including Dr. Tom Thompson and Dr. Marty Moulton of AMRDEC, Judah Milgram of ONR, and Gloria Yamauchi of NASA. I would also like to thank the experts in the field who have provided guidance and feedback on my research, including Dr. Dave Peters, Luigi Cicolani, Dan Mattle, Christina Ivler and Aviv Rosen. I would also like to thank the Aeroflightdynamics Directorate of the US Army for providing flight test data for validation of my research.

Though I've put in four years of work here at Georgia Tech, I can't really claim any successes as my own. All credit goes to God and his son Jesus, "Who is the image of the invisible God, the firstborn of every creature: for by him were all things created, that are in heaven, and that are in earth...all things were created by him and for him: and he is before all things, and by him all things consist" (Colossians 1:15–17). It is reassuring and somewhat humbling to recognize that God already holds the answer to any mystery of creation that I may devote time to studying. Furthermore, the Holy Spirit has been a divine comfort throughout this process, even in times when I questioned whether I'd be able to make it through. Knowing that "all things work together for good to them that love God"

(Romans 8:28) has provided the assurance in those times that, even if I didn't succeeed in my research, he had brought me here for a greater purpose. Now that he has graciously brought me to the last step in this process, I thank him and look forward to continuing in fellowship with him down the road of life.

I would be remiss if I didn't thank my wife. She has been my biggest supporter and encourager, and she has patiently dealt with many evenings when I had to work or study late. I think I might have gone crazy without her, or at least I wouldn't have been nearly as happy throughout the process. Also to my parents, for their loving support, their financial support of most of my undergraduate education, and for always encouraging me to pursue a career that I would really love. I would similarly like to recognize my siblings, Nathan, Jared, and Emily; my father-in-law, Milton, and mother-in-law, Karen; my brothers-in-law, Milton and Daniel, and so many other relatives who have been an encouragement to me. Similarly, my church family at University Baptist Church has truly been like a family to me since I've been here; I've been truly blessed to have found such a good church. Specifically, Pastor Gary Ledford and his wife Linda, Michael and Jennifer, Josh and Caitlyn, Tim and Mary, Ricky and Rhonda, Caleb, Bradley, Grayson, and so many others that I don't have room to mention: thank you all!

Finally, I would like to recognize some others who have been friends and mentors in my professional life at Georgia Tech. To Rajiv, Eliot, and Nic, who countless times provided advice and offered their high levels of expertise in computational fluid dynamics, not to mention much-needed diversion and companionship. All the others who have been in the lab during my time have also been great friends to me as well and provided advice. Thank you, and good luck to those of you still continuing at Georgia Tech. Last but not least, the undergraduate students Terry Ma and James Clinton have assisted in the implementation and testing of several improvements to the reduced-order model.

TABLE OF CONTENTS

DEDICATION . . . . . **iii**

ACKNOWLEDGEMENTS . . . . . **iv**

LIST OF TABLES . . . . . **ix**

LIST OF FIGURES . . . . . **x**

NOMENCLATURE . . . . . **xv**

SUMMARY . . . . . **xix**

I BACKGROUND **1**

1.1 Motivation 1

1.2 Overview of Bluff Body Aerodynamic-Dynamic Interactions 3

1.3 Bluff Body Aerodynamics 4

1.3.1 Cylindrical Bodies 4

1.3.2 Prismatic Bodies 6

1.3.3 Computational State of the Art 9

1.4 Dynamic Models for Bluff Bodies 12

1.5 Thesis Objectives 16

II COMPUTATIONAL TOOLS **19**

2.1 FUN3D 19

2.2 FUN3D/6-DoF Coupling 21

2.2.1 Evaluation of Integration Schemes 22

2.3 GTABB 25

2.4 Cable Modeling 26

2.4.1 Parallel Cables 27

2.4.2 Serial Cables 28

III THREE-DIMENSIONAL BLUFF BODY AERODYNAMICS **33**

3.1 Configurations 33

3.2 Computational Grids 35

3.3 Forces and Moments 36

3.4 Unsteady Flow Characteristics . . . 46
3.5 Time-Averaged Flow Characteristics . . . 49
3.5.1 Influence on Forces and Moments . . . 54
3.6 Empirical Modeling of Shear Layer Behavior . . . 57
IV DYNAMIC BLUFF BODY SIMULATIONS . . . 64
4.1 Prescribed Motion . . . 64
4.1.1 Description of Configurations . . . 64
4.1.2 Forces and Moments in Spinning Motion . . . 66
4.1.3 Forces and Moments in Pendulum Motion . . . 71
4.2 Tethered Load Simulations . . . 73
4.2.1 Description of Configurations . . . 74
4.2.2 Simulation Results . . . 75
4.2.3 Computational Cost . . . 81
V REDUCED-ORDER AERODYNAMIC MODELING . . . 82
5.1 Quasi-Steady Aerodynamics . . . 83
5.1.1 Crossflow Corrections . . . 86
5.2 Vortex Shedding . . . 87
5.3 Unsteady Aerodynamics Due to Body Motion . . . 92
VI MODEL VALIDATION AND TETHERED LOAD STABILITY ANALYSIS . . . 98
6.1 CFD Validation of Reduced-Order Aerodynamics . . . 98
6.1.1 Quasi-Steady Data from Other Sources . . . 101
6.1.2 Aerodynamic Yaw Moment Damping . . . 102
6.2 CFD Validation of Reduced-Order Dynamics . . . 104
6.2.1 Computational Cost . . . 110
6.3 UAV Flight Test Comparisons . . . 112
6.4 Full Scale Flight Tests and Stability . . . 116
6.4.1 Force and Moment Comparisons . . . 118
6.4.2 Assessment of Unsteady Aerodynamics . . . 120
6.4.3 Coupled Helicopter-Load Simulations . . . 123
6.4.4 Quantifying Stability . . . 127

6.4.5 Effect of Vortex Shedding 128
6.4.6 Virtual Wind Tunnel Evaluations 129
6.5 Extension to Complex Bluff Bodies 134
VII SENSITIVITY ANALYSIS 136
7.1 Computational Fluid Dynamics Sensitivities 136
7.1.1 Grid Convergence 136
7.1.2 Temporal Convergence 140
7.1.3 Sensitivity to Mounting Apparatus 141
7.1.4 Sensitivity to Slow Rotation 146
7.1.5 Sensitivity to Tunnel Blockage 147
7.2 Reduced-Order Model Uncertainty Quantification 154
7.2.1 Identification of Errors 154
VIII CONCLUSIONS 160
8.1 Recommendations for Future Work 164
REFERENCES 168
VITA 177

LIST OF TABLES

1 Coefficients for the Adams-Bashforth schemes. 23

2 Rectangular prism dimensions and flow conditions. 33

3 Cylinder dimensions and flow conditions. 34

4 Kinematic parameters for simulation of a spinning rectangular prism. 66

5 Kinematic parameters for simulation of a rectangular prism in pendulum motion. 66

6 Comparison between high-fidelity pendulum force and moment coefficients and the quasi-steady prediction. 73

7 Bluff body properties for the tethered load simulations. 75

8 Operating conditions for the tethered load simulations. 76

9 Model parameters for low- and high-frequency approximations of the Theodorsen function. 95

10 Flight test parameters. 116

11 CONEX cargo container configuration. 117

12 Comparison of mean drag, side force, and yaw moment for wind tunnel and free air numerical experiments. 149

LIST OF FIGURES

1 UH-60 Blackhawk in flight with CONEX tethered load [1]. 2

2 Lift curve for a two-dimensional rectangular bluff body with an aspect ratio of 2.0 [2]. 7

3 Illustration of shear layer behavior for a rectangular bluff body. (1) Fully separated shear layer, (2) reattaching shear layer, and (3) fully attached flow. 8

4 Numerical solution for a spring-mass system with different integration schemes and time step sizes. 24

5 GTABB flowchart. 26

6 Model of a tethered load suspended by four cables in parallel. 27

7 Tether systems requiring serial cables. 29

8 Serial cable element free-body diagram. 29

9 Bluff body types modeled and the full-scale sling loads they represent [3]. . 34

10 Convention for the angles α and β. 35

11 Side views of bluff body overset grids. 37

12 Rectangular prism computed force and moment coefficients and comparison with experimental data [4, 5]. Dashed lines represent min and max values for the unsteady simulations. 39

13 Comparison of the current computations in normal and axial flow configurations with experimental data by Wieselsberger [6], Hoerner [7], and previous computations by Lynch and Smith [8]. 41

14 Time-averaged contours of pressure coefficient and streamlines in a top-down view for the axial flow condition of the circular cylinder. 43

15 Time-averaged force and moment coefficients for circular cylinders over the range $\beta = 0^\circ - 90^\circ$, with vertical bars denoting RMS fluctuations. 45

16 RMS of force and moment coefficient fluctuations over the range of yaw angles from 0° – 90°. 47

17 Power spectrum of velocity magnitude for a cylinder with an aspect ratio of 1.0, Reynolds number (based on diameter) of 1.0×10^6, and yaw angle of 0°. 48

18 Dominant Strouhal frequencies for finite cylinders and rectangular prisms as a function of yaw angle and Reynolds number. Experimental data from Ref. [9]. 49

19 Illustration of shear layer behavior for a rectangular bluff body. (1) Fully separated shear layer, (2) reattaching shear layer, and (3) fully attached flow (reprint of Fig. 3 for convenience). 50

20 Unsteady flow snapshots on various short bluff bodies. Flow direction is from right to left. 50

21 Unsteady and time-averaged reattachment behavior for $L/D = 1$ cylinder, $Re_D = 0.96 \times 10^5$, $\beta = 2.5°$; top view shown. 51

22 Pressure distributions for reattaching and attached flow on flat cylinder faces. 52

23 Normal force and yaw moment coefficients on individual faces of the rectangular prism. The extents of the three shear layer behaviors from Fig. 19 are labeled. 54

24 Normal force and yaw moment coefficients on flat faces of the cylinder. The extents of the three shear layer behaviors from Fig. 19 are labeled. 56

25 Normal force and yaw moment coefficients on curved faces of the cylinder. The extents of the three shear layer behaviors from Fig. 19 are labeled. . . 56

26 Typical pressure distributions and definition of empirical modeling parameters. 58

27 Depiction of the incidence angle, ϕ, on two different faces, and ϕ_R on the top face. ϕ_R is equivalent to ϕ when reattachment first takes place. Arrows represent the freestream flow direction. 59

28 Normalized reattachment distance as a function of incidence angle. 2-D rectangular prism data from Robertson [10]. 60

29 Reattachment parameter variations with ϕ and empirical curve fits. 61

30 Variation of x_0 with ϕ and empirical curve fit. 62

31 Prescribed motion parameters as functions of time for spinning and pendulum simulations. 65

32 Drag, side force, and yaw moment coefficient from two revolutions of a high-fidelity computations of a spinning rectangular prism at a reduced frequency of 0.02. 67

33 Illustration of shear layer behavior for a rectangular bluff body. (1) Fully separated shear layer, (2) reattaching shear layer, and (3) fully attached flow (reprint of Fig. 3 for convenience). 68

34 Pressure distributions on left, right, and back sides of the rectangular prism in static and spinning configurations. 69

35 Drag, side force, and yaw moment coefficient from high-fidelity computations of a rectangular prism in pendulum motion defined in Table 5. 72

36 Illustration of the wind tunnel and tethered load configuration and the orientations of the relevant frames. 75

37 Euler angles from dynamic high-fidelity simulations for the CONEX rectangular prism. 77

38 Flow field visualizations at different points in time for the 40 mph case. Coloring by vorticity magnitude. 79

39 Instantaneous pressure distributions at different points in time for the 40 mph case. 80

40 Reduced-order aerodynamic model components. 83

41 Variation of side force with yaw angle for a 3-D rectangular prism, illustrating RBF interpolation and revealing significant nonlinearities. 85

42 Yaw moment comparison between HRLES and the reduced-order model with and without crossflow corrections. 86

43 Effect of modeling vortex shedding terms in a dynamic simulation of a short rectangular prism. 89

44 Frequency-domain transformation of yaw moment in a dynamic simulation of a short rectangular prism. 90

45 Shedding phases from three separate simulations and best-fit normal distribution: $\mu = 3.14$, $\sigma = 1.62$. 93

46 Response of the frequency-domain transfer function and comparison with classical unsteady aerodynamic theory (comparison of Eqs. 22 and 23). . . 95

47 Verification results for the RT Jones unsteady aerodynamic model. 97

48 Comparison between high-fidelity and reduced-order aerodynamics; 25 mph tunnel speed. For clarity, vortex shedding effects have been left out of the reduced-order results. 99

49 Comparison between high-fidelity and reduced-order aerodynamics; 40 mph tunnel speed. For clarity, vortex shedding effects have been left out of the reduced-order results. 100

50 Yaw moment for the 25-mph case with quasi-steady data from high-fidelity simulation and from wind tunnel data [4]. 102

51 Yaw moment for the 40-mph case with and without an aerodynamic yaw rate damping term. 103

52 Yaw comparisons at 25-mph tunnel speed, high-fidelity simulation vs. reduced-order model. 105

53 Yaw comparisons at 40-mph tunnel speed, high-fidelity simulation vs. reduced-order model. 107

54 Trailing angle comparisons between high-fidelity and reduced-order simulations. 109

55 Photographs of the GTMAX helicopter and tethered load. Figure used by permission of the UAV Research Facility at the Georgia Institute of Technology. 114

56 Flight test data from the UAV Research Facility and comparison between measured and simulated load positions. 115

57 Depiction of longitudinal (θ_c) and lateral (ϕ_c) cable angles. 117

58 Comparison of forces and moments versus yaw angle, 112 knots (Flight 134 Record 8). 119

59 Fast Fourier Transforms of side force, 112 knots (Flight 134 Record 8). . . . 120

60 Comparison of yaw moments for different flight speeds and reduced frequencies. 122

61 Cable angles and yaw rate at 105 knots (Flight 132 Record 10a). 124

62 Cable angles and yaw rate at 112 knots (Flight 134 Record 8). 125

63 Cable angle excursions and mean spin rate as a function of flight speed. . . 126

64 Integrated power spectral density of cable angles as a function of flight speed. 128

65 Cable angles and yaw rate at 112 knots (Flight 134 Record 8): simulated results with and without vortex shedding. 130

66 Cable angles and yaw rates for selected simulations in a virtual wind tunnel. 132

67 Illustration of single, two point, and four point suspensions. 134

68 Evaluation of various suspension types in stabilizing a truck tethered load. . 135

69 Side views of cylinder grids refined via feature-based adaptation. 137

70 Grid sensitivity study, cylinder with an aspect ratio of 1.0 at low yaw angle and a Reynolds number of 3.2×10^5. 138

71 Typical convergence of momentum and turbulent kinetic energy RMS residuals. 140

72 Cylinder with an aspect ratio of 1.0 with wind tunnel test mounting apparatus. 142

73 Sensitivity to large wind tunnel mount, aspect ratio of 1.0, yaw angle of 40°, Reynolds number based on diameter of 3.2×10^5. 143

74 Influence of mounting apparatus on separation point and vortex shedding (countours of normalized vorticity magnitude). 144

75 Static and rotating (1 RPM) time-averaged force and moment coefficients for a cylinder with aspect ratio 1.0. Dashed lines represent min and max values for the unsteady simulations. 145

76 Grid size comparisons for free air and wind tunnel simulations, cylinder with aspect ratio 2.0. Black: wind tunnel grid; red: free air grid. 148

77 Comparison of drag, side force, and yaw moment coefficient time histories for free air and wind tunnel simulations. Reynolds number based on diameter is 1.0×10^6, yaw angle is 0°. 150

78 Comparison of drag, side force, and yaw moment coefficient time histories for free air and wind tunnel simulations. Reynolds number based on diameter is 1.0×10^6, yaw angle is 5°. 151

79 Time-averaged pressure distributions on cylinder with aspect ratio 2.0 at a yaw angle of 0°. 153

80 The tethered load system of systems. Background photo from Ref. [11]. . . 155

81 Normalized shear layer reattachment distance for two- [12] and three-dimensional rectangular prisms with 2σ uncertainty bounds. 156

82 Sensitivity of tethered load response to unsteady wind characteristics. . . . 158

NOMENCLATURE

Greek

α	Angle of attack, page 35
α_C	Angle of attack for constant-lift region, page 8
α_R	Angle of attack at initial reattachment, page 7
β	Yaw or sideslip angle, page 35
η, Ω_n, Ω_n^{qs}, ϵ	Unsteady aerodynamic model parameters, page 93
ω	Frequency of body motion, page 94
ω_n	Natural frequency, $\omega_n = \sqrt{\frac{k_s}{m}}$, page 23
ω_s	Vortex shedding frequency, page 83
ϕ	Incidence angle, page 58
ϕ_c, θ_c	Lateral and longitudinal cable angles, page 117
ϕ_R	Incidence angle at which reattachment begins, page 59
σ	Standard deviation, page 157
$\xi(r)$	Radial basis function kernel, page 85

Roman

Δt	Time step size, page 23
$\mathbf{e}_r$	Direction vector of cable tension force, page 27
$\mathbf{F}_{\text{constraint}}$	Net constraint force, page 27
$\mathbf{M}_{\text{constraint}}$	Net constraint moment, page 28

$\mathbf{r}_{cg}$	Vector from bluff body center of gravity to cable attachment, page 28
b	Reference length, page 83
c	Damping coefficient, page 27
$c\,(k)$	Theodorsen function, page 94
C_ζ	Aerodynamic coefficient, $C_\zeta = \dfrac{2\zeta}{\rho U_\infty^2 S_{ref}}$ or $C_\zeta = \dfrac{2\zeta}{\rho U_\infty^2 S_{ref} b}$, page 83
C_M	Pitch moment coefficient, page 87
C_N	Yaw moment coefficient, page 87
C_{damp}	Aerodynamic rate damping coefficient, page 103
$C_{l_{peak}}$	Peak lift coefficient, page 7
D	Diameter, page 4
e_0, e_1, e_2, e_3	Quaternions, page 21
F_x, F_y, F_z	Forces in body axes, page 21
H	Height, page 35
$H_n^{(m)}$	Hankel function of order m and kind n, page 94
I_{xx}, I_{yy}, I_{zz}	Moments of inertia, page 21
I_{xy}, I_{xz}, I_{yz}	Products of inertia, page 21
k	Reduced frequency, $k = \dfrac{\omega b}{U_\infty}$, page 94
k_s	Spring constant, page 23
L	Length, page 4
L/D	Cylinder aspect ratio, page 4
L/W	Rectangular prism aspect ratio, page 40

m	Mass, page 21
M_x, M_y, M_z	Moments in body axes, page 21
p, q, r	Angular velocity components in the body frame, page 21
r	Radius in radial basis function, page 85
r_0	Reference radius in radial basis function, page 85
Re	Reynolds number, page 10
Re_D	Reynolds number based on diameter, page 40
s	Laplace transform variable, $s = i\omega$, page 94
S_{ref}	Reference area, page 83
St	Strouhal number, $St = \dfrac{\omega_s b}{2\pi U_\infty}$, page 112
t	Time, page 88
u, v, w	Velocity components in the body frame, page 21
V_X, V_Y, V_Z	Velocity components in the fixed frame, page 21
W	Width, page 35
X_{lh}, Y_{lh}, Z_{lh}	Level-heading frame coordinate directions, page 117
y^+	Non-dimensional wall distance, page 35

Subscripts and superscripts

0	Reference value of an angle or aerodynamic coefficient, page 84
ql	Quasi-linear coefficient stored in quasi-steady data set, page 87
qs	Quasi-steady quantity, page 83

Other notation

$()'$	Fluctuating quantity, page 83
$\overline{()}$	Mean-flow quantity, page 83

SUMMARY

Interactions between the aerodynamics and dynamics of bluff bodies are important in many engineering applications, including suspension bridges, tall buildings, oil platforms, wind turbine towers, air drops, and construction with cranes. In the rotorcraft field, loads are commonly suspended underneath the vehicle by tethers. This approach is often the only practical way to deliver a payload in a reasonable amount of time; for example, in disaster relief efforts such as Hurricane Katrina and the Haiti earthquake and in search-and-rescue operations. The loads are usually bluff bodies, with complex unsteady wakes capable of generating potentially destabilizing forces and moments in flight. The end result is, at best, a significantly reduced maximum speed and mission effectiveness, or, at worst, loss of the load, helicopter, or human life.

In order to improve tethered load operations and to make advancements in the numerous other fields mentioned, it is necessary to identify and quantify the aerodynamic characteristics of bluff bodies. There exists much treatment in the literature of two-dimensional bluff body aerodynamics, but significantly less of three-dimensional bluff bodies, particularly in the wide range of orientations that are experienced during tethered load operations. This lack of understanding has led to dynamic simulation models predominantly based on curve fitting or surface response techniques, which lack predictive ability for untested configurations. Due to this shortcoming, certification for tethered loads remains very expensive, relying almost completely on flight testing. This research focuses on closing these gaps in the state of the art by analyzing the aerodynamics of canonical three-dimensional bluff bodies and developing physics-based reduced-order dynamic simulation models.

The aerodynamics of several three-dimensional canonical bluff body geometries have been examined over a range of Reynolds numbers representative of wind-tunnel-scale to

full-scale models. A numerical experiment approach is taken for these investigations, leveraging prior advancements in turbulence modeling, overset grids, and mesh adaptation while carefully performing error analyses and validation of results with theoretical, wind-tunnel, and/or flight-test data. Mean and unsteady forces and moments for the geometries have been evaluated, and empirical models of the shear layer characteristics have been extracted to quantify the behaviors and provide predictive capability. In addition, a physics-based reduced-order simulation model has been developed for bluff bodies. The physics-based approach is necessary to ensure that the predicted behavior of new configurations is accurate, and it is made possible by the breakthroughs in three-dimensional bluff body aerodynamics presented in this thesis. The integrated aerodynamic forces and moments and dynamic behavior predicted by model have been extensively validated with data from wind tunnels, flight tests, and high-fidelity computations. The model is applicable to the simulation of any generic bluff body configuration, is readily extensible, and is several orders of magnitude less expensive than the high-fidelity computational approach.

CHAPTER I

BACKGROUND

1.1 Motivation

One significant benefit of rotorcraft is their unique ability to transport a wide variety of loads slung underneath by a tether system to diverse and remote locations. For this reason, *tethered load* operations are prevalent across the spectrum of civilian and military rotorcraft applications. The loads are typically bluff bodies — often box-like or cylindrical, but potentially any generic shape — with aspect ratios on the order of 1–5. The aerodynamic behavior of these loads is complex, with unsteady, three-dimensional, separated, and turbulent flow effects all playing major roles. The engineering problem is further complicated by dynamic interactions between the tethered load, helicopter, and cable system. As a result, flight certification for these operations to date has relied almost exclusively on flight testing [13], which is very expensive given the number of different permutations of the helicopter, load, and tether arrangement.

In addition to the complexity of the system, serious safety issues also arise in tethered load operations. The turbulent, three-dimensional wakes shed from bluff bodies result in large, unsteady forces and moments that increase in magnitude as the flight speed increases. At high flight speeds, these aerodynamic phenomena effect large excursions of the load, excessive vertical oscillations of the helicopter and load, instabilities in the tether system, or combinations of all three effects [12, 14]. As a result of these stability issues, the speed envelope of the helicopter is greatly reduced during tethered load operations. Figure 1 is a photograph of a UH-60 Blackhawk in flight with a common rectangular-prism tethered load known as the CONEX (CONtainer EXpress) [1]. The power-limited flight speed of this vehicle is over 100 knots, but stability issues reduce the maximum speed to just 60 knots when the load is present [15]. Such restrictions severely limit the ability to effectively carry out important operations including search-and-rescue, disaster relief as in the case of

Figure 1: UH-60 Blackhawk in flight with CONEX tethered load [1].

Hurricane Katrina or the Haiti earthquake, and delivery of supplies in military theaters.

While *ad hoc* methods have been applied to stabilize tethered loads with varying degrees of success [16, 17, 18, 19], there remains a need for improved prediction methods based on an understanding of the fundamental aerodynamics and dynamics of bluff bodies. Such improvements have the potential to significantly reduce the cost and time required for flight certification. As Dr. William Lewis, Director for Aviation Development at the Army's Aviation and Missile Research, Development & Engineering Center, stated in *Aerospace America*, "If we have to test only one-tenth of our configurations, it's a huge money savings" [20]. Recent advancements in simulation of turbulent wakes has made accurate numerical analyses feasible for bluff bodies at full-scale Reynolds numbers. Numerical experiments provide a wealth of flow field detail, allowing the factors responsible for dynamic instabilities to be determined. By leveraging this approach, with results carefully validated against physical data, breakthroughs in the understanding of three-dimensional bluff body physics are possible. This information can be applied to develop physics-based dynamic models for stability analysis, pilot training, and cost reduction during the certification phase.

The rotorcraft tethered loads application is not the only one with a need for improved

predictions of three-dimensional bluff body aerodynamics and dynamics. Other applications include air drops, store separation, missile flight, design of buildings, bridges, oil platforms, power lines, towers [21, 22, 23, 24, 2, 25, 26], along with many others. Furthermore, the availability of information on bluff bodies with short aspect ratios and predominantly three-dimensional flow in the literature is currently poor, due to the practical difficulties in analyzing them experimentally and the reliance on two-dimensional approximations. Thus, advances in the understanding of bluff body aerodynamic-dynamic interactions imply widespread benefits across the engineering community, and not just for rotorcraft applications.

1.2 Overview of Bluff Body Aerodynamic-Dynamic Interactions

Bluff bodies are defined aerodynamically as bodies that are not streamlined. They are characterized by large wakes and separated flow; thus, their drag is dominated by pressure forces instead of viscous shear stress. Several difficulties arise in aerodynamic analyses as a result of these characteristics. The large regions of separated flow negate the use of many approximations and analytical solutions available for attached flows. Bluff body wakes are inherently unsteady, and turbulence is important for Reynolds numbers encountered in most practical applications. The problem complexity is increased further when body dynamics are present, as is the case in power lines, wind turbine towers, tethered loads for rotorcraft and cranes, bridges, oil platforms, and many others. Even in situations where the structural behavior is well-known, interactions between the aerodynamics and dynamics of the system can alter the response significantly. Some examples of these interactions include the phenomenon of vortex-shedding frequency lock-in [27], in which the characteristic frequency of vortex shedding is altered by body dynamics, and alterations in the spin rate of auto-rotating three-dimensional bluff bodies due to this lock-in phenomenon [28].

The physical complexities of bluff bodies, particularly in relation to the aerodynamics, have generated a heavy reliance upon experimentation and empiricism. Since many of the applications have very large aspect ratios, there is significantly greater treatment in the literature on two-dimensional bluff body aerodynamics. In contrast, operations including

tethered loads, store separation, and air drops feature bluff bodies with short aspect ratios and predominantly three-dimensional flow. These applications suffer from a general lack of consideration of such bluff bodies in the literature, and, in consequence, dynamic simulation models for these operations are typically very limited in generality and predictive power. In the following sections, an overview of two- and three-dimensional bluff body physics, the computational state of the art in simulation of bluff body flows, and dynamic modeling approaches to date is given. Subsequently, the major gaps in the state of the art and objectives of this thesis are presented.

1.3 Bluff Body Aerodynamics

Numerous researchers have studied the aerodynamics of two-dimensional (or "infinite length") bluff bodies. Flows around bluff bodies can in general be separated into flows where separation occurs at sharp edges, as in the case of rectangular prisms and other polygonal geometries, or where separation occurs on curved faces, as in the case of circular cylinders and spheres. In the latter case, the separation location, and thus the drag, may be significantly influenced by the flow conditions, in particular the Reynolds number [29].

1.3.1 Cylindrical Bodies

Zdravkovich [30, 31] has presented a comprehensive review of the aerodynamics of circular cylinders. Aspect ratio effects as well as the effects of incidence angle are covered, although the two are considered together only in the case of long or infinite cylinders ($L/D > 20$ or with end plates). Many studies of finite circular cylinders have focused on relatively large aspect ratios with end plates or a single free end. For example, Schmidt [32] measured fluctuating lift and drag on a circular cylinder with a free end at Reynolds numbers in the range 2×10^5 – 5×10^5 for $L/D = 8.1$ and computed correlations between fluctuating pressure, lift, and drag coefficients. Ayoub and Karamcheti [33] investigated the wake structure and Strouhal frequencies of a circular cylinder with $L/D = 12$ at Reynolds numbers of 1.8×10^5 and 7.7×10^5. In the vicinity of the free end at the lower Reynolds number, the vortex shedding behavior is unstable, and the frequency content exhibited numerous prominent peaks. At the higher Reynolds number, at which the flow was supercritical, the Strouhal number

near the free end stabilizes to a value near 0.2, despite the fact that the two-dimensional vortex street behind the cylinder is no longer present.

In comparison, there has been very little focus on short, finite-length cylinders with two free ends. One of the earliest experimental studies was undertaken by Wieselsberger [6], in which the drag coefficient of cylinders in normal flow (the orientation where the curved surface is normal to the flow) was measured over a broad range of Reynolds numbers. Both infinite (without free ends) and finite cylinders with $L/D = 5$ were considered. Wieselsberger observed that, in the subcritical and transitional Reynolds number regimes, the drag of the finite cylinder was significantly less than that of the infinite cylinder. However, this difference vanished at supercritical Reynolds numbers on the order of 10^6. Additionally, the changes between subcritical, transitional, and supercritical flow occurred at similar Reynolds numbers for the infinite and short cylinders. The magnitude of the change in drag during these transitions was also comparable.

Zdravkovich et al. [9] performed wind tunnel experiments in the subcritical Reynolds number regime on finite cylinders ($2 \leq L/D \leq 10$). Their observations were similar to those of Wieselsberger, in that decreasing the aspect ratio resulted in a decrease in drag. However, below $L/D = 5$, further decreases in aspect ratio resulted in little if any additional drag decrease. Zdravkovich et al. [9] also measured the yaw moment coefficient, observing considerable variation between trials. The variation was determined to be the result of an asymmetric pressure distribution which could shift from side to side in an unpredictable fashion. Additionally, the Strouhal frequency of vortex shedding for $L/D < 5$ was found to be in the range 0.15 – 0.27, but the shedding itself was highly irregular and difficult to assign a single dominant frequency. This behavior was attributed to the highly turbulent and three-dimensional flow interactions occurring with the short cylinder geometry.

In most applications of three-dimensional bluff body aerodynamics, not only is the drag in the normal flow configuration important, but also the other force and moment components in a broad range of orientations. While the literature on small aspect ratio cylinders in normal flow is sparse, there exists even less information at other orientations. Hoerner [7] compiled data for cylinders and disks in axial flow (with the flat face normal to the flow,

instead of the curved face). In this orientation, the drag was found to decrease abruptly as L/D increased from zero (circular disk) to two, but it then remained approximately constant as L/D increased further. The abrupt drop in drag may be attributed to a change in shear layer behavior, as it begins to reattach on the curved face near $L/D = 1$, increasing the base pressure coefficient. Normal force coefficients have also been compiled by Hoerner [7] for circular disks over a range of angle of attack from 0 to 90 degrees. Ramberg [34] employed smoke visualization to study the wake structures of a yawed finite cylinder with large aspect ratios ($L/D > 20$) at low Reynolds numbers in the range of 160 to 1100. Wake patterns and frequencies were found to be related to the incidence angle, with increasing angle causing the free-end vortex structure to disappear. Similar data are also extant for subsonic flows over missiles [22, 23], which are cylindrical in cross section but typically have a rounded end and aspect ratio greater than five.

A significant number of studies have covered infinite cylinders at an angle of incidence. For example, Bursnall [35] measured the pressure distribution about a circular cylinder at yaw angles from 0 to 60 degrees at Reynolds numbers below 5.0×10^5. This and other more recent experiments are reviewed by Zdravkovich [31]. Many of these investigations have focused on the validity of the *independence principle*, or the theory that the flow in a plane normal to the circular cross-section may be treated independently of the axial flow component. The theory was presented formally by Sears [36] and is based on the assumptions that the flow is two-dimensional and laminar. It breaks down at the onset of separation and in three-dimensional configurations, as in the case of short cylinders with free ends. Nonetheless, the theory has been proven to be reasonably accurate for real cylinders in some cases, depending on the aspect ratio and and condition [35, 34].

1.3.2 Prismatic Bodies

Infinite bodies with sharp edges are representative of tall buildings, girders, long bridges, and other structures. In these applications, the forces, moments, and dynamic response are very sensitive to the angle of incidence of the incoming freestream flow [2, 37, 38]. For example, Fig. 2 illustrates the lift coefficient for two-dimensional flow about a rectangular

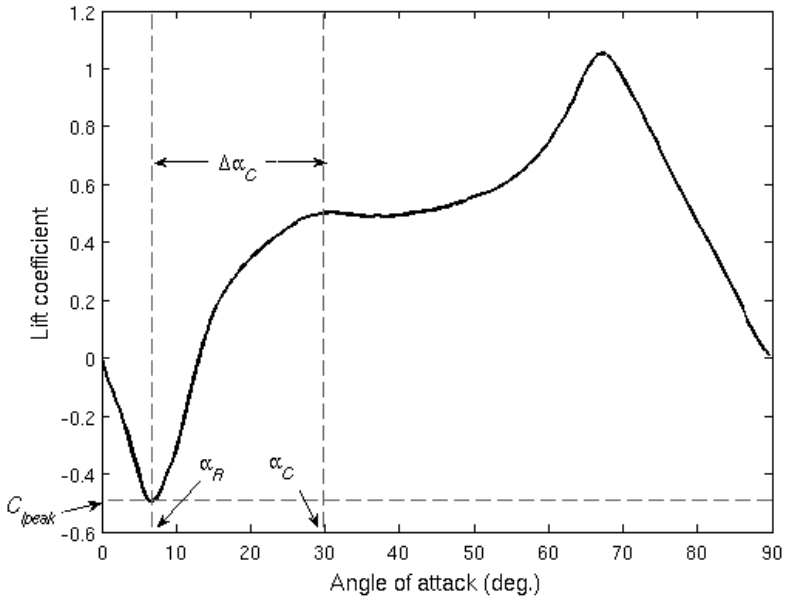

Figure 2: Lift curve for a two-dimensional rectangular bluff body with an aspect ratio of 2.0 [2].

bluff body with an aspect ratio of 2.0 as a function of angles of attack [2]. At low angle of attack, there exists a linear region in which the lift coefficient decreases from zero to $C_{l_{peak}}$, resembling the linear slope of the lift curve in attached flows over an airfoil, but with a negative slope. However, the mechanism is completely different, resulting from the rotation of the pressure forces on the fore and aft faces as the angle of attack changes. At these low angles of attack, the flow on the bottom and top faces remains fully separated.

When the angle of attack increases beyond seven degrees, a sharp change in lift coefficient occurs, corresponding to a change in shear layer behavior on the lower face. At this orientation, the shear layer begins to reattach on the lower face, producing a separation bubble and a region of attached flow. This angle of attack for reattachment is defined as α_R for this configuration. Further increasing the angle of attack causes the extent of the separation bubble to shrink and the attached flow region to grow. Since the separation bubble is characterized by low pressure, and the attached flow region by higher pressure, the reduction in size of the separation bubble produces a positive contribution to lift. It also results in significant changes in the pitching moment [12, 39] and, in the case of two-dimensional aerodynamics, the Strouhal number [2, 39]. As the angle of attack continues to

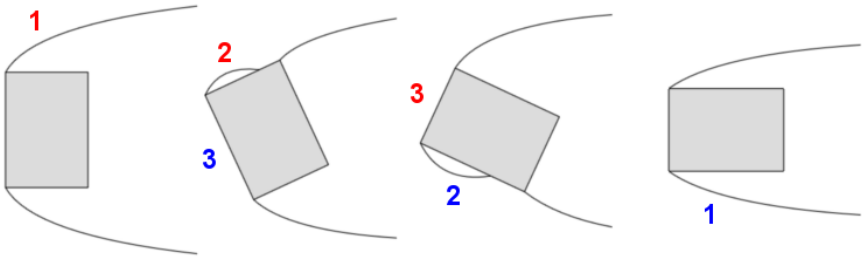

Figure 3: Illustration of shear layer behavior for a rectangular bluff body. (1) Fully separated shear layer, (2) reattaching shear layer, and (3) fully attached flow.

increase, the separation bubble eventually becomes very small, and there exists a range of angle of attack, beginning at α_C , over which the lift coefficient remains roughly constant. These trends reverse as a separation bubble forms, grows in size, and eventually separates completely on the adjacent face.

Figure 3 illustrates the general behavior of the shear layer on different faces of a rectangular bluff body during a 90-degree rotation. If the body is not square, the angles α_R and α_C vary for the two different faces. This fact is apparent in Fig. 2, as the angle of incidence for reattachment is 7 degrees on the long face and 20 degrees on the short face.

Because reattachment causes a sudden change in the forces and moments, it is very important to the stability of bluff bodies in dynamic scenarios and has been the focus of a number of studies. Norberg [39] performed experimental investigations of two-dimensional flow around rectangular bluff bodies with aspect ratios ranging from one to five at Reynolds numbers ranging from 400 to 30,000. The Strouhal number, drag, lift, and moment coefficients were measured as a function of both of the aspect ratio and Reynolds number, as well as angle of attack from 0 to 90 degrees. Variations in the forces and moments were consistent with the findings of Matsumoto et al. [2], presented in Fig. 2, in that abrupt changes in the integrated forces and moments occurred at α_R, and a flat region began at α_C. The broad range of aspect ratios evaluated confirmed that the values of these parameters are closely related to the aspect ratio.

Robertson et al. [10] recorded wall pressures of reattachment on square bluff bodies in

two-dimensional flow for angles of attack ranging from 0 to 45 degrees. This study identified the low-pressure separation bubble, pressure recovery, and attached flow region during reattachment and quantified how the extents of these distinct regions change as the angle of attack increases. It was also observed that, for the square bluff body, the separation bubble and recovery pressure distributions collapse onto a single curve when certain normalizations are applied involving the reattachment distance and maximum pressure coefficient. In addition, it was found that high freestream turbulence increased the strength of circulatory flow in the separation bubble, driving the bubble pressure more negative and thus promoting earlier reattachment. At a very high turbulence intensity of 10.4%, α_R was reduced from 14 degrees to 9 degrees for the square bluff body.

Greenwell [12] developed empirical models describing the reattachment behavior of two-dimensional rectangular bluff bodies, drawing from prior experiments [40, 2, 41, 39, 10]. A major finding of his work was the development of an empirical equation which indicated that the reattachment distance for these bluff bodies, when normalized by the dimension perpendicular to the side on which reattachment occurs, depends on the angle of incidence but not on the aspect ratio. This finding is significant in bluff body dynamics because it allows α_R, which plays a significant role in stability, to be identified. Greenwell also studied three-dimensional rectangular bluff bodies (or rectangular prisms), and presented equations describing changes in the forces and moments when crossflow is present. A comparison of the reattachment behaviors of the two-dimensional and three-dimensional geometries was made for a few specific cases, but it was not thoroughly characterized. Greenwell also developed empirical reconstructions of the attached-flow portion of the pressure distribution that can be applied to either reattaching or fully attached flow.

1.3.3 Computational State of the Art

Numerical solutions of bluff body flows are challenging primarily due to the need to resolve separated wakes at Reynolds numbers for practical applications. The direct numerical simulation (DNS) approach is capable of resolving all turbulence in a flow, but at great computational cost. For three-dimensional DNS, the required grid spacing to resolve the

dissipative turbulence scales is proportional to $Re^{9/4}$ [42, 43, 44], so that it becomes a prohibitively expensive calculation for high-Reynolds number flows. DNS has been used in the past to study bluff body flows at relatively low Reynolds numbers. It was used by Wan et al. [45], for example, to study aerodynamic-dynamic interactions of a freely falling plate at a maximum Reynolds number of 420. Other bluff-body simulations with DNS include those of Cai and Liu [46] and Gross et al. [47], but Reynolds numbers greater than a few thousand are typically avoided because of the prohibitive computational cost.

An alternative approach is to resolve only the largest scales of turbulence, while the smaller, more isotropic scales are modeled. This approach is known as large-eddy simulation (LES) and significantly reduces the computational expense compared to DNS while maintaining accuracy for a broad range of flows [48, 44]. However, it is still too costly for high-Reynolds number flows, primarily because a very fine mesh and temporal resolution are required in the boundary layer to resolve even the largest scales of turbulence [44]. The grid spacing needed to resolve the large structures in the boundary layer scales with $Re^{2/5}$ [49, 44], which is significantly coarser than DNS scales, but still becomes computationally prohibitive for practical configurations at high Reynolds numbers.

The traditional alternative to turbulence-resolving methods has been the unsteady Reynolds Averaged Navier Stokes (URANS) approach, in which all turbulence is modeled. This approach is attractive because it greatly reduces the constraints on grid resolution and time step size compared to DNS and LES. However, URANS models rely on empirical or heuristic formulations and statistical parameters from a small subset of test cases, reducing their generalizability. The models typically perform well in attached boundary layers but struggle to accurately predict flow separation when adverse pressure gradients are present, particularly for unsteady flows [50]. This shortcoming is particularly problematic for bluff body flows, as the extent and character of the separated flow region are very important in determining the loads.

Lynch [8] demonstrated that the popular two-equation k-ω SST turbulence model [50] incorrectly predicted the mean drag coefficient (by 47%) and separation location (by 14%) of a circular cylinder between walls in subcritical flow, while LES and hybrid RANS/LES

approaches accurately predicted both. Theron et al. [51] applied various RANS turbulence models to predict the drag, side force, and yaw moment for a three-dimensional rectangular bluff body. Moderately accurate results were obtained, with maximum errors in the side force and yaw moment were typically within 20% - 30% of experimental values. Significant sensitivity to the turbulence model was observed, and, surprisingly, the algebraic model of Baldwin-Barth outperformed the one- and two-equation models in the study.

In recent years, significant developments have been made in the field of hybrid turbulence approaches. Instead of strictly applying RANS models or LES throughout the entire flow field, hybrid approaches blend the two methods. The goal of this blending is normally to apply the RANS models in attached boundary layers, where they are most accurate and the grid resolution needed for LES is too high. The hybrid turbulence approach initially gained widespread use through the work of Spalart et al. [52], who applied a one-equation turbulence model modified such that the level of eddy viscosity was reduced in regions of massive flow separation. The approach was termed detached eddy simulation (DES), signifying its intended application. The original DES model suffered from errors resulting from a reliance on the local grid size to determine the transition location between RANS and LES, but a later heuristic modification effectively removed this problem by introducing a transition function [53]. Other early approaches include the work of Speziale [54], who developed a method referred to as very-large-eddy simulation (VLES).

Sánchez-Rocha and Menon [44, 55, 56] investigated a technique whereby the RANS and LES governing equations are explicitly blended. The turbulent kinetic energy was closed via the Menter k-ω SST model [50] in the near-wall region and a one-equation localized dynamic subgrid-scale model [48, 57] in the outer flow. The method was termed hybrid RANS-LES, or HRLES. The sensitivities to various blending functions and additional terms arising in the mean-flow equations due to the blending process were analyzed. This approach was implemented in the structured URANS NASA solver OVERFLOW by Liggett and Smith [58] and the unstructured URANS code FUN3D by Lynch and Smith [8]. In both cases, the function $F2$ in the Menter k-ω SST model was employed to blend the RANS and LES regions, eliminating any explicit dependence on the local grid size in determining the

transition region.

Several studies have demonstrated that the hybrid turbulence approach is able to significantly improve predictions of bluff body aerodynamics. Theron et al. [59] performed additional simulations of the three-dimensional rectangular bluff body with DES and compared the results with their previous RANS work [51]. In this case, both steady and time-accurate simulations were carried out. Drag, side force, and yaw moment predictions were improved with DES, but some variations of the side force and yaw moment with yaw angle were not captured. Lynch [8] demonstrated that HRLES greatly improved the predictions of the drag and separation location, relative to URANS models, for a circular cylinder between two walls in subcritical flow. The flow field structures resolved by HRLES in the wake were comparable to LES, whereas the wake details were smeared by the URANS models. Similar conclusions were drawn by Liggett [60, 58] and Sánchez-Rocha and Menon [61] for airfoils undergoing static and dynamic stall. The computational cost of HRLES is comparable to URANS, because the same grids may be applied in many cases, provided the wake resolution is appropriate to capture the large turbulence scales. In fact, Liggett and Smith [58] observed that dynamic stall simulations were actually less expensive with HRLES than URANS because temporal convergence was accelerated.

1.4 Dynamic Models for Bluff Bodies

Many dynamic models for bluff bodies have employed greatly simplified aerodynamics. Sampath [37] investigated the dynamics of helicopters with rectangular prism tethered loads. Static wind tunnel data for scaled 8'×8'×20' and 8'×8'×40' rectangular prisms were applied to model the load behavior in a linear stability analysis of the helicopter-load system. No unsteady aerodynamic effects were considered. This simplified linear model failed to accurately predict the stability boundaries, and it was concluded that this type of analysis should only be applied to identify important system parameters. Wind tunnel experiments were also performed to investigate flow behaviors, including separation and reattachment, and to provide a description of the unsteady and nonlinear aerodynamic effects present. One major finding was that unsteady and nonlinear aerodynamic phenomena result in

hysteresis in the yaw moment, rendering the quasi-steady linear assumptions unable to accurately evaluate stability. A mathematical model of the nonlinear yaw moment behavior was developed and shown to qualitatively agree with the experimental data.

A majority of the other early dynamic models for tethered loads paid relatively little attention to the aerodynamics. For example, Cicolani and Kanning [62] developed equations of motion for simulation of tethered load systems, demonstrating how to model complex systems with varying tether configurations and multiple rotorcraft transporting a single load. However, they did not address how to compute the aerodynamic forces and moments that act as forcing functions to the dynamic equations. A similar development has been presented more recently by Bisgaard et al. [63]. In this effort, equations of motion were derived for helicopter-load systems in which the cables, which may be elastic or inelastic, are modeled as constraint forces acting on the two bodies. The aerodynamics were basic, with an assumption that the load is spherical and with only the effects of steady drag considered. A contribution to the state of the art from this work is an approach to incorporate rotor downwash within this framework. A similar aerodynamic approach, considering only quasi-steady drag, was also applied by Guglieri and Marguerettaz [64], who studied the differences between modeling the load as a simple pendulum or six-degree-of-freedom body.

While these simplified aerodynamic models may be sufficient for very heavy and relatively small loads at low speeds, they are not accurate for large prismatic loads like those studied by Sampath [37] or the one depicted in Fig. 1. Sridharan et al. [38] considered aerodynamic nonlinearities in one- and three-degree-of-freedom simulations of helicopters with rectangular tethered loads. Quasi-steady aerodynamic forces were represented as a power series of incidence angle, while unsteady forces were modeled as a sinusoid with a magnitude and phase depending on the geometry and flow speed. Unsteady vortex shedding was neglected. To explore the influences of nonlinearities, the power-series coefficients were modified manually, and changes in dynamics were observed. The study demonstrated that aerodynamic nonlinearities result in hysteresis in the oscillation amplitude for increasing and decreasing flight speeds. Additionally, rapid changes in oscillation amplitude were observed for small perturbations in flight speed.

Cicolani and da Silva [1] developed an unsteady aerodynamic model for the CONEX rectangular bluff body. Their aerodynamic model was derived by system identification of the aerodynamics in the frequency domain. The goal was to model the unsteady effects which were hypothesized to impact the dynamic stability of the tethered load. In this work, unsteady two-dimensional RANS simulations of the bluff body undergoing frequency sweeps were performed. The time histories were transformed to the frequency domain using Fourier transforms, and a linear transfer function was constructed to permit transformation back to the time domain for dynamic simulation. The unsteady aerodynamics were limited to two-dimensional analysis of the yaw moment only. The linearized, two-dimensional model neglected higher-order harmonics but demonstrated promise in predicting the qualitatively correct dynamic yaw behavior. In particular, the unsteady aerodynamics introduced a time lag which was determined to be responsible for the observed spinning behavior in flight tests.

Further development of the model of Cicolani and da Silva was performed by Cone [65]. The same baseline approach was applied, but in here the quasi-steady yaw moment was interpolated from wind tunnel data, and the frequency-domain decomposition utilized flight test data instead of two-dimensional computational fluid dynamics (CFD) results. Different yaw moment transfer functions were constructed for each flight speed, and favorable correlation in yaw dynamics between the flight test data and dynamic simulations was obtained for some flight speeds. A major shortcoming noted in the system identification approach is that a new transfer function was required at each flight speed and configuration, preventing generalizability to different flight speeds, aspect ratios, Mach numbers, and Reynolds numbers.

The effect of wind tunnel walls on the dynamic response of a tethered load was examined by Sharma et al. [66, 67]. A two-dimensional potential flow source-image method was applied to compute the pressure on each side of the load under the influence of walls. The dynamic model for the tethered load was simplified to a rigid-pendulum representation, and a single point source, rather than a line source, was used to represent each wall. This study implied that wind tunnel walls can influence the dynamics of tethered loads, but it did not consider

unsteady aerodynamics such as vortex shedding and wake dynamics. The model employed greatly reduced degrees of freedom, rendering it as essentially a conceptual model of the wall effect only.

In a first-principles approach, Prosser and Smith [68] simulated the dynamics of a tethered load in a wind tunnel with aerodynamics evaluated at each time step via high-fidelity HRLES computations. This approach was the most complete to date, relying on a minimum number of simplifications or assumptions in either the dynamics or aerodynamics. The kinematic representation included all six degrees of freedom, with the cables modeled as linear spring and damper elements. Unsteady aerodynamics were included implicitly in the HRLES simulation. Though this approach demonstrated promise in terms of accuracy and generalizability, its cost makes it unsuitable for assessments of stability, sensitivity, and certification.

When airfoils undergo stall, they behave as bluff bodies with separated flow and large, unsteady wakes. Much research has been devoted to dynamic stall, in which an airfoil, wing, or rotor blade undergoing unsteady motion briefly exceeds the static stall angle. When dynamic stall occurs, a vortex quickly grows and convects over the upper surface of the airfoil, resulting in large, rapidly-varying fluctuations in lift and pitching moment. The unsteady aerodynamics are characterized by phase lag and force attenuation [69]. McAlister [69] proposed a dynamic filter to model the unsteady aerodynamics. The model was formulated as a second-order time-domain ordinary differential equation, facilitating the presence of attenuation and phase lags. Six parameters, which were tuned via a system identification approach, were contained within the model. The model was successful in qualitatively predicting the dynamic lift overshoot and hysteresis effects in dynamic stall, though the results were quantitatively inaccurate.

Peters [70] and Rudy [71] employed models similar to McAlister's dynamic stall model but added several improvements resulting in better numerical stability and physical accuracy. This model has undergone numerous extensions and improvements, and it has recently been applied by Ahaus and Peters [72, 73] in a unified unsteady aerodynamic theory (UAT) for dynamic stall prediction of single, multi-element, and deforming airfoils.

Though originally designed for thin airfoils in incompressible flow, the current model includes corrections for thickness and compressibility. It has been validated for attached flow cases by comparison with the classical theory of Theodorsen [74], experimental data, and high-fidelity numerical simulations for a variety of configurations and conditions. A major key in the success of this model is that it incorporates a physics-based representation unsteady aerodynamic phenomena important to the dynamic stall application.

1.5 Thesis Objectives

Accurate prediction of bluff body dynamics, particularly in applications such as tethered loads in which the aspect ratios are less than 5, suffers from a lack of understanding of the physical behavior of the bluff body aerodynamics. While two-dimensional bluff body aerodynamics are relatively well understood, much less information is available for small aspect ratio, three-dimensional bodies over a wide range of orientations and Reynolds numbers. Furthermore, though empirical models of shear layer behavior and pressure distributions have been developed for two-dimensional rectangular bluff bodies, it is currently not clear whether these models are extensible to three dimensions or other canonical bluff body shapes.

In recent years, available computational power and algorithm development have progressed to the point that computational fluid dynamics (CFD) approaches may be practically applied to high Reynolds number turbulent flows around bluff bodies. This approach promotes phenomenological understanding of the aerodynamic behavior of these configurations through the rich, complete flow field information that is available. Therefore, this computational approach, known as "numerical experimentation," may be applied to close the gap in the state of bluff body research. This thesis seeks to advance the state of the art in three-dimensional bluff body aerodynamics by:

- Applying high-fidelity numerical experiments to study *canonical* three-dimensional bluff body geometries in the range of flow conditions relevant to dynamic applications in aerospace, mechanical, and civil engineering. Canonical geometries are defined as basic geometries that are representative of a broad range of realistic configurations,

but simple enough that the basic behavior may be deduced.

- Developing equations to describe the aerodynamic behavior of these bluff bodies and relating them to the integrated forces and moments for performance predictions.

Through these advancements, this thesis also intends to advance the state of the art in dynamic modeling of bluff bodies by:

- Developing a physics-based reduced-order dynamic model for three dimensional bluff bodies. The physics-based approach is necessary so that accurate predictions can be made for new bluff bodies and configurations, and the model must also be generalizable to new configurations.

- Validating the reduced-order model with wind tunnel, flight test, and high-fidelity computational fluid dynamics data.

This thesis seeks to answer the following questions pertaining to the methodology employed and the models developed:

- **Validation:** Though the HRLES methodology has been successfully applied to bluff body flows, is it accurate for highly three-dimensional flows over the range of conditions relative to aerodynamic-dynamic interactions of bluff bodies? Can the reduced-order model accurately predict the coupled aerodynamics and dynamics of these bluff bodies?

- **Sensitivity:** To what degree is the HRLES methodology sensitive to computational uncertainties (e.g., grid refinement and time step size) for bluff body flows with highly separated wakes? Do minor geometric deviations of the bluff bodies from the canonical shapes result in significant changes in flow field behavior or integrated forces and moments?

- **Modeling assumptions:** Can unsteady aerodynamic effects for three-dimensional bluff bodies be modeled empirically similar to the successful dynamic stall models?

Are these unsteady aerodynamic effects important to bluff body dynamics, or can they safely be neglected for engineering evaluation?

- **Applicability:** Under what conditions, and for what geometry types, are the empirical models of shear layer behavior valid? Can the reduced-order model be applied to diverse and complex configurations, and is it suitable for tethered load stability analysis?

- **Cost:** What is the computational cost of the reduced-order model relative to the high-fidelity approach?

CHAPTER II

COMPUTATIONAL TOOLS

2.1 FUN3D

FUN3D is an unstructured CFD solver developed by NASA [75]. FUN3D is capable of solving the RANS equations in fully compressible or incompressible formulations on mixed-element unstructured grids. The incompressible formulation is implemented via Chorin's method of artificial compressibility [76], which replaces density in the continuity equation with pressure multiplied by an artificial compressibility term. Though low Mach number flows can also be handled within the compressible path by applying a preconditioner to improve convergence, the method of artificial compressibility is preferred because it eliminates the need to solve the energy equation, thus reducing computational cost. FUN3D employs a second-order accurate spatial discretization in space and a temporal discretization that is between second- and third-order [77], which is important for resolving large eddies in the wakes of bluff bodies. While a number of flux reconstructions are available, typically (and throughout this thesis) inviscid fluxes are resolved using Roe's approximate Riemann solver, and flow gradients for viscous fluxes are computed via least squares.

Though unstructured grid topologies are already able to handle a wide range of complex geometries, further flexibility is afforded by the overset grid approach. FUN3D supports overset grid simulations through the SUGGAR++ [78] (Structured, Unstructured, and Generalized Grid AssembleR) and DiRTlib [79] (Donor Receptor Transaction Library) libraries. SUGGAR++ determines blanked cells, donors, recipients, and orphans at overset boundaries, while DiRTlib interpolates data to and from overset grids. In addition to simplifying the grid generation process, the overset grid approach is also important for dynamic simulations, as the near-body grid is able to move while the background grid remains static. It is also beneficial for static simulations of internal flows when the body of interest must change orientations multiple times, because it allows the same grids to be reused without the need

to re-generate them in new orientations to accomodate new flow physics. An example of this situation is a simulation of a bluff body in a wind tunnel, where forces and moments are to be computed in static configurations over a range of yaw angles.

RANS solutions using statistical closures are known to be inadequate for flows around airfoils at high angles of attack and other bluff bodies [11, 80]. To mitigate this issue, FUN3D includes a hybrid turbulence approach, in which the k-ω SST two-equation near-wall RANS model is blended with LES in the wake where the larges scales may be resolved by the grid [81, 8, 61]. This approach has been demonstrated to accurately predict bluff body flows in a wide range of applications, including flows over flat plates [55], airfoils at high angles of attack, reverse flow, and dynamic stall [61, 60, 58, 80], and cylinders between walls [8].

One issue when finite volume methods are used to resolve the Navier-Stokes equations is that high grid resolution is typically required to prevent wake features from dissipating prematurely [82]. This problem impacts the wakes of rotating systems such as rotors and wind turbines as well as bluff bodies. In order to address the issue of wake dissipation, an adaptive grid refinement method is available in FUN3D. This feature-based refinement approach has recently been extended to allow near-body adaptation in overset simulations by Shenoy [83, 84, 85]. The adaptation approach is similar to the one used in the Helios framework [86, 87], but it operates on tetrahedral elements and acts on both the near-body and background grids. Feature-based adaptation attempts to refine the grid selectively in regions where it is needed, and also to remove grid vertices, based on the features of the solution computed on a baseline grid system. A flow field metric – for example, pressure, density, or vorticity magnitude – is sampled to determine where refinement or coarsening is needed. After grid adaptation, the solution is interpolated onto the new grid. This approach has been successful in accurately resolving flow fields with rotor-fuselage interactions [84], complex bluff body flow fields behind rotor hub systems [88], and improving the preservation of wind turbine wakes [82].

2.2 FUN3D/6-DoF Coupling

The six-degree-of-freedom (6-DoF) motion of a rigid body may be described completely using a system of first-order ordinary differential equations. It is most convenient to write the equations in the frame of the moving body so that the rotational inertia tensor is invariant with orientation. The orientation of the moving body may be described using four parameters known as quaternions without introducing singularities in the equations of motion [89]. This formulation leads to the following system of thirteen equations to be solved simultaneously [90, 89]:

$$
\begin{aligned}
&\dot{u} = \frac{F_x}{m} + vr - wq \quad \dot{v} = \frac{F_y}{m} - ur + wp \quad \dot{w} = \frac{F_z}{m} + uq - vp \qquad (1)\\
&\dot{p}I_{xx} - \dot{q}I_{xy} - \dot{r}I_{xz} = M_x + qr\left(I_{yy} - I_{zz}\right) + \left(q^2 - r^2\right) I_{yz} - prI_{xy} + pqI_{xz}\\
&-\dot{p}I_{xy} + \dot{q}I_{yy} - \dot{r}I_{yz} = M_y + pr\left(I_{zz} - I_{xx}\right) + \left(r^2 - p^2\right) I_{xz} - pqI_{yz} + qrI_{xy}\\
&-\dot{p}I_{xz} - \dot{q}I_{yz} + \dot{r}I_{zz} = M_z + pq\left(I_{xx} - I_{yy}\right) + \left(p^2 - q^2\right) I_{xy} - qrI_{xz} + prI_{yz}\\
&\dot{e_0} = \frac{1}{2}\left(-e_1 p - e_2 q - e_3 r\right)\\
&\dot{e_1} = \frac{1}{2}\left(e_0 p - e_3 q + e_2 r\right)\\
&\dot{e_2} = \frac{1}{2}\left(e_3 p + e_0 q - e_1 r\right)\\
&\dot{e_3} = \frac{1}{2}\left(-e_2 p + e_1 q + e_0 r\right)\\
&\dot{X} = V_X \quad \dot{Y} = V_Y \quad \dot{Z} = V_Z,
\end{aligned}
$$

where the force and moment components are resolved in the body frame. Forces and moments for bluff body dynamics arise primarily from gravity, aerodynamics, and external constraints including tether systems. FUN3D has been linked to a library for integrating Eq. 1 developed by the University of Alabama at Birmingham and Mississippi State University under the DOD PET program [91]. The library requires forces and moments computed by FUN3D to be applied at each time step. By default, fourth-order Runge-Kutta integration is applied to Eq. 1 to update the dynamic state for the next time step. This information is then returned to FUN3D, which moves the overset grids and sets nodal velocities as required, then re-computes the forces and moments, and the process is repeated.

2.2.1 Evaluation of Integration Schemes

The default integration scheme in the 6-DoF library is the fourth-order Runge-Kutta (RK4) explicit scheme. This scheme solves systems of nonlinear first-order differential equations of the form $\dot{\mathbf{x}} = f(t, \mathbf{x})$; Eq. 1 falls into this category. In the RK4 scheme, the state variables are not immediately updated from time level t_n to t_{n+1}. Instead, they are updated in four substeps. However, this process is not readily amenable to coupling with FUN3D in a simple manner, because it requires the flow solution and grid mechanics to be computed at each of these substeps. Since the time step size to resolve the aerodynamic features is already quite small, this additional work represents a significant computational expense. The default implementation of 6-DoF coupling in FUN3D does not re-compute the flow solution and grid mechanics at each substep, but rather leaves F_x, F_y, F_z, M_x, M_y, and M_z constant from t_n to t_{n+1}, introducing error in the integration.

As an alternative to RK4, the Adams-Bashforth fifth-order integration scheme (AB5) has been added to the 6-DoF library. This scheme does not require substeps, but instead uses information about previous states to achieve high-order accuracy [92]. Adams-Bashforth actually represents a family of schemes with varying order of accuracy. The Adams-Bashforth update equation is

$$\mathbf{x}_{n+1} = \mathbf{x}_n + \Delta t \sum_{j=0}^{s-1} \alpha_{s,j} f\left(t_{n-j}, \mathbf{x}_{n-j}\right). \tag{2}$$

The coefficients α for a given order of accuracy s may be determined via a Taylor series expansion of $\mathbf{x}$ and $f(t, \mathbf{x})$ in such a way that all terms above order s cancel [93]. The coefficients up to $s = 5$ are provided in Table 1 [92]. Equation 2 indicates that the AB5 scheme requires storage of f for thirteen states at five previous time steps in order to advance the solution from t_n to t_{n+1}. For a single rigid body and double precision variables, this represents a memory requirement of 520 bytes, which is one of the disadvantages of AB5 relative to RK4. However, this cost is negligible when a Navier-Stokes-based solver is used to compute the aerodynamics. Even if a reduced-order model is used to compute the aerodynamics, this memory requirement is still inconsequential on a modern desktop computer, provided only a small finite number of rigid bodies are being simulated.

Table 1: Coefficients for the Adams-Bashforth schemes.

s	α_0	α_1	α_2	α_3	α_4
1	1	—	—	—	—
2	3/2	−1/2	—	—	—
3	23/12	−4/3	5/12	—	—
4	55/24	−59/24	37/24	−3/8	—
5	1901/720	−1387/360	109/30	−637/360	251/720

To evaluate both the RK4 and AB5 integration schemes and evaluate the errors associated with neglecting the force and moment updates during the substeps in RK4, a simple spring-mass system without aerodynamics was evaluated. The mass in this test case was 40 kg, the spring constant was 1 kN/m, and gravity was not included. For both integration schemes, the time step size Δt was varied from 10^{-2} to 10^{-4} seconds to quantify the numerical error and sensitivity to time step size. In each case, the simulation was initialized with the mass at rest with the spring initially stretched by 1 meter. For an unforced spring-mass system with known initial conditions, the exact response is given by

$$x = C_1 \cos(\omega_n t) + C_2 \sin(\omega_n t), \tag{3}$$

where x is the stretched length of the spring, $\omega_n = \sqrt{\frac{k_s}{m}}$, and C_1 and C_2 are constants that depend on the initial state of the system. To satisfy the initial conditions, $x(0) = 1$ and $\dot{x}(0) = 0$, in this case, $C_1 = 1$ and $C_2 = 0$.. Therefore, the system response is given by

$$x = \cos(\omega_n t). \tag{4}$$

In assessing the accuracy of the numerical schemes, a curve fit of the form

$$x = e^{\sigma t} \cos(\omega_n t) \tag{5}$$

was applied to the numerical results. The term $e^{\sigma t}$ models the growth or decay of the numerical solution. Since there is no physical damping in the problem, a non-zero value of σ results from numerical error; furthermore, a positive value of σ indicates that the numerical error is destabilizing, whereas a negative value indicates that it is stabilizing.

Figure 4(a) and (b) present the time histories for the RK4 and AB5 schemes with different time step sizes. The numerical error in both schemes is destabilizing, as σ is

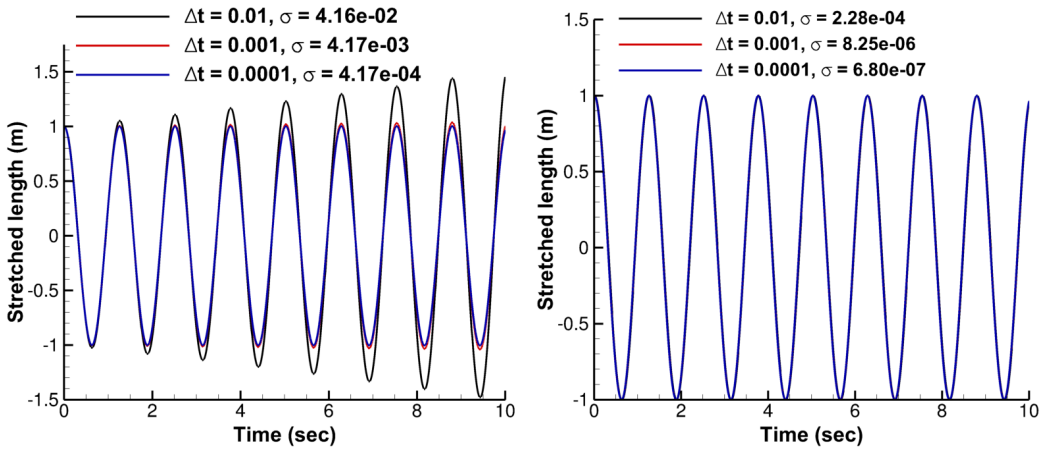

(a) RK4 without force updates at substeps

(b) AB5 scheme

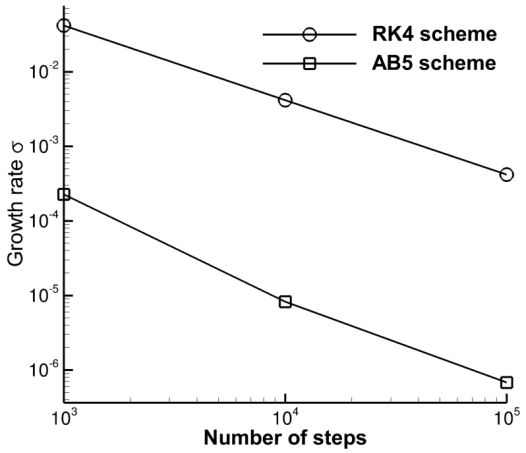

(c) Growth rates for RK4 and AB5

Figure 4: Numerical solution for a spring-mass system with different integration schemes and time step sizes.

always positive. This error is very noticeable in the time history for RK4 with $\Delta t = 10^{-2}$ seconds, which corresponds to approximately 126 steps per cycle. It is also noticeable for $\Delta t = 10^{-3}$ seconds, though the error has reduced by an order of magnitude. The error drops by one more order of magnitude for $\Delta t = 10^{-4}$ seconds. While σ is non-zero for the AB5 scheme, it is approximately two orders of magnitude less than the RK4 scheme for a given time step size, which is indicated in Fig. 4(c). Additionally, there is no significant visual variation in the time histories for AB5 as observed for RK4. Therefore, the AB5 scheme is successful in accurately simulating this spring-mass system without the need for substeps between consecutive time levels.

It should be noted that the RK4 scheme evaluated in this section is not the true Runge-Kutta 4th-order scheme, as the forces and moments are not updated during the substeps. Therefore, the results presented here are intended only to assess the amount of error involved in this type of implementation. It is expected that updating the forces and moments properly during each of the substeps would reduce the error of the RK4 scheme substantially. However, that process would significantly increase the computational cost of the coupled simulation, as the number of flow solver executions would increase by a factor of four. Therefore, AB5 represents an accurate scheme for integrating Eq. 1 without incurring this large additional cost and is used throughout the rest of this thesis.

2.3 GTABB

The Georgia Tech Aerodynamic model for Bluff Bodies (GTABB) is a reduced-order simulation model developed in MATLAB. The program design is modular so that different routines for computing the aerodynamics and cable dynamics can be easily replaced as the need arises. The algorithm flowchart is depicted in Fig. 5. The time-stepping approach is applied, in a manner nearly identical to the FUN3D/6-DoF coupling procedure, except that the aerodynamics model is reduced order and no grid mechanics are required. GTABB starts with a set of initial conditions for each of the state variables in Eq. 1. Forces and moments due to gravity, cables, and aerodynamics are computed by separate modules and then provided to the 6-DoF integrator which solves Eq. 1. As in the FUN3D/6-DoF coupling

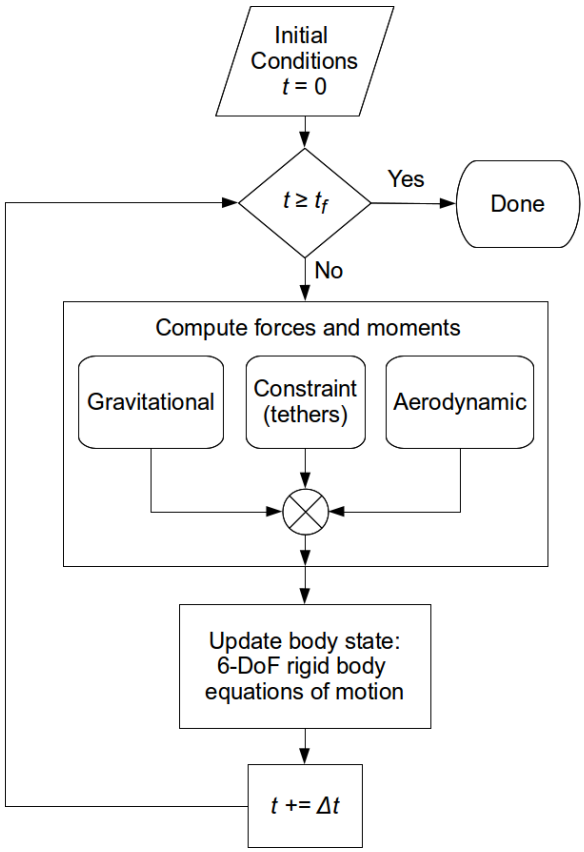

Figure 5: GTABB flowchart.

methodology, the AB5 scheme is applied to solve the rigid body equations of motion.

GTABB has a number of purposes. The most important is to develop and evaluate a physics-based reduced-order aerodynamics model for bluff bodies. The development of this model is described in detail in Chapter 5. Because of the high computational cost of the high-fidelity FUN3D/6-DoF methodology, reduced-order aerodynamic modeling serves an important role in pilot training and stability analysis. GTABB also serves as a testbed for different cable models and provides a rapid means to assess sensitivity to unknown parameters, such as friction in the tether mounting apparatus.

2.4 Cable Modeling

Models have been developed for simulating the constraint forces and moments due to cables on a tethered bluff body. The methodologies can handle both parallel and serial configurations. The cable modeling approach described in this section is developed in a way that

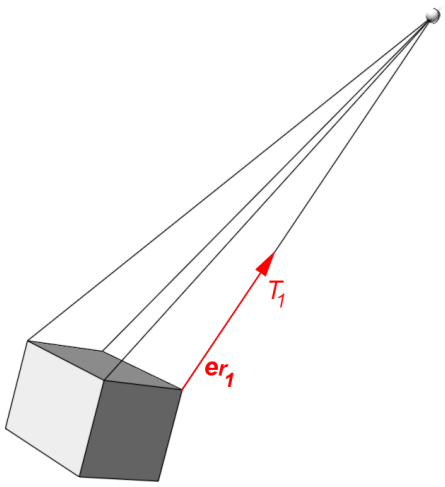

Figure 6: Model of a tethered load suspended by four cables in parallel.

allows modular implementation in either FUN3D/6-DoF coupling or GTABB, which means that the tether system communicates with the other systems (bluff body and helicopter) through forces and moments at the interface. As a result, the cable dynamics can be computed independently of the bluff body dynamics; the cables do not add any additional states to Eq. 1.

2.4.1 Parallel Cables

In the parallel cable approach, each cable is modeled as a linear spring and damper acting in the direction of the vector from the attachment point on the bluff body to the attachment point on the helicopter or top of the wind tunnel. A similar approach has also been taken by Tyson et al. [94] and Sampath [37]. This model allows a bluff body to be suspended by any number of cables in a parallel arrangement. For example, consider Fig. 6, which illustrates a box-like tethered load suspended by four cables. The tension of a cable i acts in the direction $\mathbf{e}_{r_i}$ and has tension T_i. The total constraint force acting on the bluff body is

$$\mathbf{F}_{\text{constraint}} = \sum_{i=1}^{N_{\text{cables}}} T_i \mathbf{e}_{r_i}, \tag{6}$$

where

$$T_i = \begin{cases} k_{si}\left(d_i - l_i\right) - c_i V_{r_i}, & d_i \geq l_i \\ 0 & d_i < l_i \end{cases}, \tag{7}$$

d_i represents the distance between the two cable end points, l_i is the unstretched length of the cable, and V_{r_i} is the velocity of the attachment point on the bluff body in the direction $\mathbf{e}_{r_i}$. Note that this model allows cables to go slack, which can occur when severe dynamic instability is encountered. The spring and damping constants can either be determined by measurement or by a tuning technique. For example, the spring constant can be set to produce a maximum desired stretching for some condition (e.g., in a swinging pendulum motion), and the damping constant may then be set to a value that provides adequate dynamic stability for the cable. Sampath [37] has indicated that the damping coefficient in a similar cable model did not significantly impact the dynamics of the complete bluff body system, as long as it was set to a value appropriate for damping oscillations created by the spring force.

The constraint moment created by the cables can be computed once the tension is known by the equation

$$\mathbf{M}_{\text{constraint}} = \sum_{i=1}^{N_{\text{cables}}} T_i \mathbf{r}_{cg_i} \times \mathbf{e}_{r_i}. \tag{8}$$

2.4.2 Serial Cables

Many tether systems are more complex than the parallel arrangement illustrated in Fig. 6. Often, cables are connected in serial or combined serial-parallel systems, sometimes with rigid frames included, as in the setups depicted in Fig. 7. Additionally, in systems where cable curvature is important, multiple links in a serial configuration can be employed as a discretized representation of the full cable.

Here, the links of the cable are considered to be elastic and are modeled as linear spring-damper elements, which is consistent with the parallel cable modeling approach presented in the previous section. Others, including Hembree and Slegers [95] and Bisgaard et al. [63], have formulated dynamic equations for cables with rigid links. Figure 8 presents a diagram of a cable with seven links in a serial configuration. The mass of the cable may be divided among the eight nodes (uniformly or not, as appropriate) such that each node i is assigned

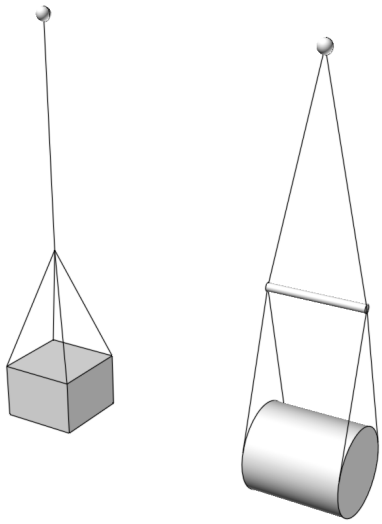

Figure 7: Tether systems requiring serial cables.

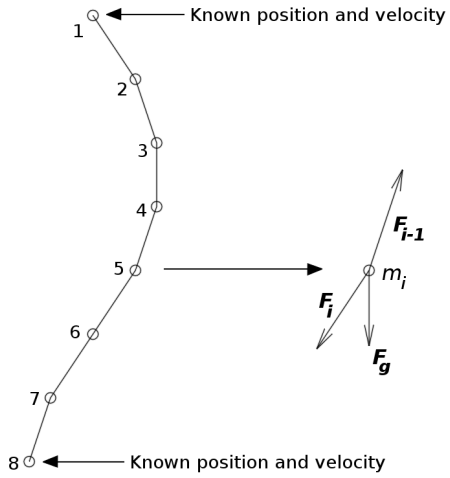

Figure 8: Serial cable element free-body diagram.

mass m_i. The equation of motion for node i, resulting from the free-body diagram, is

$$m_i \ddot{\mathbf{x}}_i = \mathbf{F}_{i-1} + \mathbf{F}_i + \mathbf{F}_{g_i}, \tag{9}$$

where $\mathbf{x}_i$ is the position of node i and F_{g_i} is the force on node i due to gravity. Modeling the adjacent links as linear spring-damper elements, Eq. 9 may be expanded in terms of $\mathbf{x}_{i-1}$, $\mathbf{x}_i$, and $\mathbf{x}_{i+1}$ as

$$\begin{aligned} m_i \ddot{\mathbf{x}}_i = {} & k_{si-1}(\mathbf{x}_{i-1} - \mathbf{x}_i) - c_{i-1}\left[(\dot{\mathbf{x}}_i - \dot{\mathbf{x}}_{i-1}) \cdot \mathbf{e}_{r_{i\to i-1}}\right] \mathbf{e}_{r_{i\to i-1}} \\ & + k_{si}(\mathbf{x}_{i+1} - \mathbf{x}_i) - c_i\left[(\dot{\mathbf{x}}_i - \dot{\mathbf{x}}_{i+1}) \cdot \mathbf{e}_{r_{i\to i+1}}\right] \mathbf{e}_{r_{i\to i+1}} + \mathbf{F}_g. \end{aligned} \tag{10}$$

Equation 10 must be written for each interior node, yielding a coupled system of second-order ordinary differential equations. The positions and velocities of the terminal nodes are known as they are connected to the bluff body or helicopter. The system of equations may be transformed into state-space form and integrated numerically using an appropriate scheme, such as Adams-Bashforth or Runge-Kutta. Strictly speaking, the direction vectors $\mathbf{e}_r$ should be written implicitly in terms of $\mathbf{x}$. However, since these vectors are contained within damping terms that serve to remove vibrational energy from the system, it is usually acceptable to compute them in an explicit sense based on the current node positions. This treatment avoids significant nonlinearities in Eq. 10 that would be introduced by an implicit approach. The tension force exerted by the cable on the bluff body is

$$\begin{aligned} \mathbf{F}_{\text{constraint}} &= k_{sN-1}(\mathbf{x}_{N-1} - \mathbf{x}_N) - c_{N-1}\left[(\dot{\mathbf{x}}_N - \dot{\mathbf{x}}_{N-1}) \cdot \mathbf{e}_{r_{N\to N-1}}\right] \mathbf{e}_{r_{N\to N-1}} \\ &= T\mathbf{e}_{r_{N\to N-1}}, \end{aligned} \tag{11}$$

where N is the number of nodes. The moment is evaluated by

$$\mathbf{M}_{\text{constraint}} = T\mathbf{r}_{cg} \times \mathbf{e}_{r_{N\to N-1}}. \tag{12}$$

Though Eq. 10 has been written for a single cable with links in a serial configuration, the same approach can be applied to more complex systems. For example, the equations of motion for a system with multiple branches involve one or more additional forces applied to the node at the branch location. Tether systems with rigid elements can also be handled

by this methodology. Consider two distinct cables like the one in Fig. 8 joined together by a rigid bar of length l_b and negligible mass at the fifth node. As each cable in this example has 8 nodes, the nodes of cable 1 are numbered 1–8 and the nodes of cable 2 numbered 9–16, and the bar joins nodes 5 and 13 in this system. The bar exerts a force of magnitude F_b on both of these nodes, in opposite directions, so that the geometric constraint $||\mathbf{x}_5 - \mathbf{x}_{13}|| = l_b$ is satisfied. The free-body equations for these two nodes are

$$\begin{aligned} m_5\ddot{\mathbf{x}}_5 &= \mathbf{F}_4 + \mathbf{F}_6 + \mathbf{F}_{g_5} + \frac{F_b}{l_b}(\mathbf{x}_{13} - \mathbf{x}_5) \\ m_{13}\ddot{\mathbf{x}}_{13} &= \mathbf{F}_{12} + \mathbf{F}_{14} + \mathbf{F}_{g_{13}} + \frac{F_b}{l_b}(\mathbf{x}_5 - \mathbf{x}_{13}). \end{aligned} \tag{13}$$

The presence of the bar adds one additional unknown, F_b, and an additional equation, $||\mathbf{x}_5 - \mathbf{x}_{13}|| = l_b$, which must be included in the system to ensure it is closed. The bar also introduces nonlinearity into the system of equations, because F_b is multiplied by the states $\mathbf{x}_5$ and $\mathbf{x}_{13}$ in Eq. 13 and also because the geometric constraint equation is nonlinear. Therefore, a numerical solution is required when a rigid bar is present. If the mass of the bar is significant, an alternative treatment must be employed in which the rigid body equations of motion for the bar are included in the system. Finally, if the mass of the tether system is small relative to the bluff body mass, the term $m_i\ddot{\mathbf{x}}_i$ in Eqs. 10 and 13 vanishes, and the dynamic equations reduce to equilibrium equations at each time step.

Regardless of the complexity of the tether system and the modeling assumptions employed, the forces and moments on the bluff body are still evaluated via Eqs. 11 and 12. If there are multiple cables or a branching cable attached to the bluff body, the total is computed by summing the contributions from each attachment point.

Though this section presents a general framework for modeling cables, some simplifying assumptions are applied with respect to the rotorcraft tethered loads problem, which is the main application of this thesis. In this application, the tethered load itself is typically heavy relative to the cables, and the cables are fairly short. As a result, the suspension system geometry changes very little during operations, provided that it is attached to the helicopter with a gimbal system that prevents cable wind-up [11, 17, 37]. In these configurations, cable stretching degrees of freedom contribute only small-amplitude, high-frequency oscillations

which are not important to the dynamic response of the tethered load [16, 17]. Therefore, it is sufficient to model the cables as massless spring-damper elements, with properties tuned to ensure that only minimal stretching and oscillations occur during the simulation. Cable aerodynamics are also neglected. This simplification is justified by the fact that the cables are of small diameter and in high tension, so aerodynamic forces do not appreciably alter their shape. Additionally, the cables are normally attached to the top of the tethered load. Though they may, therefore, have a small influence on the aerodynamics on the top face of the load, they do not alter the separation and reattachment behaviors on the sides, which are most important to the dynamic response of the load.

CHAPTER III

THREE-DIMENSIONAL BLUFF BODY AERODYNAMICS

3.1 Configurations

Several bluff body configurations have been selected for investigation. All are of small aspect ratio on the order of one to two, so three-dimensional aerodynamics are highly important. The configurations represent *canonical* configurations, meaning that basic geometries (i.e., rectangular prisms and circular cylinders) are modeled. Secondary geometric features such as surface imperfections and wind tunnel mounting hardware are not modeled except for the purpose of assessing sensitivities. This approach is important, because it ensures that the results are representative of fundamental aerodynamic behaviors that are also applicable to more complex shapes. These canonical geometries are also common in many applications, so the findings are broadly pertinent beyond the main applications of this thesis.

The specific configurations investigated are rectangular prisms and circular cylinders. These have been selected due to their importance to helicopter tethered loads as well as their prevalence in other applications. Figure 9 depicts two of the computational models evaluated and the full-scale tethered loads they represent. Figure 9(b) is a 6×6×8 ft CONEX container. Prior evaluations [4, 16] have indicated that the corrugations and skids do not play a major role in the integrated forces and moments or dynamic instabilities of this load. Short finite cylinders with aspect ratios (L/D) of 1.0 and 2.0 were also evaluated. These cylinders are also representative of common tethered loads; for instance, engine canisters (as depicted in Fig. 9(d)) and oil drums.

Table 2: Rectangular prism dimensions and flow conditions.

L (m)	W (m)	H (m)	Re	Re ref. (m)	β (°)
0.232	0.165	0.176	2.12×10^5	0.1985	0, 2, 5, 10, 25, 40, 65, 75, 80, 85, 90

The dimensions and flow conditions examined are listed in Tables 2 and 3. The Mach numbers are not listed here, but since they are very low (below 0.1), the incompressible

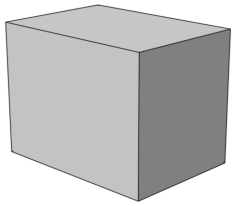

(a) Prism model

(b) CONEX container

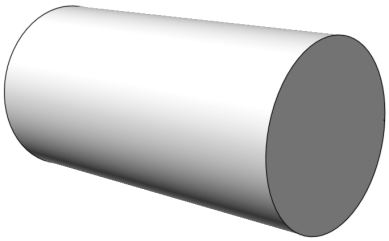

(c) $L/D = 2$ cylinder

(d) Enginer canister

Figure 9: Bluff body types modeled and the full-scale sling loads they represent [3].

Table 3: Cylinder dimensions and flow conditions.

L (m)	D (m)	Re	Re ref. (m)	β (°)
0.2191	0.2191	0.96×10^5	0.2191	0, 2.5, 5, 10, 20, 30, 45, 60, 70, 80, 90
0.2191	0.2191	1.00×10^6	0.2191	0, 10, 30, 70, 90
0.4382	0.2191	1.56×10^5	0.2191	0, 2.5, 5, 10, 20, 30, 45, 60, 70, 80, 90
0.4382	0.2191	0.96×10^5	0.2191	0, 30, 80, 90
0.4382	0.2191	1.00×10^6	0.2191	0, 10, 30, 70, 90

solver path was employed in FUN3D. Only a single Reynolds number was considered for the rectangular prism, which was selected to compare with available wind tunnel test data. It is expected that the rectangular prism should be fairly insensitive to Reynolds number, as noted by other investigators [16, 13, 17], because the separation points are fixed at the sharp leading edges. Conversely, the cylinder may be more sensitive to Reynolds number when separation occurs on its curved face. Therefore, the flow around the cylinders was examined over a broad range of Reynolds numbers ranging from values typical of a low-speed wind tunnel to full scale.

In each case, the yaw angle was varied in the range 0 to 90°, but symmetry considerations can be applied to complete the range of yaw angles from -180° to 180°. The angle of attack

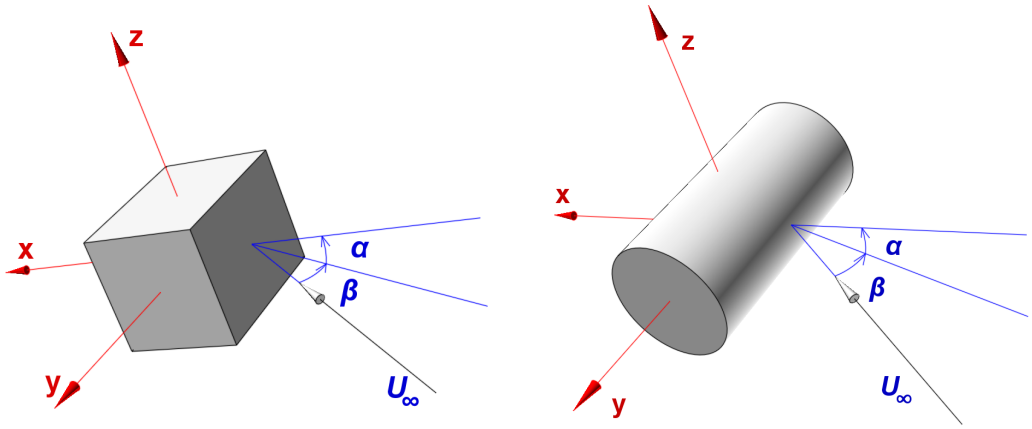

(a) Rectangular prism (b) Circular cylinder

Figure 10: Convention for the angles α and β.

was held constant at 0°. The conventions used for these angles are presented in Fig. 10. In the case of the prism, a yaw angle of 0° corresponds to the broad side facing into the flow, while for the circular cylinders it corresponds to the curved side facing into the flow. This orientation for the cylinder is also referred to as "normal flow," whereas a yaw angle of 90° is referenced as "axial flow."

3.2 Computational Grids

Grids have been created for the bluff body geometries using best practices established for similar configurations with the HRLES turbulence closure [8, 88, 80]. The grids are unstructured and overset, with hexahedral boundary layer cells aligned with the wall-normal direction. At least 35 cells are present in this normal growth layer, with y^+ less than 1.0. It has been demonstrated that this boundary layer spacing is important to capture separation and reattachment on surfaces at high angles of incidence [58, 8, 80]. Outside the boundary layer region, grid cells are tetrahedral. As the results are compared with wind tunnel data, the near-body grids are superimposed on a background grid representing the wind tunnel test section. The tunnel walls extend approximately 10.5 times the cylinder diameter upstream and downstream, and sensitivity studies indicate that the tunnel blockage is minimal (see Section 7.1.5). The wind tunnel mounting hardware is not included in the grids, except for the purpose of evaluating sensitivites, to avoid interactions that would not

be present for true canonical geometries.

Appropriate grid resolution has been determined by grid convergence studies (see Section 7.1.1), validation of integrated quantities (see Section 3.3), and established best practices. In the case of the rectangular prism, results accurate to within experimental uncertainty bounds have been verified with 3.5 million total nodes. For the cylinder, experimental data are not available over most of the range of yaw angles investigated, so a grid sensitivity study has been relied on to determine the required number of nodes. The final cylinder grids have 6.5 – 8 million nodes, with the higher count pertaining to the higher aspect ratio cylinder. The higher grid resolution required for the cylinders is attributed to the fact that the separation location on the curved face is sensitive to the grid resolution, whereas the rectangular prism has fixed separation points. The number of nodes in the finite cylinder grids is also greater than, but of the same order of magnitude as, previous validated computations for a cylinder between walls at a Reynolds number based on diameter of 3900 [8].

Three side views of the grids are presented in Fig. 11. Figure 11(a) illustrates the grid for the cylinder with an aspect ratio of 1.0 from a perspective that includes the top and bottom walls of the wind tunnel. In addition to the fact that the near-body grid has fine resolution, the background grid resolution is also increased in the vicinity of the cylinder and its wake to prevent orphans (nodes lacking an adequate interpolation stencil at overset grid boundaries) and to ensure that wake turbulence is accurately captured. Figure 11(b) depicts the same configuration, but from a closer perspective so that the normal growth region is visible. Figure 11(c) is a side view of the rectangular prism, which is coarser than the cylinder near-body grid. Similar grid resolution and characteristics are present in the top and front views, which are not shown.

3.3 Forces and Moments

Static force and moment coefficients have been compiled for the rectangular prism and circular cylinders for the configurations and flow conditions listed in Tables 2 and 3. These

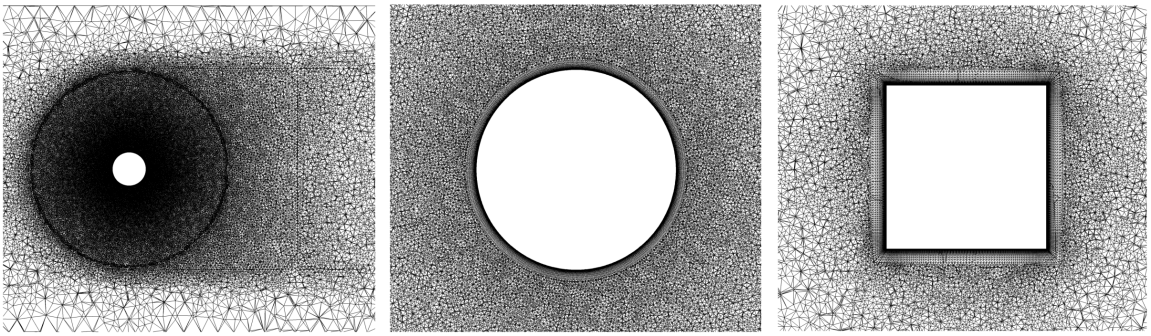

(a) Cylinder and wind tunnel grids (b) Cylinder near-body grid (c) Prism near-body grid

Figure 11: Side views of bluff body overset grids.

are compared with wind tunnel experiments performed at the Georgia Institute of Technology [5] and external data [4, 6, 7], where available. The reference area used for non-dimensionalizing the forces and moments is, for the rectangular prism, $0.5H(L + W)$, the average area of the two vertical faces. Similarly, the reference length for moments is $0.5(L + W)$, and the moments are computed about the geometric center of the prism. The cylinder force and moment coefficients are typically presented with LD as the reference area and D as the reference length for moments, which are also taken about the geometric center. The choice of the planform area (LD) as the reference for the short cylinders, as opposed to the circular face area $\frac{\pi}{4}D^2$, has been made so that force coefficients in the normal flow orientation may be compared directly with two-dimensional results, as in various experimental studies [7, 6, 9].

Grids have been refined to a level that ensures the essential behaviors are captured correctly and that accurate integrated loads are predicted, as demonstrated in Section 7.1.1. As the simulations are time-accurate and the integrated loads unsteady, the simulations are continued long enough for several full shedding cycles to complete to allow the statistical mean values to be reliably computed. Due to the unsteadiness, the computed results are typically presented by the mean value with the minimum and maximum values plotted as dashed lines (they are not uncertainties, but rather an indication of the influence of the vortex shedding fluctuations). The time step size and number of pseudo time steps are selected so that the residuals converge by several orders of magnitude, which is described

in detail in Section 7.1.2.

Figure 12 depicts the drag, side force, and yaw moment coefficients for the rectangular prism. The agreement between these quantities and both sets of experimental data is quite good, as the computed mean values are typically within 7% of at least one of the experimental data sets. There is some variation between the two sets of wind tunnel data, but in general at least one of the two experimental data sets lies within the bounds of unsteadiness of the computations. It should be noted that the experimental data by Rosen et al. [4] was taken at a lower Reynolds number ($Re = 1.5 \times 10^5$ as opposed to 2.1×10^5), but these relatively minor variations in Reynolds number are not expected to have a significant effect on the integrated loads for bodies with sharp-edge separation [16, 13, 17]. This hypothesis is supported by comparisons of forces and moments with full-scale flight test data that are presented in Section 6.4. The greatest disparities between all three sets of data occur in the drag coefficient for yaw angles between 30° and 75°, but the computed drag is between the two sets of experimental data for most of this range. Overall, the computations presented here are some of the best available in the literature to date, which is attributed in large part to the HRLES turbulence approach that resolves large turbulent wake structures. Prior efforts with tranditional RANS turbulence models have been less successful, particularly in the prediction of side force [11, 51, 59].

The force and moment curves for the rectangular prism are characterized by significant nonlinearities. At low yaw angles, the side force and yaw moment coefficient trends are linear. In these conditions, the integrated loads are dominated by the difference between stagnation pressure and base pressure on the front and back faces, respectively. These pressure forces rotate with the prism, since pressure acts normal to the faces, giving rise to the linear trend. An abrupt change occurs in both the side force and yaw moment coefficients between yaw angles of 10° and 30°, ending this linear trend. This behavior has been studied in detail by Greenwell [12] for two-dimensional rectangular prisms. A shear layer phenomenon known as reattachment is responsible for this sudden change in the forces and moments, which is investigated in detail in the following sections. Over a range of yaw angles, the side force coefficient remains approximately constant. Prosser and Smith have

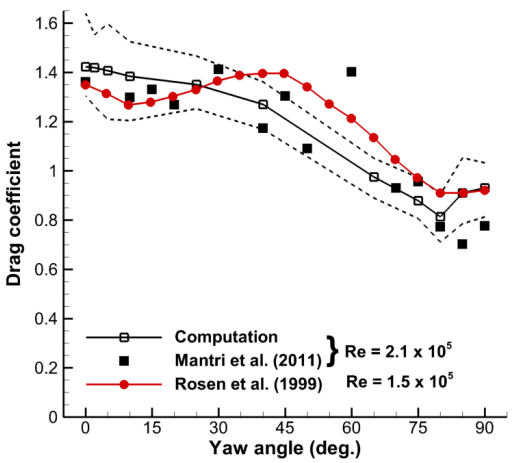

(a) Drag coefficient

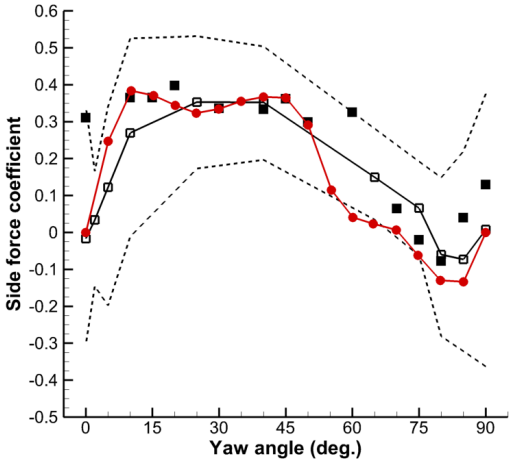

(b) Side force coefficient

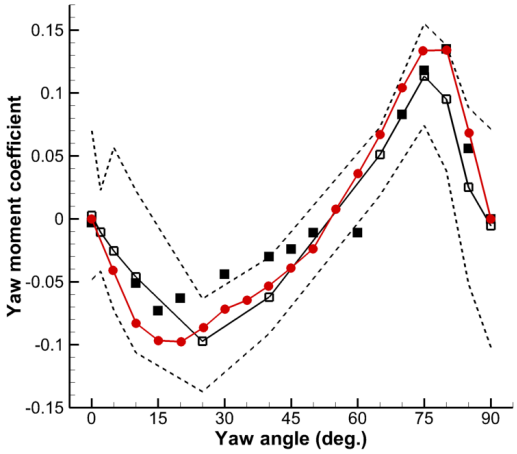

(c) Yaw moment coefficient

Figure 12: Rectangular prism computed force and moment coefficients and comparison with experimental data [4, 5]. Dashed lines represent min and max values for the unsteady simulations.

identified in prior work [96] that this range can be predicted as a function of the aspect ratio (L/W) for two-dimensional and three-dimensional rectangular prisms.

The present numerical analysis approach has been previously validated for flows over infinite cylinders via comparisons with experiments in the subcritical Reynolds number regime at $Re_D = 3900$ [8]. The drag coefficient, shedding frequency, and separation location were all well within the error bounds of experimental measurements in that study. Because most of the applications of this thesis (including rotorcraft tethered loads) typically involve larger Reynolds numbers, the current work has focused on transitional and supercritical flows. The computations are validated with experimental data at yaw angles of 0° and 90°, as other orientations are not available in the literature for short finite cylinders. Figure 13 presents the drag coefficients of the present computations in normal flow compared with the experimental data of Wieselsberger [6] and the prior computations of Lynch and Smith [8]. Here, the drag coefficient is computed with the planform area (LD) as the reference area. It is apparent from this figure that the agreement with experimental data is excellent in the supercritical regime. Furthermore, in both the transitional and supercritical regimes, the difference in drag coefficient between the two different aspect ratios is small. This result is in agreement with the experimental observations of Zdravkovich et al. [9], who found that the drag coefficient is insensitive to aspect ratio below $L/D = 5$ in the normal flow condition.

The finite cylinder drag predictions in the range of Reynolds numbers from 0.96×10^5 to 1.56×10^5 are somewhat lower than the experimental data, with only minor variation across this range. However, they are comparable to the experimental drag in the transitional regime, which occurs at a somewhat higher Reynolds number in the experiments. Hoerner [7] noted that boundary layer transition may occur at different Reynolds numbers depending on the surface roughness and wind tunnel turbulence level. Considering the excellent correlation at subcritical and supercritical Reynolds numbers, it is clear that the HRLES turbulence approach is able to accurately predict the drag in these regimes. However, the RANS model active inside the boundary layer is the two-equation k-w SST model, which assumes a fully turbulent boundary layer. The fully-turbulent RANS model

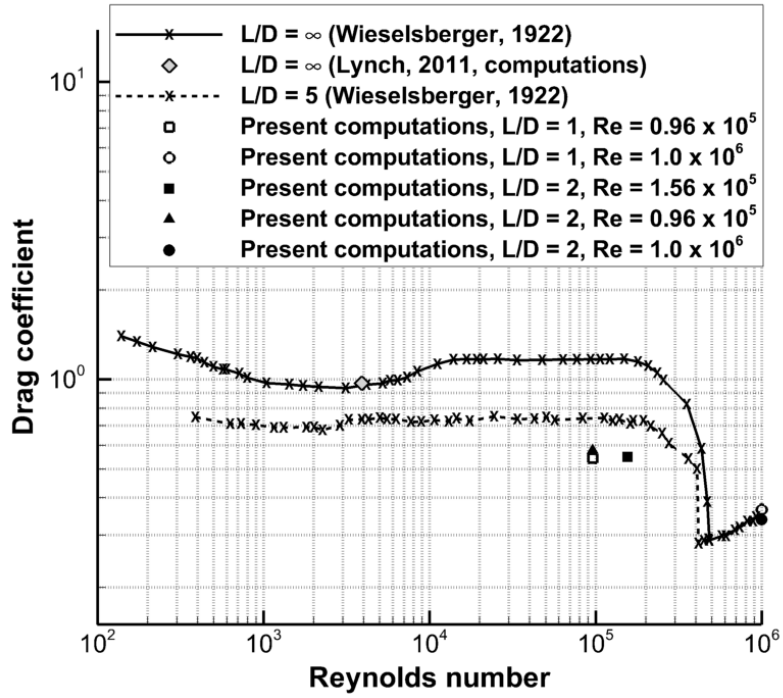

(a) $\beta = 0°$ (normal flow) orientation

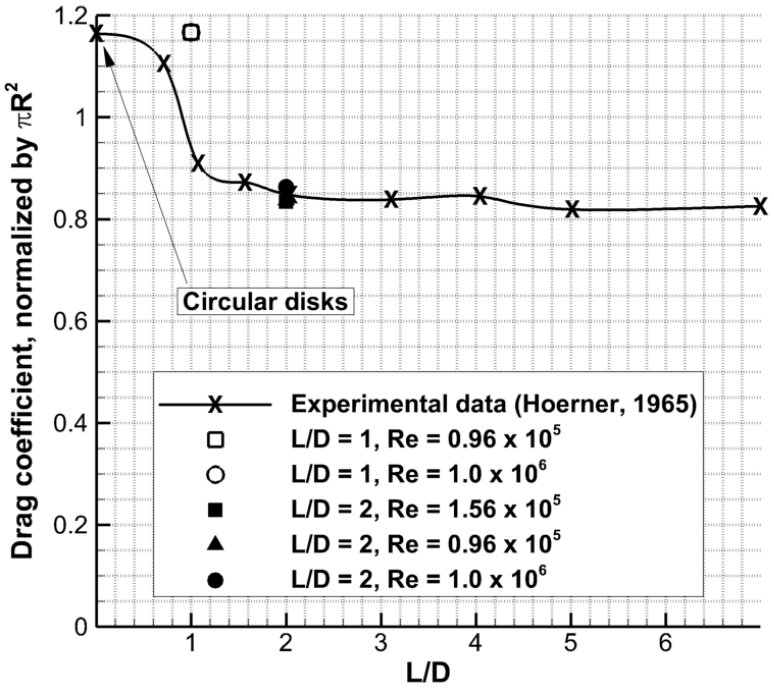

(b) $\beta = 90°$ (axial flow) orientation

Figure 13: Comparison of the current computations in normal and axial flow configurations with experimental data by Wieselsberger [6], Hoerner [7], and previous computations by Lynch and Smith [8].

is a possible reason for the lower drag in this range of Reynolds numbers, where in the experiments the boundary layer had not fully transitioned yet. It is noteworthy that the same approach gives accurate results for fully laminar flow at a Reynolds number based on diameter of 3900 despite this shortcoming of the RANS model. For applications of interest here, fully turbulent flows are most important, and boundary layer transition is of minimal importance. Furthermore, it will be shown later that this behavior primarily impacts the drag for yaw angles below 30° but has minimal effect on most other quantities of interest.

Figure 13(b) illustrates the drag in axial flow, compared with experimental data from Hoerner [7] for circular disks and finite cylinders. The drag force in this figure is normalized by the frontal area $\frac{\pi}{4}D^2$ instead of the planform area. This figure indicates that in axial flow, there is no sensitivity of the drag to Reynolds number, at least over the range of Reynolds numbers evaluated here. This result is not surprising, as in this configuration forced separation occurs at the sharp edges of the flat face, whereas in normal flow separation from the curved face depends on the boundary layer and wake turbulence characteristics. The present computations at an aspect ratio of 1.0 result in drag comparable to a circular disk in the experimental data. The data indicate that there is a sharp drop in drag near this aspect ratio corresponding to a change in the shear layer reattachment behavior. Due to the abruptness of this change and the fact that the shear layer reattachment distance is sensitive to a number of factors including the level of freestream turbulence [10], it is not unusual for the drop in drag to occur at a slightly different aspect ratio depending on the conditions. The computations for the cylinders with an aspect ratio of 2.0 are consistent with the experimental data for that aspect ratio.

Figure 14 highlights the differences in shear layer behavior for the two different aspect ratios in axial flow. Streamlines and time-averaged contours of pressure coefficients are depicted in a top-down view of each case. Separation occurs at the sharp edges of the front face, promoting the formation of low-pressure, vortical bubbles that draw the outer flow back towards the surface. For an aspect ratio of 2.0, reattachment occurs on the aft portion of the curved face, but it remains separated for an aspect ratio of 1.0, as the length is not sufficient for reattachment. Shear layer reattachment is accompanied by pressure

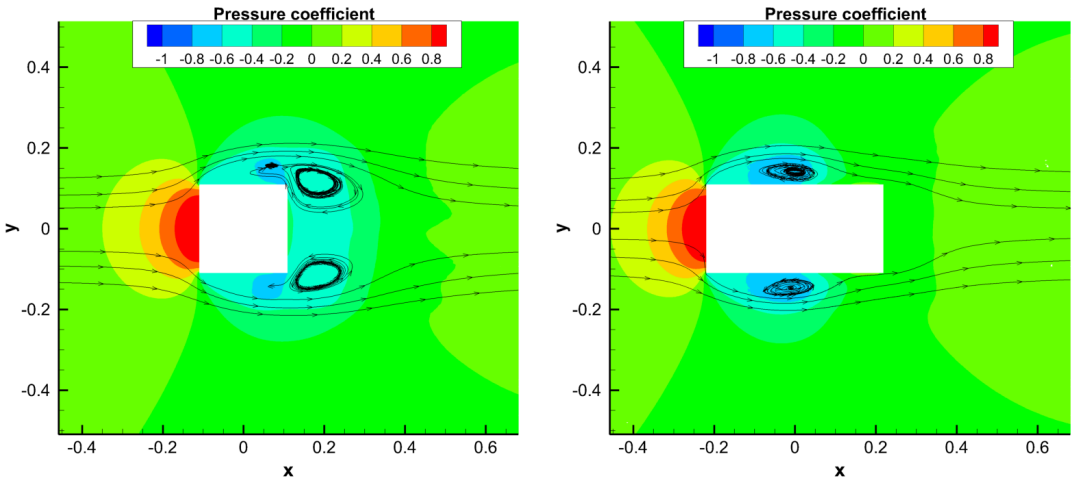

(a) $L/D = 1$ (b) $L/D = 2$

Figure 14: Time-averaged contours of pressure coefficient and streamlines in a top-down view for the axial flow condition of the circular cylinder.

recovery, resulting in significantly lower base pressure and drag for the higher aspect ratio. Reattachment occurs suddenly as the aspect ratio is increased, which explains the abrupt decrease in drag in Fig. 13(b) between aspect ratios of 1.0 and 2.0.

Figure 15 details the mean force and moment coefficients for the cylinders when the yaw angle is varied. All forces are normalized by the reference area LD, while the yaw moment is normalized by the reference area LD and the reference length D. The level of unsteadiness in each case is indicated by vertical bars, the magnitude of of which represents the root-mean-square of the fluctuation in each quantity.

The drag coefficient behavior is presented in Fig. 15(a). For each of the two aspect ratios, the most significant changes with Reynolds number occur near a yaw angle of 0°, the normal flow orientation. As has been demonstrated in Fig. 13(a), the lower Reynolds number cases are in the transitional region at a yaw angle of 0°, while the higher Reynolds number cases are supercritical. The difference in turbulence properties in the wake results in a decrease in drag at low yaw angles in this supercritical regime. However, the influence of Reynolds number on drag decreases as the yaw angle is increased; for yaw angles of 30° and above, only minor differences in drag exist for a given aspect ratio at different Reynolds numbers. This behavior indicates that fixed separation from the sharp edges becomes the

dominant factor in determining overall drag for moderate to high yaw angles, while smooth separation from the curved face has a significant impact on the drag at low yaw angles. Similar behavior, in this regard, is present for both aspect ratios; at low yaw angles, the drag coefficient depends mostly on Reynolds number, while for moderate to high yaw angles, it is primarily a function of aspect ratio.

Significant differences in drag exist between the two aspect ratios for moderate to high yaw angles. While the shear layer behavior is different between the two, as illustrated in Fig. 14, the difference in total drag is not as large as the difference in drag coefficient. The large difference in drag coefficient (the drag coefficient for the cylinder with aspect ratio 1 is 180% higher than that of the aspect ratio 2 cylinder) arises from the fact that the drag is normalized by LD in Fig. 15 over the entire range of yaw angles. The dimensional drag is 36% higher for an aspect ratio of 1.0 than it is for an aspect ratio of 2.0 at a yaw angle of 90°, as shown in Fig. 13(b).

Except for at very low yaw angles (10° or less), the side force and yaw moment are primarily functions of aspect ratio rather than Reynolds number. The side force for the cylinder with an aspect ratio of 1.0 is especially sensitive to minor flow changes, which is evident in the numerous changes in slope across the range of yaw angles. The magnitudes of fluctuations are also very large relative to the mean values. This sensitivity also results in larger changes in the mean value with Reynolds number than in the other quantities, though the large fluctuations are present at both transitional and supercritical Reynolds numbers. Less erratic behavior in the side force is observed for an aspect ratio of 2.0. The side force for this case does exhibit some sensitivity to Reynolds number, as the side force magnitude is smaller, by approximately 12% on average, for supercritical flow than it is for transitional flow over most of the range of yaw angles. The fluctuations in side force are less prominent for an aspect ratio of 2.0 than for an aspect ratio of 1.0.

The yaw moment coefficient is also primarily a function of aspect ratio over most of the range of yaw angles. The trends in yaw moment with yaw angle are similar for both aspect ratios and are characterized by linear or approximately linear variations that are abruptly interrupted and reversed at discrete yaw angles. This behavior is very similar to

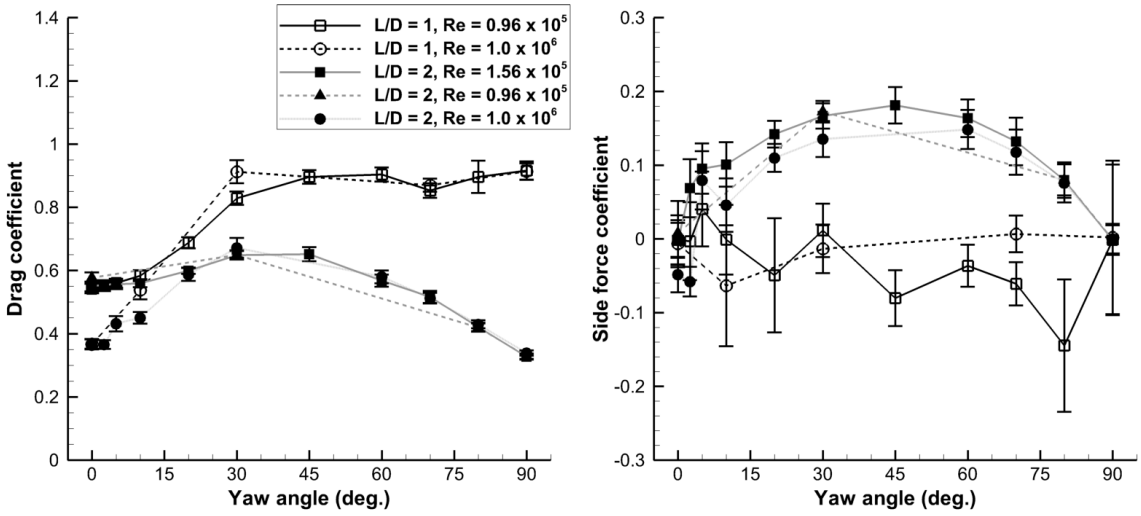

(a) Drag

(b) Side force

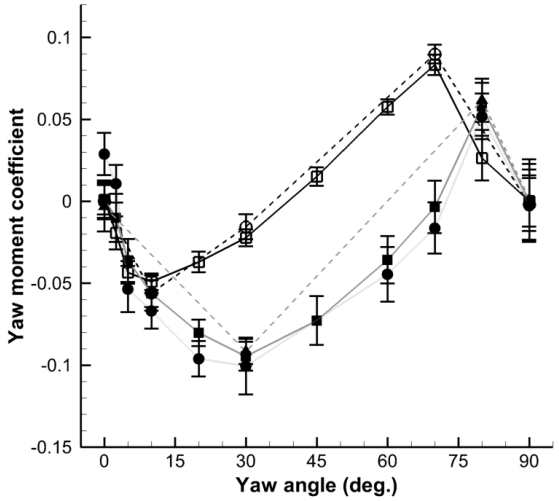

(c) Yaw moment

Figure 15: Time-averaged force and moment coefficients for circular cylinders over the range $\beta = 0° - 90°$, with vertical bars denoting RMS fluctuations.

the behavior observed for the rectangular prism (Fig. 12(c)) and is caused by changes in shear layer characteristics on the sides of the cylinder. The angles at which the shear layer behavior changes are a function of the aspect ratio, resulting in yaw moment reversals at 10° and 70° for an aspect ratio of 1.0 and at 30° and 80° for an aspect ratio of 2.0.

3.4 Unsteady Flow Characteristics

For many applications of bluff body aerodynamics, the mean flow behavior is not the only concern. Bluff body flow fields are inherently unsteady due to the shed wake, even when the configurations are static. The unsteadiness is particularly important for applications in which the dynamic response of the body is sought, including helicopter tethered loads and vortex-induced vibrations of bridges, buildings, towers, and cables [24].

Figures 12 and 15 provide an indication of the fluctuation magnitudes for each of the force and moment coefficients, but it is easier to analyze the trends when the mean values are removed. Therefore, fluctuation magnitudes for the various cylinder simulations are presented in Fig. 16. The largest fluctuations occur in the side force coefficient for cylinders of aspect ratio 1.0, particularly at low yaw angles ($\beta < 30°$) and high yaw angles ($\beta > 70°$). These fluctuations are especially significant when compared with the mean side force coefficient magnitude. Fluctuation magnitudes in all three coefficients are, in general, more closely correlated with aspect ratio than Reynolds number, but this trend does not hold uniformly. For instance, the fluctuations in drag at yaw angles below 45° follow the opposite trend, with fluctuation magnitudes that correlate with Reynolds number rather than aspect ratio. The same trends were observed in the mean drag coefficient, which suggests that the separation location on the curved cylinder surface influences not only the mean drag but also the fluctuations.

In addition to the fluctuation magnitudes, the frequencies also represent an important aspect of the unsteadiness. In order to accurately capture the relevant frequencies, it is necessary to apply large-eddy simulation in the wake [88, 97], as performed in this research. Figure 17 depicts the power spectrum for velocity magnitude in the wake four diameters downstream along the centerline of the cylinder with an aspect ratio of 1.0 at a Reynolds

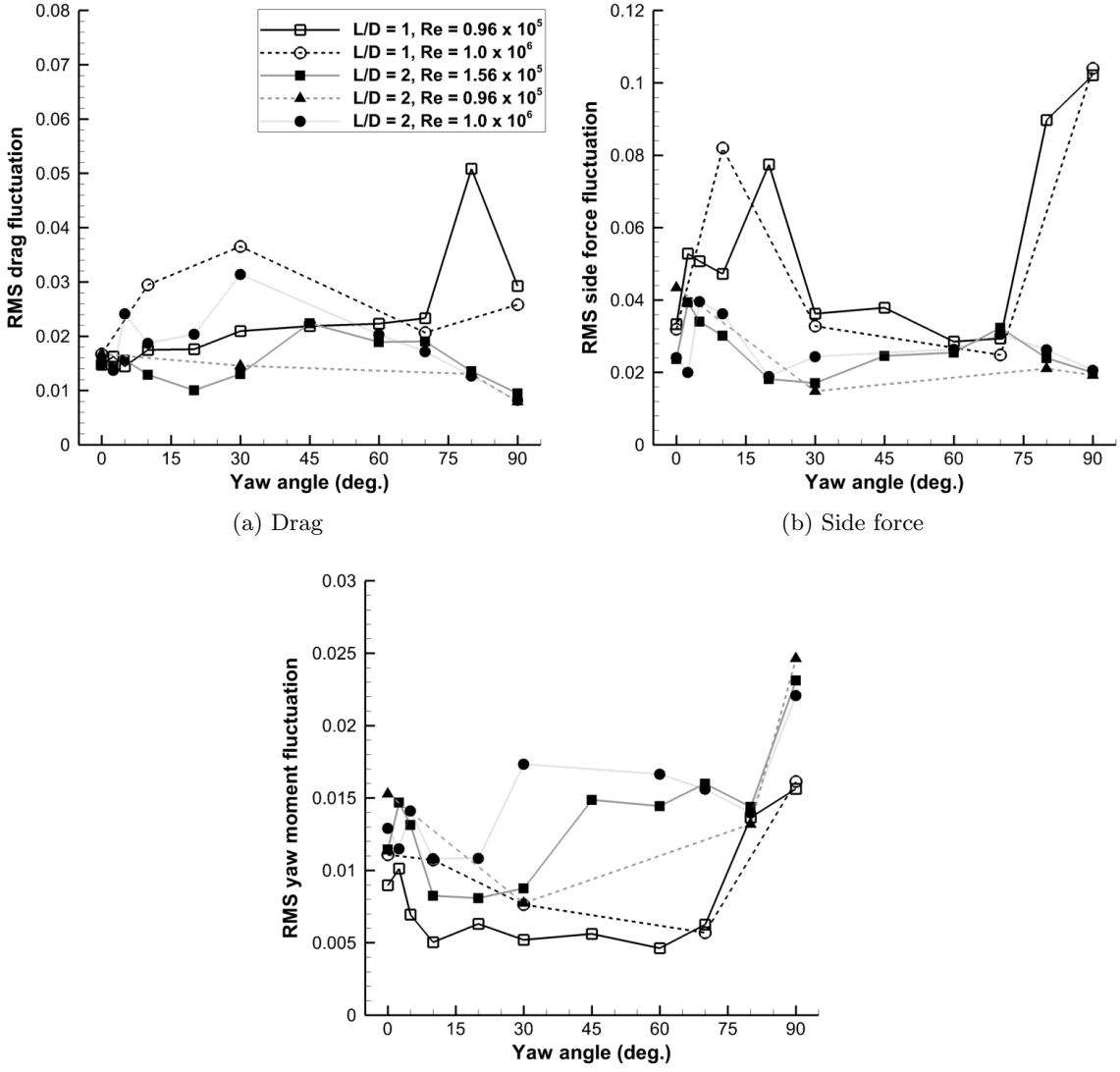

(a) Drag

(b) Side force

(c) Yaw moment

Figure 16: RMS of force and moment coefficient fluctuations over the range of yaw angles from 0° – 90°.

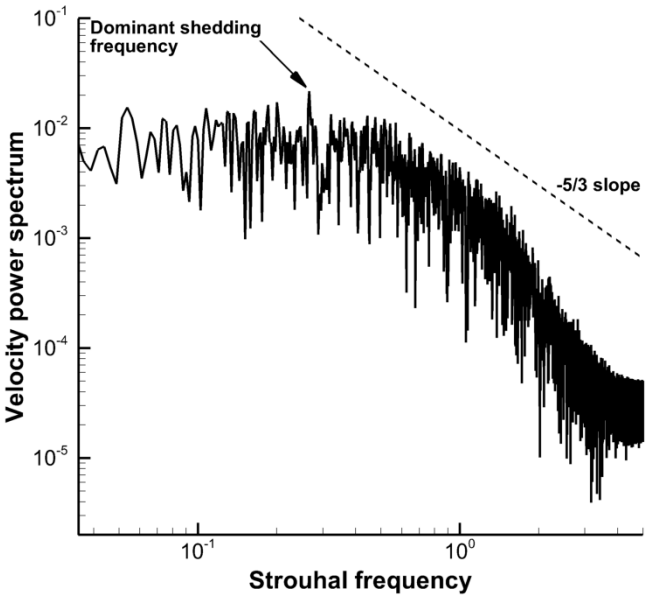

Figure 17: Power spectrum of velocity magnitude for a cylinder with an aspect ratio of 1.0, Reynolds number (based on diameter) of 1.0×10^6, and yaw angle of $0°$.

number based on diameter of 1.0×10^6. While a dominant frequency can be identified, the spectrum is broadly distributed over a range of frequencies. A significant degree of high-frequency content is also resolved by the large-eddy wake simulation. These resolved frequencies drop off with a slope of approximately $-5/3$ on a log-log scale, eventually leveling out at scales too fine to be resolved by the grid.

When the dominant Strouhal frequency is examined for each of the cases, as in Fig. 18, it encompasses a broad range from approximately 0.14 to 0.27. Clearly identifiable trends related to aspect ratio, yaw angle, or Reynolds number are absent. Clarification of this result is possible by considering experimental tests of low aspect ratio cylinders in the range 2.0 – 8.0, at Reynolds numbers in the range $1.1 \times 10^5 \leq Re_D \leq 2.1 \times 10^5$, by Zdravkovich et al. [9]. In that study, the vortex shedding peak of short aspect ratio cylinders was wider than for an infinite cylinder. Furthermore, during testing of individual cylinders with two free ends, vortex shedding would sometimes occur at a given frequency for some length of time, be interrupted by an aperiodic signal, then settle into a different identifiable frequency, and this behavior would continue indefinitely. The range of observed frequencies became smaller as the aspect ratio increased. This behavior was attributed to the fact that

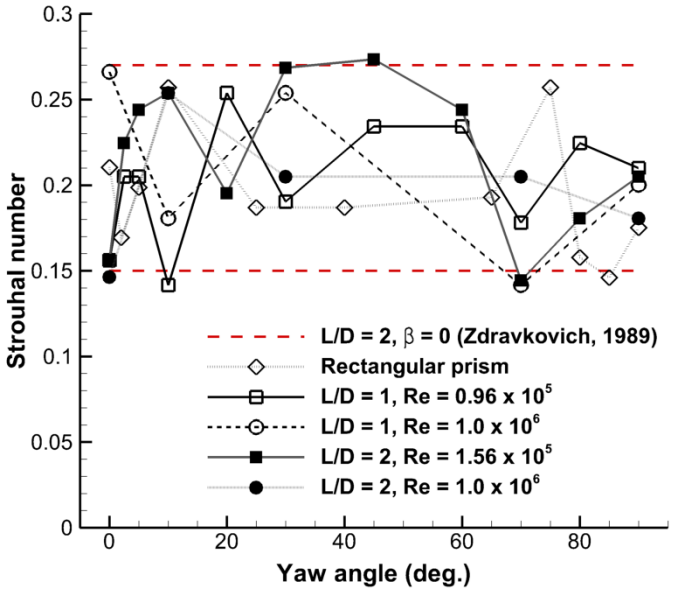

Figure 18: Dominant Strouhal frequencies for finite cylinders and rectangular prisms as a function of yaw angle and Reynolds number. Experimental data from Ref. [9].

the tip shedding behavior is unstable and intermittent [33], and for small aspect ratios the tip shedding interacts significantly with the curved-surface vortex shedding. The range of Strouhal frequencies from the present computations of both cylinders and the rectangular prism is bounded neatly by the experimental variation measured by Zdravkovich et al. [9] for a cylinder with two free ends and an aspect ratio of 2.0, as shown in Fig. 18. It is significant that the typical infinite cylinder Strouhal number of 0.2 is roughly in the center of the range for short three-dimensional bluff bodies. Therefore, a value of 0.2 represents a reasonable approximation that may be applied in dynamic simulation models, provided vortex shedding lock-in to body frequencies is not a concern.

3.5 Time-Averaged Flow Characteristics

The significant unsteadiness and complex turbulent structures in flows about short three-dimensional bluff bodies renders it challenging to study phenomena that primarily influence the mean forces and moments. To illustrate, Fig. 20 presents flow field snapshots for a cylinder with an aspect ratio of 2.0 at a yaw angle of 10° and the rectangular prism at a yaw angle of 25°. Isosurfaces of Q-criterion in the wake are rendered as smoke, while the surface

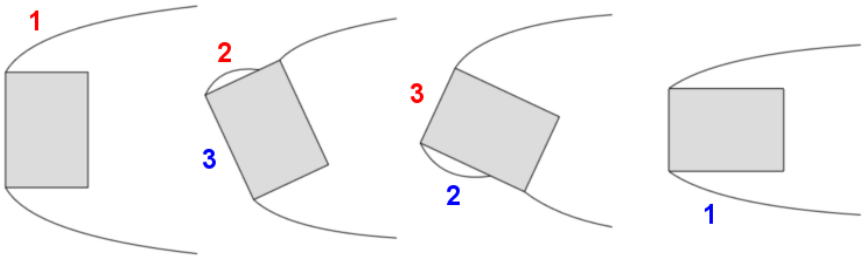

Figure 19: Illustration of shear layer behavior for a rectangular bluff body. (1) Fully separated shear layer, (2) reattaching shear layer, and (3) fully attached flow (reprint of Fig. 3 for convenience).

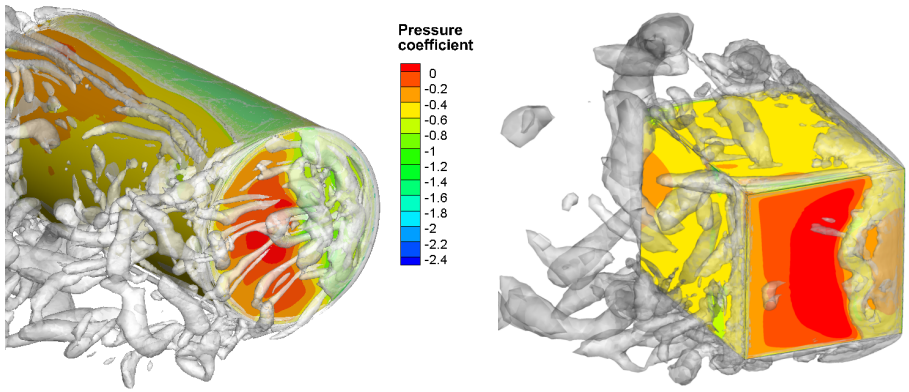

(a) Cylinder, aspect ratio of 2.0 and yaw angle of 10°

(b) Rectangular prism, yaw angle of 25°

Figure 20: Unsteady flow snapshots on various short bluff bodies. Flow direction is from right to left.

is colored by contours of pressure coefficient. In both snapshots, there exist complex, highly three-dimensional turbulent structures that are resolved by the simulation. For example, in Fig. 20(a), "roller" vortices originating from the separation point on the curved face are visible, but these structures break down as they mix with the vortices shed from the flat face that spill into the wake. The interactions between these structures emanating from the different faces of the bluff bodies are responsible for the variable, multimodal behavior in the dominant shedding frequency, as observed in experiments [33, 9] and in the computations presented in Section 3.4.

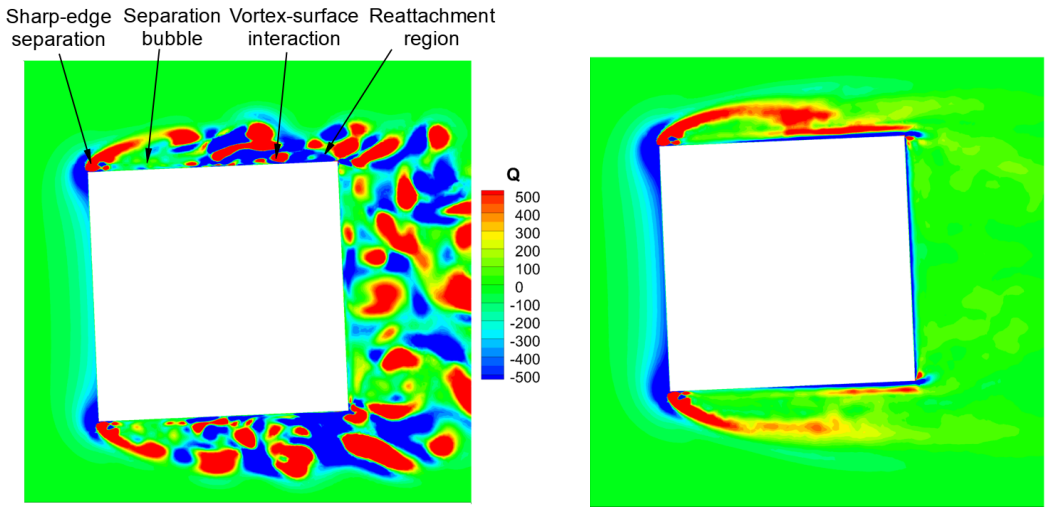

(a) Unsteady flow field

(b) Time-averaged flow field

Figure 21: Unsteady and time-averaged reattachment behavior for $L/D = 1$ cylinder, $Re_D = 0.96 \times 10^5$, $\beta = 2.5°$; top view shown.

In addition to the turbulent structures, both illustrations also include shear layer reattachment, which has been described at length in Chapter 1. Figure 3 is reprinted in Fig. 19 for convenience. Shear layer reattachment is characterized by a low-pressure separation bubble, followed by a sudden increase in pressure, and finally a region of attached flow. As illustrated in Fig. 19, in this situation, the shear layer initially separates at a sharp leading edge and then is drawn back to the surface downstream. The sudden increase in pressure is coincident with the reattachment of the shear layer on the surface. Figures 20(a) and (b) both clearly contain shear layer reattachment, as evidenced by the pressure signatures on the faces. However, the unsteady flow is more complex than the diagram from Fig. 19. After the shear layer separates, it begins to break up into discrete vortices that travel downstream. These vortices interact with the surface, either mixing with the boundary layer or breaking up further and being swept into the separation bubble. Such interactions are illustrated in a top view of the cylinder with aspect ratio 1.0 in Fig. 21(a). The unsteady, turbulent character of the shear layer and its interaction with the surface create difficulty in assessing the reattachment distance and other quantities directly related to the mean forces and moments.

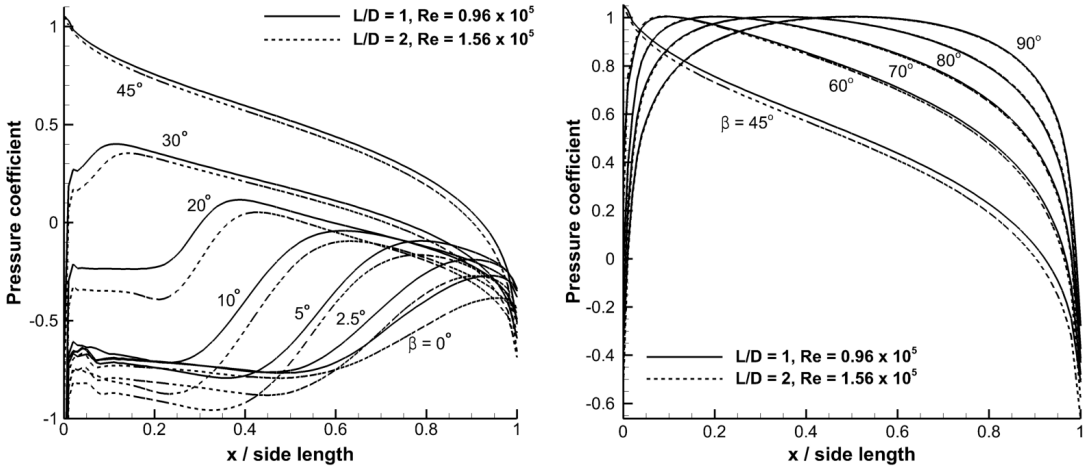

(a) Reattaching flow

(b) Attached flow

Figure 22: Pressure distributions for reattaching and attached flow on flat cylinder faces.

To overcome these difficulties related to unsteady flow, the flow fields themselves, including pressure, vorticity magnitude, and Q-criterion, have been time averaged so that the mean separation and reattachment behavior may be studied. To illustrate the effect over time, Fig. 21 presents the time-averaged version of the unsteady flow field from Fig. 21(a). The scale for Q-criterion has been reduced as the time averaging process reduces the maximum value of this quantity. The time-averaging process smears out discrete structures, resulting in a flow field that more closely resembles a typical RANS solution (though in actuality, the separated regions are resolved via LES and subsequently time-averaged). Following this process, it becomes possible to clearly identify the trajectory of the shear layer and its reattachment point on the side of the cylinder.

To ensure that no bias due to vortex shedding is present in the time averaging process, the following procedure was followed. Each numerical experiment was performed over 40–60 vortex shedding cycles based on a Strouhal number of 0.2. As the flowfields were initialized from steady-state solutions, in some cases transients were apparent in the forces and moments for up to the first ten cycles, so this period of time was not included in the averaging. The flowfields (as well as the forces and moments) were, therefore, averaged over at least 30 cycles. Additionally, the window for time averaging was selected so that the endpoints corresponded to peaks in the forces and moments, ensuring that the time averaging process

did not include partial vortex shedding cycles, which could also introduce bias.

Figure 22 presents time-averaged reattaching- and attached-flow pressure distributions along central slices of the flat faces of the circular cylinders. For clarity, only the results from a subset of the cases are presented in this figure. The time-averaging process produces smooth pressure distributions which provide insight into the behavior of the mean forces and moments. The separation bubble and attached flow distributions are apparent in Fig. 22(a). Reattachment on the flat faces of the cylinder occurs even at a yaw angle of 0°, when the flat faces are parallel to the flow. Increasing the yaw angle moves the reattachment point forward and increases the maximum pressure coefficient at reattachment. At low yaw angles, the pressure in the separation bubble changes only slightly, but it subsequently begins to increase rapidly at higher yaw angles. Once the yaw angle reaches 45°, the stagnation point is located at the corner of the face, and the separation bubble vanishes completely. Reattachment behavior has been demonstrated by Greenwell [12] and Robertson [10] to significantly influence the side force and yaw moment for two-dimensional rectangular bluff bodies, and similar influences are apparent for finite cylinders and rectangular prisms. For example, the rapidly-changing separation bubble size and pressure distribution in Fig. 22(a) result in sudden changes in the yaw moment, which are apparent in Fig. 15(c). The qualitative aspects of these reattaching pressure distributions are very similar among finite cylinders and two- and three-dimensional rectangular bluff bodies [12, 10].

Further increasing the yaw angle beyond 45°, as represented by Fig. 22(b), results in the stagnation point moving to the surface on which reattachment previously occurred. In the case of Fig. 22(b), the stagnation point has moved from the curved face to the flat face of the cylinders. The pressure coefficient is 1.0 at the stagnation point, but it moves from the edge of the flat face to the center as the yaw angle is increased to 90°. The fully-attached pressure distribution is simpler than the reattaching pressure distribution, in that the maximum pressure remains constant, and there is no separation bubble. The motion of the stagnation point changes the shape of the pressure distribution, which also affects the drag, side force, and yaw moment.

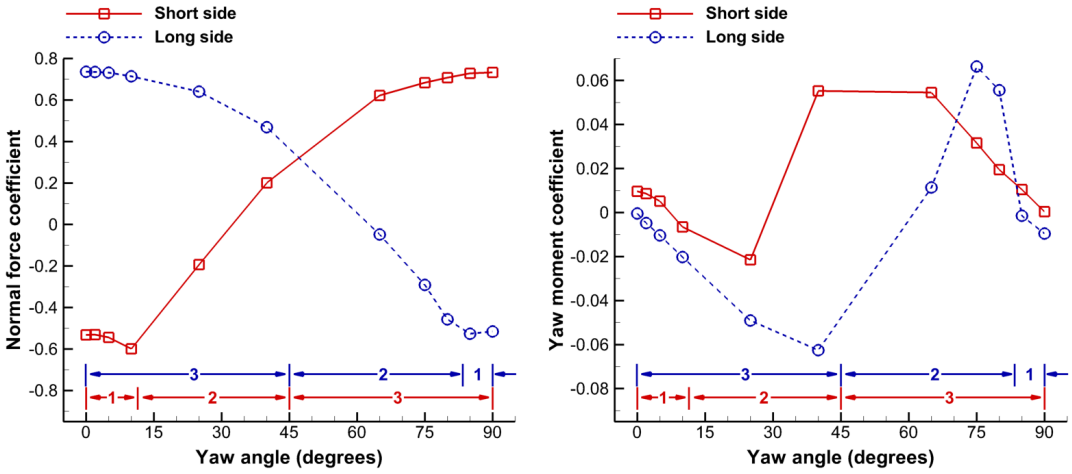

(a) Normal force coefficient (b) Yaw moment coefficient

Figure 23: Normal force and yaw moment coefficients on individual faces of the rectangular prism. The extents of the three shear layer behaviors from Fig. 19 are labeled.

3.5.1 Influence on Forces and Moments

While Figs. 12 and 15 clearly reveal significant influences of changing shear layer behavior, it is difficult to determine these effects exactly from these figures, because they represent the overall forces and moments including the net influence of all faces combined. Therefore, it is instructive to compute the forces and moments on individual faces where the different shear layer behaviors occur. Figure 23 presents the normal force and yaw moment coefficients for individual faces of the rectangular prism. The normal force coefficient is normalized by the face area, while the moment coefficient is normalized by the face area and side length. Moments are computed about the center of the face. The three different regions denoted in Fig. 19 are marked: (1) fully separated shear layer, (2) reattaching shear layer, and (3) fully attached flow. The long and short sides are also color-coded according to the convention from Fig. 19. That is, the flow over the red face is initially separated while the stagnation point is located on the blue face, and the characteristics eventually switch as the yaw angle increases. At each yaw angle, these quantities have been computed by integrating the time-averaged pressure distributions over the entire face.

Figure 23(a) demonstrates that the changing shear layer behavior is immediately related to changes in the normal force acting on the individual face of the prism. The separated

flow region (1) is characterized by a constant negative normal force arising from the low pressure across the face. When shear layer reattachment (2) occurs, a positive linear trend begins. This change is due to the relatively higher pressure in the attached portion, as shown in the curves in Fig. 22(a). The normal force continues to increase as the separation bubble shrinks and the attached portion grows. In fully attached flow (3), the normal force continues to rise and finally reaches a maximum when the stagnation point is at the center of the face. These trends do not significantly change with side length, as they are apparent in both the red and blue curves in Fig. 23(a). The main difference between the two is the angle at which reattachment occurs, which varies with the side length.

The influence of shear layer behavior is also apparent in the yaw moment (Fig. 23(b), though the changes are larger than in the normal force, and there are also greater differences corresponding to side length. In separated flow (1), the yaw moment magnitude slowly changes as the yaw angle is increased. When reattachment occurs (2), the yaw moment trend does not immediately reverse as the normal force trend. Instead, it initially becomes more severe because of the higher pressure on the aft portion of the face and the lower pressure on the forward portion. As the bubble shrinks, the high pressure region begins to cover the forward portion as well, and the yaw moment about the face center abruptly changes sign. It returns to zero in fully attached flow (3) when the freestream is normal to the face. The fact that the yaw moment trend does not immediately reverse in reattaching flow is also reflected in the overall yaw moment for the rectangular prism in Fig. 12(c). In contrast, the side force immediately responds to reattachment, as is seen in Fig. 12(b).

Figure 24 depicts the normal force and yaw moment acting on the flat faces of the cylinders, corresponding to the lower Reynolds number computations for each. The forces and moments are normalized by the area of the face, $\pi D^2/4$, with D selected as the reference length for moments, and moments are computed about the center of the face. Reattachment occurs on the flat face even at a yaw angle of 0° for both cylinders, so the completely separated flow region (1) is absent. Reattaching and fully attached shear layer behaviors are still present, and their characteristics are qualitatively very similar to those of the rectangular prism. Notably, the behaviors are nearly identical for the two different aspect

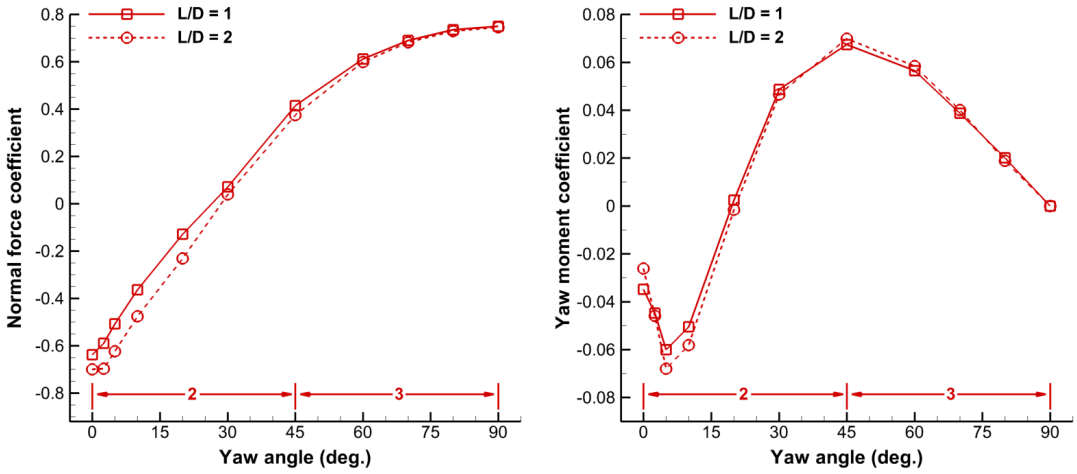

(a) Normal force coefficient (b) Yaw moment coefficient

Figure 24: Normal force and yaw moment coefficients on flat faces of the cylinder. The extents of the three shear layer behaviors from Fig. 19 are labeled.

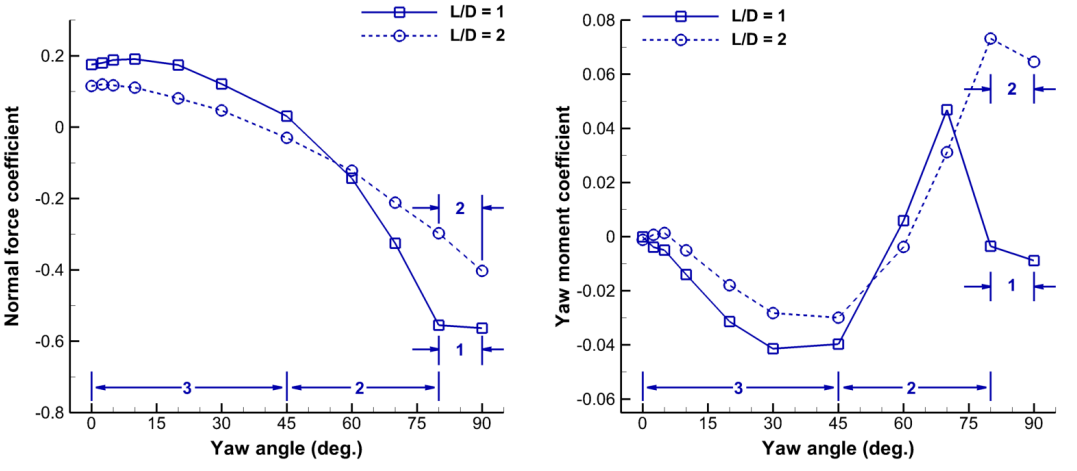

(a) Normal force coefficient (b) Yaw moment coefficient

Figure 25: Normal force and yaw moment coefficients on curved faces of the cylinder. The extents of the three shear layer behaviors from Fig. 19 are labeled.

ratios; the shear layer behavior and its influences on the forces and moments of the flat faces are independent of the aspect ratio for these cases.

The forces and moments have also been computed on the individual curved faces for both cylinders. To isolate the influence of each of the three shear layer behaviors, these are integrated only over the half of the face on which the behavior occurs; the "back" half of the curved face, which experiences fully separated flow at all yaw angles, has been left out of the calculation. The reference area for normalization is the projected face area, LD, and the reference length is L. Yaw moments are computed about the centroid of the half of the face included in the calculation. The results are depicted in Fig. 25. Unlike on the flat faces of the cylinder, here the shear layer behavior does depend on the aspect ratio. For example, for an apsect ratio of 2.0, the fully-separated shear layer region (1) is absent, while it is present for an aspect ratio of 1.0. This difference is due to the fact that reattachment occurs on the curved face of the cylinder with an aspect ratio of 2.0 at a yaw angle of 90°, due to its greater length, as previously discussed in relation to Fig. 14(b). The same qualitative trends related to the three shear layer behaviors that were observed for the flat faces of the rectangular prism and cylinder are also apparent on the curved cylinder faces, as demonstrated in Fig. 25. However, a main differentiator in the quantitative trends is the angle at which reattachment occurs, which may vary with bluff body type, aspect ratio, and face type (flat or curved).

3.6 Empirical Modeling of Shear Layer Behavior

Due to the inherent unsteadiness and nonlinearity of bluff body flows resulting from transition, separation, and reattachment, simplified analytical theories are generally not available. This fact poses significant difficulties in developing reduced-order models for pilot training, certification, and stability analysis. As a result, costly suites of experiments, flight tests, or high-fidelity numerical simulations are typically performed to build a database of quasi-steady force and moment information for each geometry under consideration [65, 11]. Empirical modeling presents an alternative to analytical modeling, with similar benefits to applications such as flight simulation which require a method with low computational cost.

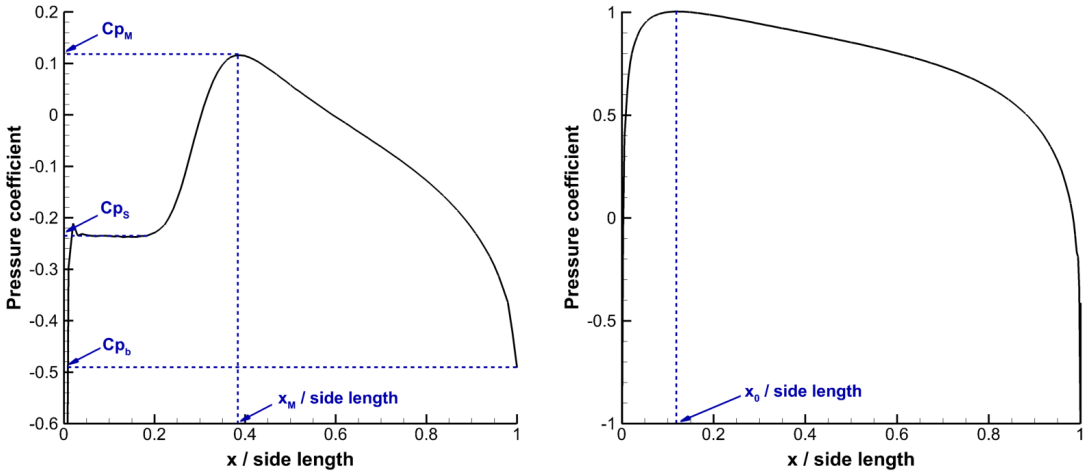

(a) Reattaching flow (b) Attached flow

Figure 26: Typical pressure distributions and definition of empirical modeling parameters.

Some development in this area has been published by Greenwell [12] for two-dimensional rectangular bluff bodies. The current work develops similar empirical models for the quasi-steady behavior of short three-dimensional bluff bodies. This analysis provides insight regarding where there exist similarities and differences among different geometry types, as well as quantify sensitivities with respect to surface shape, Reynolds number, and aspect ratio.

Figure 26 presents typical pressure distributions for reattaching and attached flow. In attached flow (Fig. 26(b)), the maximum pressure coefficient remains constant at 1.0 and there is no separation bubble. As a result, this pressure distribution can be characterized by just the stagnation point location, x_0. Meanwhile, the reattaching pressure distribution (Fig. 26(a)) requires four parameters: c_{p_b}, the base pressure coefficient, c_{p_S}, the separation bubble pressure coefficient, c_{p_M}, the maximum pressure at reattachment, and x_M, the distance from the leading edge to the location of c_{p_M}. These parameters can be assessed using the time-averaged pressure distributions from the numerical experiments.

One key parameter related to the reattachment behavior is the angle at which reattachment on a given face first occurs. For this analysis, it is more instructive to consider the incidence angle ϕ – the angle of the freestream relative to a given face – instead of the yaw angle. The angle ϕ is related to the yaw angle but also depends on the orientation of the face

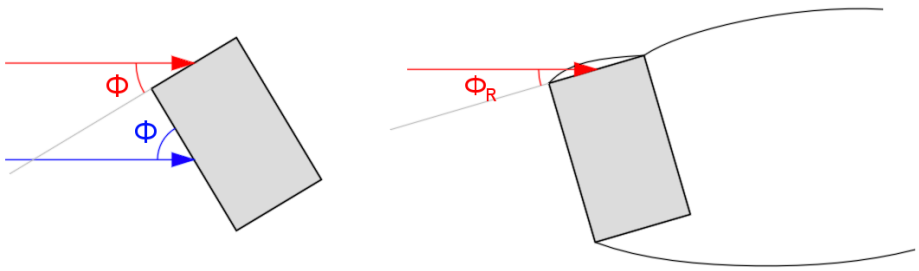

(a) Incidence angle ϕ (b) Reattachment incidence ϕ_R

Figure 27: Depiction of the incidence angle, ϕ, on two different faces, and ϕ_R on the top face. ϕ_R is equivalent to ϕ when reattachment first takes place. Arrows represent the freestream flow direction.

at a yaw angle of 0°. This angle is depicted for two different faces of a bluff body in a top view in Fig. 27(a). The quantities for the top face are red in the diagram, while those for the front face are blue. The incidence angle at which reattachment first begins is identified as ϕ_R, which is illustrated in Fig. 27(b). In the illustration, the separation bubble spans the entire face when $\phi = \phi_R$. If the yaw angle is further increased, the incidence angle will increase equivalently on the top face (while decreasing on the front face), and the separation bubble will shrink. The incidence angle at which reattachment begins can be considered constant for a given face of a bluff body at a particular freestream flow condition.

Figure 28 illustrates the variation of the normalized reattachment distance with incidence angle. For the rectangular prism and two-dimensional rectangular bluff body [10], the reattachment distance is normalized by the length of the side adjacent to the face with reattachment; for the cylinders it is normalized by the diameter. These figures clearly indicate that the normalized reattachment distance does not depend on the aspect ratio or the Reynolds number, but rather on the geometry type and face shape. Though similar trends exist in all three cases, the normalized reattachment distance is largest for a given incidence angle on the rectangular prism, followed by the curved cylinder faces, and it is smallest on the flat cylinder faces. The incidence angle at which reattachment begins can be determined from these empirical models by setting the reattachment distance equal to the length of the relevant face and determining the incidence angle from the curve fit.

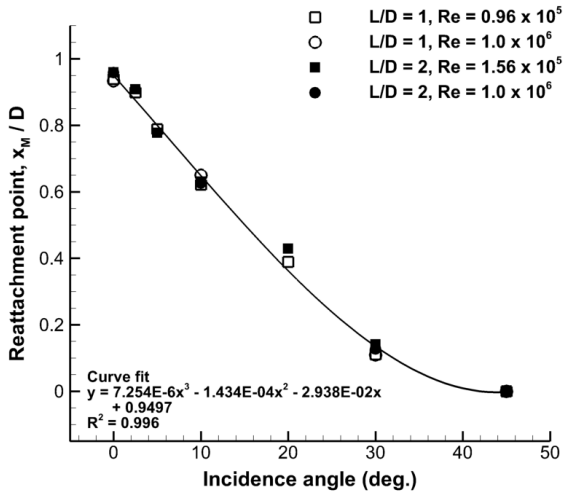

(a) Flat cylinder faces

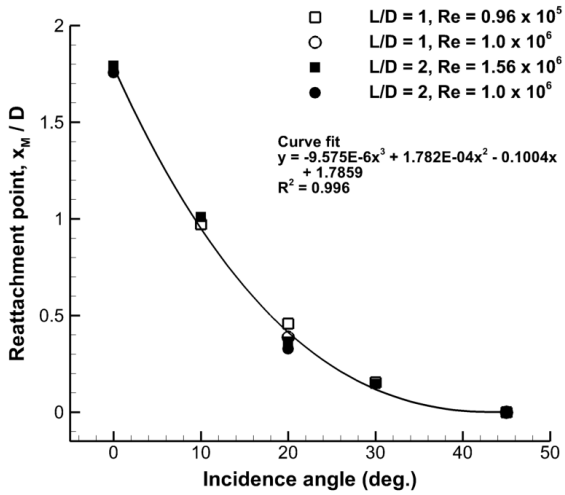

(b) Curved cylinder faces

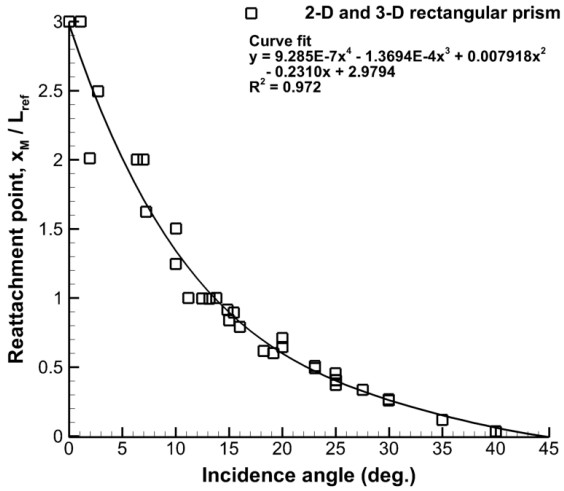

(c) Rectangular prism faces

Figure 28: Normalized reattachment distance as a function of incidence angle. 2-D rectangular prism data from Robertson [10].

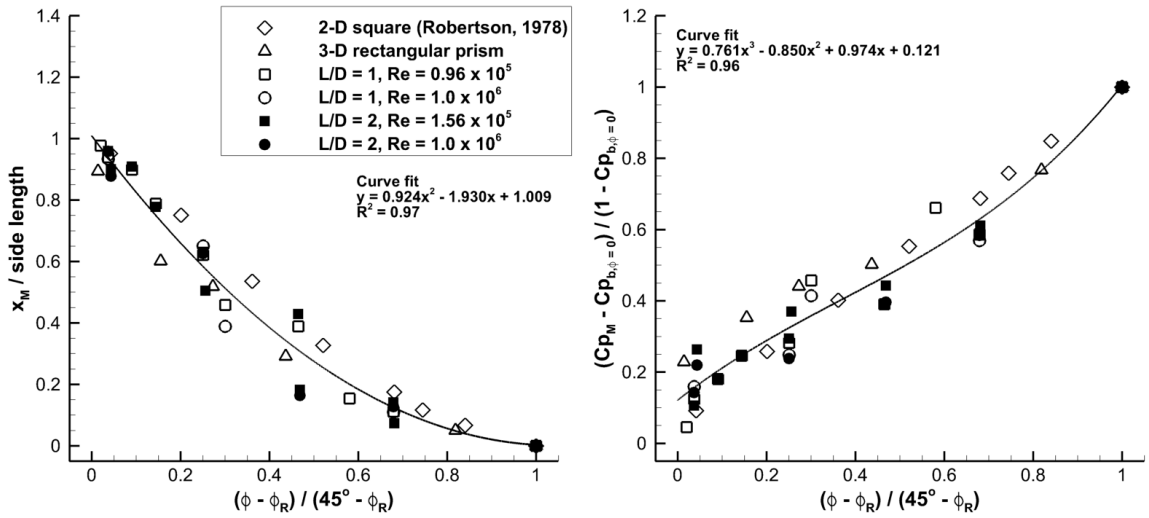

(a) x_M

(b) c_{p_M}

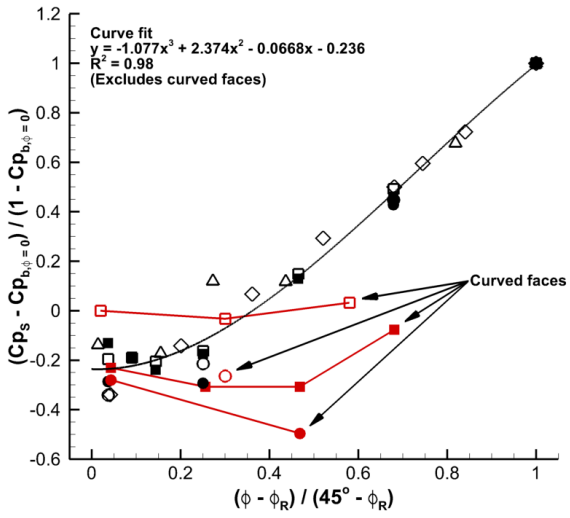

(c) c_{p_S}

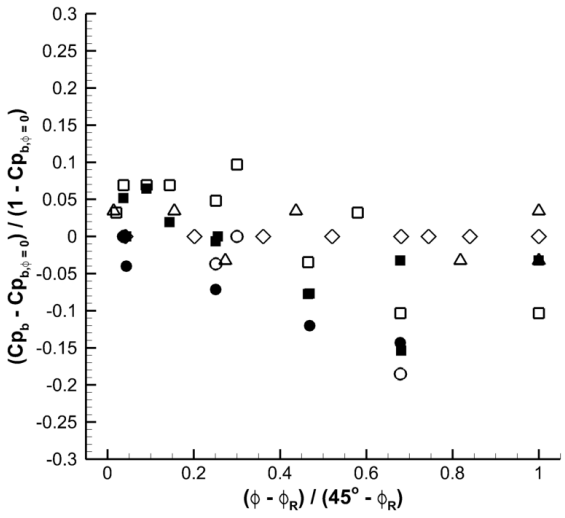

(d) c_{p_b}

Figure 29: Reattachment parameter variations with ϕ and empirical curve fits.

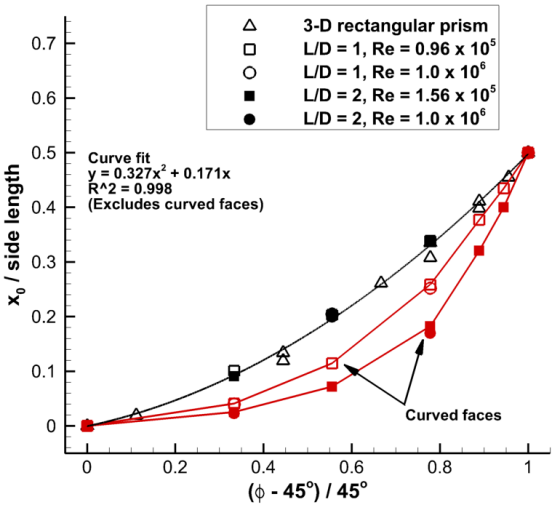

Figure 30: Variation of x_0 with ϕ and empirical curve fit.

Empirical models of the four reattachment pressure distribution parameters are presented in Fig. 29. Many of them collapse onto a single curve when normalized appropriately. The incidence angle, for instance, is normalized as $\dfrac{\phi - \phi_R}{45° - \phi_R}$. The pressure coefficients are normalized as $\dfrac{c_p - c_{p_{b,\phi=0}}}{1.0 - c_{p_{b,\phi=0}}}$, where $c_{p_{b,\phi=0}}$ is the base pressure coefficient at an incidence angle of 0°. When normalized in this manner, the variation in normalized reattachment distance collapses onto a single quadratic curve with coefficient of determination (R^2) of 0.97, and the relationship becomes independent of the surface type, canonical geometry type (it applies to cylinders and two- and three-dimensional rectangular bluff bodies), aspect ratio, and Reynolds number. If ϕ_R is not subtracted out, as in Fig. 28, then the empirical equations vary with geometry and surface type. This result indicates that these geometric differences have a significant effect on the incidence angle at which reattachment begins, but the variation of the reattachment distance with incidence angle after reattachment begins follows a similar trend in all cases. Therefore, the models provided in Fig. 28 should be used to determine the incidence angle at which reattachment begins, and then the model in Fig. 29(a) may be applied once this angle is known.

The maximum pressure coefficient during reattachment, c_{p_M}, exhibits similar independence when normalized appropriately. All geometries evaluated collapse onto a single empirical curve with a coefficient of determination of 0.96, and the maximum pressure coefficient

increases with incidence angle in a cubic relationship. The separation bubble pressure coefficient, c_{p_S}, collapses in a similar manner, but in this case, there are differences with respect to the type of surface. For reattachment on flat faces (whether they are flat faces of cylinders or rectangular bluff bodies), the separation bubble pressure can be modeled by an empirical curve fit with a coefficient of determination of 0.98. However, curved faces do not fit this trend; data for curved faces are highlighted in red in Fig. 29(c). In fact, the separation bubble pressure on curved faces is found to depend not only on the incidence angle but also the aspect ratio and Reynolds number. The base pressure coefficient, c_{p_b}, exhibits significant scatter and is not amenable to fitting by an empirical curve. However, this parameter is difficult to determine, as the pressure coefficient drops off rapidly at the aft end of the face (see Fig. 22(a)). Due to this rapid drop-off, the value of this coefficient does not significantly influence the integrated loads, and a representative value for a given geometry may be applied at all yaw angles.

Figure 30 presents the variation of the stagnation point with incidence angle. As stagnation on a given face implies that reattachment does not occur on the same face, the incidence angle at which reattachment begins is not subtracted from the incidence angle for normalization. Instead, since the transition from reattaching to fully-attached flow occurs at 45°, the incidence angle is normalized as $\frac{\phi - 45^\circ}{45^\circ}$. Figure 30 demonstrates that the stagnation point, when normalized in this manner, also depends on the surface type. As was the case with the separation bubble pressure, the normalized stagnation point collapses onto a single empirical curve for flat faces, including both finite cylinders and rectangular bluff bodies. However, curved-face stagnation (highlighted in red) does not fit the same trend. On curved faces, the stagnation point is found to depend on the aspect ratio but not the Reynolds number.

CHAPTER IV

DYNAMIC BLUFF BODY SIMULATIONS

4.1 Prescribed Motion

Two prescribed-motion high-fidelity numerical simulations have been performed to evaluate changes in the forces and moments and flow behavior relative to the static configurations. Though many prescribed motions are possible, the two chosen are representative of basic spinning and pendulum-like dynamics that are common in tethered load operations.

4.1.1 Description of Configurations

The bluff body selected for the prescribed-motion evaluations is the $1/11^{\text{th}}$-scale model of the CONEX rectangular prism, the static aerodynamics of which have been investigated in detail in Chapter 3. Two different prescribed motions have been applied in separate simulations:

1. Spinning motion about the bluff body's vertical axis. The spin angle as a function of time is illustrated in Fig. 31(a).

2. Pendulum-like motion in the lateral direction via simple harmonic rigid rotation about a point directly above the bluff body's initial position. The position of the bluff body's geometric center as a function of time is illustrated in Fig. 31(b). The roll angle also varies in a simple harmonic fashion due to the rigid rotation but is not depicted in Fig. 31.

In each case, the rectangular prism is initially centered in the background grid, which is representative of the John J. Harper 9' $\times$ 7' foot wind tunnel test section at the Georgia Institute of Technology, with the broad side facing forward corresponding to a yaw angle of 0° according to the convention in Chapter 3. While the size of the bluff body is representative of a wind-tunnel-scale model, the relevant non-dimensional kinematic parameters for these evaluations have been set to match the observed response of a full-scale tethered load

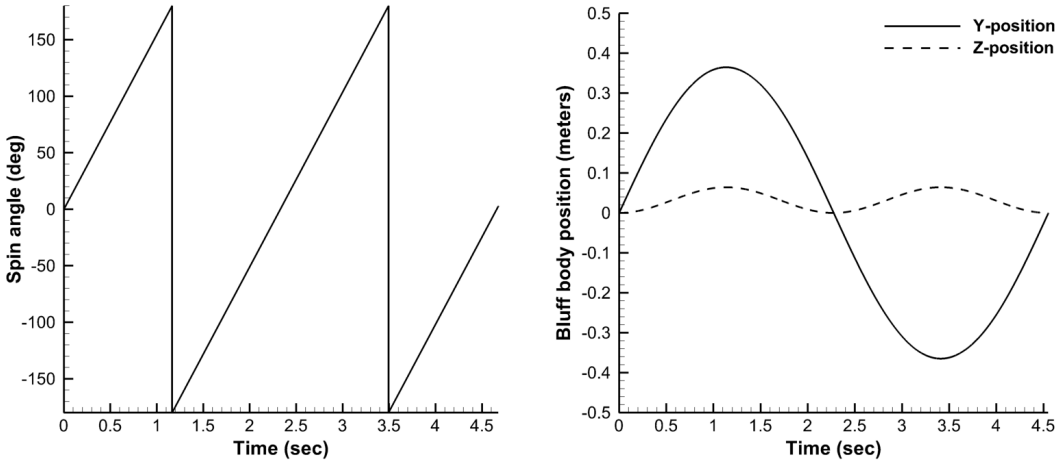

(a) Yaw angle in spinning motion

(b) Body position in pendulum motion

Figure 31: Prescribed motion parameters as functions of time for spinning and pendulum simulations.

at a flight speed that is considered to be unstable. For example, the reduced-frequency of spinning motion in a particular flight test of a CONEX tethered load at a speed of 112 knots is 0.02 (see Section 6.4) based on the mean spin rate and with half the longest side of the bluff body taken as the reference length, and this reduced frequency has been maintained in the $1/11^{\text{th}}$-scale simulation. The pendulum oscillations from this flight test correspond to a reduced frequency of 0.03. The maximum yaw angle induced due to pendulum motion is very small (2.7°), so the forces and moments are not expected to be affected significantly by this motion. Therefore, instead of matching the reduced frequency in this case, the period of oscillation from the flight test was maintained, resulting in a maximum yaw angle more representative of the flight test than would have resulted from matching the reduced frequency. The pendulum oscillation amplitude of 20° has also been maintained in the prescribed-motion simulation. Dimensional and non-dimensional forced motion parameters for these two evaluations are presented in Tables 4 and 5.

The computational approach for these prescribed motion cases is the same as the approach taken in the static simulations of Chapter 3. The grids, turbulence model, discretization, and solver settings have all been duplicated from those evaluations. The time step size has been taken to be nearly identical to the static simulations but modified slightly (by less

Table 4: Kinematic parameters for simulation of a spinning rectangular prism.

	Simulation	Full-scale reference
Freestream speed	15.647 m/sec	57.618 m/sec
Spin rate	0.172 rad/sec	0.953 rad/sec
Reduced frequency	0.02	0.02
Simulated revolutions	2	—

Table 5: Kinematic parameters for simulation of a rectangular prism in pendulum motion.

	Simulation	Full-scale reference
Freestream speed	15.647 m/sec	57.618 m/sec
Period	4.55 sec	4.55 sec
Amplitude	20°	20°
Pendulum length	1.151 m	18.8 m
Maximum induced yaw angle	1.9°	2.7°
Simulated periods	1	—

than 2%) to allow an even number of time steps during a period of oscillation. Flowfield initialization for both dynamic runs utilized the flow solution from the final timestep of the static simulation at a yaw angle of zero degrees, thus minimizing any transients at the beginning of the simulations. Due to this approach, only one or two revolutions were required to evaluate the basic unsteady aerodynamic response. Two revolutions were performed for the spinning case, due to the large range of yaw angles encoutered and greater possibility for variations from cycle to cycle, while only one revolution was performed for the pendulum case.

4.1.2 Forces and Moments in Spinning Motion

A primary goal in evaluating these spinning cases is to determine the influence of motion on the integrated forces and moments. Furthermore, it is valuable to compare the results with the prediction obtained by interpolating the static-configuration data of Section 3.3, which is known as the *quasi-steady* prediction. This comparison sheds light on unsteady aerodynamic phenomena that may influence the dynamic behavior. Figure 32 presents the force and moment coefficients for the spinning case as a function of the yaw angle (β). Because the bluff body undergoes two revolutions, two distinct black curves are present in each plot corresponding to the two different revolutions. The red curve represents the

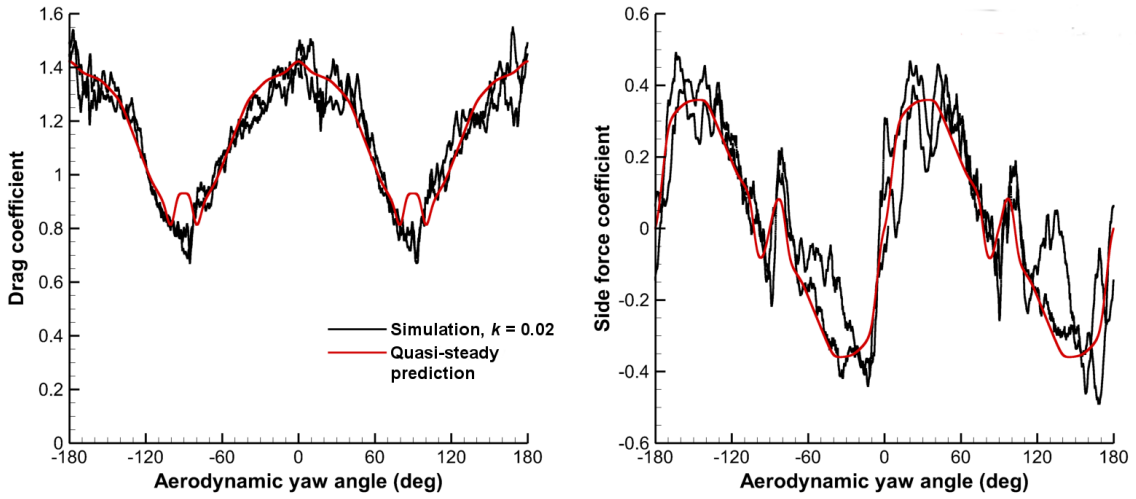

(a) Drag coefficient

(b) Side force coefficient

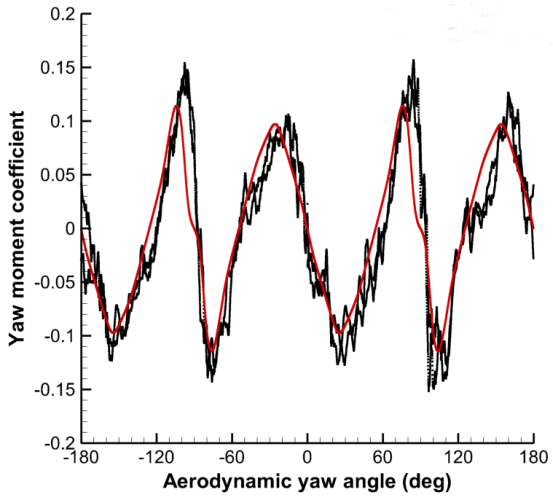

(c) Yaw moment coefficient

Figure 32: Drag, side force, and yaw moment coefficient from two revolutions of a high-fidelity computations of a spinning rectangular prism at a reduced frequency of 0.02.

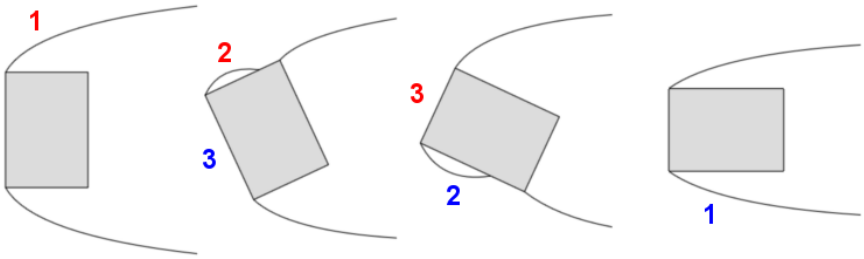

Figure 33: Illustration of shear layer behavior for a rectangular bluff body. (1) Fully separated shear layer, (2) reattaching shear layer, and (3) fully attached flow (reprint of Fig. 3 for convenience).

quasi-steady prediction. The normalization parameters used to calculate the coefficients are the same as were employed in Chapter 3; the reference area is the average vertical side area ($0.5H(L+W)$), while the reference length for computing moments is the average of length and width. Moments are computed about the geometric center, which is at the origin.

For the most part, the quasi-steady prediction provides a good approximation of the spinning forces and moments. The majority of the variation between the two is attributed to the large-scale turbulent vortex shedding, which creates aperiodic fluctuations in the forces and moments, as discussed in Section 3.4. These fluctuations also prevent the CFD data from the two revolutions from being exact duplications of each other. Some small phase lags in the high-fidelity data relative to the quasi-steady prediction are also apparent, particularly in the yaw moment, but these are difficult to quantify due to their small magnitude and the relatively large unsteady fluctuations.

One aspect of the spinning simulation that is markedly distinct from the quasi-steady prediction is the drag coefficient at yaw angles between 80° and 100°, and similarly between −80° and −100°. In both static and spinning configurations, the drag decreases monotonically between yaw angles of 45° and 80°, as the frontal area of the bluff body is decreasing. In the static configurations, this trend suddenly reverses between yaw angles of 80° and 85°. This change is coincident with reversals in both side force and yaw moment, which suggests (based on the investigation of shear layer behavior in Chapter 3) that the variation is due

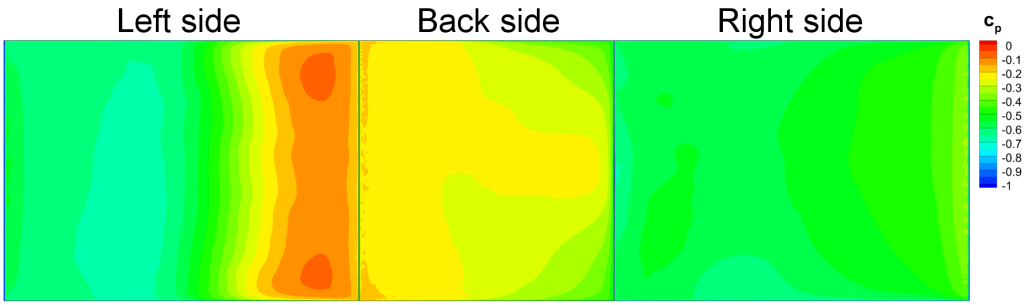

(a) Static, yaw angle of 80°

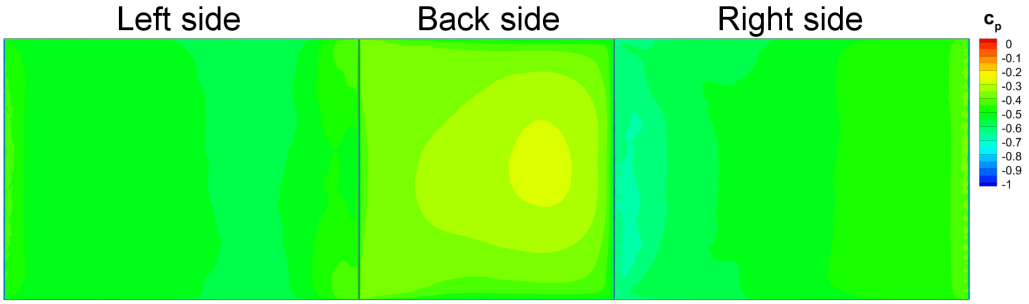

(b) Static, yaw angle of 85°

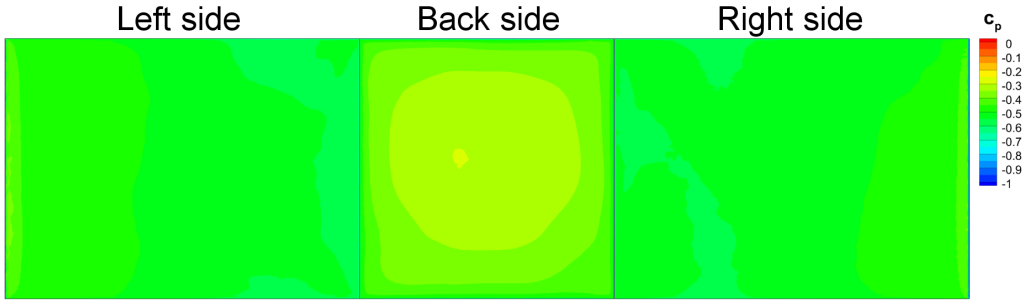

(c) Static, yaw angle of 90°

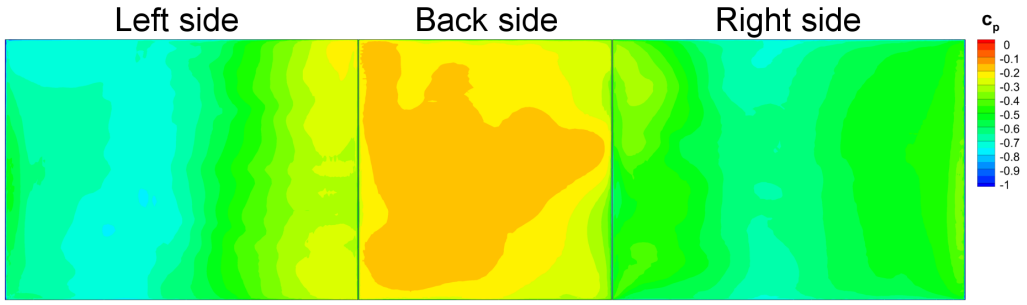

(d) Spinning, time average from yaw angles of 85° – 95°

Figure 34: Pressure distributions on left, right, and back sides of the rectangular prism in static and spinning configurations.

to changing shear layer behavior. In contrast, in the spinning configuration, the drag trend in this range of yaw angles is quite different. Instead of reversing directions at a yaw angle of 80°, it continues to decrease and then suddenly increases again at an angle of 100°.

Illustrations of possible shear layer behaviors are provided in Fig. 33, which has been discussed in detail in Chapters 1 and 3. The behaviors of interest between yaw angles of 80° and 90° correspond to the last two diagrams from the right in Fig. 33. To demonstrate the changing shear layer characteristics, the pressure distributions on various faces of the bluff body at a yaw angle of 80° are presented in Fig. 34(a). Time-averaged pressures are depicted on three different faces in this figure. The stagnation point is located on the front face (not shown), the shear layers separate from the sharp edges of the right and left faces, and the back face is in the wake and subjected to the base pressure. At a yaw angle of 80°, the left side undergoes shear layer reattachment, as evidenced by the sudden increase in pressure on the aft end; this behavior corresponds to the second diagram from the right in Fig. 33. When the yaw angle is increased to 85° (Fig. 34(b)), shear layer reattachment ceases to occur on the left side, as no pressure recovery occurs. The base pressure on the back side is also lower in this case, resulting in the increase in drag that is observed in the quasi-steady prediction in Fig. 32(a). The flow remains separated on the right side as well. The behavior at a yaw angle of 90°, shown in Fig. 34(c), is very similar but more symmetric and with a slightly lower average base pressure. The shear layer behavior observed in this figure at 85° and 90° is consistent with the far right diagram illustrated in Fig. 33.

The flow patterns in the spinning configuration have been examined in a similar manner. Time averaging has been applied to extract the mean behaviors, because instantaneous snapshots contain significant unsteady content from turbulent wake interactions. However, since the bluff body is constantly spinning, this time average is, of necessity, a moving average describing the flow characteristics over a range of yaw angles. A window of 85° – 95° was chosen for this purpose. This window was chosen to highlight changes in the flow behavior relative to the static simulations. As the flow is completely separated over this window in the static simulations, the pressure recovery and higher base pressure characteristic of reattaching flow are not expected to be observed if the behavior is truly quasi-steady. The

result of this time-averaging process, presented in Fig. 34(d), indicates that the quasi-steady trend does not, in fact, hold in the spinning simulation. Unlike in the static evaluations, there remains shear layer reattachment on the left side in the spinning case over this range of yaw angles, which is indicated by the pressure recovery on the aft portion of the face and the higher base pressure relative to the time-averaged static results at yaw angles of 85° and 90° in Figs. 34(b) and (c). This higher base pressure accounts for the lower drag relative to the quasi-steady prediction. Additionally, despite the fact that the time window is centered around a yaw angle of 90°, about which the bluff body is symmetric, the pressure distribution is clearly asymmetric from left to right when the time average is taken, which indicates that a phase lag occurs in the flowfield relative to the static configurations.

The differences in shear layer behavior for the spinning bluff body relative to the static configurations confirm that unsteady bluff body motion, even at the low reduced frequency of 0.02, introduces changes in both the flow behavior and the mean forces and moments. Body dynamics create phase lags and magnitude discrepancies between the quasi-steady aerodynamic prediction and the unsteady response. In the spinning configuration evaluated here, the shear layer characteristics exhibit a phase lag relative to the quasi-steady flow, and this phenomenon is largely responsible for the observed difference in the integrated forces and moments. This result illustrates the need for unsteady terms in dynamic simulation models of bluff bodies.

4.1.3 Forces and Moments in Pendulum Motion

The integrated drag, side force, and yaw moment coefficients for the pendulum case are provided in Fig. 35. The coefficients are normalized using the same reference quantities as in the spinning case, and moments are computed about the geometric center. Time is normalized by the oscillation period in these figures. In addition to the high-fidelity and quasi-steady predictions, a moving average of the high-fidelity forces and moments (averaged over $1/10^{\text{th}}$ of the cycle) is also included.

As in the spinning case, the largest deviations of the computed forces and moments from the quasi-steady prediction are due to bluff body shedding. This fact is evidenced by

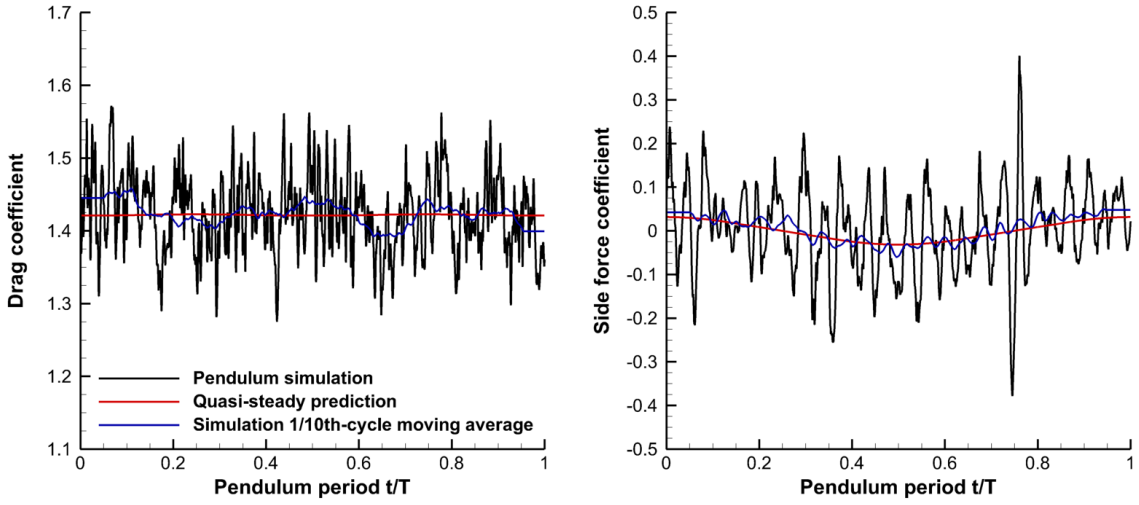

(a) Drag coefficient

(b) Side force coefficient

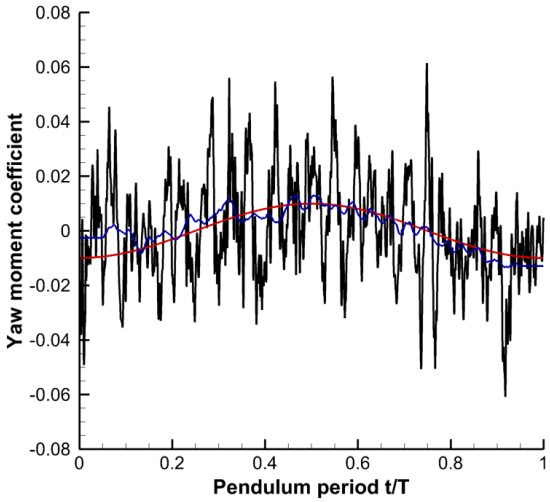

(c) Yaw moment coefficient

Figure 35: Drag, side force, and yaw moment coefficient from high-fidelity computations of a rectangular prism in pendulum motion defined in Table 5.

the convergence of the high-fidelity forces and moments towards the quasi-steady prediction when the moving average is applied. For each of the drag, side force, and yaw moment, the moving average varies from the quasi-steady prediction by less than 20% of the maximum vortex shedding fluctuation magnitude; therefore, the quasi-steady prediction is an accurate representation of the mean forces and moments for this pendulum motion. The mean drag, side force, and yaw moment coefficients for the high-fidelity simulation and quasi-steady prediction are also in close agreement and are listed in Table 6.

Table 6: Comparison between high-fidelity pendulum force and moment coefficients and the quasi-steady prediction.

	Drag	Side force	Yaw moment
Simulation	1.42	5.3×10^{-3}	5.4×10^{-4}
Quasi-steady	1.42	0	0

Additionally, by comparison of the changes in these forces and moments throughout the cycle with the spinning case, it is clear that the pendulum motion does not significantly affect the aerodynamics. The quasi-steady drag remains almost unchanged during the simulation, while the side force and yaw moment vary to a small extent (in both cases by less than 30% of the shedding fluctuations). The small magnitude of these quasi-steady variations is not unexpected, as the pendulum motion induces a maximum yaw angle of only 1.9°. Though this angle is slightly larger (2.7°) in full-scale flight test data of an unstable tethered load at 112 knots (see Section 6.4), it is still very small and remains well below the angle required for shear layer reattachment on this bluff body. Therefore, even extreme pendulum motions that occur in unstable tethered load situations are not expected to induce a significant quasi-steady or unsteady aerodynamic response, and spinning behavior is likely to be more important than pendulum motion from an aerodynamic perspective.

4.2 Tethered Load Simulations

High-fidelity simulations of tethered load dynamics have been performed for the purpose of investigating the flow characteristics in six-degree-of-freedom dynamic configurations and for validating the reduced-order model which will be introduced in Chapter 5.

4.2.1 Description of Configurations

As in Section 4.1, the tethered load for these simulations is the $1/11^{\text{th}}$-scale model of the CONEX rectangular prism, the static aerodynamics of which have been investigated in detail in Chapter 3. It is attached by four cables from a single point on the ceiling of a virtual wind tunnel test section representing the John J. Harper wind tunnel at the Georgia Institute of Technology. Figure 36 illustrates the wind tunnel and tethered load configuration and the orientations of the relevant frames. Since the simulations occur in a wind tunnel, the wind frame is equivalent to the inertial frame in this case. As in Chapter 3, the tethered load is modeled as a plain rectangular prism without details such as skids or corrugations.

Two different cases have been evaluated, representing two different wind speeds. The tethered load parameters and operating conditions for the simulations are given in Tables 7 and 8. Instead of allowing the tethers to wind up when the load spins, they are attached to a freely spinning gimbal mount. A linear yaw rate damping term has been added to the cable model to represent the friction in this gimbal. The two different cases also represent two different initial conditions. At 25 mph, the load is initially suspended with a trailing angle of 8.8°, which is the estimated "steady-state" orientation based on the drag in the narrow-side-forward condition. The initial pitch angle of the tethered load is accordingly adjusted so that the cables do not become unequally stretched. At 40 mph, the tethered load is initially suspended directly below the attachment point at the top of the tunnel, with all Euler angles initially zero. This condition results in large trailing angle oscillations as the load swings during the beginning of the simulation. The effects of this behavior on the aerodynamic characteristics will be described later in this chapter. In both cases, the initial yaw Euler angle is zero, which corresponds to the narrow side facing into the freestream flow.

The simulations have been performed using the same near-body and background grids as described in Chapter 3. Similar solver parameters, including the time step size, number of subiterations, and discretization schemes as in Chapter 3 have also been applied. The time step size for the HRLES simulations corresponds to 0.0003 seconds of dimensional time,

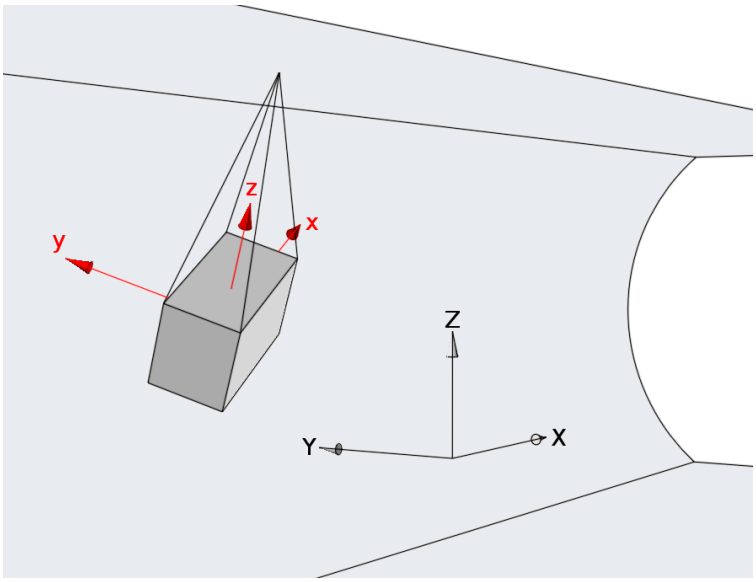

Figure 36: Illustration of the wind tunnel and tethered load configuration and the orientations of the relevant frames.

Table 7: Bluff body properties for the tethered load simulations.

Bluff body properties	
Length (m)	0.23368
Width (m)	0.16764
Height (m)	0.17145
Mass (kg)	1.49
I_{xx} (10^{-3} kgm^2)	7.77
I_{yy} (10^{-3} kgm^2)	11.04
I_{zz} (10^{-3} kgm^2)	10.49

which has been selected based on previously established criteria for turbulent separated flow [58, 8] to adequately resolve the shed vortices in time. As such a small time step size results in a high computational cost (over 3000 steps per second of simulated time), the simulations are carried out for 15–20 seconds. The cables attaching the tethered load to the ceiling of the wind tunnel are modeled as massless spring–damper elements, as described in Section 2.4.1.

4.2.2 Simulation Results

The simulations involve significant dynamic motions of the tethered load, particularly at the higher wind speed. During the simulations, the load swings longitudinally, resulting in changes in pitch angle; laterally, resulting in changes in roll angle; and oscillations about the

Table 8: Operating conditions for the tethered load simulations.

Operating conditions	Case 1	Case 2
Initial roll (deg.)	0.0	0.0
Initial pitch (deg.)	-8.8	0.0
Initial yaw (deg.)	0.0	0.0
U_∞ (mph)	25	40
$Re_{0.5(L+W)}$	1.51×10^5	2.42×10^5
Yaw damping (N-m-sec.)	0.003	0.003

body-fixed $z-$axis result in changes in yaw angle. The three Euler angles for each simulation are depicted in Fig. 37. In both cases, yaw oscillations develop and grow throughout the simulation, for the 25-mph case resulting in a rotation such that the broad side faces into the freestream flow after 15 seconds. For the 40-mph case, the yaw oscillations quickly diverge and the tethered load spins continuously throughout the rest of the simulation. The rotating and spinning behaviors occurring in these cases have also been observed in wind tunnel tests of similar rectangular-prism tethered loads at comparable speeds [98, 99] and in flight tests [11, 17], though the current results cannot be directly compared with these prior examinations due to differences in the configurations or lack of quantitative measurements of the dynamic behavior and cable attachment parameters. As the different degrees of freedom are coupled both in terms of the equations of motion and the aerodynamics, the yaw rotation induces large lateral and longitudinal excursions of the tethered load, which are manifested as oscillations in the pitch and roll angles in Fig. 37.

The aerodynamic forces and moments are investigated in more detail in Section 6.1, as this information is used to validate the reduced-order model predictions. A significant benefit of numerical experiments, in addition to the forces and moments that result from the solution, is the large amount of rich flow field information available without the need for expensive instrumentation. As has been demonstrated in Chapter 3, these data can provide valuable insight into the flow physics. For example, shear layer behavior with time can be characterized. Figure 38 illustrates the flow field near the rectangular prism at different points in time at the 40 mph speed. In these images, the grid is sliced along the $X-Z$ axis and colored by vorticity magnitude. The near-body grid moves along with the rectangular

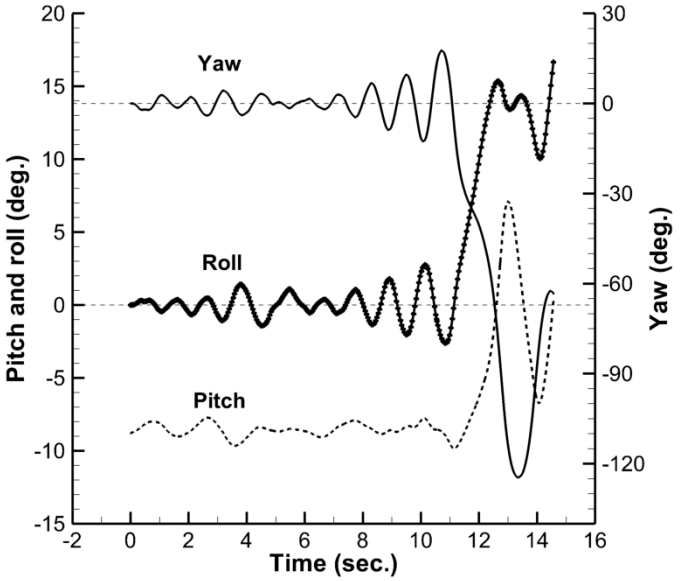

(a) 25 mph case

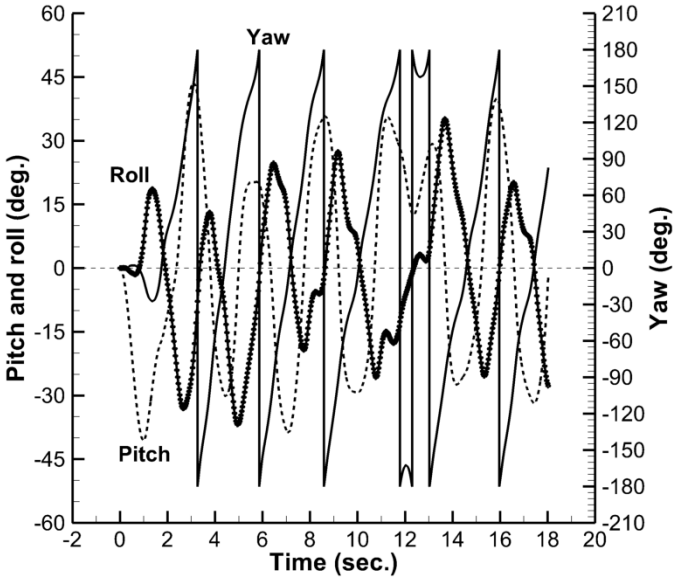

(b) 40 mph case

Figure 37: Euler angles from dynamic high-fidelity simulations for the CONEX rectangular prism.

prism, while the background grid remains static. The hole-cutting procedure within the SUGGAR++ library occurs at each time step to establish overset connectivity.

The three images in Figs. 38(a), (b), and (c) correspond to the tethered load near the beginning, middle, and end of the initial swing, respectively. Of particular interest is the differing shear layer behavior between the three. Initially, both the top and bottom surfaces experience fully separated flow. After 1700 steps, the top shear layer is reattaching, while the bottom shear layer remains fully separated. After 3450 steps, the tethered load is nearing the apex of its backswing, and the top shear layer is fully attached. Because the weight and cable tension oppose aerodynamic forces and moments generated by the top and bottom surfaces, these behaviors do not have a large influence on the dynamic response of the tethered load, but they do demonstrate that the static phenomena investigated in Chapter 3 are also present in this six-degree-of-freedom dynamic case. These aerodynamic phenomena also occur on the sides of the rectangular prism and are largely responsible for the dynamic yaw response of the tethered load.

Figure 39 compares the pressure distributions on the top and bottom surfaces of the rectangular prism at the same time steps. The regions of separated, reattaching, and attached flow can be clearly identified by their pressure signatures, which have been defined and quantified in Chapter 3. Separated flow is characterized by a relatively constant low pressure. In reattaching flow, there is a low pressure separation bubble which rapidly gives way to a higher pressure attached-flow region on the aft portion of the face. Fully-attached flow is characterized by a smooth pressure distribution with a maximum pressure coefficient of 1.0 at the stagnation point. As Fig. 39 presents snapshots of the pressure coefficient, the separated flow regions in particular are not smooth; this behavior is a result of vortex-surface interactions. Time averaging smooths out the pressure distributions and allows the mean flow behaviors to be quantified, as demonstrated for static configurations in Section 3.5.

Both the integrated aerodynamic loads and dynamic responses from these simulations are compared in detail with reduced-order model predictions for validation of the model in Chapter 6.

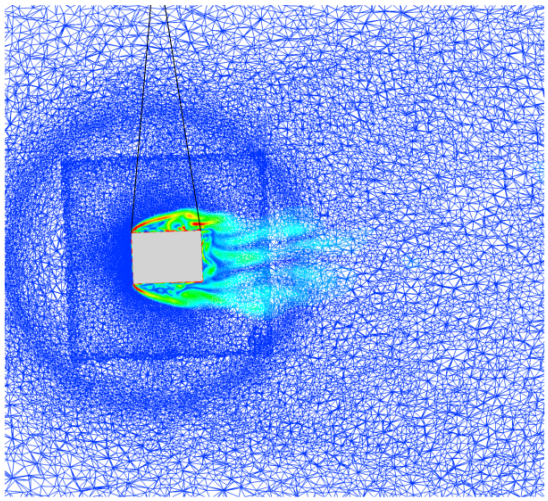

(a) Step 500 ($t = 0.15$ sec)

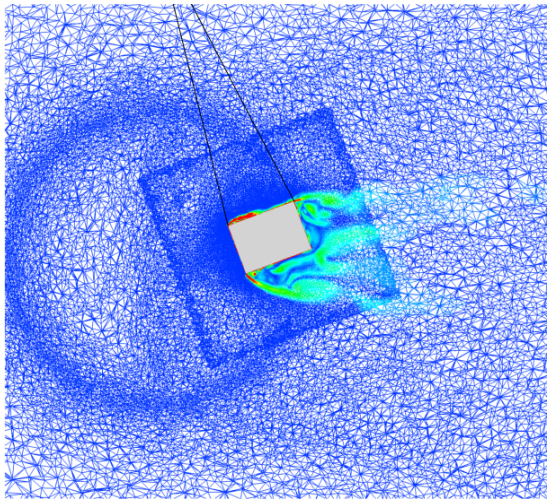

(b) Step 1700 ($t = 0.51$ sec)

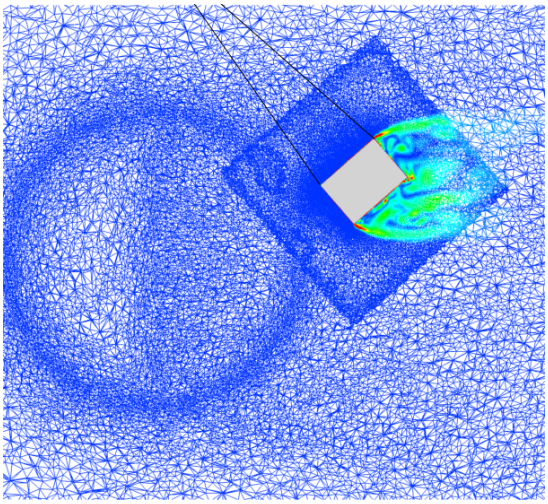

(c) Step 3450 ($t = 1.035$ sec)

Figure 38: Flow field visualizations at different points in time for the 40 mph case. Coloring by vorticity magnitude.

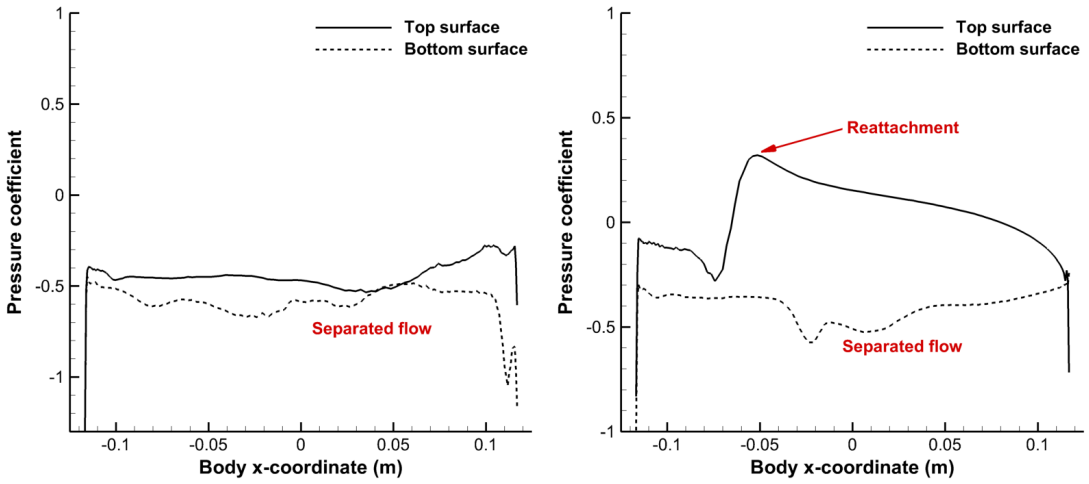

(a) Step 500 ($t = 0.15$ sec)

(b) Step 1700 ($t = 0.51$ sec)

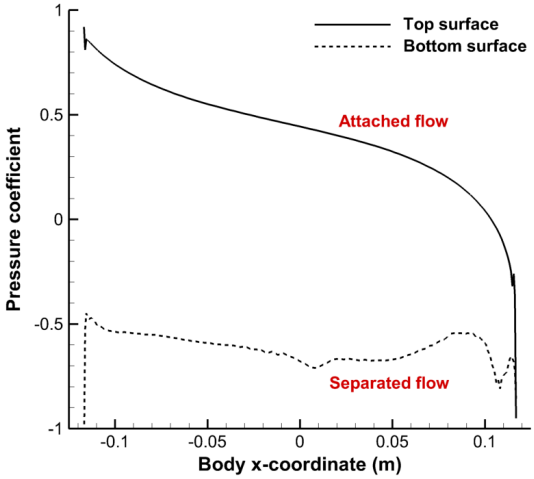

(c) Step 3450 ($t = 1.035$ sec)

Figure 39: Instantaneous pressure distributions at different points in time for the 40 mph case.

4.2.3 Computational Cost

The computational cost of the dynamic tethered load CFD simulations is very high. For the 25 mph case, the HRLES simulation required 50,000 steps for 15 seconds of physical simulation time. This translates to approximately 625 hours on 128 cores of a Cray XE6 cluster, with each core rated at 2.5 GHz, for a total of 80,000 CPU-hours. The cost for the 40 mph case was even higher, as it was run for over 18 seconds of physical time. While the cost is high, a limited number of specific cases can be performed at conditions in which the dynamic or aerodynamic behavior is known to be of interest. However, this approach is not suitable for stability or sensitivity analyses, in which many cases must be evaluated. The high cost of this dynamic CFD approach is one of the main motivations for the development of the reduced-order aerodynamic model, which is described in Chapter 5 and subsequently validated with CFD and flight test data.

CHAPTER V

REDUCED-ORDER AERODYNAMIC MODELING

Due to the high cost of CFD-based dynamic simulations for bluff bodies, a physics-based reduced-order model has been developed. The primary goal in the development of the reduced-order model has been the accurate incorporation of the appropriate causal physics to permit extension of the model to future applications. In the case of bluff bodies, there are three classes of aerodynamic phenomena that contribute significantly to the overall forces and moments:

1. Quasi-steady aerodynamics, or the time-averaged forces and moments in an unsteady flow around a body in a static configuration for a given orientation and flow condition.

2. Vortex shedding behavior, which contributes unsteady fluctuations to the forces and moments. In high Reynolds number three-dimensional bluff body flows, vortex shedding is turbulent and aperiodic [9], leading to fluctuations that appear chaotic. These fluctuations are of considerable magnitude and can contribute significantly to the dynamic response.

3. When unsteady body motion is present, as in dynamic tethered load simulations, additional unsteady aerodynamic phenomena arise. These effects are a consequence of the time required for the wake to respond to changes in the body's equilibrium (i.e., changes in orientation or velocity), creating phase lags and magnitude attenuations relative to the quasi-steady aerodynamics. These phase and magnitude changes impact the dynamic stability of the system.

All three classes must be adequately modeled to accurately predict the dynamics of a bluff body. Figure 40 illustrates how these phenomena are incorporated into the reduced-order model, from a high-level perspective in terms of aerodynamic coefficients. In this figure (and throughout this chapter), C_ζ represents a generic aerodynamic coefficient. Any

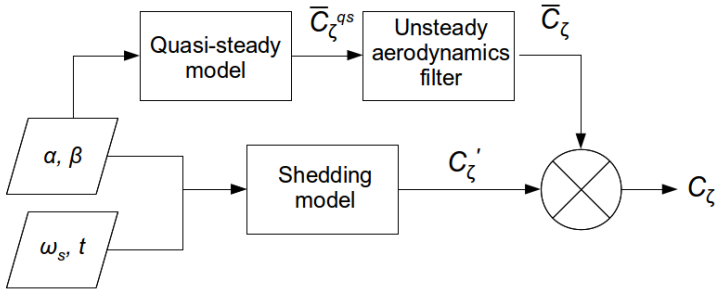

Figure 40: Reduced-order aerodynamic model components.

such coefficient can be decomposed, without loss of accuracy or generality, into mean-flow and fluctuating components, $C_\zeta = \overline{C}_\zeta + C'_\zeta$. Though in reality it is possible for the vortex shedding and mean-flow aerodynamics to become coupled (for example, the shedding frequency can "lock in" to body frequencies [27, 28]), the reduced-order model assumes that these two components can be computed independently. The mean-flow component, $\overline{C}_\zeta$, is computed in two parts: the quasi-steady contribution ($\overline{C}_\zeta^{qs}$), which is a function only of orientation (angle of attack and yaw angle), and the unsteady contribution, which takes $\overline{C}_\zeta^{qs}$ as an input while also incorporating past history of $\overline{C}_\zeta$. The fluctuating component, C'_ζ, is a function of orientation, the vortex shedding frequency (ω_s), and time.

5.1 Quasi-Steady Aerodynamics

An accurate representation of the quasi-steady aerodynamics is the first step in creating a physics-based reduced-order model. Unfortunately, for three-dimensional bluff body flows, it is not a simple task to approximate the quasi-steady aerodynamics. Unlike in attached flows, where simple linear relationships derived from theory can be employed, there are no such simple theories for bluff body flows, due to the inherent unsteadiness and first-order importance of viscosity. Development of empirical relationships to predict the quasi-steady behavior has been the subject of recent research; see, for example, Greenwell [12] and Section 3.6 of this thesis. While these efforts have demonstrated the potential to develop a general prediction method based on empirical descriptions of shear layer behavior, currently, supplemental data sets must still be relied upon to inform the quasi-steady model. Data from HRLES simulations validated for turbulent bluff body flows including dynamic cases

(for example, Refs. [8, 58, 61, 80] and Section 3.3 of this thesis) have been primarily employed to generate the quasi-steady data set, while wind tunnel [4] and analytical [99] data sets are also evaluated. The HRLES data informing the model are drawn from the static simulations presented in Chapter 3.

A full quasi-steady data set contains data encompassing the entire range of possible orientations. However, computing such an extensive data set is impractical, as each static simulation must allow the unsteady wake to develop fully. Similarly, while data sets have been developed through wind tunnel testing [4], they still involve large costs in setting up and performing the experiments. A more cost-effective approach is to independently assess the variation of the quasi-steady aerodynamic coefficients as a function of one angle (angle of attack or yaw angle) while the other is held constant at a reference value (denoted as α_0 or β_0), and then repeat the process for the other angle. These sensitivities are then superimposed, with corrections for crossflow effects applied. This approach permits nonlinearities to be captured while maintaining manageable cost in developing the data set. The resulting form is referred to as "quasi-linear," because it employs superposition of nonlinear functions of the two angles. The quasi-steady aerodynamic coefficient is computed as

$$\begin{aligned} \overline{C}_{\zeta}^{qs}(\alpha,\beta) = \overline{C}_{\zeta}^{qs}(\alpha_0,\beta_0) &+ \left[\overline{C}_{\zeta}^{qs}(\alpha,\beta_0) - \overline{C}_{\zeta}^{qs}(\alpha_0,\beta_0)\right] \\ &+ \left[\overline{C}_{\zeta}^{qs}(\alpha_0,\beta) - \overline{C}_{\zeta}^{qs}(\alpha_0,\beta_0)\right]. \end{aligned} \tag{14}$$

The reference angle of attack is typically 0°, and variations with angle of attack are measured twice, once with the reference yaw angle equal to 0° and again with it equal to 90°, to facilitate predictions over the entire range of yaw angles. The quasi-steady aerodynamic coefficients from these two sweeps are then blended based on the relative dynamic pressure acting on the faces corresponding to yaw angles of 0° and 90°.

Storing quasi-steady data in tables necessitates some type of interpolation to compute coefficients at angles between discrete data points in the data set. Linear interpolation is a cost-effective method, but it is inaccurate in nonlinear regions when the data set is sparse.

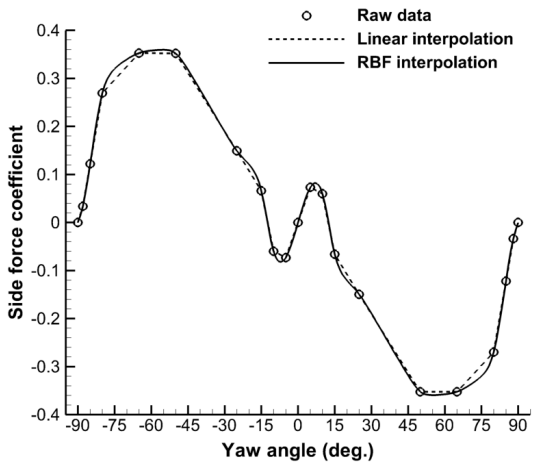

Figure 41: Variation of side force with yaw angle for a 3-D rectangular prism, illustrating RBF interpolation and revealing significant nonlinearities.

Hodara and Smith [100] explored the use of radial basis functions (RBF) for smooth interpolation without overshoots or oscillations. Since RBF interpolation is expensive, they recommended performing the interpolation as a pre-processing step to increase the resolution of a coarse data set, and then applying linear interpolation during the actual simulation. That approach has been adopted here, with a multiquadratic RBF kernel of the form $\xi(r) = \sqrt{(r^2 + r_0^2)}$ with a reference radius $r_0 = 3°$.

Figure 41 illustrates the effect of RBF interpolation on the side force as a function of yaw angle, or $\overline{C}^{qs}_{Y_\beta}(\beta)$, for a rectangular prism representative of the CONEX container. The original data set was computed using HRLES simulations, which have been presented and discussed in Section 3.3. This data set was non-uniform, with 11 points over the range of yaw angles from 0° to 90°. Via RBF interpolation, the resolution was increased to one point per degree. For this geometry, computations are only required for this 90°-range in yaw angle, as symmetry relations can be applied to extend the data set to yaw angles above 90° and below 0°. Figure 41 demonstrates that the RBF interpolation approach does not create artificial overshoots or oscillations in the nonlinear regions. It also reveals that nonlinearities, resulting in part from shear layer reattachment, are captured by the quasi-linear model.

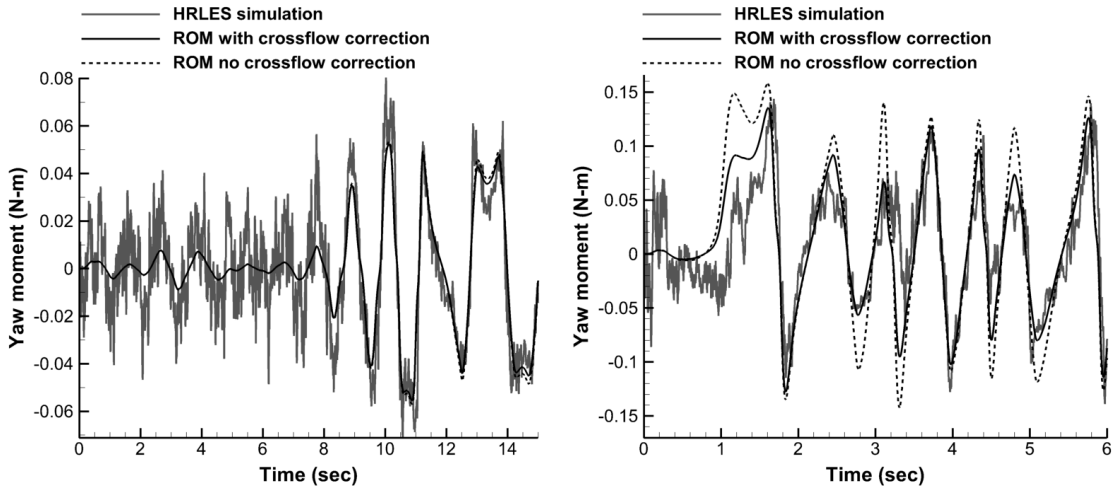

(a) 25-mph wind speed

(b) 40-mph wind speed

Figure 42: Yaw moment comparison between HRLES and the reduced-order model with and without crossflow corrections.

5.1.1 Crossflow Corrections

In the quasi-linear approach, discrepancies in the limiting behavior of body-axis moments can occur when both the angle of attack and yaw angle are far from their reference values. For instance, consider the rectangular prism with an angle of attack of 0° and a yaw angle of 20°. In this orientation, a negative quasi-steady yaw moment is experienced, as is observed in Fig. 12(c). As the angle of attack increases, the normal component of wind velocity is washed out with a crossflow component, reducing the yaw moment. As the angle of attack approaches 90°, the crossflow component is dominant and the yaw moment goes to zero. Such behavior is apparent in CONEX wind tunnel data sets including the full landscape of angle of attack and yaw [4]. However, in the quasi-linear approach, the yaw moment does not approach zero in this situation. Instead, the yaw moment for an angle of attack of 0° and a yaw angle of 20° is added to the yaw moment for an angle of attack of 90° and yaw angle of 0°, resulting in the wrong limiting behavior.

Greenwell [12] has shown that fairly simple corrections can be applied in such situations, at least in the case of the rectangular prism. These corrections are known as crossflow corrections because the off-axis velocity component makes up a significant part of the total velocity vector. Basic crossflow corrections for the pitch and yaw moment, respectively,

have been developed with the following form originally recommended by Greenwell:

$$\overline{C}_M^{qs} = \frac{1}{2}\left(\cos(2\beta)+1\right)\overline{C}_{M_{ql}}^{qs} \qquad (15)$$
$$\overline{C}_N^{qs} = \frac{1}{2}\left(\cos(2\alpha)+1\right)\overline{C}_{N_{ql}}^{qs},$$

where the subscript ql denotes the quasi-linear value stored in the quasi-steady data set. To ensure the correct limiting behavior is realized in the body-axis moments, Eq. 15 has been applied in the reduced-order model. Figure 42 demonstrates the effect on yaw moment during two separate dynamic simulations. Both simulations involve the $1/11^{\text{th}}$-scale wind tunnel model of the CONEX rectangular prism. The first (Fig. 42(a)) is at a wind speed of 25 mph. In this case, the trailing angle of the tethered load remains small, so the angle of attack remains close to the reference angle of attack (0°). At 40 mph (Fig. 42(b)), the trailing angle repeatedly exceeds 30°, and the magnitude of the angle of attack is similar to the trailing angle because of the single-point suspension system used in these trials. Results from dynamic HRLES simulations are also included in this figure. (For the sake of clarity, only the mean-flow yaw moment is shown in the reduced-order model results.) At the lower tunnel speed, the crossflow correction only has a minor influence on the yaw moment. In contrast, the crossflow correction makes a significant difference in the higher-speed case, as the angle of attack deviates significantly from the reference value of 0°. Including the crossflow correction in this case results in significantly improved agreement with the HRLES yaw moment.

5.2 Vortex Shedding

In bluff body flows, significant unsteady effects from the wake are present. This unsteadiness results from vortical structures shed during flow separation. Mathematical modeling of vortex shedding has received significant treatment in the wind engineering field. The fluctuating force components are typically modeled either using deterministic [101, 102] or statistical [103, 104] representations of the excitation. In the latter approach, the vortex shedding model as well as the response are typically cast in the frequency domain. The present model contains aspects of both approaches. It is formulated in the time domain,

with fluctuation magnitudes and frequencies prescribed, but randomness is introduced in the phase to model the aperiodic, chaotic nature of turbulent vortex shedding.

Vortex shedding introduces a perturbation of the quasi-steady aerodynamic coefficients, denoted here as C'_ζ. In order to adequately represent the contributions of these fluctuating terms in three-dimensional turbulent flows, it is necessary to account for the largest energy-containing vortices. Employing a separation of variables approach, the fluctuating terms may be modeled as

$$C'_\zeta(\alpha, \beta, t) = \sum_{i=1}^{N} C'_{\zeta,i}(\alpha, \beta)\nu(\omega_{s,i}, t), \tag{16}$$

where ν is a function giving the time dependence of the fluctuation and N is the number of vortex shedding harmonics included. In this model, the fluctuation magnitudes, $C'_{\zeta,i}$, are assumed to depend only on the angle of attack and yaw angle. Here, they have been compiled into data sets similar to the quasi-steady coefficients using the same set of static HRLES simulations. A simple harmonic sinusoidal representation of the time-dependent function is adequate for for two-dimensional laminar flow. However, the simple harmonic representation does not incorporate the chaotic nature of three-dimensional, turbulent, separated flow. A more accurate form is based on a statistical representation of the turbulence effects, which may be obtained from a frequency-domain transformation of the unsteady forces or wake behavior in physical or numerical experiments.

The computational approach has been applied to develop a statistical model of vortex shedding. Three dynamic simulations of a short rectangular prism have been performed using HRLES, and the resulting forces and moments computed on the bluff body during the simulations have been compared with predictions from the reduced-order model. Figure 43(a) presents a comparison of the HRLES and mean-flow reduced-order model prediction of the yaw moment during the first six seconds of a dynamic simulation. The mean-flow contribution contains unsteadiness from body motion but lacks the fluctuations apparent in the HRLES simulation. Figure 43(b) illustrates the effect of adding a simple harmonic vortex shedding term to model the fluctuations. The form of $\nu(\omega_{s,i}, t)$ here is

$$\nu(\omega_s, t) = \sin(\omega_s t). \tag{17}$$

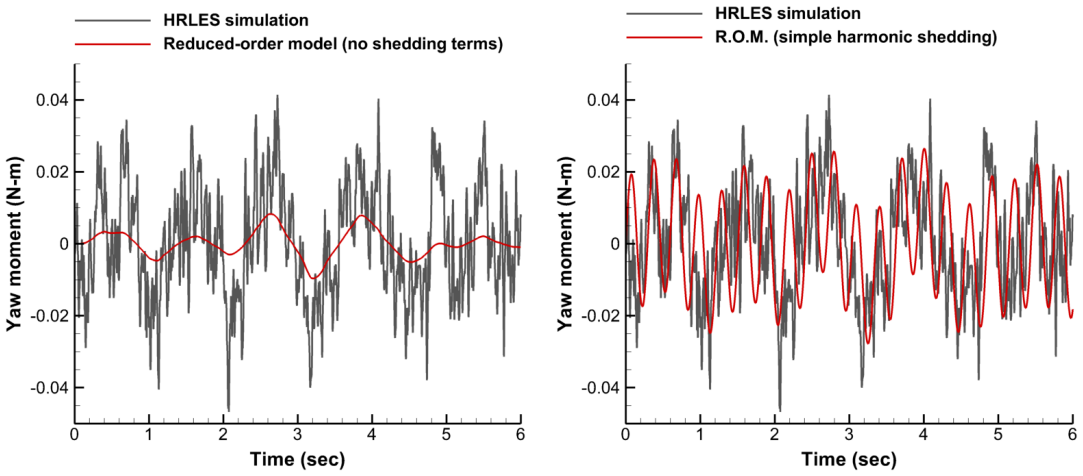

(a) No shedding

(b) Simple harmonic shedding

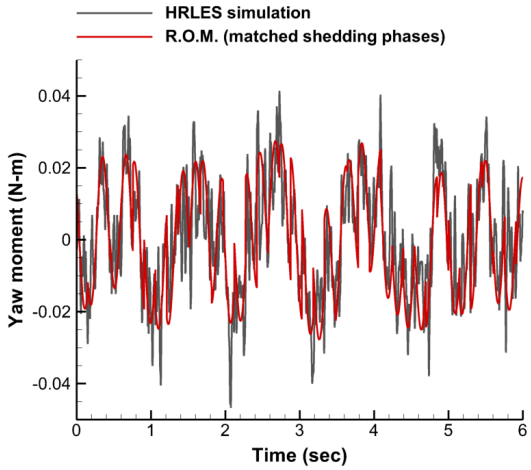

(c) Shedding with phases matched to HRLES

Figure 43: Effect of modeling vortex shedding terms in a dynamic simulation of a short rectangular prism.

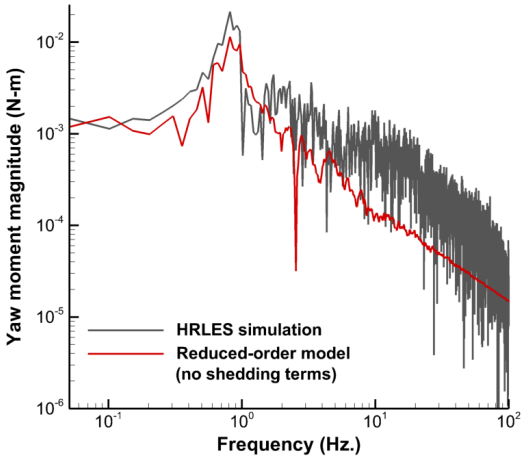

(a) No shedding

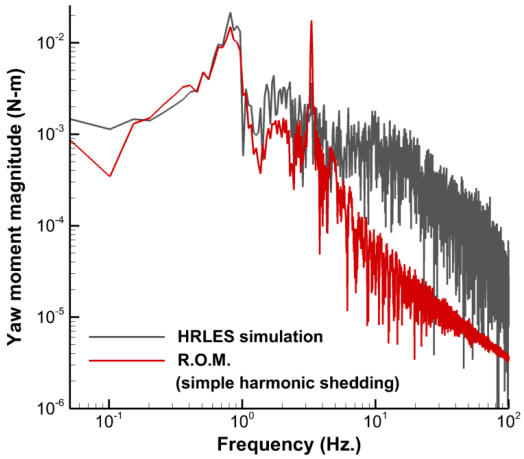

(b) Simple harmonic shedding

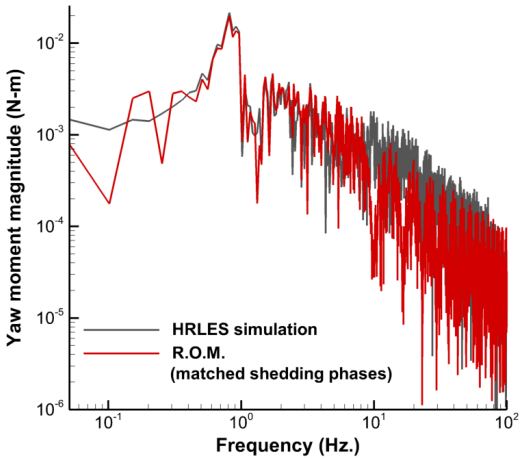

(c) Shedding with phases matched to HRLES

Figure 44: Frequency-domain transformation of yaw moment in a dynamic simulation of a short rectangular prism.

Only a single term has been modeled; thus $N = 1$ in Eq. 16. This simple harmonic form represents a clear improvement over the mean-flow yaw moment, as the fluctuations appear, by visual inspection of Fig. 43(b), to be of similar magnitude and frequency to the dominant fluctuations in the HRLES simulation. However, the fluctuations are clearly periodic, unlike the HRLES simulation, resulting in mismatched phases over much of the time history and an unrealistic shedding behavior. These characteristics of the actual vortex shedding can be modeled by modifying Eq. 17 to include aperiodic behavior. The modification involves adding a phase offset to the sinusoidal function:

$$\nu(\omega_s, t) = \sin(\omega_s t + \Psi_m), \tag{18}$$

where Ψ_m is the phase of the fluctuation m active at time t. In practice, the functional form of Ψ should incorporate randomness in such a way that models the nature of the actual turbulence. The current work employs a random function based on a normal distribution,

$$\Psi_m = \mathrm{rand_n}\left(\mu, \sigma\right), \tag{19}$$

with the probability density function for the normal distribution given by

$$f\left(x, \mu, \sigma\right) = \frac{1}{\sigma\sqrt{2\pi}} e^{-\frac{(x-\mu)^2}{2\sigma^2}}. \tag{20}$$

The final step in closing the model is to determine realistic values of the constants μ and σ. The dynamic HRLES simulations have been used for this purpose. In each of the cases, reduced-order simulations have been performed with prescribed dynamics to match the HRLES simulations, and the mean-flow portion of the forces and moments have been computed, as in Fig. 43(a). Equation 16 was then applied, with $N = 1$ and with Eq. 18 used to specify ν. However, instead of computing the phases with Eq. 19, Ψ_m was varied to match the HRLES data as closely as possible. The result of this procedure in one of the cases is presented in Fig. 43(c). Inclusion of the shedding terms with matched phases significantly improves the vortex shedding effects over the simple harmonic model while providing a means to introduce aperiodicity in the simulation.

Transformation of the yaw moment time histories from Fig. 43 to the frequency domain allows quantitative differences between the different vortex shedding representations to be

assessed. The results of this transformation are shown in Fig. 44. When no vortex shedding terms are included, the same low-frequency peaks in the yaw moment are present in both the reduced-order model and the HRLES simulation. These low-frequency peaks result from the mean-flow aerodynamic response to the body dynamics. Though the peaks are present at the correct frequencies, the magnitude is underpredicted when shedding fluctuations are neglected, which can also be observed in the time-domain response (Fig. 43(a)). The higher frequency content is completely missed when no vortex shedding is included in the model. Simple harmonic shedding (Fig. 44(b)) results in a better capture of the magnitudes at low frequencies and also produces some higher-frequency content. However, this higher-frequency content is concentrated into a single large spike at the dominant shedding frequency. This behavior is in contrast with the HRLES data, in which the high-frequency content is spread out over a much broader spectrum. When aperiodicity is introduced by matching the phases of the shedding model to the HRLES yaw moment, the frequency content is accurate over a broad range from 0.5 to 10 Hz even with $N = 1$.

Of course, it is not practical to perform the phase-matching procedure for each reduced-order simulation, because an identical HRLES simulation would be required for each case. Instead, this procedure has been applied to accumulate phase distribution data for the purpose of developing a representative statistical model. The phase distributions from each of the three HRLES simulations have been compiled and are plotted in Fig. 45. A best-fit normal distribution has been applied to model the phase data. The distribution has a mean value $\mu = 3.14$ and standard deviation $\sigma = 1.62$. The data are also fairly well represented by a simple uniform distribution over the range $0 \leq \Psi \leq 2\pi$ rad. Throughout the remainder of this thesis, the best-fit normal distribution has been applied to compute the shedding phase.

5.3 Unsteady Aerodynamics Due to Body Motion

When a body's orientation or velocity in a fluid flow changes, the aerodynamic response is not instantaneous. As a result, the unsteady aerodynamic response lags the quasi-steady

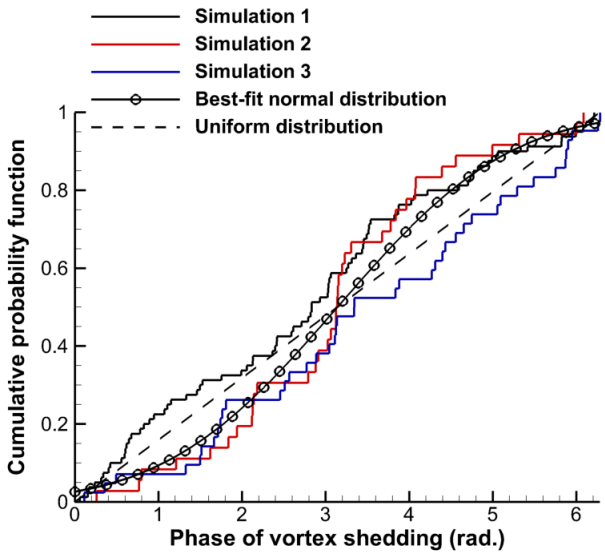

Figure 45: Shedding phases from three separate simulations and best-fit normal distribution: $\mu = 3.14$, $\sigma = 1.62$.

values, and magnitude attenuation also occurs during continuous accelerations. These concepts form the basis of classical unsteady aerodynamic theory, which includes Theodorsen's theory for simple harmonic motion of thin airfoils and the indicial methods of Wagner and Küssner [74, 105, 106, 107].

Though the classical unsteady aerodynamic theories are formulated for potential flow, similar responses have been observed in viscous, separated flows. Dynamic stall is one such case, which has been described in Section 1.4. Unsteady effects in dynamic stall have been successfully modeled as a second-order dynamic filter of the quasi-steady aerodynamic coefficients [69, 70, 71, 72, 73]. A similar unsteady model has been developed here to predict aerodynamic-dynamic interactions of bluff bodies. The model is a second-order differential equation, with the quasi-steady aerodynamics acting as a forcing function. For a generic mean-flow aerodynamic force or moment coefficient, $\overline{C}_\zeta$, the form of the model is given by

$$\ddot{\overline{C}}_\zeta + \eta\frac{U_\infty}{b}\dot{\overline{C}}_\zeta + \Omega_n^2\frac{U_\infty^2}{b^2}\overline{C}_\zeta = \Omega_{nqs}^2\frac{U_\infty^2}{b^2}\overline{C}_\zeta^{qs} + \epsilon\frac{U_\infty}{b}\dot{\overline{C}}_\zeta^{qs}, \tag{21}$$

where η, Ω_n, Ω_n^{qs}, and ϵ are model parameters. The differential equation model is necessary for the practical reason that it is able to produce phase lags and magnitude attenuation as expected from unsteady theory. The time derivatives also dictate that historical values of

the aerodynamic coefficients influence the solution at a given time, which is analogous to the wake in an unsteady flow. A significant benefit of Eq. 21 is that the flight speed and configuration scale are inherent in the model, so the model parameters are non-dimensional and can be applied over a broad range of flight conditions and sizes.

While it is possible to use system identification to determine the model parameters (see Refs. [1, 65, 11]), such an approach is not physics-based, and therefore the accuracy for new configurations is unknown. Instead, it is preferable to base the model on a theoretical unsteady aerodynamics framework. Theodorsen's theory [74] is one such framework. The theory is derived for a thin airfoil undergoing sinusoidal motion in potential flow, with the additional assumption that the wake is planar. Clearly, many of these assumptions are violated by three-dimensional bluff body flow. Nonetheless, the theory has been shown to provide moderately accurate results even in viscous cases with separation [108, 109, 110]. Therefore, it is expected that applying the theory to unsteady bluff body flow should at minimum produce the correct trends, and it represents a reasonable physics-based starting point for assessing the impact of unsteady aerodynamics on bluff body dynamics. The accuracy of the model is assessed later in Sections 6.1 and 6.4.2 using both HRLES simulations and full-scale flight test data.

The Theodorsen function is a frequency-domain transfer function between unsteady circulatory and quasi-steady aerodynamics:

$$\frac{\overline{C}_\zeta}{\overline{C}_\zeta^{qs}}(k) = c(k) = \frac{H_1^{(2)}(k)}{H_1^{(2)}(k) + iH_0^{(2)}(k)}. \tag{22}$$

The reduced frequency, $k = \dfrac{\omega b}{U_\infty}$, can be transformed between the frequency domain and the Laplace domain via the substitution $s = i\omega$. Here, the reference length, b, is taken as half the length of the longest side of the bluff body. Eq. 21 can also be written in terms of k by first taking the Laplace transform and then transforming the ratio of the left and right side to the frequency domain. Following this procedure, the dimensional quantities U_∞ and b vanish, and the frequency-domain transfer function corresponding to Eq. 21 becomes

$$\frac{\overline{C}_\zeta}{\overline{C}_\zeta^{qs}}(k) = \frac{ik\epsilon + \Omega_{nqs}^2}{-k^2 + ik\eta + \Omega_n^2}. \tag{23}$$

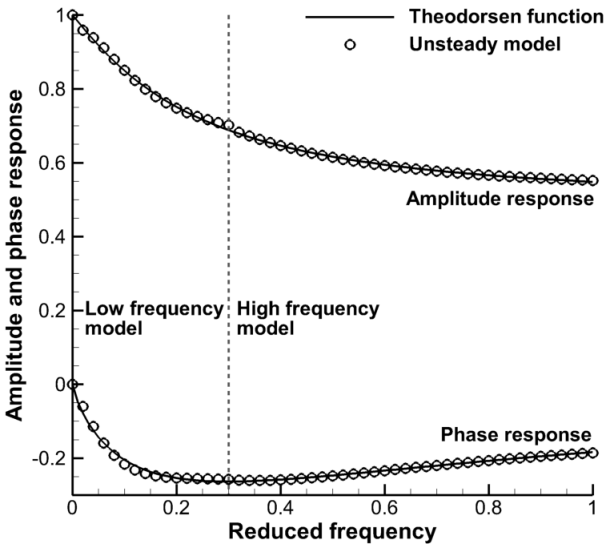

Figure 46: Response of the frequency-domain transfer function and comparison with classical unsteady aerodynamic theory (comparison of Eqs. 22 and 23).

Using the reduced-frequency form of Eq. 23, the model parameters can now be determined via an error-minimization procedure such that the best possible match between Eqs. 23 (the model) and 22 (the theory) is achieved over a range of reduced frequency. This procedure has been performed over two separate intervals, $k < 0.3$ and $0.3 \leq k \leq 1$. The resulting values of the parameters for these low reduced frequency and high reduced frequency models are listed in Table 9. Figure 46 compares the amplitude and phase responses of the reduced-order model to Theodorsen theory. Excellent agreement is achieved by splitting the response into two separate intervals. The same approach can also be used to develop a higher-order filter with additional model parameters to achieve equivalent accuracy over a broader range of reduced frequency.

Table 9: Model parameters for low- and high-frequency approximations of the Theodorsen function.

	$k < 0.3$	$0.3 \leq k < 1$
η	2.891	31.27
Ω_n	0.573	2.857
ϵ	1.822	16.24
Ω_{nqs}	0.563	2.659

For most dynamic problems, there is no specified reduced frequency because the motion

is not simple harmonic. However, usually the engineer is aware of an expected range of frequencies, so the selection of a set of applicable model parameters from Table 9 is not problematic. In all the dynamic bluff body simulations investigated here, the reduced frequency is expected to remain small, so the low-frequency model parameters are employed. This assumption is supported by the frequency information from Fig. 44(a). The largest peak in these figures corresponds to a reduced frequency of only 0.05. The $k = 0.3$ threshold for the high-frequency model parameters is crossed at a frequency of 4.6 Hz, by which point there remain no more singificant peaks corresponding to body dynamics.

A number of alternative rational function approximations to Theodorsen theory are available [108]. One such approximation, which is very similar in form to the original unsteady model in Eq. 21, was developed by RT Jones in 1938 [111]. When converted to the time domain, this model has the form

$$\ddot{\overline{C}}_\zeta + d_1 \frac{U_\infty}{b} \dot{\overline{C}}_\zeta + d_2 \frac{U_\infty^2}{b^2} \overline{C}_\zeta = n_1 \ddot{\overline{C}}_\zeta^{qs} + n_2 \frac{U_\infty}{b} \dot{\overline{C}}_\zeta^{qs} + n_3 \frac{U_\infty^2}{b^2} \overline{C}_\zeta^{qs}, \tag{24}$$

where $n_1 = 0.5$, $n_2 = 0.2808$, $n_3 = 0.01365$, $d_1 = 0.3455$, and $d_2 = 0.01365$. The only difference between the form of the RT Jones model and that of the original unsteady Theodorsen model in Eq. 21 is the presence of the $\ddot{\overline{C}}_\zeta^{qs}$ term. By including this additional term, the RT Jones model approximates the response of of Theodorsen theory accurately over a much larger range of reduced frequency with only a single set of model parameters (n_1, n_2, etc.). The RT Jones model has been transformed to state space form and incorporated in the reduced-order aerodynamics model, where it is solved using an Adams-Bashforth numerical integration scheme. The same numerical scheme has also been applied during simulations to integrate Eq. 21 in state-space form.

In order to verify the implementation, the RT Jones model has been used to simulate the unsteady response of a thin airfoil in simple harmonic motion, whose solution is known from Theodorsen theory. The amplitude and phase response have been measured for simulations at five discrete values of reduced frequency. The measured response compares favorably with the expected response in the frequency domain, as illustrated in Fig. 47. This figure also demonstrates that the RT Jones transfer function tracks the magnitude and phase

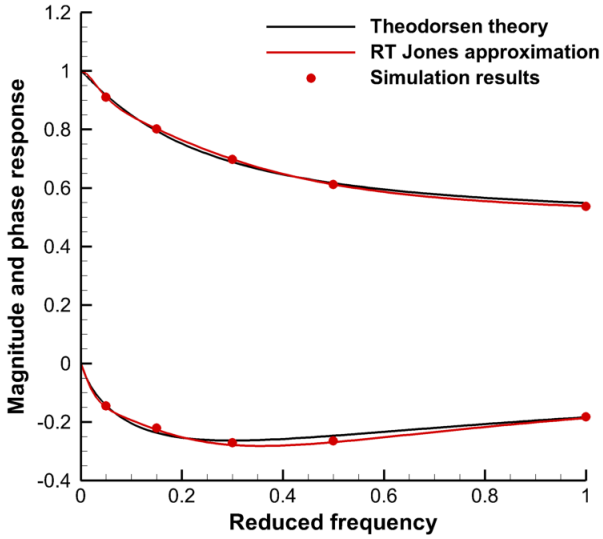

Figure 47: Verification results for the RT Jones unsteady aerodynamic model.

characteristics of Theodorsen theory accurately over a broad range of reduced frequencies. Both models are utilized throughout the rest of this thesis, as the model of Eq. 21 was developed first and subsequently applied in many of the initial simulations. However, both are essentially equivalent at low reduced frequencies, and tests have been performed to ensure that the dynamic behavior remains the same when the unsteady model is changed for the cases presented in this thesis. In general, the RT Jones model is recommended because of its broader applicability with a single set of model parameters.

CHAPTER VI

MODEL VALIDATION AND TETHERED LOAD STABILITY ANALYSIS

In this chapter, the reduced-order model is validated using multiple methods. The high-fidelity hybrid RANS-LES simulations presented in Section 4.2 are especially useful for this purpose, because uncertainties with respect to the tether and attachment system, mass distribution, initial conditions, atmospheric turbulence, and other parameters can be eliminated by simulating these characteristics identically in both numerical methods. Validation with experimental flight test data is also valuable to ensure that the model's predictions are representative of real behaviors. Both validation approaches are presented in this chapter. Predictions of tethered load stability by the model are also assessed and validated against flight test data.

6.1 CFD Validation of Reduced-Order Aerodynamics

The reduced-order model has been validated using the high-fidelity CFD tethered load simulations presented in Section 4.2. These simulations involve a $1/11^{\text{th}}$-scale model of the CONEX rectangular prism cargo container in a virtual wind tunnel without helicopter degrees of freedom. The tethered load properties and operating conditions for these simulations are given in Tables 7 and 8, respectively. The aerodynamic predictions of the model are initially evaluated by applying the 6-DoF dynamic states from the two CFD simulations as prescribed-motion inputs to the model. This procedure permits a direct comparison between the reduced-order model and high-fidelity aerodynamic predictions.

Figures 48 and 49 present comparisons of the drag (in the wind tunnel X-direction), the side force (in the tunnel Y-direction), and the yaw moment (about the tethered load's vertical axis) for the high-fidelity simulations and the reduced-order model. Vortex shedding fluctuations have been removed from the reduced-order model results to permit a clearer comparison of the mean-flow effects. In the 25-mph case (Fig. 48), the reduced-order

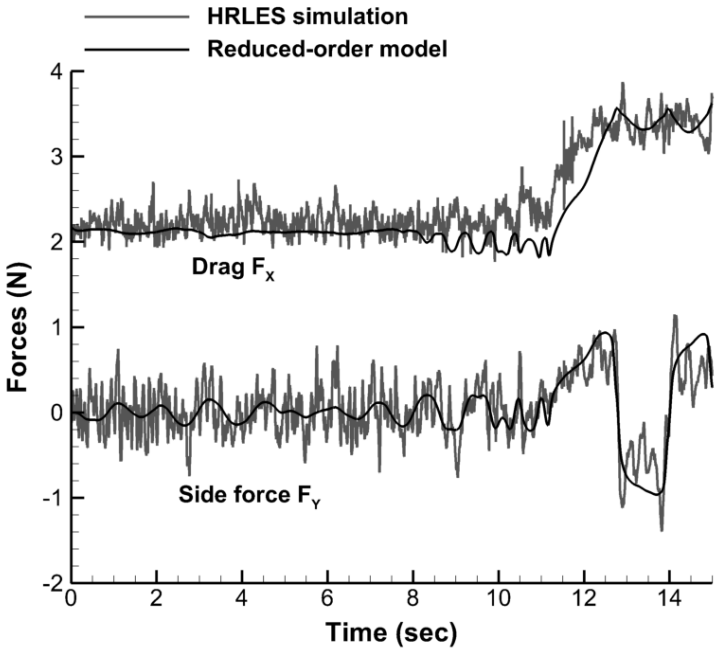

(a) Drag and side force

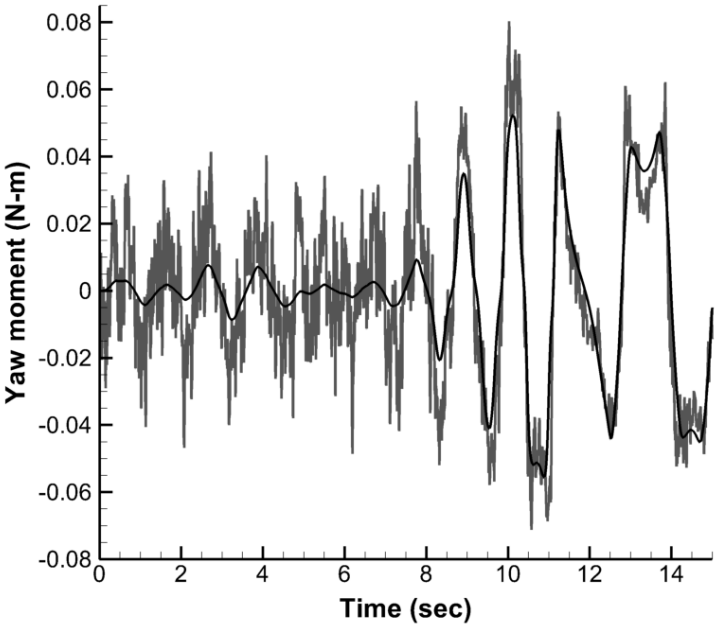

(b) Yaw moment

Figure 48: Comparison between high-fidelity and reduced-order aerodynamics; 25 mph tunnel speed. For clarity, vortex shedding effects have been left out of the reduced-order results.

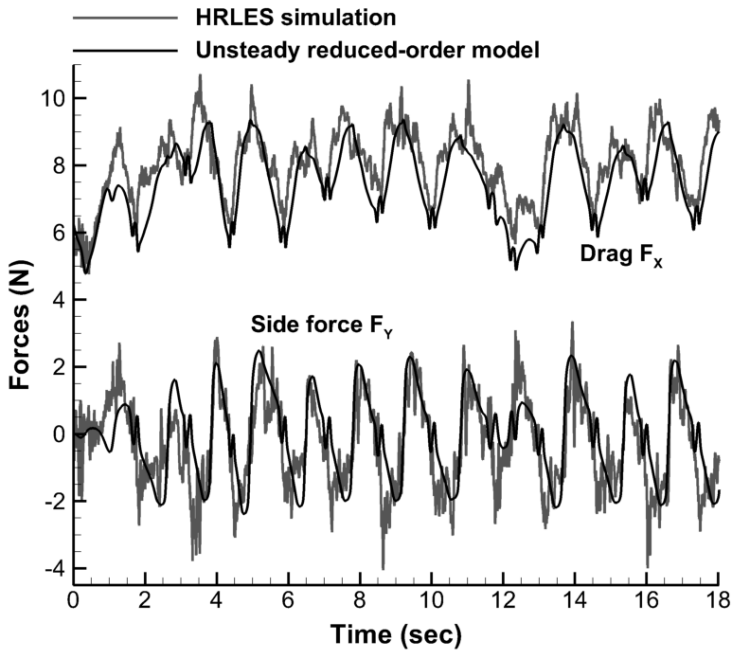

(a) Drag and side force

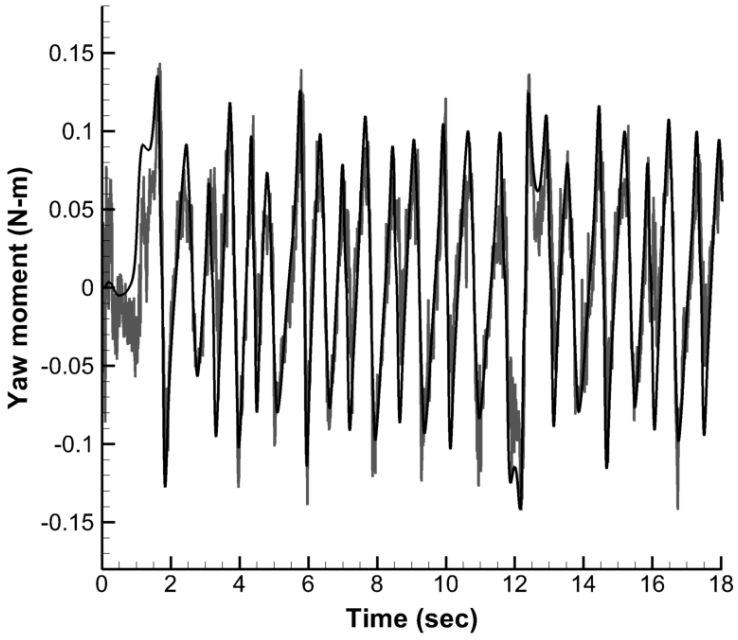

(b) Yaw moment

Figure 49: Comparison between high-fidelity and reduced-order aerodynamics; 40 mph tunnel speed. For clarity, vortex shedding effects have been left out of the reduced-order results.

prediction of all three of these quantities is in excellent agreement with the high-fidelity simulation. Of particular interest is the fact that the model captures the changes in these forces and moments after the rotation from narrow-side-forward to broad-side-forward has occurred, which takes place after approximately 12 seconds (see Fig. 37(a)). The drag is slightly underpredicted during this rapid transitional period, but otherwise the model prediction passes through the middle of the fluctuating high-fidelity data. The yaw moment and side force, in particular, exhibit significant nonlinearities during the last half of the simulation while the yaw angle begins to grow large. These nonlinearities result from shear layer reattachment on the faces of the rectangular prism, which is captured by the model.

Figure 49 presents a comparison between high-fidelity and reduced-order aerodynamics for the 40-mph case. Despite the more complex dynamics and larger trailing angle excursions at this speed, the reduced-order model still accurately predicts the forces and moments. All three quantities (drag, side force, and yaw moment) are well-captured in terms of both magnitude and phase. The side force and yaw moment oscillate about a mean value of zero, while the mean drag is 7.5 N, which is significantly higher than in the 25-mph case. The periodic nature of the aerodynamics is due to the fact that the tethered load is spinning, as evidenced by the yaw angle time history in Fig. 37(b).

6.1.1 Quasi-Steady Data from Other Sources

Though most of the reduced-order simulations in this thesis make use of quasi-steady data from static time-accurate high-fidelity simulations, it is also equally valid to apply data from other sources, such as flight tests or wind tunnel tests, provided they encompass the needed range of orientations and flight conditions. To illustrate this point, the 25-mph case has been evaluated with wind tunnel data from Rosen et al. [4] used to inform the quasi-steady aerodynamic model. Though the Reynolds number is in this test is smaller than in the high-fidelity simulations, this sharp-edged bluff body is insensitive to Reynolds numbers in this range [16, 13, 17], and good agreement has been observed between this experimental data and the high-fidelity simulations (see Fig. 12).

Figure 50 depicts the yaw moment from the 25-mph case when the quasi-steady data

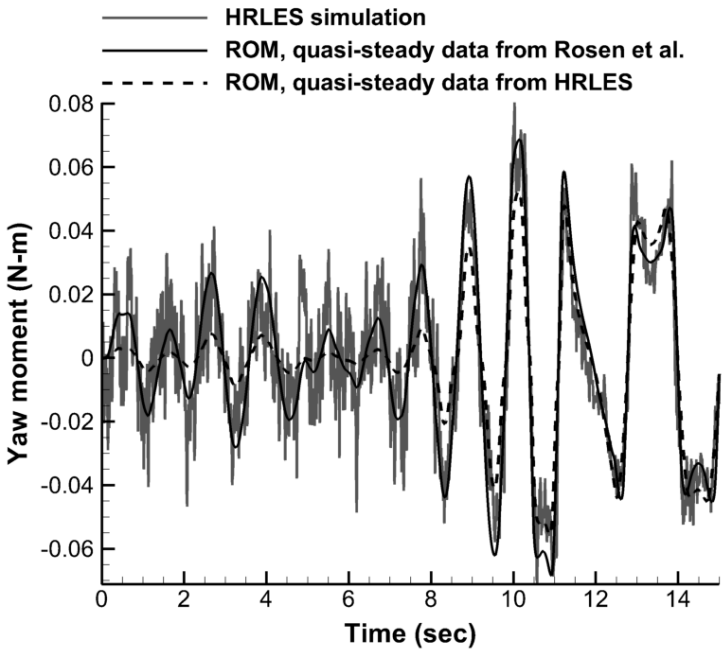

Figure 50: Yaw moment for the 25-mph case with quasi-steady data from high-fidelity simulation and from wind tunnel data [4].

from high-fidelity simulations are substituted with the wind tunnel data from Rosen et al. [4]. At first glance, the prediction of the peak values actually appears improved with the wind tunnel data, which is unexpected. However, this appearance results from the removal of the vortex shedding terms, as has been done in the previous figures, for the sake of clarity. When these terms are included, the quasi-steady data interpolated from static CFD data sets more accurately represent the high-fidelity dynamic simulation results, as expected (see Fig. 43(c)). In the wind tunnel tests, shear layer reattachment occurred at a slightly lower yaw angle than in the static high-fidelity simulations, resulting in a higher yaw moment slope and relatively greater yaw moment at low yaw angles in the wind tunnel data. Despite these differences, which are to be expected with a different data set, the overall agreement with high-fidelity data is still quite satisfactory and demonstrates that the model is robust with respect to the source of quasi-steady data.

6.1.2 Aerodynamic Yaw Moment Damping

Due to the short aspect ratio of the CONEX cargo container and the lack of any stabilizing fins, it has so far been assumed that aerodynamic moment damping terms are negligible. To

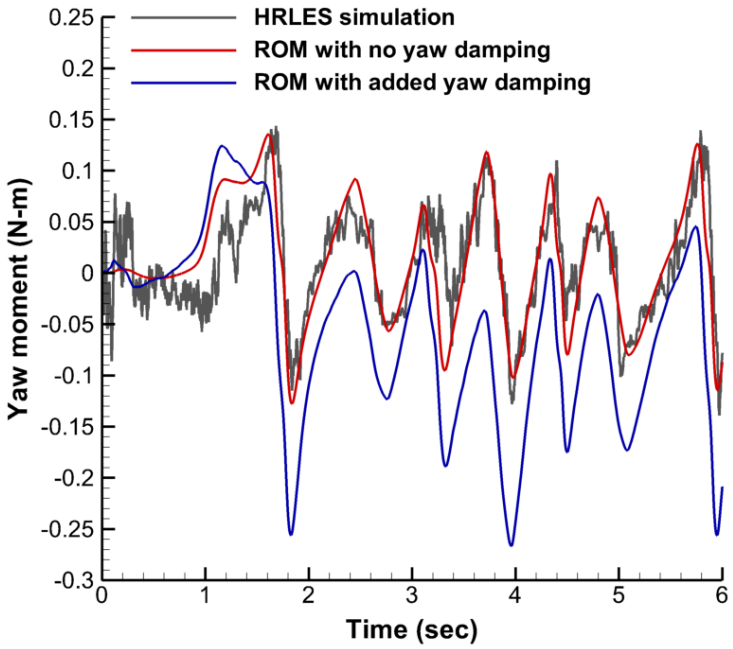

Figure 51: Yaw moment for the 40-mph case with and without an aerodynamic yaw rate damping term.

evaluate this assumption as well as establish the influence of such terms, yaw rate damping has been investigated for the 40-mph tunnel speed. This term has the form

$$\overline{C}^{qs}_{N,damp} = C_{damp} r, \tag{25}$$

which is added to Eq. 14 for the yaw moment. As an estimate of this damping coefficient is not available for the CONEX, a representative value has been selected based on the peak yaw moment during spinning motion at 40 mph (0.1 N-m) and the mean spin rate (2.2 rad/sec). The yaw rate damping coefficient, C_{damp}, based on these parameters is -0.04 sec/rad after converting the peak yaw moment to non-dimensional form. The negative sign indicates that the damping opposes yaw rotation.

Figure 51 presents the yaw moment over the first six seconds for the high-fidelity simulation and the reduced-order simulation with and without aerodynamic yaw rate damping. (As in previous figures, the vortex shedding fluctuations have been left out of the model results for clarity.) Prior to the spinning motion, which occurs after approximately two seconds at this wind speed, the rate damping term introduces a small phase lead relative to the yaw moment from the high-fidelity simulation. After the tethered load begins to spin,

the rate damping term produces an offset on the order of 0.1 N-m in the negative direction, which is expected based on the selected value for C_{damp} and the mean spin rate. However, compared to the reduced-order prediction with no aerodynamic yaw rate damping, the prediction with damping is significantly worse. Both the phase lead prior to spinning and the yaw moment offset during spinning are not present in the high-fidelity data. Furthermore, the reduced-order model prediction without the damping term is within the vortex shedding fluctuations from the high-fidelity data throughout most of the simulation, while it differs significantly from the high-fidelity data when the damping term is included. The good correlation between the model and the high-fidelity simulation without aerodynamic rate damping and the significantly degraded prediction when this term is included indicate that aerodynamic moment damping is negligible for this bluff body. Therefore, these damping terms are neglected in the remainder of the simulations for the CONEX tethered load. On the other hand, for bluff bodies with stabilizing fins (i.e., those evaluated by Raz et al. [16]), such damping terms are required and may provide stabilization of the spin mode.

6.2 CFD Validation of Reduced-Order Dynamics

The previous section has demonstrated that the aerodynamic predictions of the reduced-order model are accurate when compared with high-fidelity simulations incorporating identical dynamics. The next step is to evalute the dynamic behavior when the reduced-order model is allowed to drive to motion. For this purpose, the same two CONEX cases from Tables 7 and 8 have been repeated with the reduced-order model computing both the aerodynamics and dynamics. In each of these cases, the model has been assessed in two configurations: (1) with all unsteady terms included, and (2) with only quasi-steady aerodynamics applied to compute the mean-flow terms. In all cases, the vortex shedding terms have been included.

Figure 52(a) presents the yaw dynamics for the complete reduced-order model with all unsteady terms compared with the yaw dynamics from high-fidelity simulation. The behavior is similar for both; while initially small, yaw oscillations increase over time and eventually cause the rectangular prism to rotate 90° so that the broad side faces forward

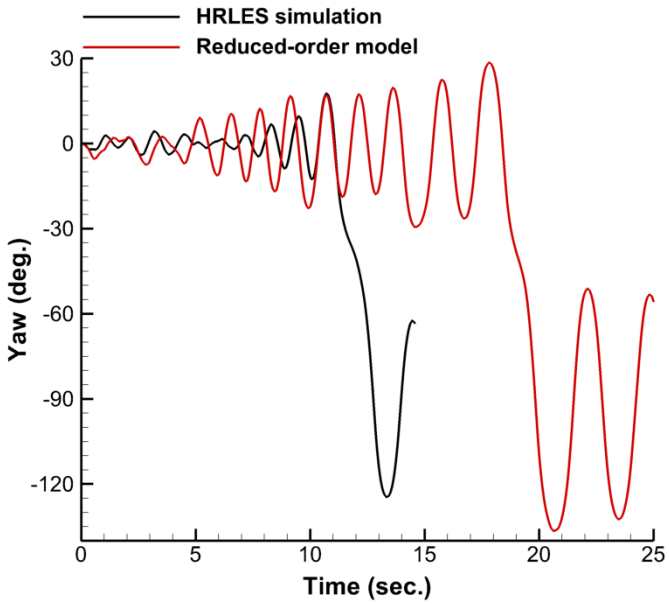

(a) Complete ROM

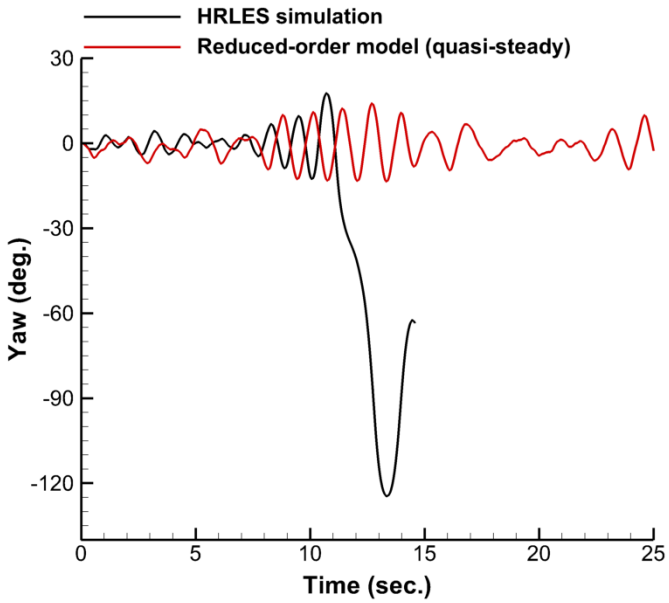

(b) Quasi-steady ROM

Figure 52: Yaw comparisons at 25-mph tunnel speed, high-fidelity simulation vs. reduced-order model.

instead of the narrow side. Furthermore, in each case a steady spin is not developed, but instead the bluff body settles into a periodic oscillation behavior about this new equilibrium orientation. The rotation from narrow-side-forward to broad-side-forward does not occur at the same time in each simulation; the transition is delayed by eight seconds in the reduced-order simulation. However, the random nature of vortex shedding plays a role in determining when the rotation occurs, and even in the high-fidelity simulation or in flight tests, small changes in turbulence or initial conditions are expected to similarly alter the time history of dynamic states due to unpredictable changes in the chaotic 3-D vortex shedding. Therefore, it is more important to focus on the dynamic characteristics instead of the specific times at which the behaviors occur, and this figure demonstrates that the reduced-order model predicts the correct yaw behavior.

Figure 52(b) presents a similar comparison, but this time including only the quasi-steady effects in the mean-flow aerodynamics of the reduced-order model. Though the initial behavior is similar – the rectangular prism experiences growing yaw oscillations – the characteristic rotation from narrow-side-forward to broad-side-forward never occurs. Instead, a limiting yaw angle of 15° is reached but never exceeded. Though the yaw rotation behavior is dependent upon random vortex shedding, repeated tests have confirmed that the rotation does not occur unless unsteady effects of body motion are included. This result is of particular interest, as it indicates that unsteady aerodynamics play a significant role in the dynamic response of bluff bodies even at low reduced frequencies.

Though vortex shedding effects were omitted in Figs. 48 and 49, it is important to describe their roles in the dynamic response of a bluff body. The first role is to provide a perturbation to the dynamic state. Without such a perturbation, some modes may never be excited during the simulation, while they would be in a real flow. The second role is to modify the time at which changes in dynamics occur. For example, the yaw rotation behavior in Fig. 52(a) has been found to occur at different times depending on the random shedding fluctuations that are applied by the model, but this behavior always occurs at some point in time provided the unsteady terms are included.

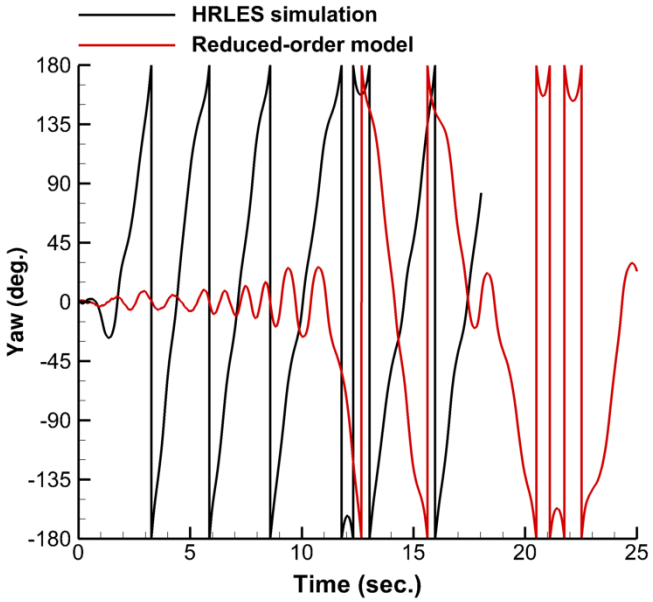

(a) Complete ROM

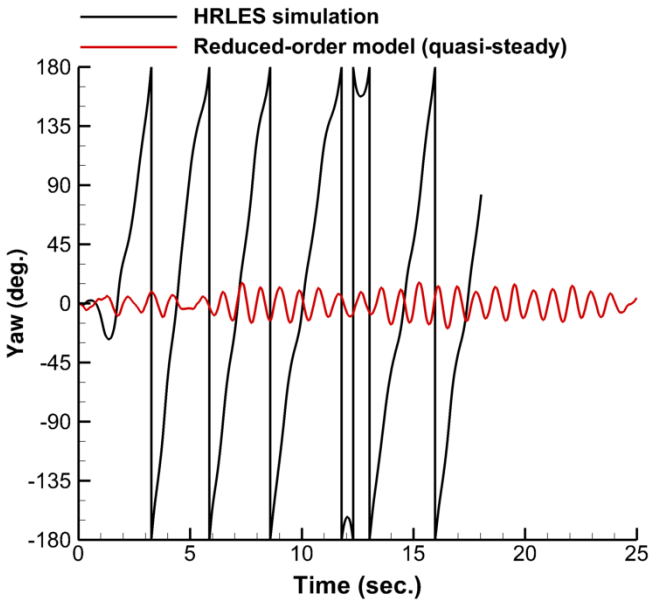

(b) Quasi-steady ROM

Figure 53: Yaw comparisons at 40-mph tunnel speed, high-fidelity simulation vs. reduced-order model.

A similar comparison is presented in Fig. 53 for the 40-mph case. The narrow-side-forward position has been found to be particularly unstable in the high-fidelity simulation at this speed, with yaw divergence occuring within the first few seconds and then a counterclockwise rotation developing. After eleven seconds of growing yaw oscillations, the rectangular prism begins to rotate in the clockwise direction, which is the same behavior as predicted by the high-fidelity numerical simulation, though the direction of rotation is opposite. It should be noted that the direction of rotation is also influenced by the random vortex shedding fluctuations and may change from one simulation to the next, and similar observations have also been reported in prior wind tunnel tests [98]. In the high-fidelity simulation, the spinning behavior pauses briefly at 12 seconds and then continues. The reduced-order model response includes similar pauses as well as reversals in spin direction. Though the initial onset of spinning is delayed relative to the high-fidelity dynamics, it occurs significantly earlier in the reduced-order model compared to the 25-mph case, so the correct trend in sensitivity of this behavior to tunnel speed is captured.

The average magnitude of yaw rotation rate for the reduced-order model during the complete rotation occurring between simulation times of 12 and 16 seconds is 2.1 rad/sec, while it is 2.3 rad/sec in the high-fidelity simulation during the two complete rotations between simulation times of 3 and 9 seconds. This result represents an error of 8.7%. Furthermore, the mean rotation rate varies between cycles, and including the third complete rotation that takes place between 9 and 12 seconds results in an average spin rate of 2.2 rad/sec in the high-fidelity simulation, representing an error of only 4.6%.

Figure 53(b) demonstrates, once again, that incorrect behavior results if only quasi-steady effects are considered in the mean-flow aerodynamics. Despite the fact that the high-fidelity simulations indicate that the narrow-side-forward orientation is even less stable at this speed, the quasi-steady reduced-order model still does not produce yaw divergence in this case. Instead, a limit-cycle yaw oscillation is established, as in the 25-mph case. These results confirm that unsteady aerodynamics are important to bluff body dynamics, and models neglecting them should not be expected to produce the correct response.

The trailing angle, or the angle that the vector from the tethered load center of gravity to

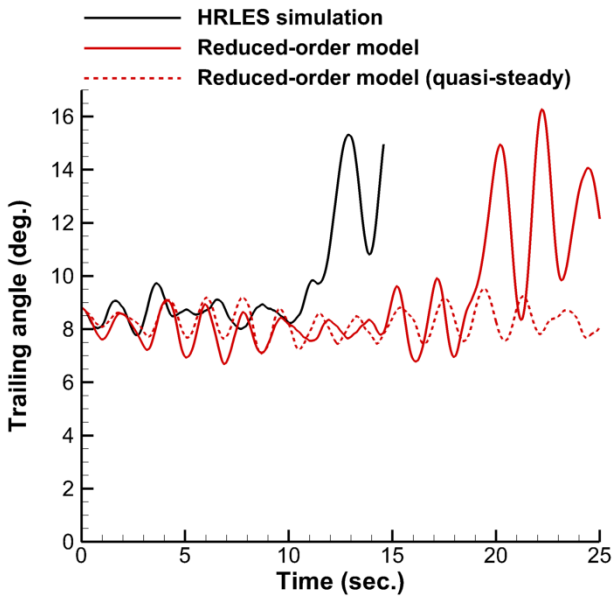

(a) 25-mph case

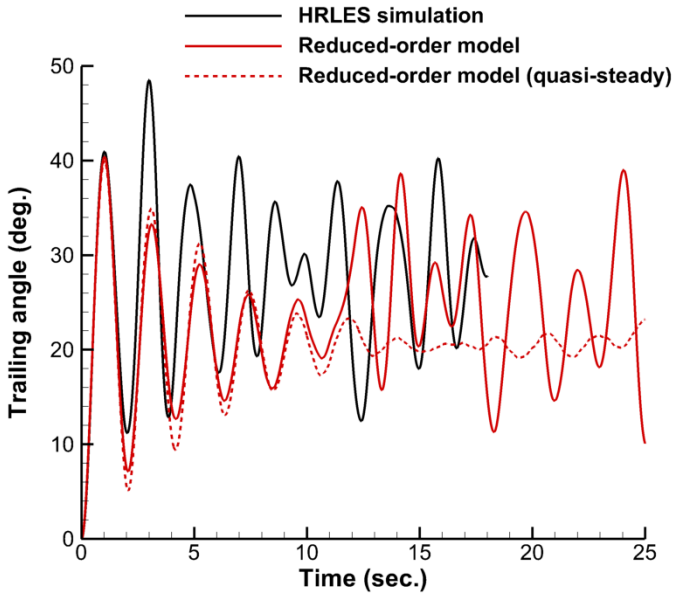

(b) 40-mph case

Figure 54: Trailing angle comparisons between high-fidelity and reduced-order simulations.

the attachment point makes with respect to the vertical, is shown in Fig. 54. Reduced-order model results include both the complete model and the quasi-steady version. In the 25-mph case, initial oscillations in the trailing angle are small, as the initial condition is set such that the aerodynamic and gravitational moments acting about the tether attachment point are nearly balanced. The oscillations remain small until yaw rotation takes place, at which point the trailing angle increases significantly due the to higher drag in the broad-side-forward orientation. The behavior is very similar between the high-fidelity simulation and the complete reduced-order model, with the main difference being the time at which rotation occurs. After yaw rotation, the mean trailing angle is 13.7° in the high-fidelity simulation and 12.3° in the reduced-order model, representing a difference of 10%. With quasi-steady aerodynamics in the reduced-order model, the prism never undergoes the characteristic yaw rotation, so the trailing angle remains significantly smaller. Prior to yaw rotation, the mean trailing angle is 8.6° in the high-fidelity simulation, 8.0° in the complete reduced-order model, and 8.2° in the quasi-steady model, all representing an error of less than 7% between high- and low-fidelity simulations. These predictions also compare favorably with similar wind tunnel tests, in which the observed trailing angle was 9° [5].

At 40-mph, the rectangular prism initially has a trailing angle of 0°, resulting in large initial trailing angle oscillations due to the unbalanced moment about the cable attachment point at the top of the wind tunnel from drag on the tethered load. The mean trailing angle is 27.2° for the high-fidelity simulation, 24.7° for the reduced-order simulation with all unsteady terms included (9.1% error), and 20.5° for the reduced-order simulation with only quasi-steady mean-flow aerodynamics (24.6% error). The larger error for the quasi-steady simulation is due to the fact that the incorrect yaw behavior is predicted; the narrow side remains facing forward throughout the simulation, resulting in lower drag.

6.2.1 Computational Cost

The computational cost of the reduced-order model is significantly lower than CFD-based dynamic simulations. For the 25-mph case, the high-fidelity simulation required approximately 80,000 CPU-hours to complete 50,000 time steps, corresponding to 15 seconds of

dimensional time. Run on 128 cores of a Cray XE6 cluster, each rated at 2.5 GHz, this cost translates to 625 hours of wall time. In contrast, 50,000 steps for the reduced-order model required only 2.95 minutes on a single processor rated at 2.33 GHz, for a total cost of 0.05 CPU-hours, representing a reduction of over six orders of magnitude in terms of CPU-hours and over four orders of magnitude in wall time. This large difference in cost is mainly due to the need to resolve multiple millions of degrees of freedom, associated with the conserved variables at each grid node, in high-fidelity simulations.

In addition to the much smaller number of computations required per time step in the reduced-order model, several cost-saving techniques have also been applied. One is the use of a simplified interpolation routine, instead of the built-in function in MATLAB, to speed up the retrieval of quasi-steady data (for more information, see Prosser and Smith [112]). As described in Section 5.1, radial basis function (RBF) interpolation has been applied to improve the interpolation accuracy with a relatively coarse data set. Hodara and Smith [100] found that using RBF to interpolate data in a simulation increased interpolation cost by a factor of ten, compared to linear interpolation, for a model with 220 data points. However, as recommended by Hodara and Smith, this cost is converted to a one-time preprocessing cost by applying RBF to first interpolate the quasi-steady data set to a finer resolution and then using linear interpolation during the actual simulations. This approach results in the accuracy of RBF interpolation combined with the speed of linear interpolation.

Of course, generation of the quasi-steady data set required by the model also represents a significant pre-processing cost. For example, the numerical data set for the rectangular prism used prominently throughout this effort involved eleven individual static orientations. Each of these required approximately 20% the number of time steps as the 25-mph dynamic case in order to ensure that a sufficiently long time history was available for computing mean force and moment coefficients. Thus, approximately 176,000 CPU-hours were required for all eleven cases. Similarly, performing wind tunnel or flight tests for this purpose is also costly.

Further cost savings are also possible within the reduced-order model. High-fidelity simulations of bluff bodies require a very fine time step to resolve turbulence scales, but the

reduced-order model is not constrained to the same extent. The time step can be increased significantly in the reduced-order simulation, though it is recommended that at least ten steps per fluctuation in the vortex shedding model be employed to prevent aliasing; therefore $\frac{\Delta t U_\infty}{b} \leq \frac{0.1}{St}$. For the 25-mph case, this upper bound corresponds to $\Delta t = 0.0037$ sec, which is approximately an order of magnitude larger than the time step used in the dynamic CFD simulations. Additionally, tests to date have indicated that integration of the dynamic equation for unsteady aerodynamics (Eq. 24) requires a smaller time step for stability than the 6-DoF rigid body equations (Eq. 1). In the 25-mph simulation, the maximum time step possible using third-order Adams-Bashforth integration was approximately 0.002 seconds, above which the unsteady aerodynamic model would become unstable. However, the time integration scheme can be changed to improve stability if desired; for example, by reducing the order of accuracy. Significant additional cost savings can also be realized via implementation in a compiled language with optimization, as opposed to the current implementation in MATLAB, and through parallel processing applied to retrieve coefficients from the quasi-steady data tables. It is expected that with the latter two changes alone, the performance can be easily improved sufficiently for real-time simulations.

6.3 UAV Flight Test Comparisons

The reduced-order aerodynamic model has been incorporated into the Georgia Tech UAV Simulation Tool (GUST) [113] for tethered load simulations by the UAV Research Facility at the Georgia Institute of Technology. The GUST framework is employed in simulation to develop and test control algorithms for helicopter and tethered load guidance. The realism of the reduced-order aerodynamic model for the tethered load is important to ensure that the control laws perform as well in the real world as they do in simulation.

Flight tests have been performed by the UAV Research Facility to evaluate control algorithms for tethered loads. In these flight tests, an unmanned helicopter called GTMAX carries an approximately cylindrical tethered load, as portrayed in Fig. 55. The tethered load has length 0.26 meters, diameter 0.28 meters, and mass 5.2 kg. The tether consists of a single line of length 14 meters. As the load configuration is similar to a short cylinder

with aspect ratio 1.0, quasi-steady high-fidelity simulation data from simulations of this geometry, presented in Chapter 3, were utilized to create quasi-steady data sets and to determine the magnitude of vortex shedding fluctuations. Other than substituting these data sets, no other changes were required to apply the reduced-order model to a new bluff body geometry.

During the flight test, the GTMAX helicopter flew along a straight path without turning. Several linear accelerations in both the forward and backward directions were commanded in the flight velocity profile (Fig. 56(a)), with only small deviations in the lateral direction. The position of the load was measured with a downward-facing camera. For comparison with the flight test data, the helicopter position has been integrated from the velocity profile and applied as a prescribed motion at the top of the tether in simulation. The resulting load positions in both the longitudinal (along the flight path) and lateral (normal to the flight path) directions are presented in Fig. 56(b). The helicopter position is subtracted to provide a clearer comparison. To demonstrate the superiority of the present model over simpler models that consider only constant quasi-steady drag (e.g., Ref. [63]), an additional simulation was performed with only quasi-steady drag included in the aerodynamic model. The constant drag coefficient was set to 0.74, which is representative of a low-aspect-ratio cylinder in subcritical flow [6, 31].

During the accelerations, the load tends to lag behind the helicopter, and it swings back and forth in the constant-speed portions of the flight profile. The motion in the lateral direction is dominated by a pendulum-like behavior. Though the position in both axes is generally well predicted by the simulation, the measured data are characterized by significantly more high-frequency oscillations. However, when compared with the mean change in the helicopter's position in each direction (approximately 25 meters), these discrepancies are well within the range of uncertainty due to uncontrolled wind gusts, measurement error, and the initial state. The difference between the measured and simulated maximum load excursions is less than 10% of the total change in helicopter position in the longitudinal direction, and less in the lateral direction. When only quasi-steady drag is included in the aerodynamic model, the longitudinal motion is largely unaffected. However, the lateral

(a) GTMAX helicopter with load

(b) Close-up of load

Figure 55: Photographs of the GTMAX helicopter and tethered load. Figure used by permission of the UAV Research Facility at the Georgia Institute of Technology.

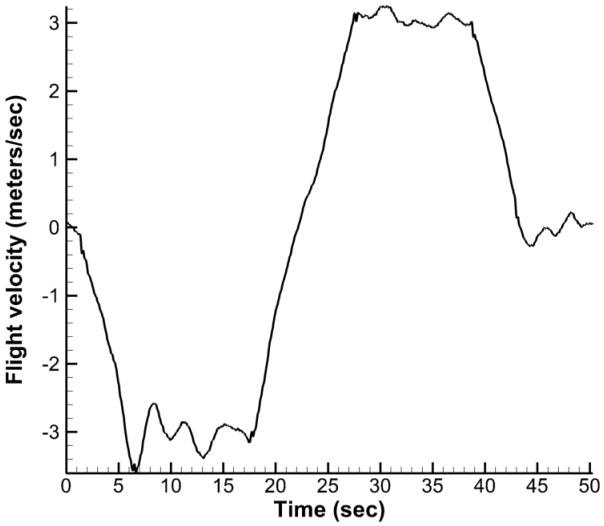

(a) Helicopter velocity profile

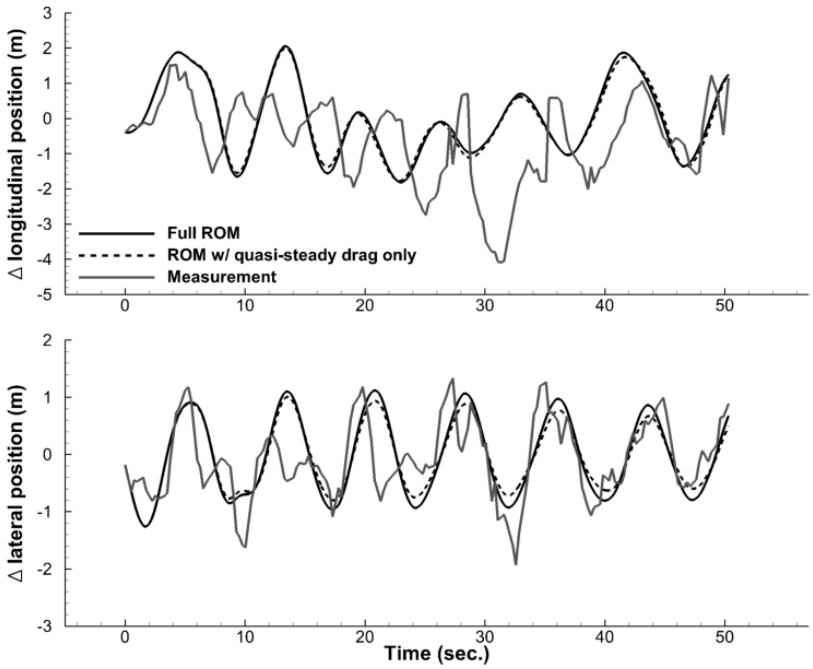

(b) Load position subtracted from helicopter position

Figure 56: Flight test data from the UAV Research Facility and comparison between measured and simulated load positions.

motion is captured more accurately with the full model, as oscillations do not die out as quickly. Therefore, even in this flight test at relatively low speeds with a relatively heavy tethered load, the current reduced-order model produces noticeably better dynamic predictions than the simpler drag-only method. The flight test comparison serves as additional validation of dynamic predictions by the reduced-order model and also demonstrates that the model is able to handle diverse bluff body types.

6.4 Full Scale Flight Tests and Stability

The previous sections have demonstrated validation of the reduced-order model with high-fidelity CFD simulations, wind tunnel data, and UAV-scale flight tests. However, the modeling approach and assumptions cannot be validated until correlation with full-scale flight test data is confirmed. In particular, as dynamic instability is the main factor limiting helicopter flight speed and increasing certification costs for tethered load operations, the ability to predict this instability with a simulation model is highly valued.

Flight test data have been provided by the Aeroflightdynamics Directorate (AFDD) of the U.S. Army for a full-sized CONEX cargo container over a range of flight speeds. The details of the load and flight test conditions are provided in Tables 10 and 11.

Table 10: Flight test parameters.

Flight number	Record number	Mean airspeed (kts)	Mean yaw rate (deg/sec)
132	2	55.3	127.2
132	3	69	160.0
132	4	77	167.1
132	6	86	152.6
132	8	97	128.2
132	10a	105.6	89.7
134	8	112	54.6

The load is secured in flight using a system of four cables attached between the top four corners of the CONEX and a single hook underneath the helicopter. The hook attachment includes a gimbal to allow the entire tether system to spin freely, rather than winding up when the load spins. The friction due to the gimbal was measured by AFDD and found to vary with the load weight according to the relationship in Table 11, but it remains constant

Table 11: CONEX cargo container configuration.

Quantity	Value	Units
L, W, H	8.48, 6.11, 6.41	ft
Weight, including tethers	4774.0 (Flight 132) 4700.0 (Flight 134)	lbf
I_{xx}, I_{yy}, I_{zz}	993.0, 1382.3, 1254.6	slug-ft^2
G.C.-to-C.G. (x, y, z)	-0.082, -0.048, -1.323	ft
Gimbal friction	0.60723 + 0.00099575 $\times$ Weight	ft-lbs

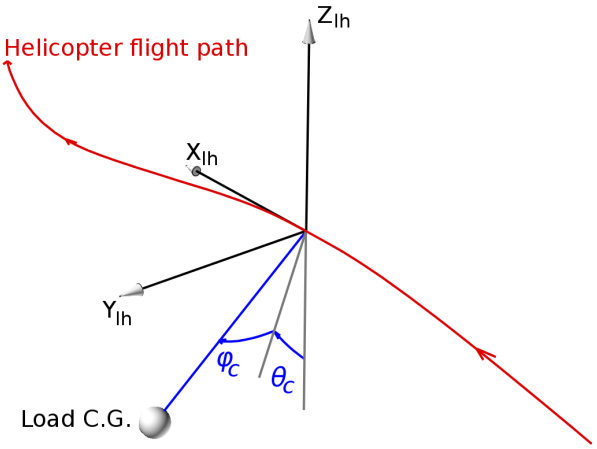

Figure 57: Depiction of longitudinal (θ_c) and lateral (ϕ_c) cable angles.

as the spin rate changes (it does not behave as a damping term proportional to the spin rate) [11].

Two different sets of flight data were provided by AFDD. Flight 132 included six records over a broad range of flight speeds below the stability boundary. At these speeds, the tethered load was observed to spin at a steady rate whose mean value was constant from one revolution to the next but varied throughout a revolution. The lateral and longitudinal cable angles relative to the flight path also typically exhibited relatively small oscillations about their mean values during this flight. These angles define the transformation between the hook-to-load-C.G. vector and the negative Z-axis of the level heading frame, which is the coordinate system aligned with the helicopter flight path. The cable angles are depicted in Fig. 57. A single record is included for Flight 134, above the critical flight speed for stability. At this speed, the spin rate reduced and included several direction reversals, while the cable angle excursions from the mean values grew in excess of 20°.

6.4.1 Force and Moment Comparisons

Before simulating the dynamics of the tethered load, it is important to ensure that the reduced-order model accurately predicts the aerodynamic forces and moments. The aerodynamic predictions have been previously validated with high-fidelity numerical computations of a 1/11th-scale CONEX container (see Section 6.1). Here, data from Flight 134 are employed to validate the model for the full-scale flight tests. The fight record included all dynamic state information (position, velocity, orientation, and angular rates) for the tethered load as well as the wind velocity. In the simulation, the motion of the load was prescribed to match the flight test data and included the wind speed. During this test, the load spun with an average rate of 54.6 deg/sec, as listed in Table 10, with the direction of rotation reversing several times. The resulting drag, side force, and yaw moment, compared with measured quantities from the flight test, are presented in Fig. 58 as functions of β. As the tethered load spun several times during the flight test, each plot has multiple curves corresponding to different times in the test.

Figure 58 demonstrates that the reduced-order model is able to accurately predict the forces and moments from the flight test data. The drag and yaw moment are particularly well predicted, especially considering the model aerodynamics draw from computations of a wind-tunnel-scale CONEX. This result confirms that the aerodynamics of the CONEX are insensitive to Reynolds number, which is expected because shear layer separation is fixed at the sharp edges of the geometry. The fact that the yaw moment magnitude is accurately predicted also provides further validation for the quasi-steady crossflow correction. The magnitude of side force is somewhat over-predicted in the simulation, although the phase and trends with yaw angle are still accurate. The lift is not shown, as it is not a strong function of yaw angle, but the model prediction of lift is also satisfactory.

The higher-frequency variations in the forces and moments apparent in Fig. 58 are due to three-dimensional unsteady vortex shedding. The qualitative shedding behavior is similar between the flight test and reduced-order simulation in Fig. 58. To ensure that the quantitative behavior is also accurate, Fast Fourier Transforms (FFTs) have been applied to transform the time histories of the forces and moments to the frequency domain. The FFT

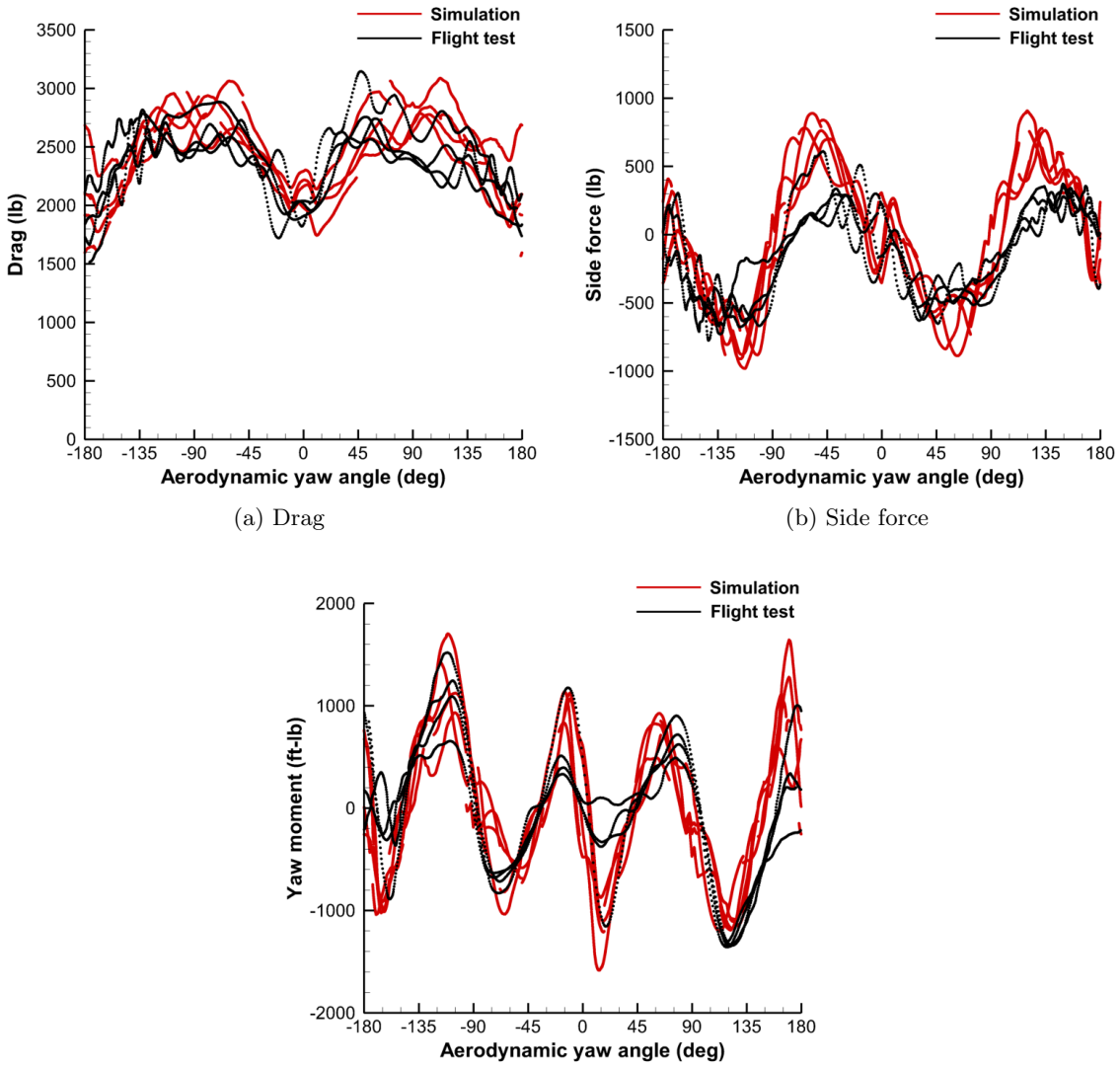

(a) Drag

(b) Side force

(c) Yaw moment

Figure 58: Comparison of forces and moments versus yaw angle, 112 knots (Flight 134 Record 8).

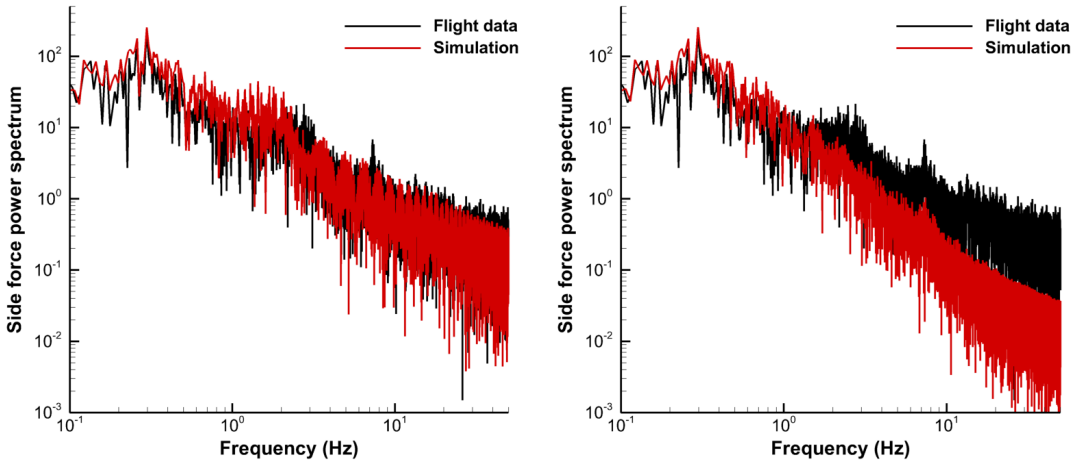

(a) Shedding model on

(b) Shedding model off

Figure 59: Fast Fourier Transforms of side force, 112 knots (Flight 134 Record 8).

function in MATLAB has been employed for this purpose. Figure 59 illustrates the power spectrum of side force from the flight test and simulation. This figure demonstrates that the fluctuations from the shedding model possess similar frequency content to actual flight test data. When the shedding model is disabled, as in Fig. 59(b), the higher-frequency content on the order of the vortex shedding frequency tends to be under-predicted. The same trend persists for the other forces and moments, which are not included here, though for this flight record the higher-frequency content of the yaw moment is over-predicted when the shedding model is activated.

6.4.2 Assessment of Unsteady Aerodynamics

The reduced-order aerodynamic predictions at a flight speed of 112 knots (Flight 134 Record 8) are quite satisfactory, as demonstrated in the previous section. However, the reduced frequency, k, in this case is only 0.02 when the mean yaw rate (given in Table 10) is applied as ω, $L/2$ as the reference length, and the mean airspeed as U_∞. In the other flight records, the spin rate is higher and the airspeed lower, resulting in a higher reduced frequency. For example, the reduced frequency is 0.1 at 55 knots (Flight 132 Record 2) and 0.08 at 86 knots (Flight 132 Record 6). To assess the unsteady aerodynamic model, Fig. 60 presents the yaw moment as a function of yaw angle for these three cases. The unsteady results

are compared with the flight test data, and model predictions with the RT Jones unsteady aerodynamics disabled (quasi-steady aerodynamics) are also included for reference.

Figure 60 clearly illustrates that in all cases (even at a reduced frequency of 0.02) the quasi-steady prediction of yaw moment magnitude is larger than the measured value. Inclusion of the unsteady model reduces the peaks in yaw moment and generally results in better agreement with the flight test data. The error in peak yaw moment is typically less than 25%, though there are still some unexpected behaviors, particularly around a yaw angle of 0°, that are not currently captured by the model. The phase lag of the unsteady model prediction relative to the quasi-steady data is accurate at low reduced frequency, with an average phase error of 4°. As the reduced frequency increases, the phase lag is under-predicted, with an average error of 8° at a reduced frequency of 0.08 and 17° at a reduced frequency of 0.1. This result suggests that the phase response of the RT Jones model is too mild for bluff body flows. The relation of this deficiency to the dynamic behavior is discussed in the following sections.

Though models suited to bluff body flows have been developed in the past [1, 65, 11], these have typically relied on the system identification approach, making them applicable to only a specific configuration and requiring a new model at each flight speed and yaw rate. For future improvements to the current unsteady model, it is recommended to modify the RT Jones transfer function in the reduced frequency domain so that a more general model is developed that scales with load size, flight speed, and yaw rate. Ideally, a single model would be sufficient for a wide range of bluff body types, but it is not currently known whether a universal model is possible. However, it will be demonstrated in the following sections that the current reduced-order model is capable of predicting tethered load stability in the low speed cases as well as the onset of instability at high speed. Therefore, for the purpose of this work, it is not considered crucial to accurately reproduce the phase lag at higher reduced frequencies on the order of 0.1, but sensitivity to the unsteady model for the unstable case will nonetheless be discussed in the following sections.

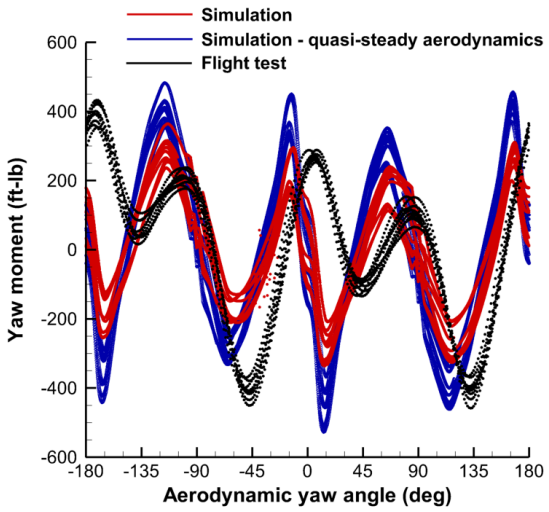

(a) 55 knots, $k = 0.1$

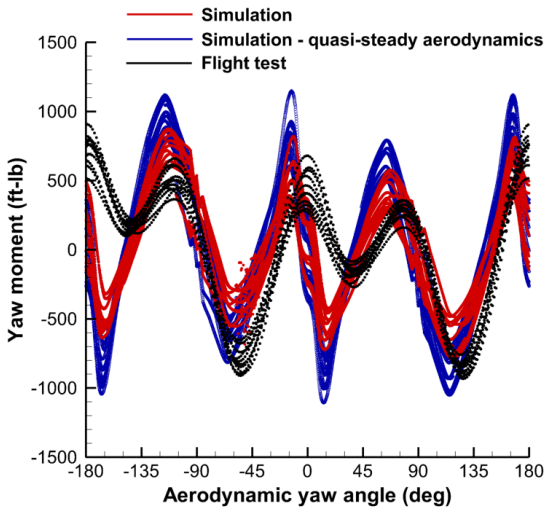

(b) 86 knots, $k = 0.08$

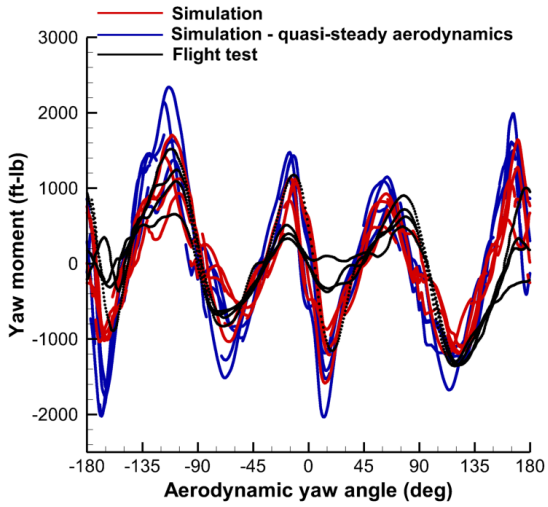

(c) 112 knots, $k = 0.02$

Figure 60: Comparison of yaw moments for different flight speeds and reduced frequencies.

6.4.3 Coupled Helicopter-Load Simulations

Simulations have been performed, corresponding to each of the flight record numbers listed in Table 10, with the reduced-order model to assess its effectiveness for tethered load stability analysis. To ensure that the conditions are as consistent as possible between the flight test and the simulation, the recorded position of the hook below the helicopter has been applied as a prescribed input for the simulation. The position, orientation, velocity, and angular rates from the beginning of the flight record are applied as the initial conditions, and both the aerodynamics and dynamic response of the load are subsequently simulated. Thus, these simulations include the influence of helicopter dynamics on the tethered-load subsystem, though any coupling acting in the opposite direction is neglected, as the helicopter's motion is prescribed to match the flight test data.

Figures 61 and 62 depict the cable angles and yaw rate time histories for flight speeds of 105 and 112 knots, respectively. These speeds were just below and just above the stability boundary in the flight tests. At 105 knots, the tethered load dynamics are considered stable, as the excursions of both the longitudinal and lateral cable angles from their mean values are within manageable levels. The mean yaw rate per revolution remains fairly constant throughout the flight. The sudden increase in the lateral cable angle during the last portion of the flight is due to the fact that the helicopter is executing a right turn, not because of instability. The reduced-order model's predicted response of this complex six-degree-of-freedom, coupled, nonlinear system is very good; the mean cable angles differ from the flight test data by a few degrees, and the magnitudes of oscillations about the mean value are within a degree of the measured values. The difference in mean cable angles relative to flight data is likely due to differences in the magnitudes of aerodynamic forces. The magnitudes of oscillations about the mean value are of greater importance, as they indicate the level of tethered load stability or instability.

The load dynamics at 112 knots (Fig. 62) are starkly different from those at 105 knots, despite the fact that the airspeed has only been increased by 7 knots. Both the longitudinal and lateral cable angle excursions become very large, with flight test deviations from the mean in excess of 20° for longitudinal (θ_c) and 15° for lateral (ϕ_c) angle. The reduced-order

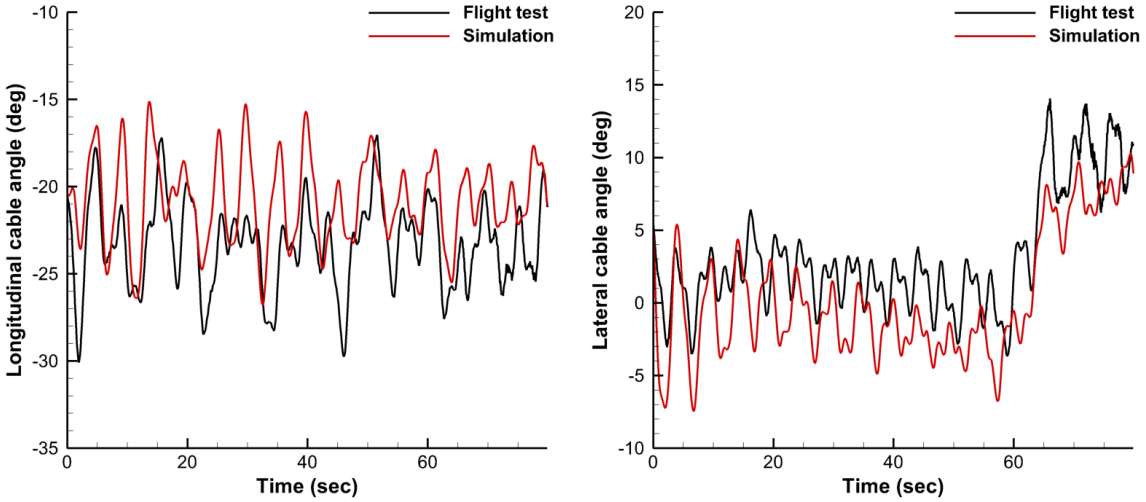

(a) Longitudinal (θ_c)

(b) Lateral (ϕ_c)

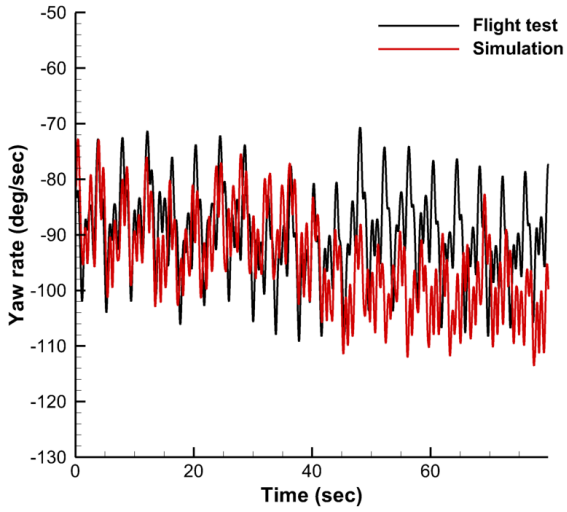

(c) Yaw rate

Figure 61: Cable angles and yaw rate at 105 knots (Flight 132 Record 10a).

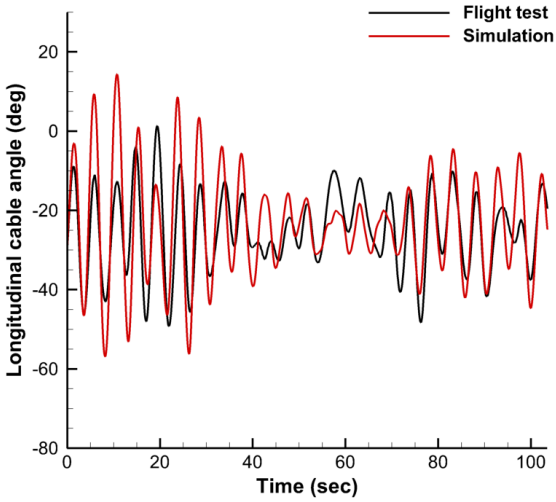

(a) Longitudinal (θ_c)

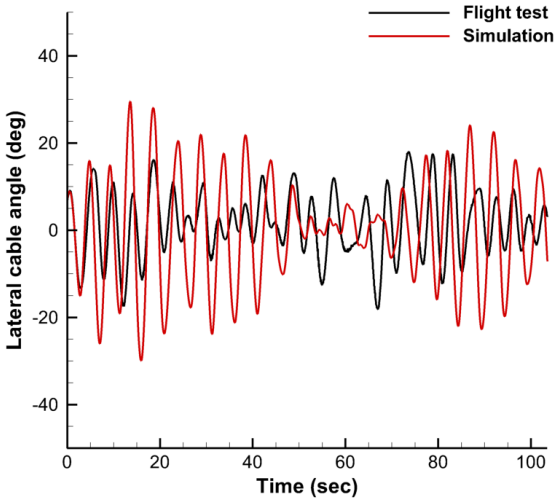

(b) Lateral (ϕ_c)

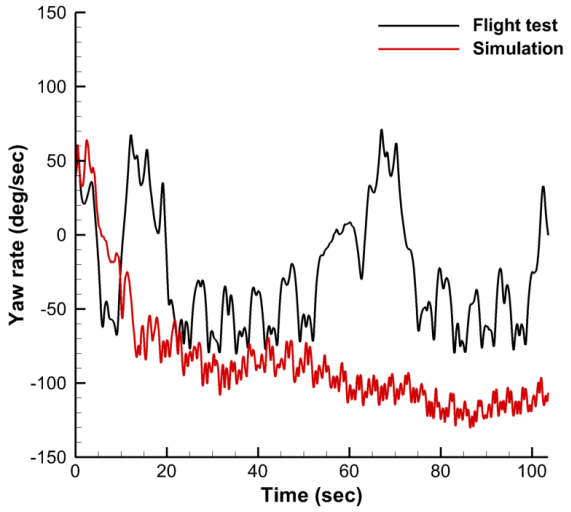

(c) Yaw rate

Figure 62: Cable angles and yaw rate at 112 knots (Flight 134 Record 8).

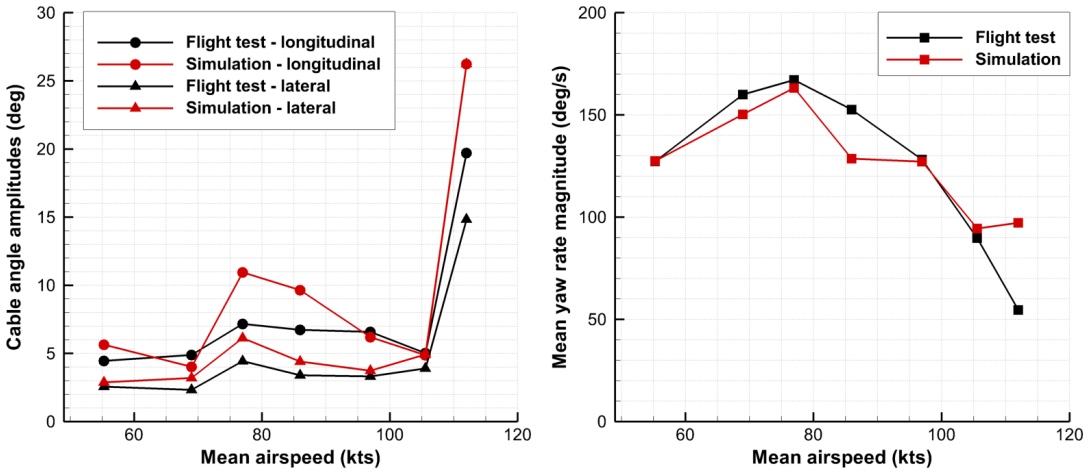

(a) Cable angle excursions

(b) Mean spin rate

Figure 63: Cable angle excursions and mean spin rate as a function of flight speed.

model captures the same behavior; these excursions are sometimes over-predicted relative to the flight data. However, this result is considered acceptable since it is more conservative than the measured response (i.e., the simulation predicts a more unstable behavior than was observed in the flight test). In the flight test, the spin rate is also unstable, with multiple reversals and a reduced mean rate compared to the lower flight speed. While the reduced-order model does capture a spin rate reversal near the beginning of the flight record, the load eventually settles into a more steady spin rate than in the flight test. This may be due to rotor downwash or other uncertainties, and the sensitivity of the spin rate to such factors will be evaluated in Chapter 7.

Despite the large peak yaw moments in excess of 1500 ft-lb at the higher flight speeds (see Fig. 58(c)), the total torque, or cycle-averaged yaw moment, is only 6.3 ft-lb to sustain the spinning motion in the simulation at 105 knots. Cone [65] also observed that a similar amount of torque was required in flight tests of a 4000-lb CONEX at comparable flight speeds. Therefore, by supplying this small opposing torque via a spread attachment method, the spinning motion may be stabilized. An example of this stabilization approach is described later in this thesis in Section 6.5.

Figure 63 depicts the cable angle angle excursions and mean yaw rate for all the flight records. Since the magnitude of cable angle deviations from the mean values changes

throughout both the flight data and simulation results (due to the helicopter dynamics and the nonlinear, highly-coupled response of the tethered load), the amplitudes in Fig. 63(a) have been computed as twice the standard deviation of each angle over the entire time history. This figure illustrates what is meant by dynamic stability; the cable angle excursions suddenly become very large at 112 knots. At most flight speeds, the reduced-order model over-predicts the magnitudes of both angles, but not by an amount that would indicate the wrong stability behavior. The longitudinal angle is over-predicted by 18% on average, while the lateral angle is over-predicted by 33%. These percentages may seem large, but the measured angles in flight test for the stable cases are between 0 and 7 degrees, so the 33% lateral angles mismatch amounts to a difference of only 1–2 degrees.

What is more important than the exact magnitudes of the errors is that not only are the correct trends predicted by the model, but the onset of instability is also correctly captured. These results are quite promising, as they demonstrate the the model is capable of meaningful assessments of stability for this complex system. As shown in Fig. 63(b), the yaw rate prediction is accurate at some flight speeds, but not all. In many of the simulations, a steady mean value is not reached by the end of the simulation or flight record. For example, in Fig. 61(c), the yaw rate magnitude is still slowly increasing at the end of the simulation. These discrepancies in the yaw rate are hypothesized to be due in large part to the phase response of the yaw moment, which has been observed to be sensitive to unsteady effects (see Section 6.2 and Refs. [1, 65, 11]).

6.4.4 Quantifying Stability

In Section 6.4.3 it was demonstrated that the reduced-order model is capable of predicting the onset of tethered load instability. However, the definition of instability remains a heuristic one, as experience is required to determine whether particular load motion characteristics are too dangerous to fly. Recently, there have been some efforts to quantify tethered load stability. For example, Nyren et al. [19] integrated the cable forces in the frequency domain to develop a "stability coefficient" that correlated well with qualitative descriptions of tethered load stability from pilot interviews. A similar process has been performed here,

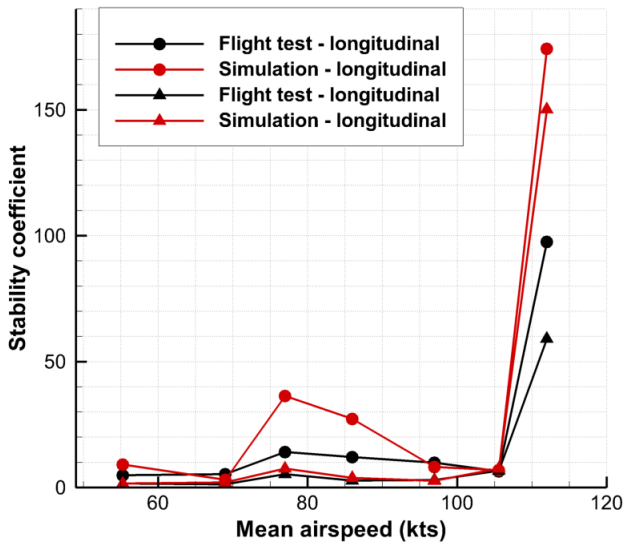

Figure 64: Integrated power spectral density of cable angles as a function of flight speed.

albeit with the power spectral density of the cable angles integrated instead of the cable forces. The result of this analysis is presented in Fig. 64 for each flight speed.

The behavior of the stability coefficient in Fig. 64 is very similar to the cable angle excursion amplitudes in Fig. 63(a). In both the flight test and simulation, the longitudinal stability coefficient is larger than the lateral one, and the simulation is conservative in that these quantities are typically larger in the simulation than in the flight test. Most importantly, the large and sudden increase at 112 knots is also present, which indicates instability. As the trends in this stability coefficient are very similar to the cable angle excursions themselves, this quantity does not offer any additional information, but it does provide an additional indication of the unstable flight speed. Therefore, in simulations and experiments in which the cable angle excursions are readily available, they can be used directly to effectively quantify the instability. Alternatively, in experimental and flight tests where the cable forces are measured but not the cable angle excursions themselves, this stability coefficient may be used as an indicator of stability.

6.4.5 Effect of Vortex Shedding

The influence of vortex shedding on tethered load dynamics has been evaluated for the unstable flight test at 112 knots by performing an additional simulation with vortex shedding

fluctuations removed from the reduced-order model.

Figures 65(a) and (b) depict the longitudinal and lateral cable angles, respectively. For the sake of clarity, the flight test data are not included. However, recall that the reduced-order model overpredicted the cable excursions in this case (see Fig. 62). When the vortex shedding fluctuations are omitted from the model, the cable angle excursions are even more extreme. Both the lateral and longitudinal angle excursions are in excess of 40° from the mean. While this prediction is still conservative in that the excursions are larger than in the flight test, it is less accurate than the standard reduced-order model with vortex shedding effects included. The influence on yaw rate can be observed in Fig. 65(c). Here, the case without vortex shedding is also less realistic, because it does not include a spin direction reversal. The final spin rate magnitude is similar to, but more steady than, the result with vortex shedding. This demonstration reveals that vortex shedding has a non-negligible effect on bluff body dynamics, and the model predictions are more accurate when vortex shedding is included.

6.4.6 Virtual Wind Tunnel Evaluations

In the assessment thus far, the reduced-order model has been validated directly from flight test data. Cicolani et al. [11] raised the importance of modeling the vehicle/attachment dynamics coupling with tethered load dynamics. Their joint analysis, performed in a wind tunnel whose configuration was carefully scaled and modeled to mimic known flight test hardware and conditions, appeared to minimize these modeling uncertainties for the configurations that they examined. However, the potential influence of wind tunnel walls during the dynamic tests, the lack of helicopter degrees of freedom, the absence of atmospheric turbulence, and difficulties in accurately reproducing the cable attachment in a geometrically scaled test may add bias to the wind tunnel tests. In that analysis, it was found that wind tunnel tests were sometimes able to capture the correct unstable flight speed, but in other cases they were too conservative, resulting in stable spinning behaviors with small cable angle oscillations while the load became unstable in flight tests. The absence of helicopter degrees of freedom was cited as the main source of inaccuracy.

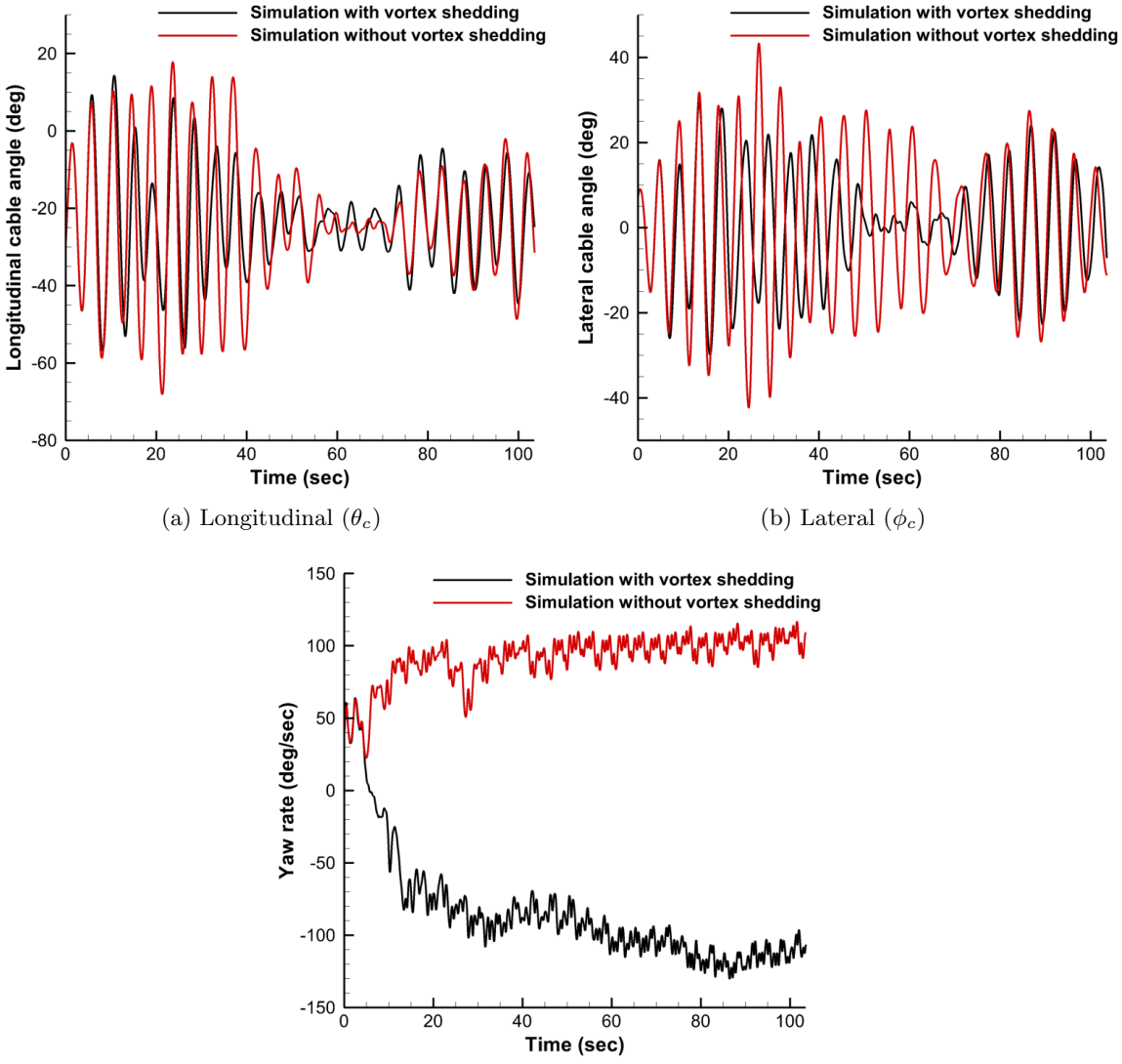

(a) Longitudinal (θ_c)

(b) Lateral (ϕ_c)

(c) Yaw rate

Figure 65: Cable angles and yaw rate at 112 knots (Flight 134 Record 8): simulated results with and without vortex shedding.

As the present reduced-order model correlates well with flight test data with vehicle dynamic coupling included, its ability to predict the same conditions, without this coupling, is evaluated. This type of evaluation is referred to as a "virtual wind tunnel" environment, as it mimics dynamic testing in wind tunnels (albeit without the inclusion of blockage or wall effects). The cases from Table 10 have been simulated with a fixed hook position and constant freestream speed, which is comparable to wind tunnel testing. The expected mean longitudinal cable angle and yaw rate are applied as the initial conditions, while the other Euler angles, velocities, and angular rates are initially set to zero. All other conditions in the numerical analysis are identical. This approach permits a "deconstruction" of the system, allowing the competing errors to be isolated.

Figure 66 depicts the cable angles and yaw rates during the first 60 seconds of simulation for wind speeds of 105 and 112 knots, which were also studied as part of the flight test comparisons in Fig. 61 and 62. Figure 66(a) shows the result at 105 knots. The behavior is similar to the flight test comparison, as relatively small cable angle oscillations are present in both the lateral and longitudinal directions. The yaw rate magnitude also gradually increases, as was observed in the flight test simulation. Though only the first 60 seconds are shown in this figure, there is no sudden increase in the lateral cable angle as in the flight test, which resulted from the helicopter turning. When the simulation is allowed to continue for 150 seconds, the yaw rate reaches an average magnitude of 130 deg/sec and the cable angle oscillation magnitudes are decreased somewhat compared to what is observed during the first 60 seconds in Fig. 66(a).

The simulation results at 112 knots are presented in Fig. 66(b). As in the flight test, both the lateral and longitudinal cable excursions are large during the first 40 seconds of the simulation. During this time period, the yaw rate changes direction multiple times before eventually producing a relatively steady spin, which also occurred in the flight test simulation. If the simulation is allowed to continue for 150 seconds, the yaw rate increases to 110 deg/sec and the cable angles stabilize. Similar spinning behavior occurred in the flight test comparison (Fig. 62(c)), but in that case the cable angle excursions remained large at the end of the 104-second simulation as opposed stabilizing after approximately 60

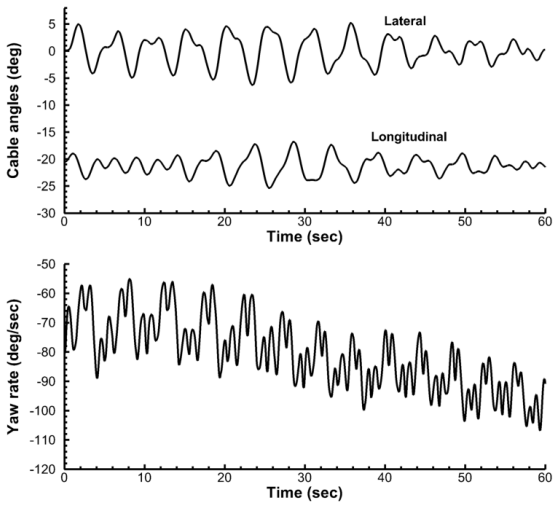

(a) 105 knots

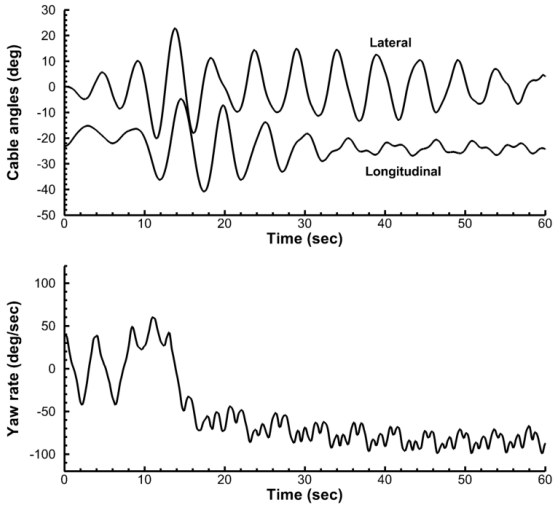

(b) 112 knots

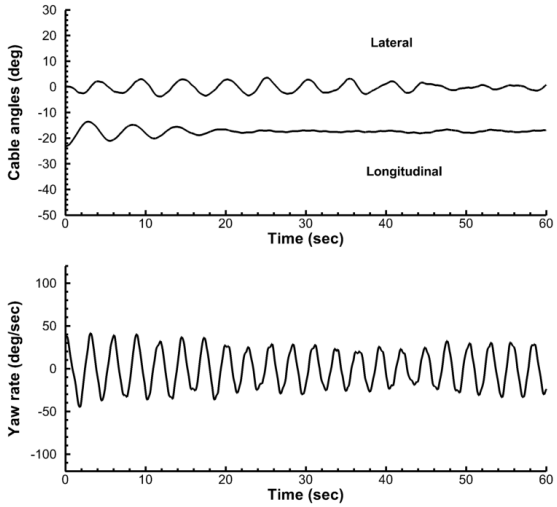

(c) 112 knots, quasi-steady

Figure 66: Cable angles and yaw rates for selected simulations in a virtual wind tunnel.

seconds. Though the results of each flight speed are not included here, all display similar behavior, as initial transients die out and only small oscillations persist after approximately 50 seconds.

To illustrate the importance of unsteady aerodynamics, the same case has been evaluated with the unsteady RT Jones model disabled, and the results are presented in Fig. 66(c). With the quasi-steady approach, the cable angle excursions remain much smaller and become very nearly zero after a relatively short time. The yaw rate settles on a steady oscillation about zero, indicating that the spinning behavior is absent. Thus, it is reinforced that bluff body dynamic behavior is sensitive to unsteady aerodynamics, and quasi-steady aerodynamic models fail to capture the instability. The same behavior has been observed in comparisons with high-fidelity simulations in Section 6.2. Despite the fact that the spinning flight results at this speed correspond to a reduced frequency of only 0.02, and the quasi-steady aerodynamics are close in phase to the measured aerodynamics in flight at this speed (see Fig. 60(c)), the dynamic results are still highly sensitive to unsteady aerodynamics.

Several conclusions can be drawn from these virtual wind tunnel tests:

1. The yaw rate in the virtual wind tunnel does not always match the behavior in flight test. This discrepancy may be related to the fact that the swirling helicopter wake, which influences the tethered load spin during takeoff, is not currently included in the simulation, nor are ambient wind, atmospheric turbulence, and helicopter dynamics.

2. The cable angle excursions are smaller when the motion of the helicopter is not included in the simulation. Though the yaw behavior clearly plays a role, the large cable angle excursions damp out in the virtual wind tunnel simulation at 112 knots, while they remain large in the flight test simulation despite similar yaw rate behavior. Therefore, coupled helicopter-load oscillations exacerbate instability, and a wind tunnel test or virtual wind tunnel simulation is likely to overestimate the flight speed when instabilities of this nature are encountered. Similar results have been found in physical wind tunnel tests [11].

3. In addition to the helicopter degrees of freedom, tunnel blockage and wall effects for

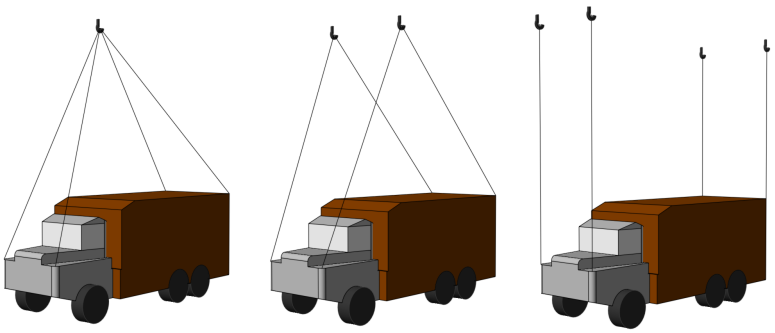

Figure 67: Illustration of single, two point, and four point suspensions.

dynamic tethered load configurations are likely to play a role in the stability of the tethered load [66], while accurate modeling of the wind is also important, as will be discussed in Chapter 7.

Based on the findings of these evaluations, it is recommended that simulations for the purpose of tethered load stability analysis include both the helicopter degrees of freedom and realistic atmospheric turbulence.

6.5 Extension to Complex Bluff Bodies

Most of the tethered loads studies published to date have focused on canonical bluff body configurations, such as box (CONEX) and cylindrical (engine canister) tethered loads. This focus is due to the prevalence of these shapes in a number of different applications and to the lack of available quasi-steady data for more complex bluff bodies. Liu [99] developed an analytical method based on a combination of slender body theory and viscous cross-flow theory to estimate the quasi-steady forces and moments for trucks and other complex geometries. While this analytical method only approximates bluff body behavior, it can provide an appraisal of the reduced-order model's ability to predict dynamic behavior of complex geometries and to analyze basic trends. Experimental or computational data can subsequently replace the analytical approximation to improve the dynamic predictions.

The truck was analyzed with three different tether arrangements, which are illustrated in Fig. 67. They are referred to as *single-point*, *two-point*, and *four-point* suspensions, respectively. The truck is modeled as full-size, with a length of 23 feet and a weight of 13,700 lbf. Liu [99] noted that the truck, as well as other complex bluff bodies including

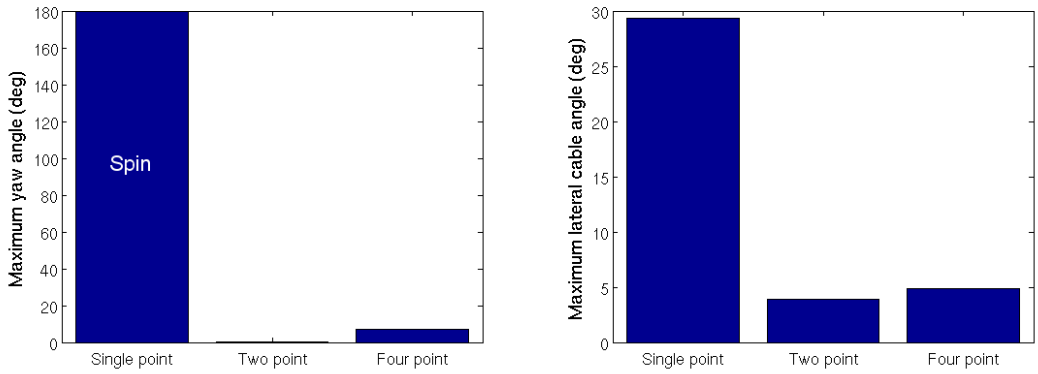

(a) Maximum yaw angle

(b) Maximum lateral cable angle

Figure 68: Evaluation of various suspension types in stabilizing a truck tethered load.

tanks, is unstable in yaw at a flight speed of 150 knots with the single-point suspension, but it is effectively stabilized by moving to a spread attachment approach like the two-point suspension. The same stabilization technique has also been successful in dynamic wind tunnel tests of various other types of tethered loads [98, 114].

Reduced-order simulations of the truck reproduce similar dynamic behavior to that observed in experimental tests at 150 knots. With the single-point suspension, the truck begins spinning and exhibits large cable excursions. Modifying the tether arrangement to either the two-point or four-point configuration successfully stabilizes the tethered load by eliminating spinning behavior and significantly reducing the maximum cable angle excursions. The maximum yaw angles and lateral cable angles from the simulations are compared in Fig. 68. While both the two-point and four-point suspensions stabilize the tethered load, the two-point suspension is the most effective. As the reduced-order model is able to replicate the observed behavior from the experiment with the simple quasi-steady analytical model, this result demonstrates its potential for extension to new configurations and evaluating proposed stabilization techniques.

CHAPTER VII

SENSITIVITY ANALYSIS

7.1 Computational Fluid Dynamics Sensitivities

7.1.1 Grid Convergence

While comparisons with wind tunnel data have confirmed that accurate integrated loads are obtained for the rectangular prism on 3.5-million node grids, a grid convergence study is necessary for the circular cylinder. This necessity arises both from the fact that the separation point on the curved face must be accurately resolved and that less validation data are available for the finite cylinder over the complete range of yaw angles. Grid sensitivity of the cylinder configurations has been evaluated by comparison of the forces and moments on grids with various levels of refinement at low yaw angles, where the sensitivity is expected to be highest. The Reynolds number for the grid sensitivity study is 3.2 $\times 10^5$, which is between the low and high range of Reynolds numbers investigated. The aspect ratio of the cylinder is 1.0 for this study. Two different refinement techniques have been applied:

1. uniform refinement, and

2. feature-based adaptation based on vorticity magnitude.

Feature-based adaptation capability has been introduced in FUN3D for overset grids by Shenoy et al. [84, 85]. In this technique, flow features of interest (such as separated shear layers and shed vortices) can be resolved while reducing the number of grid points in regions of smooth flow. The baseline grid contains 3.7 million nodes, which is roughly the same as the rectangular prism grids, while the finest grid has 8.5 million nodes. In both the feature-based and uniform refinement approaches, the node count has been increased by clustering points near the surface and in the wake. Illustrations of the uniformly-refined grids are included in Figs. 11(a) and (b). Figures 69(a) and (b) present similar depictions of the cylinder grids after one and two cycles of feature-based refinement, respectively. These

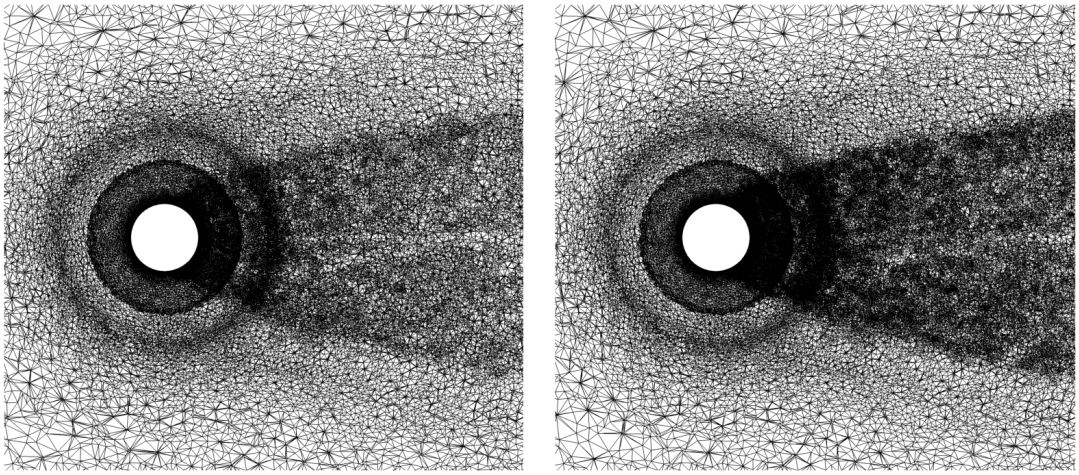

(a) First adaptation (5.5 million nodes) (b) Second adaptation (8.5 million nodes)

Figure 69: Side views of cylinder grids refined via feature-based adaptation.

grids have been refined by tracking the vorticity magnitude over enough time steps to resolve several cycles of vortex shedding, and subsequently the adaptation algorithm refines and coarsens the grid selectively based on this vorticity magnitude "metric." As is apparent in Fig. 69, this approach is effective in clustering grid points in the wake region between the two separated shear layers where vorticity magnitude is large. The figure also shows that the algorithm is able to traverse overset boundaries effectively.

Figure 70 presents the results of the grid sensitivity study. Increasing the mesh node count tends to reduce drag, and the 5.5-million node grid is within 5% the drag of the finest grid. The drag coefficient at a yaw angle of zero is approximately 0.5, which is slightly lower than the transitional value of 0.56 in Fig. 13(a) but higher than the supercritical value of 0.37. The Reynolds number, 3.2×10^5, is also between the transitional value of 0.96×10^5 and the supercritical value of 1.0×10^6. These results indicate that the flow behavior is also transitional at this Reynolds number. Increasing the yaw angle from zero initially has only a small effect on the drag, but beyond a yaw angle of five degrees, the drag starts to increase more rapidly, as was observed in Fig. 15(a).

The side force behavior in Fig. 70(b) is more sensitive to grid refinement than the drag, at least between the coarsest grid with 3.7 million nodes and the finer grids. The coarsest grid predicts an incorrect trend in side force between yaw angles of 0° and 2.5°; on the

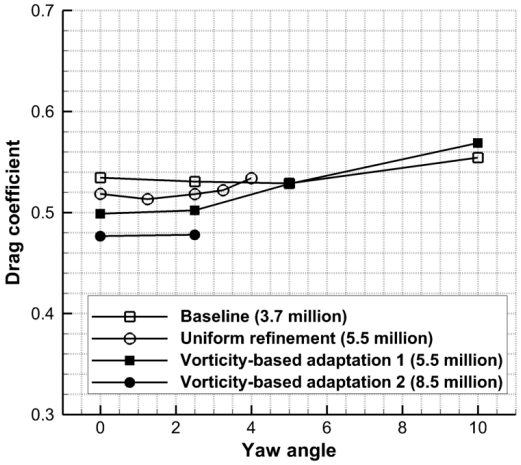

(a) Drag coefficient

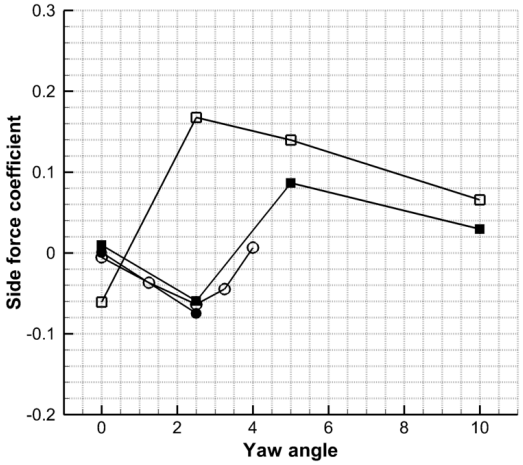

(b) Side force coefficient

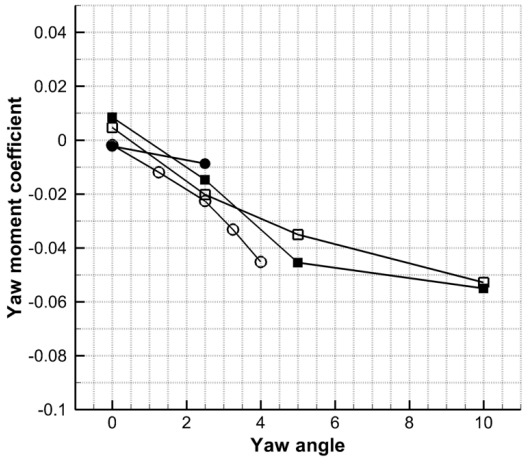

(c) Yaw moment coefficient

Figure 70: Grid sensitivity study, cylinder with an aspect ratio of 1.0 at low yaw angle and a Reynolds number of 3.2×10^5.

coarsest grid the side force is positive at a yaw angle of 2.5°, while it is negative on the finer grids. The side force at a yaw angle of zero is also further from the expected value of zero (based on geometric symmetry) on the coarsest grid. Zdravkovich et al. [9] have indicated that such asymmetric behavior also occurs in wind tunnel testing due to the fact that the three-dimensional vortex shedding pattern is bi-stable at very low yaw angles. Furthermore, it was found that this asymmetry may switch directions from one trial to another and is presumably sensitive to small asymmetries in geometry (i.e., surface roughness) or ambient conditions. In the case of numerical experiments, the unstructured grid may provide similar small asymmetries. In the present sensitivity analysis, increasing the grid resolution moves the mean side force at a yaw angle of zero closer to the value of zero, indicating that this asymmetric behavior is minimized. However, asymmetric flow patterns were still observed in refined-grid evaluations in Section 3.3 at a supercritical Reynolds number of 1.0×10^6 for the cylinder with an aspect ratio of two, which is evidenced by the side force at a yaw angle of zero in Figs. 15(b) and (c). In terms of the side force, all of the finer grids with node counts of 5.5 million or above offer comparable results.

The yaw moment is similar among all grids evaluated. The yaw moment trends are the same for all grids evaluated, and the variation amongst the different cases is less than the variation in drag coefficient. Drawing from the results of the grid sensitivity analysis, the final grid node counts are in the range 6.5 - 8 million, as discussed in Section 3.2, but vary based on the Reynolds number and aspect ratio. This level of grid refinement is expected to produce the correct side force and yaw moment trends while also remaining within a few percent of the grid-converged drag. This range (6.5 - 8 million nodes) is also somewhat finer than the previous computations by Lynch and Smith [8] at a Reynolds number of 3900. Though feature-based adaptive refinement has been applied for some of the grids in the grid refinement study, uniform refinement has been leveraged to generate the final grids, as the adaptation needs to be performed at each yaw angle to account for changing shear layer behavior.

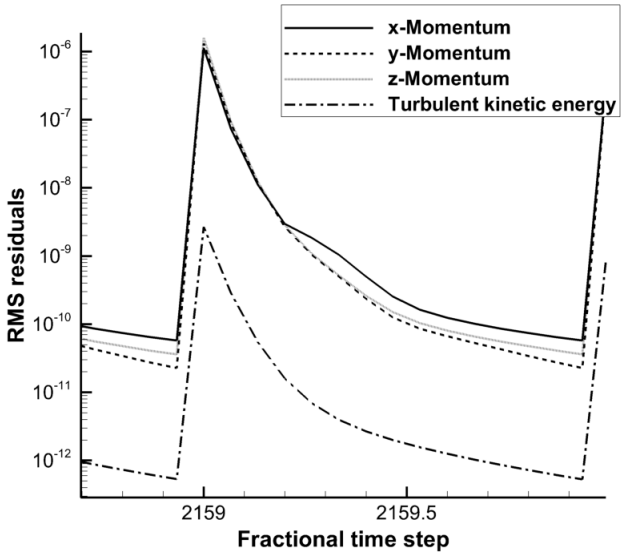

Figure 71: Typical convergence of momentum and turbulent kinetic energy RMS residuals.

7.1.2 Temporal Convergence

As bluff body flows are highly unsteady, time-accurate computations are required. FUN3D applies a backwards differentiation scheme to achieve time accuracy between second-order and third-order. The form of this scheme is given by Eq. 26 (see Biedron et al. [77]):

$$\frac{V}{\Delta t}\left(\theta_{n+1}\mathbf{Q}^{n+1} + \theta_n\mathbf{Q}^n + \theta_{n-1}\mathbf{Q}^{n-1} + \theta_{n-2}\mathbf{Q}^{n-2}\right) = \mathbf{R}^{n+1}. \tag{26}$$

Here, V is the cell volume, n is the physical time level, Δt is the physical time step size, $\mathbf{Q}$ is the vector of conserved variables, $\mathbf{R}$ is the residual vector, and θ are the backwards differentiation coefficients. Since $\mathbf{R}^{n+1}$ is not known, it is typically evaluated using a Taylor-series linearization of the form

$$\mathbf{R}^{n+1} \approx \mathbf{R}^n + \frac{\partial \mathbf{R}^n}{\partial \mathbf{Q}^n}\left(\mathbf{Q}^{n+1} - \mathbf{Q}^n\right), \tag{27}$$

and the term $\left(\mathbf{Q}^{n+1} - \mathbf{Q}^n\right)$ is abbreviated as $\Delta\mathbf{Q}^n$. However, this linearization introduces error into the scheme, and furthermore, approximations are typically applied in evaluating $\frac{\partial \mathbf{R}^n}{\partial \mathbf{Q}^n}$, resulting in additional error. These errors can be eliminated by introducing an additional term, known as a pseudo time term, into Eq. 26, as described in Ref. [77]:

$$V\frac{\partial \mathbf{Q}}{\partial \tau} + \frac{V}{\Delta t}\left(\theta_{n+1}\mathbf{Q}^{m+1} + \theta_n\mathbf{Q}^n + \theta_{n-1}\mathbf{Q}^{n-1} + \theta_{n-2}\mathbf{Q}^{n-2}\right) = \mathbf{R}^{m+1}, \tag{28}$$

where τ is known as the pseudo time, and m represents the pseudo time level. Within each physical time step, a number of pseudo time steps are performed. Provided the pseudo time stepping process is convergent, the term $\frac{\partial \mathbf{Q}}{\partial \tau} \rightarrow 0$, indicating that the original scheme in Eq. 26 is recovered, and $\mathbf{R}^{m+1} \rightarrow \mathbf{R}^{n+1}$, thus eliminating any linearization errors and ensuring design-order temporal accuracy. As the pseudo time stepping procedure only needs to be convergent, a simple first-order discretization can be applied to the operator $\frac{\partial \mathbf{Q}}{\partial \tau}$:

$$\frac{\partial \mathbf{Q}}{\partial \tau} \approx \frac{\mathbf{Q}^{m+1} - \mathbf{Q}^{m}}{\Delta \tau} \equiv \frac{\Delta \mathbf{Q}^{m}}{\Delta \tau}, \tag{29}$$

where $\Delta\tau$ is the pseudo time step size. Substituting Eqs. 27 and 29 into Eq. 28, the resulting scheme is given by

$$\left[\left(\frac{V}{\Delta \tau} + \frac{V\theta_{n+1}}{\Delta t}\right)\mathbf{I} - \frac{\partial \mathbf{R}^{m}}{\partial \mathbf{Q}^{m}}\right]\Delta \mathbf{Q}^{m} = \mathbf{R}^{m} - \frac{V}{\Delta t}\left(\theta_{n+1}\mathbf{Q}^{m} + \theta_{n}\mathbf{Q}^{n} + \theta_{n-1}\mathbf{Q}^{n-1} + \theta_{n-2}\mathbf{Q}^{n-2}\right). \tag{30}$$

Unlike steady simulations, convergence of time-accurate computations does not imply that the residual approaches machine zero during the pseudo time stepping process. Rather, when $\Delta\mathbf{Q}^{m} \rightarrow 0$, $\mathbf{R}^{m} \rightarrow \frac{V}{\Delta t}\left(\theta_{n+1}\mathbf{Q}^{n+1} + \theta_{n}\mathbf{Q}^{n} + \theta_{n-1}\mathbf{Q}^{n-1} + \theta_{n-2}\mathbf{Q}^{n-2}\right)$, which depends on Δt and represents the change in the flow solution during the physical time step from t^{n} to t^{n+1}. Here, 15 – 20 subiterations were applied with a CFL number of 35 – 50 to ensure that the RMS residuals of momentum and turbulent kinetic energy coverged at least three orders of magnitude and leveled out when plotted on a semi-log scale. Typical convergence of these residuals during a time step is illustrated in Fig. 71. This figure depicts the residuals for the cylinder with an aspect ratio of 1.0 at a Reynolds number of 0.96×10^{5}, but it was observed that the number of subiterations and CFL number for temporal convergence did not change significantly across the different cases and flow conditions evaluated.

7.1.3 Sensitivity to Mounting Apparatus

The configurations evaluated in this thesis are canonical, meaning that uncertainties due to surface imperfections, geometric errors (i.e., out-of-roundness for a circular cylinder), and wind tunnel mounting hardware are omitted from the simulations. However, one of the

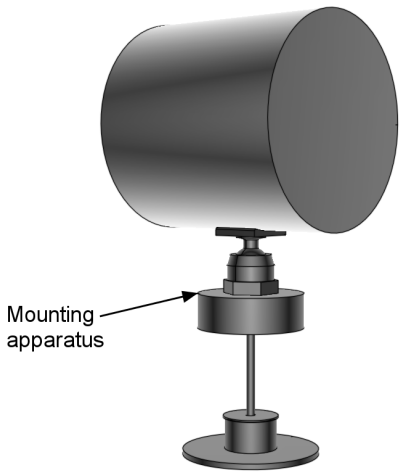

Figure 72: Cylinder with an aspect ratio of 1.0 with wind tunnel test mounting apparatus.

benefits of the numerical experiment approach is that such uncertainties can be isolated and quantified. For example, the resulting flow fields and integrated loads for a clean geometry can be compared to one with the mounting apparatus included to assess its sensitivity.

Figure 72 depicts an otherwise clean cylinder with aspect ratio $L/D = 1.0$ mounted on a particular wind tunnel test apparatus. This mount is relatively large in comparison to the size of the cylinder and is expected to influence the separation point on the bottom surface while also shedding large turbulent vortices, since the mount itself is a bluff body. This is the mounting apparatus that was used in the wind tunnel tests by Mantri et al. [5] for the CONEX rectangular prism (see Fig. 12). Though no formal sensitivity analysis to the mount has been performed for the rectangular prism, the sensitivity is expected to be less than it is for the cylinder due to the fixed separation points on the rectangular prism. The present numerical study was performed in part to guide future experiments for the circular cylinder, and from this analysis it was determined that a new mount was required.

Simulations have been performed for this cylinder at a yaw angle of 40° and a Reynolds number based on diameter of 3.2×10^5. Time-averaged drag, side force, and yaw moment coefficients are compared in Fig. 73 for simulations with and without the mounting apparatus. The drag coefficient was increased by 6% when the mount is included. The mount also affects the side force and yaw moment, as for both of these variables the sign was reversed

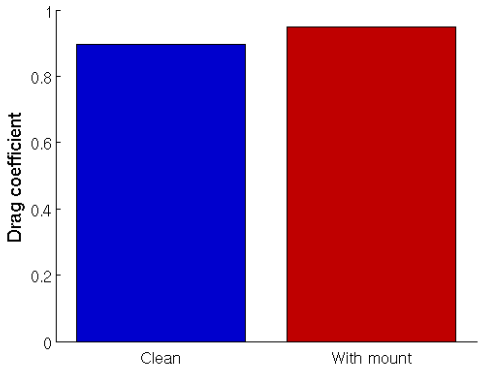

(a) Drag coefficient

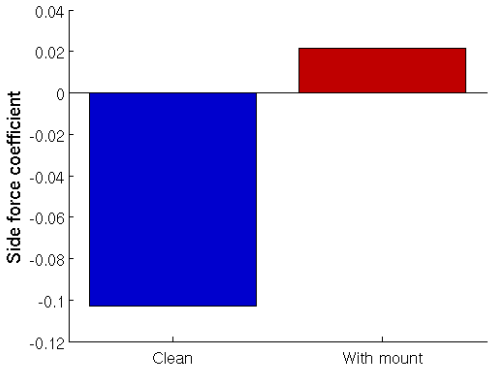

(b) Side force coefficient

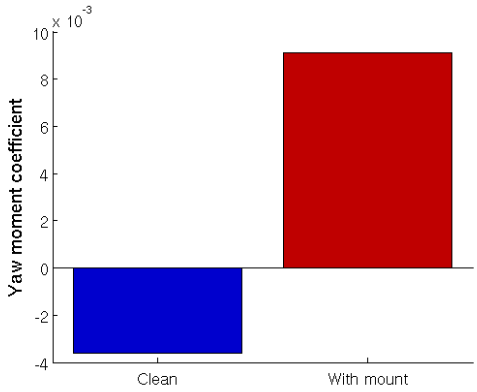

(c) Yaw moment coefficient

Figure 73: Sensitivity to large wind tunnel mount, aspect ratio of 1.0, yaw angle of 40°, Reynolds number based on diameter of 3.2×10^5.

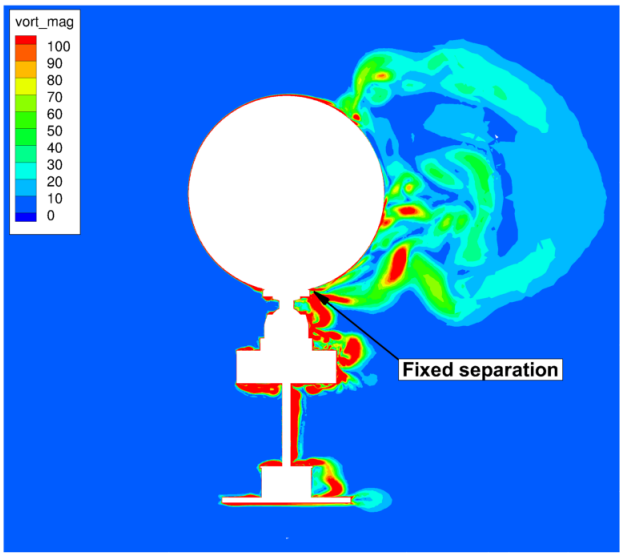

Figure 74: Influence of mounting apparatus on separation point and vortex shedding (countours of normalized vorticity magnitude).

when the mount was included. Figure 74 illustrates the normalized vorticity magnitude in a slice of the flow field at a particular instant in time. Here, it is shown that the mount induces an artificial separation point on the bottom surface of the cylinder. This separation point is further upstream than than separation on the top surface, which experiences free separation. Thus, a greater portion of the lower surface is experiences separated flow than is the case without the mount, increasing drag. Vortices shed from the mount are observed to interact with vortices shed from the cylinder, altering the wake characteristics.

This study highlights the importance of minimizing modeling uncertainties when performing wind tunnel tests. Mounts should be designed to be as unobtrusive as possible, ideally contacting the bluff body in a location where the flow is already separated, such as an aft sting mount. Interactions between the flow fields of the bluff body and the mount dictate that it is not accurate to simply subtract the mount-only loads from the total loads if the mounting apparatus is poorly designed. Numerical simulations are capable of assessing these sensitivities and guiding the methods applied in wind tunnel experiments.

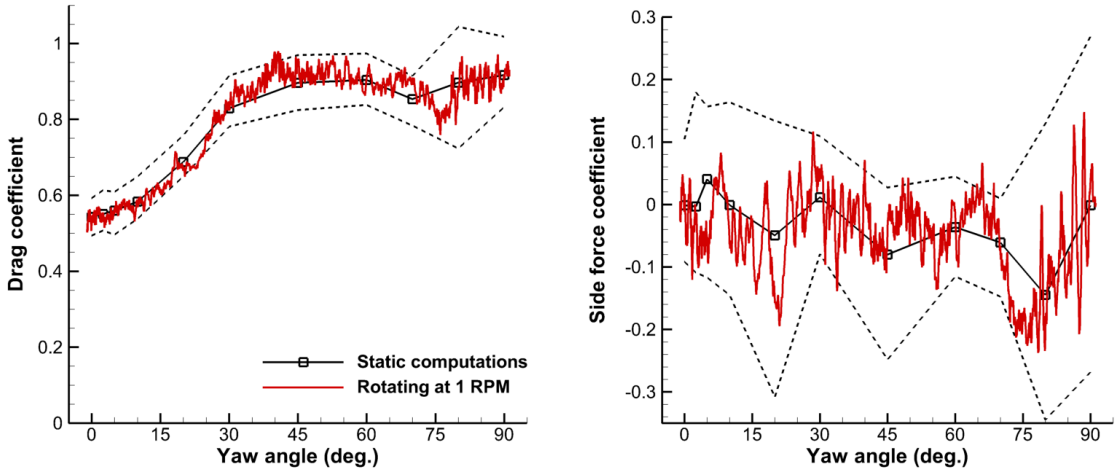

(a) Drag coefficient

(b) Side force coefficient

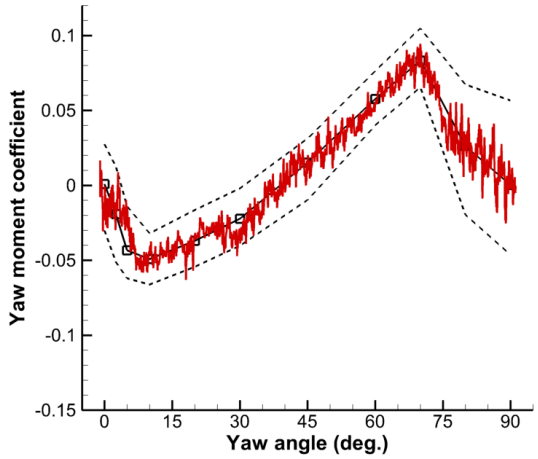

(c) Yaw moment coefficient

Figure 75: Static and rotating (1 RPM) time-averaged force and moment coefficients for a cylinder with aspect ratio 1.0. Dashed lines represent min and max values for the unsteady simulations.

7.1.4 Sensitivity to Slow Rotation

Another sensitivity commonly encountered in wind tunnel testing is due to slow rotation. This technique is usually applied in experiments so that data can be recorded continuously for an entire range of yaw angles or angles of attack. For example, the technique has been applied in dynamic stall studies since the 1980s [115]. Provided the rotation speed is sufficiently slow, unsteady effects related to the rotation are expected to be minimal, so that the forces and moments recorded at a given angle are an accurate representation of the static values. In bluff body flows, vortex shedding complicates the picture, as the flow field is never truly quasi-steady, requiring some form of time averaging before the mean static values can be extracted.

Here, the static predictions of the cylinder with an aspect ratio of 1.0, at a Reynolds number based on diameter of 0.96×10^5, have been compared to a slowly rotating cylinder at 1 RPM. This comparison provides an estimate of the errors due to differing yaw angles (i.e., measurement errors in wind tunnel and flight tests) as well as an indication of how the vortex shedding behavior may vary in static and slowly-rotating configurations. Figure 75 presents the drag, side force, and yaw moment coefficients for a yaw angle sweep of $0 \leq \beta \leq 90°$. The static simulations include minimum and maximum bounds, illustrated as dashed lines, to provide an indication of the unsteadiness. With very few exceptions, the rotating case results fall within these bounds, and the trends with yaw angle are also comparable for the two cases. The sensitivity of the side force coefficient is also demonstrated in the rotating results, as the fluctuations are large and exhibit considerable low-frequency oscillations which make extracting a mean value of side force at a given yaw angle problematic.

This rotating case also highlights yaw angles where additional static simulations are desirable. For example, the drag and side force change abruptly between yaw angles of 75 and 80°. Given the excellent agreement between the static and rotating forces and moments, it is confirmed that a rotation speed of 1 RPM is sufficiently slow to reflect quasi-steady flow. However, due to the significant fluctuations from vortex shedding, it is recommended that the sweep be performed several times during experiments so that meaningful time-averaged loads can be extracted. It is also recommended that the rotation be performed

in both directions, as wind tunnel investigations [37] have indicated that hysteresis effects may be present due to unsteady aerodynamics.

7.1.5 Sensitivity to Tunnel Blockage

The bluff body configurations examined in Chapter 3 are intended to be *canonical*, meaning that basic geometries without secondary influences (i.e., surface imperfections and wind tunnel mounting hardware) are not modeled. However, all these evaluations were performed inside a computational model of a wind tunnel test section for the purpose of comparing with experimental results. Therefore, it is important to ensure that wind tunnel blockage does not play a significant role; otherwise, the configurations could not be considered truly canonical.

In order to assess tunnel blockage, the cylinder with aspect ratio 2.0 has been evaluated for two additional cases. The Reynolds number based on diameter for both is 1.0×10^6. The two different configurations correspond to yaw angles of 0° and 5°. This cylinder has been selected for this investigation because it is the largest of the bluff bodies examined in Chapter 3 and should, therefore, produce the largest amount of blockage. Provided blockage effects are minimal with this geometry, it is reasonable to assume the same is true for the other static simulations as well. Additionally, the low yaw angle orientations are expected to be the most sensitive to blockage and other potential sources of error because the separation points are not fixed.

A new free air background grid has been generated for this sensitivity analysis, which has the shape of a cube and extends 30 diameters from the center of the cylinder in all directions. Non-reflecting freestream boundary conditions are applied on all outer boundaries. Side and back views of both the original wind tunnel grid (in black) and the free air grid (in red) are depicted in Fig. 76. The wind tunnel test section extends approximately 10.5 diameters in front and back of the cylinder. The cross section is a 9-foot cylinder with the top and bottom cut so that the height is 7 feet, as illustrated in Fig. 76(b). The blockage, based on the frontal area of the cylinder at a yaw angle of 0° and the cross-sectional area of the wind tunnel test section, is 1.85%. As the frontal area of the cylinder decreases with increasing

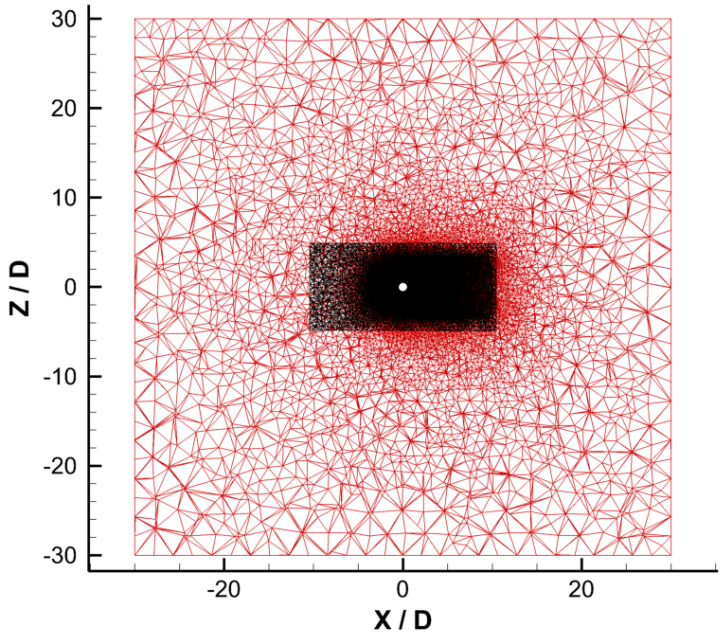

(a) Side $(X - Z)$ view

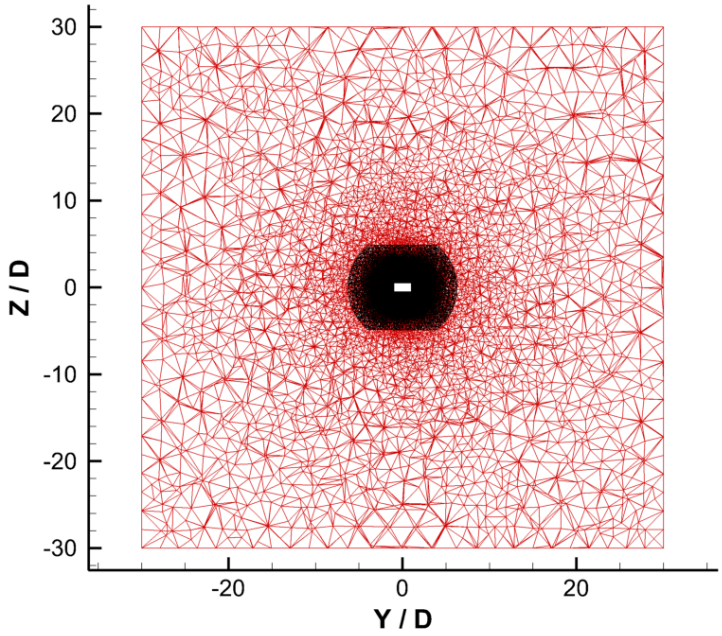

(b) Back $(Y - Z)$ view

Figure 76: Grid size comparisons for free air and wind tunnel simulations, cylinder with aspect ratio 2.0. Black: wind tunnel grid; red: free air grid.

Table 12: Comparison of mean drag, side force, and yaw moment for wind tunnel and free air numerical experiments.

		Drag	% Error	Side force	% Error	Yaw moment	% Error
$\beta = 0°$	Tunnel	0.3674	–	-0.04842	–	0.02887	–
	Free air	0.3691	0.5	-0.04240	12.4	0.02674	7.4
$\beta = 5°$	Tunnel	0.4316	–	0.07946	–	-0.05353	–
	Free air	0.4192	2.9	0.06543	17.7	-0.04779	10.7

yaw angle, this orientation represents the maximum blockage.

Though overset unstructured grids would typically not be needed for free-air static configurations such as these, the overset approach is applied here to ensure that the grid characteristics are as similar as possible between the free air and wind tunnel cases. The near-body grids applied in the wind tunnel cases have been overset on the free air background grid for this purpose. Additionally, the same volume sources used to generate the wind tunnel background grid have been included in the free air background grid to ensure similar grid density in the wake region. The wake grid clustering is visible in Fig. 76(a).

Table 12 compares the mean values of drag, side force, and yaw moment for the wind tunnel and free air numerical experiments, along with percent errors of the latter relative to the former. The reference area for non-dimensionalization is the planform area (LD), while the reference length for computing moments is the diameter (D), and the moments are computed about the geometric center located at the origin. These numerical experiments have been performed with identical solver parameters (i.e., time step size, discretization, and turbulence model) as the cases presented in Chapter 3; the only difference is the presence of walls. This table demonstrates that the difference in drag between the two cases is very small, with a relative error of 2.9% or less. However, the error in yaw moment is larger, with a maximum and 10.7%, and the maximum error in mean side force is 17.7%.

Though the errors in side force and yaw moment seem large and suggest that these quantities are sensitive to wind tunnel blockage, this is not actually the case. Consider, for example, Figs. 77 and 78, which present the drag, side force, and yaw moment coefficients as a function of non-dimensional time, $t^* = t\dfrac{StU_\infty}{D}$. When time is non-dimensionalized this way, $t^* = 1.0$ corresponds to the length of time required for a single nominal vortex

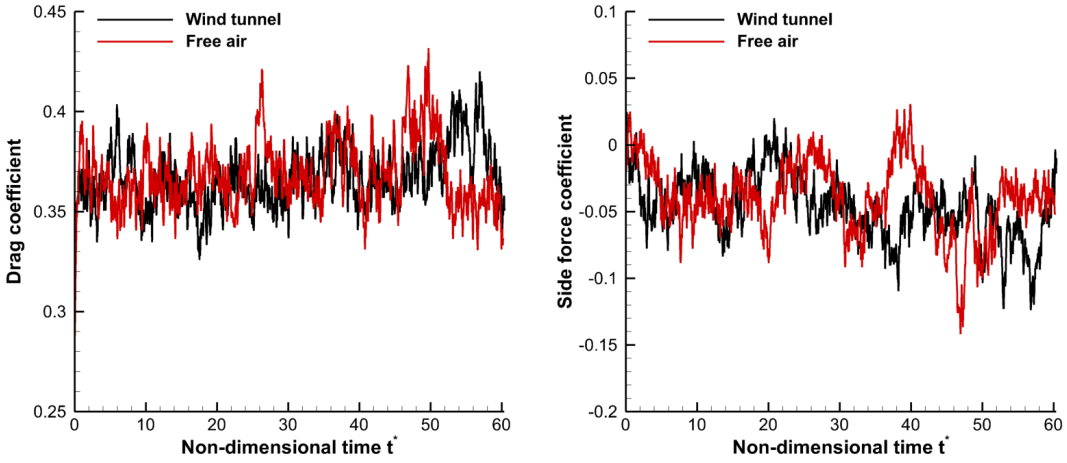

(a) Drag

(b) Side force

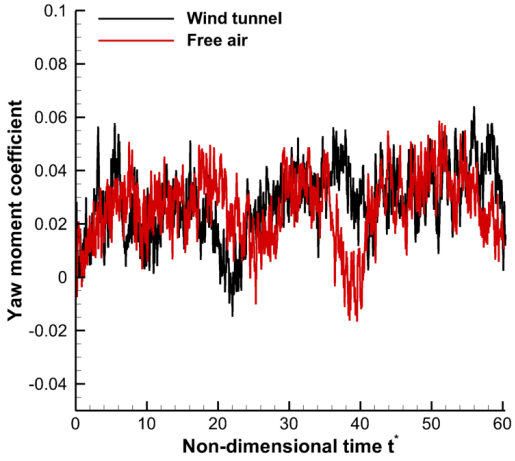

(c) Yaw moment

Figure 77: Comparison of drag, side force, and yaw moment coefficient time histories for free air and wind tunnel simulations. Reynolds number based on diameter is 1.0×10^6, yaw angle is $0°$.

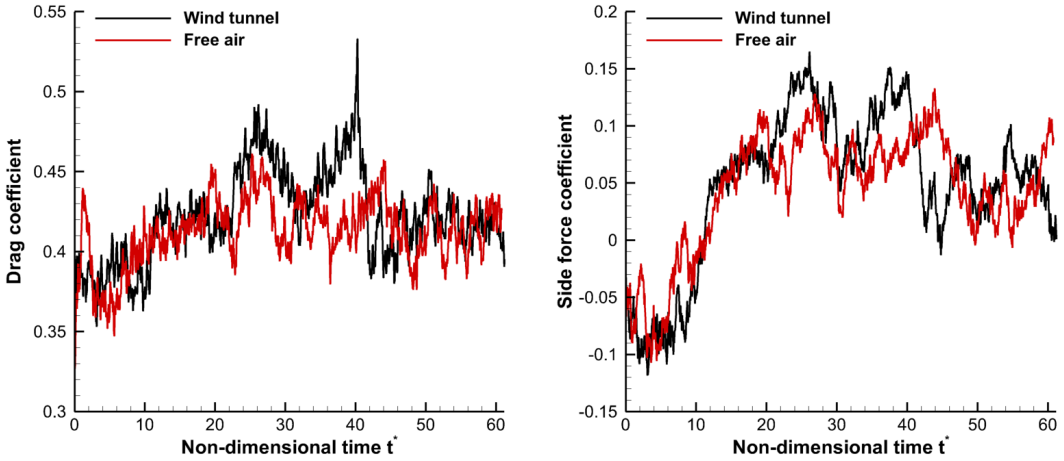

(a) Drag

(b) Side force

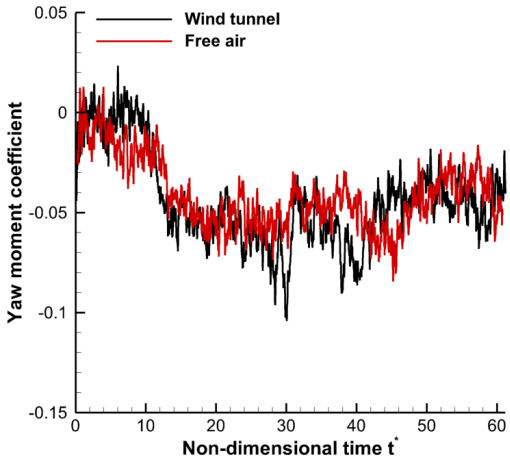

(c) Yaw moment

Figure 78: Comparison of drag, side force, and yaw moment coefficient time histories for free air and wind tunnel simulations. Reynolds number based on diameter is 1.0×10^6, yaw angle is 5°.

shedding fluctuation. Here, the nominal Strouhal number is identified as 0.2 based on the results of Section 3.4. These figures demonstrate that long-period changes in unsteady characteristics, with a period of 10 – 15 times the nominal shedding period, can occur in these highly three-dimensional bluff body flows. Similar behavior has also been observed in experiments [9]. These long-period changes introduce differences in the time-averaged force and moment coefficients. While such behaviors are present in all three of the quantities presented in Fig. 77, they have the largest influence on the relative errors for the side force and yaw moment, as the mean values are close to zero for these quantities. Therefore, any differences in the time histories resulting from unsteady behavior are magnified when the percent errors are computed. Because the relative error in mean drag is so small and the long-period oscillations are similar for all three quantities, the differences in mean values are completely attributable to natural variations in unsteady behavior and not to tunnel blockage effects.

Figure 77 and Table 12 also reveal an unexpected result, in that the side force and yaw moment at a yaw angle of 0° are not zero. As has been discussed in Section 7.1.1, Zdravkovich et al. [9] observed similar behavior in wind tunnel tests of short cylinders with aspect ratios in the range 1.0 – 2.0. In those experiments, the vortex shedding at very low yaw angles ($\beta < 3°$) was bi-stable and produced asymmetric pressure distributions on the cylinder surface. Figure 79 illustrates this asymmetry in the time-averaged pressure distribution from the free air numerical experiment at a yaw angle of 0°. In Fig. 79(a), the round cylinder surface is "unwrapped" and visualized with the azimuth angle along the vertical axis and the span along the horizontal axis. An azimuth angle of 0° corresponds to the front of the cylinder, while an angle of 90° corresponds to the top, and an angle of 180° corresponds to the back. The asymmetry is most apparent on the top and bottom surfaces, where the suction peak is offset to the left side. Consequently, the back left half of the back of the cylinder is subjected to a lower base pressure than the right half, resulting in non-zero yawing moment. This asymmetry also affects the pressure distributions on the flat sides of the cylinder, as illustrated in Fig. 79(b); the separation bubble pressure is lower on the left face than on the right, resulting in a negative mean side force. All these characteristics are

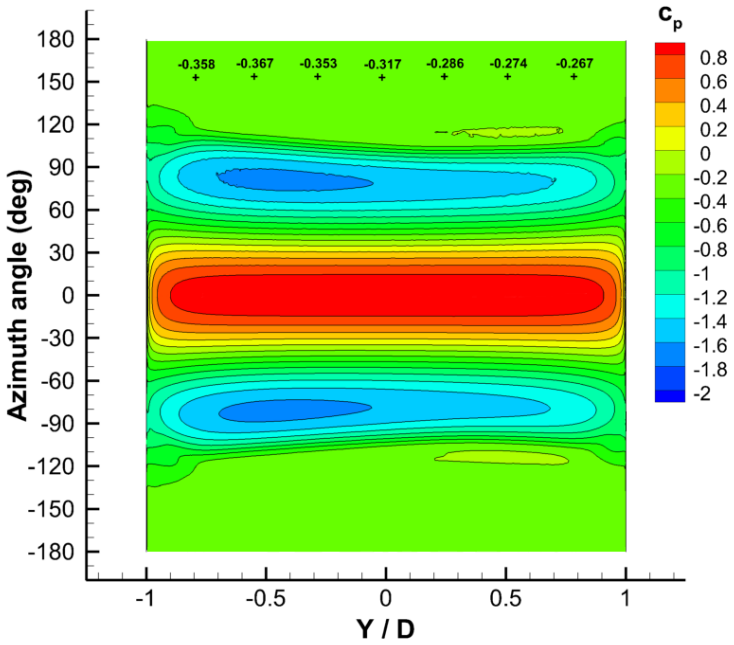

(a) Pressure on round cylinder face

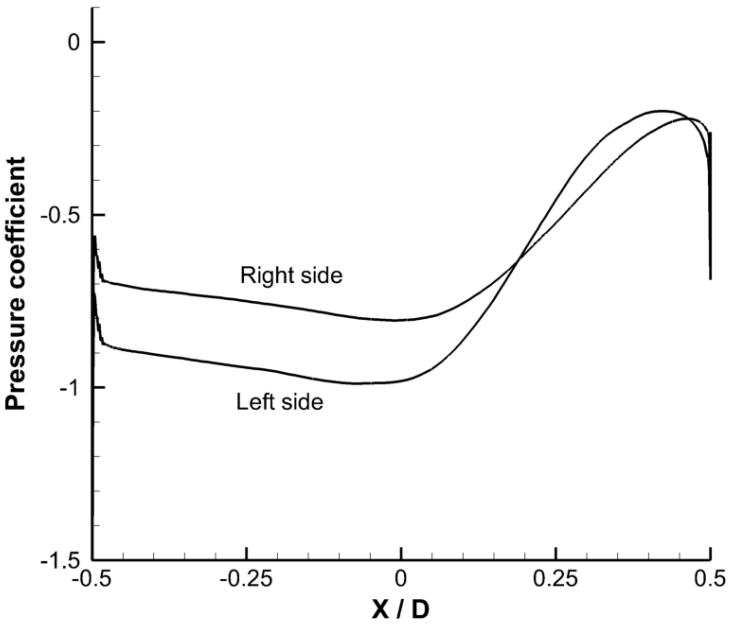

(b) Pressure on centerline of flat faces

Figure 79: Time-averaged pressure distributions on cylinder with aspect ratio 2.0 at a yaw angle of 0°.

consistent with the experimental observations of Zdravkovich et al. [9].

7.2 Reduced-Order Model Uncertainty Quantification

Uncertainty quantification is an area of mathematical analysis necessary for accurate validation, design, and certification of engineering systems. The use of uncertainty quantification in engineering is not new, but significant research, particularly since the beginning of the new millenium, has rapidly expanded its application, primarily in design. In the context of tethered loads analysis, for example, uncertainty quantification has several functions. It can first be utilized to identify the errors associated with any one component of the tethered load configuration. It can also be modified via a system-of-systems approach to assess entire tethered load configurations.

It is crucial that any dynamic tethered experiment or simulation be analyzed as a realistic system of systems. Failure to account for any one system or component of the configuration can lead to erroneous conclusions and limits the extension to new configurations. Some examples of the importance of this system-of-systems concept that have already been discussed include (1) the change in dynamic behavior when the unsteady aerodynamics subsystem is neglected (see Sections 6.1 and 6.4.6) and (2) the more stable dynamic response of the system without helicopter dynamics (see Section 6.4.6).

7.2.1 Identification of Errors

Once a realistic system (experimental or computational) has been designed, then each component in the system is individually assessed for errors that must be quantified. For tethered loads, the system is defined in Fig. 80. The errors that will impact the behavior of the tethered load must be identified for each system: load (structural, inertial, and aerodynamic) and operational (helicopter dynamics, rotor downwash, and atmospheric turbulence). These errors are classified into to categories: epistemic and aleatory [116]. *Epistemic* errors are errors that arise due to the lack of knowledge about a physical system or environment, i.e., the in-operation wear on a point attachment, such as a gimbal. *Aleatory* errors are those that describe the variability inherent in any physical system or environment, such as geometric perturbations or vehicle motion. Any aleatory uncertainty can be characterized, if

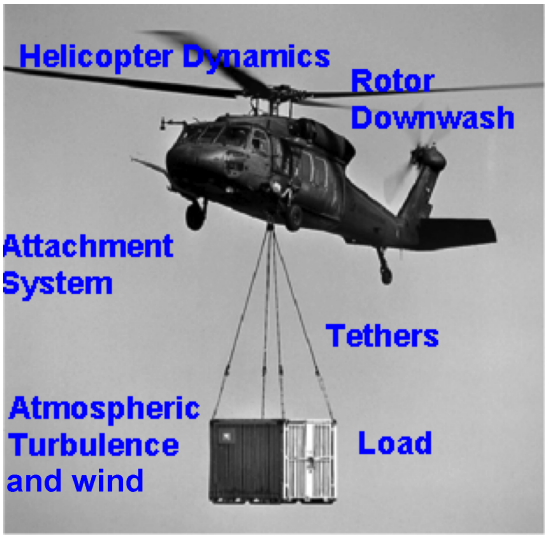

Figure 80: The tethered load system of systems. Background photo from Ref. [11].

sufficient samples exist, by a probability density distribution, and this uncertainty applies to most of the component system-level errors. Epistemic uncertainties, given the unknowns in an actual operational environment and the unpredictability of offsetting errors in different configurations, will exist in the final system output (i.e., dynamic tethered load behavior). These uncertainties are more difficult to assess with respect to a true operational environment. Again, it must be underscored that the design of the uncertainty analysis must include individual component analysis, followed by a system-of-systems uncertainty analysis.

The approach adopted here is that proposed by Overkampf and his collaborators [117, 118]. The process includes the identification and characterization of pertinent sources of uncertainty; elimination or, at least, estimation of code and solution verification errors; identification of the uncertainties in the system response quantities of interest due to propagation of input uncertainties through the model; quantification of mathematical model uncertainty; and estimation of mathematical model uncertainty when extrapolating to new applications and conditions. Examples, as applied to tethered load simulation, are provided to illustrate this process.

Parameter Importance: Consider the errors associated with the tethered load. The load itself is a complex system. Errors that can impact the dynamic behavior of a known

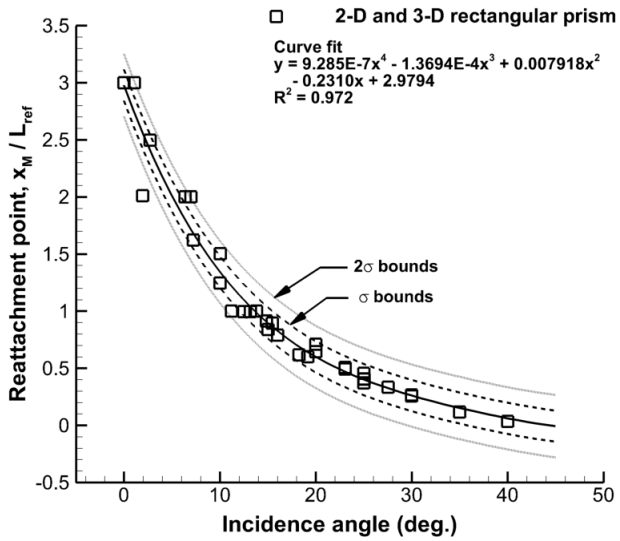

Figure 81: Normalized shear layer reattachment distance for two- [12] and three-dimensional rectangular prisms with 2σ uncertainty bounds.

load include, but are not limited to, geometric perturbations (e.g., manufacturing, small protuberances), geometric variations (e.g., aspect ratio, curvature, dimensions), and inertial properties. The quasi-steady aerodynamic model described in Section 5.1 is an additional subsystem, as it is obtained from a separate set of engineering data (wind tunnel, theory, high-fidelity computations), each with its own set of uncertainties. Each source of the data must be examined, which has been the primary purpose of the validation and sensitivity analyses in Sections 3.3 and 7.1.

Mathematic Uncertainty: A process for the assessment of computational errors in high performance computing was proposed by Oberkampf and Trucano [116] in 2002, refined by Roy and Oberkampf [118], and adopted by many in the computational field. Since 2011, computational uncertainties have been quantified using these principles and include the methodology employed [83] and simulations performed as part of Section 7.1. By evaluating errors associated with the inputs, grid quality and size, numerical discretization, and round-off, estimates of the computational error for the forces and moments fall within 2–5% when compared to canonical configurations.

Aleatory Error: One example of aleatory error relevant to helicopter tethered loads is the shear layer of bluff bodies, which has been examined in Section 3.5.1. Figure 81 presents

the normalized shear layer reattachment distance for two- [12] and three-dimensional (see Section 3.5) rectangular prisms. This figure is the same as Fig. 28(c), but with uncertainty bounds included. For each rectangular prism, the reattachment distance decreases as the angle of the face relative to the freestream flow increases, and this behavior can be modeled by an empirical curve as illustrated in the figure. Though variability exists within this physical system, so that the empirical trend curve is not a perfect model of reattachment at each angle and geometry, nearly all measurements lie within the 2σ-bounds. If this model of shear layer attachment is employed to develop a prediction model for the quasi-steady forces and moments, the uncertainty quantification represented by these bounds can be propagated through the model to provide an estimate of the uncertainty in the final calculation due to physical variability in this phenomenon.

Epistemic Error: More difficult to quantify are epistemic errors, such as the unsteady wind and atmospheric turbulence. These change for every flight, and the conditions cannot be predicted from a known set of data. It is first necessary to identify the sensitivity to the wind and determine if it is an important quantity, and this determination should be based on realistic wind data (i.e., data from flight test) rather than how the model might predict the behavior in general.

To evaluate this sensitivity, the wind speed information from flight test data at 112 knots (see Table 10 and Section 6.4) is examined in Fig. 82(a). All three components have relatively small mean values of approximately 5% the flight speed. Large- and small-scale fluctuations are also present due to atmospheric turbulence. A tempting modeling assumption would be to ignore this wind in simulation, due to its relatively small magnitude, but this assumption can result in significant errors. Figure 82(b) illustrates the influence of this subsystem on the yaw behavior. Different situations have been considered: (1) with the full wind included, (2) with no wind, (3) with only individual components of wind tangential and normal to the flight path, and (4) with each component of wind replaced by its mean value, thus eliminating atmospheric turbulence. The yaw rate is similar among the different cases for only the first ten seconds. After that, yaw rate reversals, which were also observed in the flight tests, occur only in cases with the full wind included or the tangential

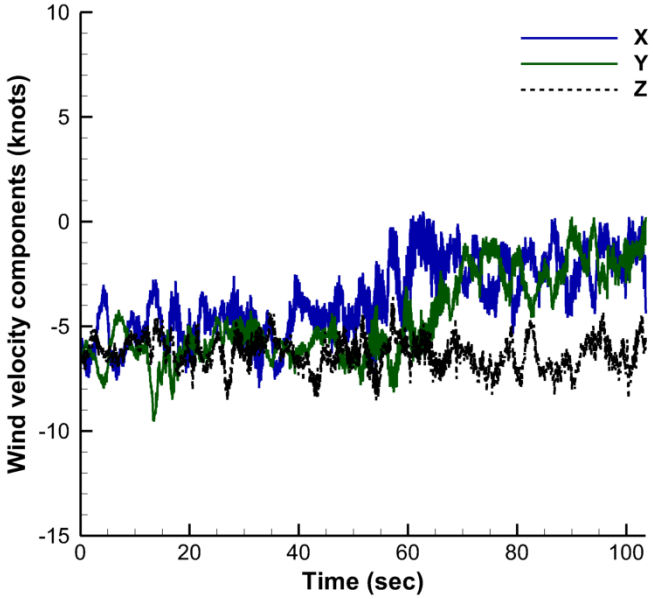

(a) Measured wind speed

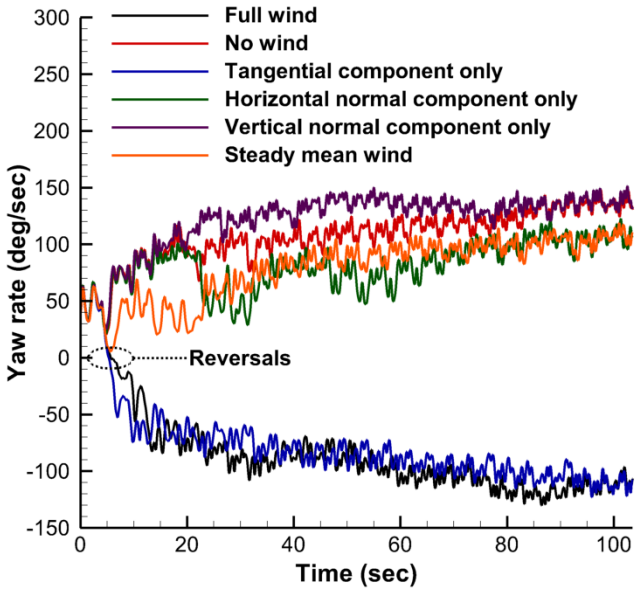

(b) Yaw rate behavior with and without wind

Figure 82: Sensitivity of tethered load response to unsteady wind characteristics.

component only. An evaluation of the influence of the mean contributions indicates that the unsteadiness of the wind also has a significant impact on the dynamic yaw behavior, although there was no immediate correlation of the wind frequency with the model response frequency.

The sensitivity of the long term yaw rate prediction appears to be affected to a large extent by the wind. This result implies that, for realistic operational tethered loads behavior, wind tunnel testing (virtual or physical) that lacks both the wind and helicopter dynamics may not predict the behavior observed in operational use. This example also underscores the need for dynamic efforts to include rational design or scaling of *all* components of the flight system. Though a full investigation of these uncertainties is beyond the scope of this thesis, it is recommended for future work.

CHAPTER VIII

CONCLUSIONS

Advanced computational techniques have been applied to study the aerodynamic-dynamic interactions of bluff bodies, culminating in the following two contributions to the state of the art:

- Detailed investigation and characterization of the aerodynamics of short, canonical three-dimensional bluff bodies in both static and dynamic configurations have been accomplished through numerical experiments. An unstructured solver with a hybrid RANS-LES turbulence approach has been employed for this purpose. Mean and unsteady flow behaviors have been analyzed, while empirical relationships have been developed to quantify and characterize the principal shear layer behaviors that drive the forces and moments and to identify variations with bluff body type, aspect ratio, and Reynolds number. These behaviors were previously unknown for the short aspect ratio bluff bodies evaluated.

- A physics-based reduced-order model has been developed for three-dimensional bluff bodies. This physics-based model draws from the results of numerical experiments and characterization of bluff body flow. Quasi-steady aerodynamics are modeled via a quasi-linear superposition of static data from computational fluid dynamics, wind tunnel tests, or flight test data, with empirical corrections applied as required. Unsteady aerodynamics are comprised of three-dimensional vortex shedding, which contributes an aperiodic fluctuation to the mean-flow aerodynamics, and the mean-flow response to unsteady body motion based on classical theory.

Sensitivity studies have been performed to ensure that the numerical experiments are free of discrepancies due to grids, temporal convergence, wind tunnel mounting apparatus, and wind tunnel blockage. With respect to the evaluations of the aerodynamics of short,

canonical three-dimensional bluff bodies in static orientations, the following observations can be made:

- The hybrid RANS-LES turbulence approach has been validated in unsteady three-dimensional flows about short rectangular prisms and finite cylinders.

- Turbulent transition primarily affects the drag predictions of finite circular cylinders for yaw angles below 30° but has not been found to significantly affect the side force or yaw moment. As the forces and moments are primarily pressure-driven, surface roughness is not expected to significantly alter the results except in that it may change the critical Reynolds number for turbulent transition.

- The flow is highly unsteady and three-dimensional. Frequency-domain transformation of quantities in the wake results in a broad, multimodal spectrum, and clear trends in the Strouhal shedding frequency are not apparent with respect to aspect ratio, yaw angle, or Reynolds number. The dominant Strouhal shedding frequency ranges from 0.14 – 0.27, and 0.2 may be taken as a representative value, which has also been observed in physical experiments.

- Time averaging of the unsteady flowfields is required to quantify the characteristics of the phenomena reponsible for trends in the mean forces and moments. This procedure permits clear identification of shear layer behavior through evaluation of surface pressure indicators.

- When the time-averaged pressure distributions are integrated over individual bluff body faces, the effects of shear layer reattachment are readily apparent. This phenomenon causes an immediate increase in normal force on a given face, while the yaw moment trend reverses sharply when reattachment reaches the midpoint of the face.

- The reattachment distance can be correlated with bluff body type and surface type. In the configurations evaluated, this distance is greatest, at a given incidence angle, for the rectangular prism. The next greatest distance corresponds to the curved faces of the cylinder, while the shortest distance corresponds to the flat faces of the cylinder.

- The distance to reattachment and the maximum pressure coefficient at reattachment may be modeled empirically as a function of incidence angle only. These quantities have been found to be independent of geometry type, surface type, Reynolds number, and aspect ratio for the configurations examined, provided the proper normalization is applied taking into account the conditions when reattachment first begins.

- The pressure coefficient in the separation bubble can be modeled empirically as a function of incidence angle only for flat bluff body faces when normalized appropriately. On curved cylinder faces, this parameter is also correlated with Reynolds number and aspect ratio.

- The normalized stagnation point location can be modeled empirically as a function of incidence angle only for flat bluff body faces. On curved cylinder faces, this parameter has been found to also depend on aspect ratio but not Reynolds number.

For the numerical investigations of bluff bodies in unsteady motion, the following conclusions can be drawn:

- Spinning motion, even at a low reduced frequency, alters the mean-flow aerodynamic response by introducing phase lags and magnitude changes in the forces and moments.

- Phase lag in shear layer behavior occurs as a result of spinning motion. For a spinning rectangular prism, shear layer reattachment was observed over the range of yaw angles from $85° - 95°$, whereas the shear layer was fully separated in static configurations at these angles. This prolonged reattachment behavior resulted in higher base pressure and lower drag in the spinning simulations at these yaw angles.

- The pendulum motion which typically occurs in unstable tethered load configurations induces only very minor changes in yaw angle. Therefore, this motion does not significantly influence the unsteady aerodynamic response.

- Six-degree-of-freedom tethered bluff body simulations have been demonstrated with the hybrid RANS-LES flow solver. The dynamic behaviors of the load, including coupled lateral-longitudinal pendulum oscillations and spinning, are similar to

experimentally-observed results. While the approach is of high fidelity and completely general, it is too computationally expensive for practical use in stability and sensitivity analyses where many cases must be evaluated.

The following observations may be made in regard to the physics-based reduced-order model:

- The aerodynamic predictions of the reduced-order model closely match those of high-fidelity hybrid RANS-LES numerical simulations undergoing the same dynamic motions, including nonlinearities in the aerodynamic response.

- Crossflow corrections for the body-axis moments improve the accuracy of the model while retaining the quasi-linear form of the quasi-steady aerodynamics. The accuracy is particularly improved when the angle of attack or yaw angle is far from the reference value at which the quasi-steady data were recorded.

- Quasi-steady data for the model may be drawn from validated computational fluid dynamics simulations, wind tunnel experiments, or flight tests.

- Dynamic simulations have demonstrated the importance of unsteady aerodynamics in producing the correct dynamic response of the bluff body, even when the reduced frequency of spinning motion or other oscillations is on the order of 0.02. Neglecting these terms in dynamic simulations results in incorrect dynamic behavior.

- The unsteady aerodynamic model, based on classical unsteady aerodynamic theory, captures within 25% the magnitude attenuation in the forces and moments, relative to quasi-steady predictions, as observed in full-scale flight testing.

- The phase lag in yaw moment is captured within 4° at high flight speeds with low spin rates (reduced frequency of 0.02), but it is underpredicted by up to 17° at lower flight speeds with higher spin rates (reduced frequency of 0.1). This result suggests that the phase response of the classical unsteady aerodynamic model is too mild for bluff body flows. As tethered load instability typically occurs at low reduced frequency,

the diminished accuracy at higher reduced frequency is not considered to be of crucial importance here.

- The model is able to capture tethered load instabilities observed in flight tests when the helicopter motion is included in the simulation. Cable angle excursions are typically 3–5 degrees larger than the measured values, representing a conservative stability estimate.

- Tethered load stability predictions in virtual wind tunnel configurations have been found to be less accurate and less conservative than simulations including helicopter dynamics and atmospheric turbulence.

- Spin rates in tethered load simulations have been found to be sensitive to both unsteady aerodynamics and unsteady wind.

- Computational cost is reduced by six orders of magnitude relative to hybrid RANS-LES simulations, while the most important physics are retained.

- Initial comparisons indicate the ability of the model to be extended to complex configurations (a truck), requiring only the quasi-steady data to be changed in the algorithm.

8.1 Recommendations for Future Work

Several areas of improvement are possible for both the canonical bluff body numerical investigations and the physics-based reduced-order dynamic model. To further improve the state of the art in bluff body aerodynamics, the following recommendations are made:

- Expanded static canonical bluff body evaluations

  While the investigations in this thesis represent a large improvement in the understanding of finite three-dimensional bluff body aerodynamics, they are limited to a single rectangular prism and circular cylinders with aspect ratios of 1.0 and 2.0. Future work should include additional canonical bluff bodies, such as flat plates, while the range of aspect ratios should be expanded for the rectangular prism and circular cylinders. Such examinations will allow the empirical quantifications of shear layer

behavior to be made more comprehensive, and variations in these phenomena with respect to bluff body type and aspect ratio may be further assessed and confirmed. Additionally, the angle of attack has been held at zero degrees in these evaluations. Future studies should include simultaneous non-zero values of both yaw angle and angle of attack.

- Further validation for finite cylinders

  The numerical computations have been validated using available wind tunnel data for both rectangular prisms and finite cylinders. However, currently, experimental data for finite cylinders are only available at yaw angles of 0° and 90°. The computations can be further validated for finite cylinders if experimental data becomes available over the entire range of yaw angles.

- Shear layer behavior analysis for complex bluff bodies

  The quantitative shear layer behavior models developed here are representative of simple canonical geometries. It is currently unknown whether these empirical representations may be extended to more complex geometries. Future work should investigate this question through numerical experiments of bluff bodies with incrementally increasing complexity. For example, two stacked rectangular prisms of different dimensions can be considered as a rough model of a truck geometry. This form of analysis will provide insight into how basic canonical shear layer behaviors may be combined to develop approximations for more complex shapes.

- Approximate force and moment reconstructions

  Because bluff body forces and moments are primarily pressure-driven, it is possible to leverage the empirical shear layer models here to develop approximate force and moment reconstructions for bluff bodies. This advancement will be beneficial in assessing the dynamics of bluff bodies when quasi-steady data are not available from computations, wind tunnel experiments, or flight tests.

- Additional numerical experiments with prescribed dynamics

Individual prescribed spinning and pendulum-motion evaluations have been performed here, which indicate that unsteady bluff body motion may produce an aerodynamic response that is not fully captured by quasi-steady predictions. It is recommended to expand this analysis to additional bluff bodies and reduced frequencies to fully characterize these unsteady aerodynamic effects.

Improvements to the reduced-order model are also recommended to improve its accuracy, generality, and performance. They are as follows:

- Unsteady aerodynamic model

  The current model incorporates classical unsteady aerodynamics resulting from dynamic motion of the bluff body. While it has been demonstrated that this model represents a significant improvement over quasi-steady aerodynamics, further improvements are possible. In particular, the phase response at reduced frequencies of spinning motion on the order of 0.08–0.1 is too mild in this model, compared with helicopter tethered load flight test observations. The model may be improved through characterization of unsteady effects through additional numerical experiments, which have been recommended in a previous point. However, it is stressed that the model must remain physics-based and general; system identification of single configurations should be avoided to maintain the generality of the model.

- Extension to complex bluff bodies

  The reduced-order approach is designed to be general, so that any bluff body can be modeled, and this capability has been demonstrated through simulation of a truck using approximate analytical quasi-steady expressions available from Liu [99]. However, more accurate quasi-steady data are desirable for this purpose, and currently such information is lacking for complex bluff bodies such as trucks, tanks, and other typical tethered loads.

- Sensitivity analysis

Sensitivity analyses of the model to unsteady aerodynamics, wind, and helicopter degrees of freedom have been performed. However, the entire tethered loads system comprises numerous other subsystems, including the attachment system (i.e., gimbals and fixed hooks), tethers, and rotor downwash. It is important to understand and characterize the sensitivities in each of these subsystems in order to avoid instabilities in real-world operations.

- Incorporation of second-order effects

  It is possible to incorporate second-order effects, such as wind tunnel walls, ground effect, and rotor wakes, within the framework of the reduced-order model. Such extensions are outside the current scope but should be implemented in the future.

- Computational speed improvements

  Several opportunities for computational speed improvements in the model have been identified to permit real-time simulations. These include parallel processing of quasi-steady data interpolations and implementation in a compiled language with optimization. It is also recommended that semi-implicit or implicit temporal schemes be explored for integrating the unsteady aerodynamic model, which may reduce timestep size restrictions.

REFERENCES

[1] Cicolani, L. and da Silva, J, G., "Unsteady Aerodynamic Model of a Cargo Container for Slung-Load," *The Aeronautical Journal*, vol. 108, pp. 357–368, July 2004.

[2] Matsumoto, M., Ishizaki, H., Matsuoka, C., Daito, Y., Ichikawa, Y., and Shimahara, A., "Aerodynamic Effects of the Angle of Attack on a Rectangular Prism," *Journal of Wind Engineering and Industrial Aerodynamics*, vol. 77–78, pp. 531–542, September 1998.

[3] Cicolani, L., Lusardi, J., Greaves, L., Robinson, D., Rosen, A., and Raz, R., "Flight Test Results for the Motions and Aerodynamics of a Cargo Container and a Cylindrical Slung Load," Tech. Rep. NASA/TP2010-216380, National Aeronautics and Space Administration, 2010.

[4] Rosen, A., Cecutta, S., and Yaffe, R., "Wind Tunnel Tests of Cube and CONEX Models," Tech. Rep. TAE 844, Technion – Institute of Technology, Faculty of Aerospace Engineering, November 1999.

[5] Mantri, R., Raghav, V., Komerath, N., and Smith, M. J., "Stability Prediction of Sling Load Dynamics Using Wind Tunnel Models," in *Proceedings of the 67th American Helicopter Society Annual Forum*, (Virginia Beach, Virginia), May 3–5, 2011.

[6] Wieselsberger, C., "Further Data on the Law of Liquid and Air Drag," *Physikalische Zeitschrift*, vol. 23, pp. 219–224, 1922. in German, reprinted in Zdravkovich [31].

[7] Hoerner, S., *Fluid-Dynamic Drag*. Midland Park, NJ: Hoerner Fluid Dynamics, 1958.

[8] Lynch, C. E. and Smith, M. J., "Extension and Exploration of a Hybrid Turbulence Model on Unstructured Grids," *AIAA Journal*, vol. 49, pp. 2585–2590, Nov. 2011.

[9] Zdravkovich, M., Brand, V., Mathew, G., and Weston, A., "Flow Past Short Cylinders with Two Free Ends," *Journal of Fluid Mechanics*, vol. 203, pp. 557–575, June 1989.

[10] Robertson, J., Wedding, J., Peterka, J., and Cermak, J., "Wall Pressures of Separation – Reattachment Flow on a Square Prism in Uniform Flow," *Journal of Wind Engineering and Industrial Aerodynamics*, vol. 2, pp. 345–359, January 1978.

[11] Cicolani, L. S., Cone, A., Theron, J., Robinson, L. D., Lusardi, J., Tischler, M. B., Rosen, A., and Raz, R., "Flight Test and Simulation of a Cargo Container Slung Load in Forward Flight," *Journal of the American Helicopter Society*, vol. 54, pp. 1–18, July 2009.

[12] Greenwell, D., "Modelling of Static Aerodynamics of Helicopter Underslung Loads," *The Aeronautical Journal*, vol. 115, pp. 201–219, April 2011.

[13] Raz, R., Rosen, A., Cicolani, L. S., Lusardi, J., Gassaway, B., and Thompson, T., "Using Wind Tunnel Tests for Slung Loads Clearance," in *Proceedings of the 67th American Helicopter Society Annual Forum*, (Virginia Beach, Virginia), May 3–5, 2011.

[14] Matheson, N., "The Stability of Portable Bridges Carried on Slings Beneath Helicopters," Tech. Rep. 154, Defence Science and Technology Organisation, 1980.

[15] Raz, R., Rosen, A., Carmeli, A., Lusardi, J., Cicolani, L. S., and Robinson, L. D., "Wind Tunnel and Flight Evaluation of Stability and Passive Stabilization of Cargo Container Slung Load," in *Proceedings of the 64th American Helicopter Society Annual Forum*, (Montreal, Canada), April 29 – May 1, 2008.

[16] Raz, R., Rosen, A., Carmeli, A., Lusardi, J., Cicolani, L. S., and Robinson, L. D., "Wind Tunnel and Flight Evaluation of Passive Stabilization of a Cargo Container Slung Load," *Journal of the American Helicopter Society*, vol. 55, July 2010.

[17] Raz, R., Rosen, A., Cicolani, L. S., and Lusardi, J., "Using Wind Tunnel Tests for Slung-Load Clearance, Part 1: The CONEX Cargo Container," *Journal of the American Helicopter Society*, vol. 59, pp. 1 – 12, Oct. 2014.

[18] Raz, R., Rosen, A., Cicolani, L. S., Lusardi, J., Gassaway, B., and Thompson, T., "Using Wind Tunnel Tests for Slung-Load Clearance, Part 2: Other Loads," *Journal of the American Helicopter Society*, vol. 59, pp. 1 – 12, Oct. 2014.

[19] Nyren, D., Tardiff, M., and Desabrais, K., "Passive Stabilization of Helicopter Sling Load Payloads," in *Proceedings of the 71st American Helicopter Society Annual Forum*, (Virginia Beach, VA), May 5–7 2015.

[20] Shechter, E., "Bearing heavy loads," *Aerospace America*, pp. 18–20, June 2014.

[21] Cheng, M. and Liu, G., "Effects of Afterbody Shape on Flow around Prismatic Cylinders," *Journal of Wind Engineering and Industrial Aerodynamics*, vol. 84, pp. 181 – 196, January 2000.

[22] Clarkson, M. H., Malcolm, G. N., Brittain, V. A., and Intemann, P. A., "Subsonic High-Angle-Of-Attack Aerodynamic Characteristics of a Cone and Cylinder with Triangular Cross Sections and a Cone with a Square Cross Section," Tech. Rep. NASA TM 84377, National Aeronautics and Space Administration, 1983.

[23] Keener, E. R., Chapman, G. T., Cohen, L., and Taleghani, J., "Side Forces on a Tangent Ogive Forebody with a Fineness Ratio of 3.5 at High Angles of Attack and Mach Numbers from 0.1 to 0.7," Tech. Rep. NASA TM X-3437, National Aeronautics and Space Administration, 1977.

[24] Matsumoto, M., "Vortex Shedding of Bluff Bodies: A Review," *Journal of Fluids and Structures*, vol. 13, pp. 791–811, October 1999.

[25] Modi, V. and Slater, J., "Unsteady Aerodynamics and Vortex Induced Aeroelastic Instability of a Structural Angle Section," *Journal of Wind Engineering and Industrial Aerodynamics*, vol. 11, pp. 321–334, May 1983.

[26] Zaki, T., Sen, M., and Gad-el Hak, M., "Numerical and Experimental Investigation of Flow Past a Freely Rotatable Square Cylinder," *Journal of Fluids and Structures*, vol. 8, no. 7, pp. 555–582, 1994.

[27] Barnes, F. and Grant, I., "Vortex Shedding in Unsteady Flow," *Journal of Wind Engineering and Industrial Aerodynamics*, vol. 11, pp. 335–344, May 1983.

[28] Greenwell, D. and Garcia, M., "Autorotation Dynamics of a Low-Aspect-Ratio Rectangular Prism," *Journal of Fluids and Structures*, vol. 49, pp. 640–653, August 2014.

[29] Bearman, P., "Vortex Shedding from Oscillating Bluff Bodies," *Annual Review of Fluid Mechanics*, vol. 16, pp. 195–222, January 1984.

[30] Zdravkovich, M., *Flow Around Circular Cylinders*, vol. 1: Fundamentals. Oxford University Press, 2003.

[31] Zdravkovich, M., *Flow Around Circular Cylinders*, vol. 2: Applications. Oxford University Press, 2003.

[32] Schmidt, L., "Measurements of Fluctuating Air Loads on a Circular Cylinder," *AIAA Journal of Aircraft*, vol. 2, pp. 49 – 55, January – February 1965.

[33] Ayoub, A. and Karamcheti, K., "An Experiment on the Flow Past a Finite Circular Cylinder at High Subcritical and Supercritical Reynolds Numbers," *Journal of Fluid Mechanics*, vol. 118, pp. 1–26, May 1982.

[34] Ramberg, S., "The Effects of Yaw and Finite Length Upon Vortex Wakes of Stationary and Vibrating Circular Cylinders," *Journal of Fluid Mechanics*, vol. 128, pp. 81–107, Mar. 1983.

[35] Bursnall, W. J. and Loftin Jr., L. K., "Experimental Investigation of the Pressure Distribution about a Yawed Circular Cylinder in the Critical Reynolds Number Range," Tech. Rep. NACA TN-2463, National Advisory Committee for Aeronautics, 1951.

[36] Sears, W., "The Boundary Layer of Yawed Cylinders," *The Journal of Aeronautical Sciences*, vol. 15, no. 1, pp. 49–52, 1948.

[37] Sampath, P., *Dynamics of a Helicopter-Slung Load System*. PhD thesis, University of Maryland, College Park, Maryland, 1980.

[38] Sridharan, A., Celi, R., and Chopra, I., "On the Role of Aerodynamic Non-Linearities in Helicopter Sling Load Operations," in *Proceedings of the 67th American Helicopter Society Annual Forum*, (Virginia Beach, Virginia), May 3–5, 2011.

[39] Norberg, C., "Flow around Rectangular Cylinders: Pressure Forces and Wake Frequencies," *Journal of Wind Engineering and Industrial Aerodynamics*, vol. 49, pp. 187–196, December 1993.

[40] Da Matha Sant'Anna, F., Laneville, A., Trepanier, J., and Lu, Z., "Detailed Pressure Field Measurements for Some 2-D Rectangular Cylinders," *Journal of Wind Engineering and Industrial Aerodynamics*, vol. 28, pp. 241–250, August 1988.

[41] Mulhearn, P., "Stagnation and Reattachment Lines on Cylinder of Square Cross-Section in Smooth and Turbulent Flows," *Nature Physical Science*, vol. 241, pp. 165–167, Feb. 1973.

[42] Davidson, P. A., *Turbulence: An Introduction for Scientists and Engineers*. New York: Oxford University Press, 2004.

[43] Pope, S. B., *Turbulent Flows*. New York: Cambridge University Press, 1 ed., 2000.

[44] Sánchez-Rocha, M., *Wall-Models for Large Eddy Simulation Based on a Generic Additive-Filter Formulation*. PhD thesis, Georgia Institute of Technology, Atlanta, Georgia, 2009.

[45] Wan, H., Dong, H., and Liang, Z., "Vortex Formation of Freely Falling Plates," in *50th AIAA Aerospace Sciences Meeting and Exhibit*, no. AIAA-2012-1079, (Nashville, Tennessee), January 9–12, 2012.

[46] Cai, J. and Liu, F., "Numerical Simulations of Vortex Shedding from 2D Bluff Bodies with Base Cavities," *Modern Physics Letters B*, vol. 24, pp. 1279–1282, May 2010.

[47] Gross, A., Jagadeesh, C., and Fasel, H., "Numerical Investigation of Three-Dimensional Separation on Axisymmetric Bodies at Angle of Attack," in *50th AIAA Aerospace Sciences Meeting and Exhibit*, no. AIAA-2012-0097, (Nashville, Tennessee), January 9–12, 2012.

[48] Kim, W.-W. and Menon, S., "An Unsteady Incompressible Navier-Stokes Solver for Large Eddy Simulation of Turbulent Flows," *International Journal for Numerical Methods in Fluids*, vol. 31, pp. 983–1017, Nov. 1999.

[49] Piomelli, U. and Balaras, E., "Wall-Layer Models for Large-Eddy Simulations," *Annual Review of Fluid Mechanics*, vol. 34, no. 1, pp. 349–377, 2002.

[50] Menter, F., "Two-Equation Eddy-Viscosity Turbulence Models for Engineering Applications," *AIAA Journal*, vol. 32, no. 8, pp. 598–605, 1994.

[51] Theron, J. N., Duque, E. P. N., Cicolani, L., and Halsey, R., "Three-Dimensional Computational Fluid Dynamics Investigation of a Spinning Helicopter Slung Load," in *31st European Rotorcraft Forum*, (Florence, Italy), September 13–15, 2005.

[52] Spalart, P., Jou, W.-H., and Strelets, M., "Comments on the Feasibility of LES for Wings, and on a Hybrid RANS/LES Approach," in *Advances in DNS/LES* (C. Liu and Z. Liu, ed.), Greyden Press, Columbus, OH, 1997.

[53] Spalart, P., Deck, S., Shur, S., Squires, M., Strelets, M., and Travin, A., "A New Version of Detached-Eddy Simulation, Resistant to Ambiguous Grid Densities," *Theoretical Computational Fluid Dynamics*, vol. 20, pp. 181 – 195, July 2006.

[54] Speziale, C. G., "Turbulence Modeling for Time-Dependent RANS and VLES: A Review," *AIAA Journal*, vol. 36, no. 2, pp. 173–184, 1998.

[55] Sánchez-Rocha, M. and Menon, S., "The Compressible Hybrid RANS/LES Formulation Using an Additive Operator," *Journal of Computational Physics*, vol. 228, pp. 2037–2062, April 2009.

[56] Sánchez-Rocha, M. and Menon, S., "An Order-of-Magnitude Approximation for the Hybrid Terms in the Compressible Hybrid RANS/LES Governing Equations," *Journal of Turbulence*, vol. 12, pp. 1–22, Mar. 2011.

[57] Menon, S. and Kim, W.-W., "A New Dynamic One-Equation Subgrid Model for Large-Eddy Simulations," in *33rd Annual AIAA Aerospace Sciences Meeting and Exhibit*, no. AIAA-1995-0356, (Reno, NV), January 9–12 1995.

[58] Liggett, N. and Smith, M. J., "Temporal Convergence Criteria for Time-Accurate Viscous Simulations of Separated Flows," *Computers & Fluids*, vol. 66, pp. 140–156, 2012.

[59] Theron, J. N., Gordon, R., Rosen, A., Cicolani, L., Duque, E. P., and Halsey, R. H., "Simulation of Helicopter Slung Load Aerodynamics: Wind Tunnel Validation of Two Computational Fluid Dynamics Codes," in *AIAA 36th Fluid Dynamics Conference and Exhibit*, no. AIAA-2006-3374, (San Francisco, CA), pp. 1–14, June 5–8, 2006.

[60] Liggett, N., *Numerical Investigation of Static and Dynamic Stall of Single and Flapped Airfoils*. PhD thesis, Georgia Institute of Technology, Atlanta, Georgia, 2012.

[61] Sánchez-Rocha, M., Kirtas, M., and Menon, S., "Zonal Hybrid RANS-LES Method for Static and Oscillating Airfoils and Wings," in *4th AIAA Aerospace Sciences Meeting and Exhibit*, no. AIAA-2006-1256, (Reno, NV), Jan. 2006.

[62] Cicolani, L. S. and Kanning, G., "Equations of Motion of Slung Load Systems with Results for Dual Lift," Tech. Rep. NASA TM-102246, National Aeronautics and Space Administration, 1990.

[63] Bisgaard, M., Bendtsen, J. D., and la Cour-Harbo, A., "Modeling of a Generic Slung Load System," *Journal of Guidance, Control, and Dynamics*, vol. 32, pp. 573 – 585, March–April 2009.

[64] Guglieri, G. and Marguerettaz, P., "Dynamic Stability of a Helicopter with an External Suspended Load," *Journal of the American Helicopter Society*, vol. 59, pp. 1–12, October 2014.

[65] Cone, A. C., "Simulation of a Cargo Container Slung Load at Speeds with Signficiant Aerodynamic Effects," Master's thesis, California Polytechnic State University, 2007.

[66] Sharma, S., Raghav, V., Komerath, N., and Smith, M., "Efficient Modeling of Dynamic Blockage Effects for Unsteady Wind Tunnel Testing," in *Proceedings of the 69th American Helicopter Society Annual Forum*, (Phoenix, Arizona), May 20–24 2013.

[67] Sharma, S., Raghav, V., Komerath, N., and Smith, M., "Wall Effect on Fluid-Structure Interactions of a Tethered Bluff Body," *Physics Letters A*, vol. 377, pp. 2079 – 2082, Nov. 2013.

[68] Prosser, D. T. and Smith, M. J., "Navier-Stokes-Based Dynamic Simulations of Sling Loads," in *Proceedings of the 54th AIAA/ASCE/AHS/ASC Structures, Structural Dynamics, and Materials Conference*, no. AIAA-2013-1922, (Boston, Massachusetts), April 8 – April 11 2013.

[69] McAlister, K., Lambert, O., and Petot, D., "Application of the ONERA Model of Dynamic Stall," Tech. Rep. NASA TP 2399, ONERA, 1984.

[70] Peters, D. A., "Toward a Unified Lift Model for Use in Rotor Blade Stability Analysis," *Journal of the American Helicopter Society*, vol. 30, pp. 32 – 42, July 1985.

[71] Rudy, D. J., "Comparison of Rotor Blade Flapping Response with Three Different Dynamic Stall Models," Master's thesis, Washington University, May 1993.

[72] Ahaus, L., Liggett, N., Peters, D. A., and Smith, M. J., "Unsteady Aerodynamics of Single and Multi-Element Airfoils," in *Proceedings of the 36th European Rotorcraft Forum*, (Paris, France), September 7–9 2010.

[73] Ahaus, L. A. and Peters, D. A., "Unified Airloads Model for Morphing Airfoils in Dynamic Stall," in *Proceedings of the American Helicopter Society Specialist's Conference on Aeromechanics*, (San Francisco, California), January 20–22 2010.

[74] Theodorsen, T., "General Theory of Aerodynamic Instability and the Mechanism of Flutter," Tech. Rep. NACA 496, National Advisory Committee for Aeronautics, 1935.

[75] Anderson, W., Rausch, R., and Bonhaus, D., "Implicit/Multigrid Algorithms for Incompressible Turbulent Flows on Unstructured Grids," *Journal of Computational Physics*, vol. 128, no. 2, pp. 391–408, 1996.

[76] Chorin, A., "A Numerical Method for Solving Incompressible Viscous Flow Problems," *Journal of Computational Physics*, vol. 2, no. 1, pp. 12–26, 1967.

[77] Biedron, R. T., Vatsa, V. N., and Atkins, H. L., "Simulation of Unsteady Flows Using an Unstructured Navier-Stokes Solver on Moving and Stationary Grids," in *Proceedings of the 23rd AIAA Applied Aerodynamics Conference*, no. AIAA 2005-5093, (Toronto, Ontario, Canada), June 6–9 2005.

[78] Noack, R., "SUGGAR: A General Capability for Moving Body Overset Grid Assembly," in *17th Computational Fluid Dynamics Conference*, no. AIAA-2005-5117, (Toronto, Ontario), American Institute of Aeronautics and Astronautics, June 2005.

[79] Noack, R., "DiRTlib: A Library to Add an Overset Capability to Your Flow Solver," in *17th Computational Fluid Dynamics Conference*, no. AIAA-2005-5116, (Toronto, Ontario), American Institute of Aeronautics and Astronautics, June 2005.

[80] Smith, M. J., Liggett, N. D., and Koukol, B. C., "Aerodynamics of Airfoils at High and Reverse Angles of Attack," *AIAA Journal of Aircraft*, vol. 48, pp. 2012–2023, November–December 2011.

[81] Lynch, C. and Smith, M., "Hybrid RANS-LES Turbulence Models on Unstructured Grids," in *Proceedings of the 38th AIAA Fluid Dynamics Conference and Exhibit*, (Seattle, WA), June 2008.

[82] Lynch, C. E., Prosser, D. T., and Smith, M. J., "An Efficient Actuating Blade Model for Unsteady Rotating System Wake Simulations," *Computers & Fluids*, vol. 92, pp. 138 – 150, March.

[83] Shenoy, R., *Overset Adaptive Strategies for Complex Rotating Systems*. PhD thesis, Georgia Institute of Technology, Atlanta, Georgia, 2014. https://smartech.gatech.edu/handle/1853/51796.

[84] Shenoy, R., Smith, M., and Park, M., "Unstructured Overset Mesh Adaptation with Turbulence Modeling for Unsteady Aerodynamic Interactions," *AIAA Journal of Aircraft*, vol. 51, pp. 161–174, Jan. 2014.

[85] Shenoy, R. and Smith, M., "Unstructured Overset Grid Adaptation for Rotorcraft Aerodynamic Interactions," in *Proceedings of the 67th American Helicopter Society Annual Forum*, (Virginia Beach, Virginia), May 3–5 2011.

[86] Sitaraman, J., *et al.*, "Evaluation of a Multi-Solver Paradigm for CFD using Unstructured and Adaptive Cartesian Grids," in *46th AIAA Aerospace Sciences Meeting and Exhibit*, (Reno, NV), AIAA-2008-0660, January 2008.

[87] Wissink, A. *et al.*, "Multi-Code Python-Based Infrastructure for Overset CFD with Adaptive Cartesian Grids," in *46th AIAA Aerospace Sciences Meeting and Exhibit*, (Reno, NV), AIAA-2008-0927, January 2008.

[88] Shenoy, R., Holmes, M., Smith, M. J., and Komerath, N., "Scaling Evaluations on the Drag of a Hub System," *Journal of the American Helicopter Society*, vol. 58, pp. 1–13, July 2013.

[89] Phillips, W., Hailey, C., and Gebert, G., "A Review of Attitude Kinematics for Aircraft Flight Simulation," in *AIAA Modeling and Simulation Technologies Conference and Exhibit*, no. AIAA-2000-4302, (Denver, Colorado), August 14–17, 2000.

[90] Nelson, R. C., *Flight Stability and Automatic Control*. New York: McGraw-Hill, 2 ed., 1998.

[91] Biedron, B., "FUN3D Training Workshop Session 9: Overset and 6-DOF Simulations." `http://fun3d.larc.nasa.gov`, July 27–28, 2010.

[92] Hairer, E., Nørsett, S. P., and Wanner, G., *Solving Ordinary Differential Equations I: Nonstiff Problems*. Berlin: Springer-Verlag, 2nd ed., 1993.

[93] Durran, D. R., "The Third-Order Adams-Bashforth Method: An Attractive Alternative to Leapfrog Time Differencing," *Monthly Weather Review*, vol. 119, pp. 702–720, March 1991.

[94] Tyson, P. H., Cicolani, L. S., Tischler, M. B., Rosen, A., Levine, D., and Dearing, M., "Simulation Prediction and Flight Validation of UH-60A Black Hawk Slung-Load Characteristics," in *Proceedings of the 55th American Helicopter Society Annual Forum*, (Montral, Canada), May 25–27 1999.

[95] Hembree, B. and Slegers, N., "Efficient Tether Dynamic Model Formulation Using Recursive Rigid-Body Dynamics," *Proceedings of the Institution of Mechanical Engineers, Part K: Journal of Multi-Body Dynamics*, vol. 224, pp. 353–363, December 2010.

[96] Prosser, D. T. and Smith, M. J., "Characterization of Flow Around Rectangular Bluff Bodies at Angle of Attack," *Physics Letters A*, vol. 376, no. 45, pp. 3204 – 3207, 2012.

[97] Smith, M., Cook, J., Sánchez-Rocha, M., Shenoy, R., and Menon, S., "Improved Prediction of Complex Rotorcraft Aerodynamics," in *Proceedings of the 69th American Helicopter Society Annual Forum*, (Phoenix, Arizona), May 21–23 2013.

[98] Sheldon, D. and Pryor, J., "Study in Depth of a Single Point and Two Point Lateral and Tandem (Longitudinal) Suspensions of Rectangular Box Loads," Tech. Rep. AM/38, The Royal Military College of Science, 1973.

[99] Liu, D. T., "In-Flight Stabilization of Externally Slung Helicopter Loads," Tech. Rep. USAAMRDL Technical Report 73-5, U.S. Army, Fort Eustis, Virginia, 1973.

[100] Hodara, J. and Smith, M. J., "Improvement of Crossflow Aerodynamic Predictions for Forward Flight at All Advance Ratios," in *Proceedings of the 40th European Rotorcraft Forum*, (Southampton, UK), Sept. 2–5 2014.

[101] Larsen, A., "A Generalized Model for Assessment of Vortex-Induced Vibrations of Flexible Structures," *Journal of Wind Engineering and Industrial Aerodynamics*, vol. 57, pp. 281–294, July 1995.

[102] Gupta, H., Sarkar, P. P., and Mehta, K. C., "Identification of Vortex-Induced-Response Parameters in Time Domain," *Journal of Engineering Mechanics*, vol. 122, pp. 1031–1037, November 1996.

[103] Vickery, B. and Basu, R., "Across-Wind Vibrations of Structures of Circular Cross-Section. Part I. Development of a Mathematical Model for Two-Dimensional Conditions," *Journal of Wind Engineering and Industrial Aerodynamics*, vol. 12, pp. 49–73, June 1983.

[104] Solari, G., "The Role of Analytical Methods for Evaluating the Wind-Induced Response of Structures," *Journal of Wind Engineering and Industrial Aerodynamics*, vol. 90, pp. 1453–1477, December 2002.

[105] Bisplinghoff, R., Ashley, H., and Halfman, R., *Aeroelasticity*. Addison-Wesley Publishing Company, Inc, 1955.

[106] Leishman, J. G., *Principles of Helicopter Aerodynamics*. Cambridge: Cambridge University Press, 2nd ed., 2006.

[107] Johnson, W., *Rotorcraft Aeromechanics*. Cambridge: Cambridge University Press, 2013.

[108] Brunton, S. L. and Rowley, C. W., "Empirical State-Space Representations for Theodorsen's Lift Model," *Journal of Fluids and Structures*, vol. 38, pp. 174 – 186, April 2013.

[109] Brunton, S. L., Dawson, S. T., and Rowley, C. W., "State-Space Model Indentification and Feedback Control of Unsteady Aerodynamic Forces," *Journal of Fluids and Structures*, vol. 50, pp. 253 – 270, October 2014.

[110] Kang, C.-k., Baik, Y. S., Bernal, L., Ol, M. V., and Shyy, W., "Fluid Dynamics of Pitching and Plunging Airfoils of Reynolds NUmber Between 1×10^4 and 6×10^4," in *47th AIAA Aerospace Sciences Meeting and Exhibit*, no. AIAA-2009-0538, (Orlando, Florida), January 5–8, 2009.

[111] Jones, R. T., "Operational Treatment of the Nonuniform-Lift Theory in Airplane Dynamics," Tech. Rep. NACA 667, National Advisory Committee for Aeronautics, October 1938.

[112] Prosser, D. T. and Smith, M. J., "Physics-Based Aerodynamic Simulation Models Suitable for Dynamic Behavior of Complex Bluff Body Configurations," in *Proceedings of the 71st American Helicopter Society Annual Forum*, (Virginia Beach, VA), May 4 – 7 2015.

[113] De La Torre, G., Johnson, E. N., and Theodorou, E., "Guidance for Slung Load Operations through Differential Dynamic Programming," in *Proceedings of the 70th American Helicopter Society Annual Forum*, (Montreal, Quebec, Canada), May 20–22, 2014.

[114] Sheldon, D. and Pryor, J., "A Study on the Stability and Aerodynamic Characteristics of Particular Military Loads Underslung from a Helicopter," Tech. Rep. AM/40, The Royal Military College of Science, 1973.

[115] McCroskey, W., "The Phenomenon of Dynamic Stall," Tech. Rep. NASATM-81264, 1981.

[116] Oberkampf, W. and Trucano, T. G., "Verification and Validation in Computational Fluid Dynamics," *Progress in Aerospace Sciences*, vol. 38, pp. 209–272, 2002.

[117] Oberkampf, W., DeLand, S. M., Rutherford, B. M., Diegert, K., and Alvin, K. F., "Error and Uncertainty in Modeling and Simulation," *Reliability Engineering & System Safety*, vol. 35, pp. 333–357, 2002.

[118] Roy, C. J. and Oberkampf, W. L., "A comprehensive framework for verification, validation, and uncertainty quantification in scientific computing," *Comput. Methods Appl. Mech. Engrg.*, vol. 200, pp. 2231–2144, 2011.

VITA

Daniel T. Prosser is the son of Neil and Holly Prosser. He was born and grew up in Buffalo, NY. He attended Starpoint Central School during middle school and high school. As a child, he developed a strong interest in flying things, including airplanes, helicopters, and birds. In high school, he became excited about math and physics and decided to go into engineering. Daniel studied Mechanical Engineering with a concentration in Aerospace at the Rochester Institute of Technology, where he obtained both a Bachelor's and Master's degree in 2011. He came to the Georgia Institute of Technology in August 2011 as a graduate research assistant, where he worked in the field of computational fluid dynamics under Professor Marilyn Smith.

While at Georgia Tech, Daniel remained an active member of both the American Helicopter Society, where he served as treasurer of the Atlanta chapter from 2013–2014 and president from 2014–2015, and the American Institute of Aeronautics and Astronautics. His awards and honors include the RIT Outstanding Undergradute Scholar Award, the Georgia Tech President's Fellowship, the Vertical Flight Foundation scholarship, and the Achievement Rewards for College Scientists (ARCS) Award. Outside of work, he enjoys playing soccer, baseball, and hockey, playing the piano and organ, and designing, building, and flying model airplanes and helicopters. Upon completion of his PhD, he plans to join the Naval Air Systems Command (NAVAIR) in Patuxent River, Maryland.